THE UNIVERSITY *of* EDINBURGH

A Novel Immersed Boundary Method for Direct Numerical Simulations of Solid-Fluid Flows

Pei Shui

A thesis submitted for the degree of Doctor of Philosophy.
The University of Edinburgh.
February 12, 2015

Abstract

Solid-fluid two-phase flows, where the solid volume fraction is large either by geometry or by population (as in slurry flows), are ubiquitous in nature and industry. The interaction between the fluid and the suspended solids, in such flows, are too strongly coupled rendering the assumption of a single-way interaction (flow influences particle motion alone but not vice-versa) invalid and inaccurate. Most commercial flow solvers do not account for two-way interactions between fluid and immersed solids. The current state-of-art is restricted to two-way coupling between spherical particles (of very small diameters, such that the particle-diameter to the characteristic flow domain length scale ratio is less than 0.01) and flow. These solvers are not suitable for solving several industrial slurry flow problems such as those of hydrates which is crucial to the oil-gas industry and rheology of slurries, flows in highly constrained geometries like microchannels or sessile drops that are laden with micro-PIV beads at concentrations significant for two-way interactions to become prominent. It is therefore necessary to develop direct numerical simulation flow solvers employing rigorous two-way coupling in order to accurately characterise the flow profiles between large immersed solids and fluid. It is necessary that such a solution takes into account the full 3D governing equations of flow (Navier-Stokes and continuity equations), solid translation (Newton's second law) and solid rotation (equation of angular momentum) while simultaneously enabling interaction at every time step between the forces in the fluid and solid domains.

This thesis concerns with development and rigorous validation of a 3D solid-fluid solver based on a novel variant of immersed-boundary method (IBM). The solver takes into account full two-way fluid-solid interaction with 6 degrees-of-freedom (6DOF). The solid motion solver is seamlessly integrated into the Gerris flow solver hence called Gerris Immersed Solid Solver (GISS). The IBM developed treats both fluid and solid in the manner of "fluid fraction" such that any number of immersed solids of arbitrary geometry can be realised. Our IBM method also allows transient local mesh adaption in the fluid domain around the moving solid boundary, thereby avoiding problems caused by the mesh skewness (as seen in common mesh-adaption algorithms) and significantly improves the simulation efficiency.

The solver is rigorously validated at levels of increasing complexity against theory and experiment at low to moderate flow Reynolds number. At low Reynolds numbers ($Re\ 1$) these include: the drag force and terminal settling velocities of spherical bodies (validating translational degrees of freedom), Jeffrey's orbits tracked by elliptical solids under shear flow (validating rotational and translational degrees of freedom) and hydrodynamic interaction between a solid and wall. Studies are also carried out to understand hydrodynamic interaction between multiple solid bodies under shear flow. It is found that initial distance between bodies is crucial towards the nature of hydrodynamic interaction between them: at a distance smaller than a critical value the solid bodies cluster together (hydrodynamic attraction) and at a distance greater than this value the solid bodies travel away from each other (hydrodynamic repulsion). At moderately high flow rates ($Re\ O(100)$), the solver is validated against migratory motion of an eccentrically placed solid sphere in Poisuelle flow. Under inviscid conditions (at very high Reynolds number) the solver is validated against chaotic motion of an asymmetric solid body.

These validations not only give us confidence but also demonstrate the versatility of the GISS towards tackling complex solid-fluid flows. This work demonstrates the first important step towards ultra-high resolution direct numerical simulations of solid-fluid flows. The GISS will be available as opensource code from February 2015.

Declaration of originality

I declare that this thesis has been composed by myself and is all my own work except where otherwise stated. This thesis has not been submitted for any other degree or professional qualification except as specified.

Acknowledgements

I gratefully acknowledge the generous financial support of the Principal's Career Development PhD Scholarship and Edinburgh Global Research Scholarship from the University of Edinburgh, and also thank to the travelling support to France from the Richard Brown Scholarship, and to China and United States from the ThermaPOWER project.

I would like to thank my supervisor Dr. Prashant Valluri for guiding and supervising my work. Dr. Prashant Valluri has provided his expert advice and encouragement which lead me through my PhD. He also enlightened me about the importance of contribution to science and society. It has been a great pleasure working with him. I would also like to thank my second supervisor, Dr. Martin Crapper who provided many useful suggestions on my research.

I am grateful to Professor Stéphane Zaleski (Université Pierre et Marie Curie, Paris) and Dr. Stéphane Popinet (now at Centre National de la Recherche Scientifique at UPMC Paris and previously at National Institute of Water and Atmospheric Research at New Zealand). The Gerris program they developed was used as the base of my research. It has been a pleasure collaborating with Professor Zaleski's team in France. I am also grateful to Professor Chris Lawrence in the SPT group of Schlumberger at Norway, who provided very valuable suggestion on the research direction.

I would like to express my gratitude to Professor Khellil Sefiane who enrolled me into the ThermaPOWER project, where I can extend my research with thermal effect and obtain great cooperation experience with the colleagues from Shanghai Jiao Tong University and The University of Maryland, College Park.

The PhD degree is a summing-up of my student life, therefore I would like to thank memorable teachers in my life: Tingyin Feng, Shuchao Wang, Professor Minghou Liu in the University of Science and Technology of China, Dr. Chunho Liu and Professor Yuguo Li in the University of Hong Kong.

I am also very thankful to my friends and colleagues Dr. Xianfeng Fan, Dr. Mike Davidson,

Dr. Pedro Saénz, Dr. Emad Alhseinat, Dr. Yuan Wang, Patrick Schimidt, Xu Xu, Yunning Li, Xingxun Li and other students in the office for their friendship, advice and support.

I thank my parents for their unwavering love. Their encouragement strengthened my faith and confidence. I am also thankful to the friends in Edinburgh and in China who have always been supporting.

Contents

List of figures

List of tables

Acronyms and abbreviations

CFD	Computational fluid dynamics
DNS	Direct numerical simulation
DOF	Degree of freedom
DLM	Distributed Lagrange multiplier
GISS	Gerris immersed solid solver
IBM	Immersed boundary method
LBM	Lattice Boltzmann method

Nomenclature

$\mathbf{A}$	area vector of the cut face
a	volume fraction of fluid on the cell
C_d	drag coefficient on the particle
D	diameter of sphere
D_i	initial distance between particle centre
Δ_x	grid size
δ	boundary layer thickness
e_x	component of Eulerian angle
ε	geometric aspect ratio of ellipsoid
E	kinetic energy ratio
F_d	drag force on the particle
F_{d0}	drag force on the sphere
$\mathbf{f_s}$	solid force term
F_{shear}	shear component of the drag force
$F_{pressure}$	drag component of the drag force
γ	shear rate
g	gravitational acceleration
$\mathbf{g}_{eff}$	effective gravitational acceleration
k_r	rotational kinetic energy
k_t	translational kinetic energy of solid and surrounding fluid
k_{tot}	total kinetic energy
L	domain size
L_c	characteristic length
λ_f	ratio between shear force and pressure force
λ_L	Lyapunov exponent
M	mesh resolution
μ	dynamic viscosity of fluid

N	refinement level of mesh
ν	kinematic viscosity of fluid
Ω	angular velocity
ω	vorticity
q_0	component of quaternions
R	radius of sphere
Re_f	pipe Reynolds number
Re_p	particle Reynolds number
ρ_f	fluid density
σ_ω	square root of the sum of every variants of the angular velocity components
S	separation distance
S_t	Strouhal number
s_x	fluid fraction on the cell surface of x direction
ς	relative error
T	rotation period
θ	phase position of solid
$\mathscr{T}$	torque from fluid applied on the solid surface
$\mathscr{T}_n$	normal component of torque
$\mathscr{T}_t$	tangential component of torque
$\mathbf{U}$	velocity vector of the solid centroid
u_{bla}	boundary layer velocity
U_c	characteristic velocity
U_0	Incident velocity of the fixed solid case
U_s	slip velocity in stream-wise direction
U_t	terminal velocity of the settling solid case
VOF	Volume of fluid
ξ	mesh refinement criterion
$\mathbf{X_c}$	coordinates of the particle centroid in global frame
$\mathbf{X_p}$	coordinates of the tracked point in global frame
$\mathbf{X_r}$	relative location of the tracked point to the particle centroid
$\mathbf{x_1}$	the centroid position of solid with initial location at $(0., 0, 0)$

$\mathbf{x_2}$	the centroid position of solid with initial location at $(0.5, 0, 0)$	

Chapter 1
Introduction

1.1 Research Background

A solid-fluid flow represents a two-phase flow of a fluid continuum carrying immersed solids suspended and conveyed by the coupled interaction between the flow environment and the solid body. The purpose of studying those liquid-solid flow process can be chemical reactions between liquid and solids, or the physical processes of the solids' transport itself. Such kind of flow can be characterized in two different way: when the flow mechanism bounded by the boundary is of the main interest, the flow can be characterized by the *Pipe Reynolds Number (Re_f)* and when the flow mechanism between fluid and solids is of the main interest, the flow can be characterized by *Particle Reynolds Number (Re_p)*. Re_p is a major characteristic parameter in this thesis work and its definition for corresponding problem can be found in each chapter.

The strategy to study the solid-fluid flow can also be categorized to two different ways: One is to treat the mixture of massively distributed solid particles in the flow and the carrier fluid as an unified mixture, and the existence of the solid part can change mixture behaviour from Newtonian to Non-Newtonian. In such cases, the individual characteristics of each solid particle is usually simplified and the overall behaviours of the solid particles are considered. On the other hand, when the scale of the solid particle is large, both the fluid and solid phase can strongly interact with each other, thereby great influencing the whole system. The focus in this thesis is on solid bodies that have a size that is comparable to the domain size. Hence, the solid bodies are generally referred to as a '*solid*'. It must be noted that a solid body would behave as a '*particle*' when its size is much smaller than the domain size.

Solid-fluid flows exist in a wide range of engineering applications in petroleum industries [1], chemical process industries [2] and even the medical science [3]. In oil-gas industry, the petroleum or natural gas transported in the subsea pipelines usually contain a large amount of

ice crystals called hydrates whose sedimentation can cause clogging of pipelines and is a major hazard. Thus a study of this phenomenon can reveal key hydrate rheology characteristics that can be exploited to improve oil transport performance (Fig. 1.1). Closed domain simulating multi-particle motion and sedimentation (Fig. 1.2) can be utilised for improving catalytic performance and hence increase yields for fluidization process. The transport of blood cells in the vessels is another important application of solid-fluid flows where red blood cells can be represented as elastic solids. These simulations can inform the design of microfluidic devices for blood-plasma separation (Fig. 1.3). Most recently, micro-PIV methods are being used to study droplet evaporation [12]. However, at the contact line where evaporation is maximum, the relative concentration of particles is very high, which means that hydrodynamics there are intricately coupled to the motion of the micro-PIV beads. Detailed simulations will help reveal the behaviour of these micro-PIV beads in such constrained environments near the contact line, also demonstrating the efficacy of micro-PIV methods towards accurate determining of contact line motion.

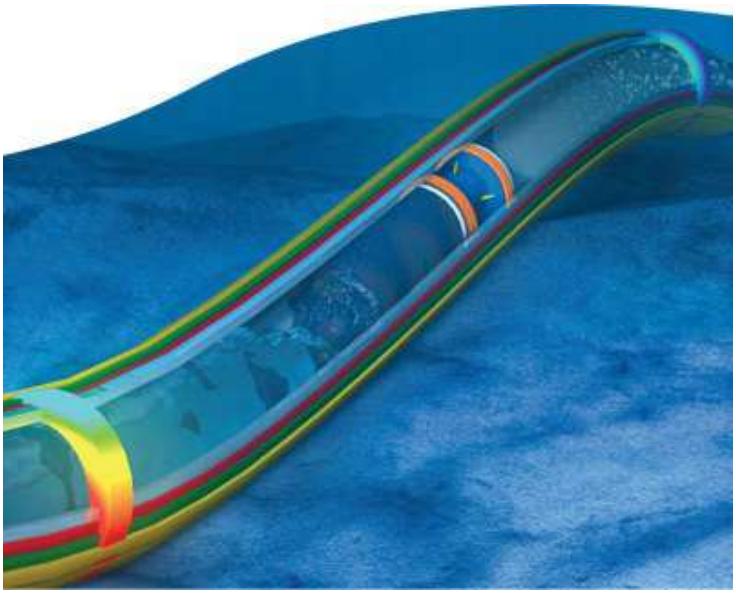

Figure 1.1: *Petroleum transport blocked by the sedimentation in the sub-sea pipeline. [1]*

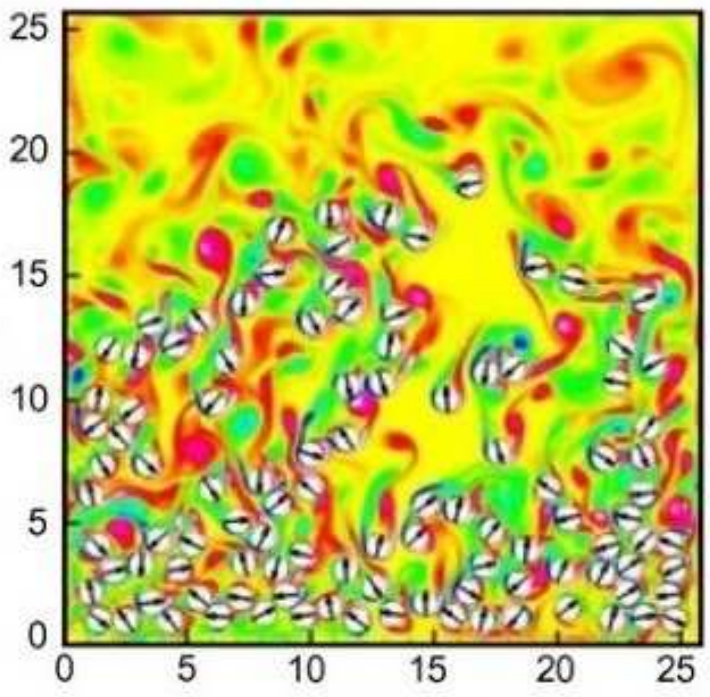

Figure 1.2: *IB method simulation study of sedimentation process of multi particles system in a close domain. [2]*

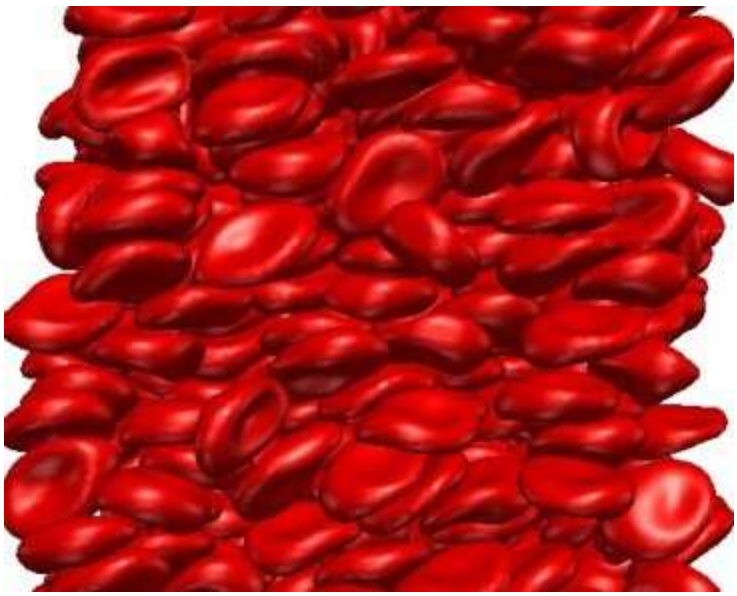

Figure 1.3: *IB method simulation study of the blood cells flowing in the vessel. [3]*

1.2 Research Targets

It is essential to point out the current design of these applications is mostly based on a high-level of empiricism. An in-depth understanding of these flows can bring about a significant step-change in the current state-of-art while economising the costs simultaneously. This thesis work describes and validates (at increasing physical complexity) a novel, powerful and a bespoke direct numerical simulation (DNS) solver that has been developed to study the dynamic solid-fluid coupling interaction in three-dimensions (3D) and accounting for six degrees-of-freedom (6DOF) solid motion. This DNS solver comprises of two major subsolvers that interact simultaneously: a solid motion subsolver which calculates the dynamic location of solid particles via the solution of equations of translational and rotational momentum and a fluid subsolver based on Gerris [13] which calculates the local velocity and pressure fields as a solution of the 3D Navier-Stokes equations. The Gerris fluid solver is fully parallelised. Hence the solver is named as the Gerris Immersed Solid Solver (GISS). The fluid solver employs a novel variant of the immersed boundary method:

- The solver allows both fluid phase and solid phase to be described by one universal frame using volume of fluid (VOF) method;
- The solver can describe arbitrary geometry features with Cartesian mesh and greatly simplifies the procedure of mesh generation.
- The solver can perform dynamical quad/octree mesh optimization and significantly improves the simulation efficiency.
- The solver can handle arbitrary number of solids with arbitrary geometry features and 6DOF motion.
- The solver allows solid-fluid coupling that both phases dynamically interact with each other at every timestep.

The DNS solver would be rigorously validated against key theories in this thesis work and intends to reveal several new flow features:

1. Find the necessary simulation configuration requirement by validating the settling and rotating of spheres and ellipsoids at wide range of Re_p including Stokesian regime separately

2. Validate the solution of rotational equations of the immersed solid solver by simulating the Jeffery's orbits [14] tracked by neutrally buoyant ellipsoids in shear flows.

   The above two studies would ensure the reliability and requirements of the simulation.

3. Validate the hydrodynamic interaction between walls and solids (spheres and ellipsoids) against Stokesian analysis of Hsu and Ganatos [5]. The capability of handling the coexistence of both translation and rotation behaviour of solids would be validated. And the relation between migration patterns and solid geometry and initial position would be studied in this thesis work.

4. Study the hydrodynamic interactions with two-solids in shear flow (for the first time in 3D) and reveal the factors responsible for hydrodynamical clustering (attraction) or repulsion (separation).

5. For the first time, validate the chaotic motion of a general ellipsoid in inviscid and viscous fluids using 3D simulations and and try to quantify the conditions triggering the chaotic behaviour.

Gerris Immersed Solid Solver (GISS) is the ultimate product of this thesis study (Fig .1.4). GISS constructs the immersed solids in the Cartesian grids with the complex solid geometry described by GTS library, enforces the no-slip boundary condition on the immersed solid surface during the flow calculation of Gerris, and calculates forces and torques applied to the immersed solid, and calculates the solid motion with assistance of ODE.

It is important at this point to indicate that the GISS developed during this thesis work is a DNS solver with the ability to account for 3D flows of immersed solids of any shape and number. However, the tool is undergoing development to account for several levels of parallelisation in order that DNS of a wider range of flows (from viscous to inertial, $0.1 \leq Re_p \leq 50$) can be accurately simulated. As indicated earlier, though the Gerris flow solver is completely parallelised, parallelisation of the solid motion solver is beyond the scope of this work due to

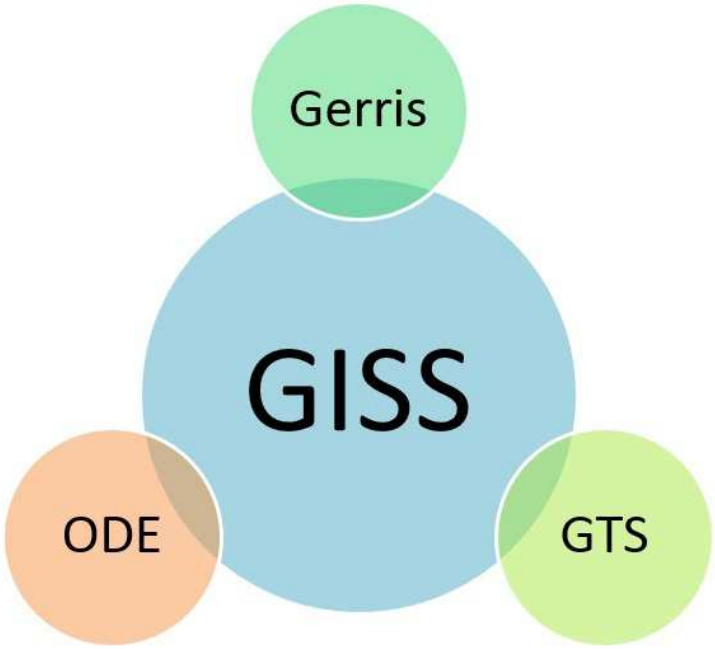

Figure 1.4: *The structure of GISS*

complexities involved with the immersed boundary method and the coupled dynamic interaction with the flow solver. It must be noted that this is being pursued independently. Hence the thesis focusses mainly on rigorous validation at low Re_p within this thesis with the DNS strategy of the full Navier-Stokes equations.

1.3 Thesis Outline

This thesis work is organized as follows:

1. Chapter 2 reviews relevant literature and provides the development history of the solid-fluid flow simulation technique. The advantages and disadvantages of those different simulation techniques are both introduced and compared.

2. Chapter 3 details the methodology of GISS, explaining how the Gerris flow solver couples to the immersed solid motion solver, how the immersed boundary method is employed, its efficient mesh adaptation technique, as well as the additional 6DOF solid moving module developed and adopted by this research.

3. Chapter 4 focusses on validation of the GISS against standard case-studies of single settling solid under various conditions including: drag coefficient comparison with particle Reynolds number (Re_p) covering from Stokes' regime to Newtonian regime, Stokes' settling case which has analytical solution to compare with and experimental work with Re_p covering from 1 to 1000.

4. Chapter 5 validates GISS for solid rotation against the classical Jeffery's orbit [14] case and the influence of wall-particle hydrodynamic interaction on the translation-rotation of a tumbling mono ellipsoid particle testing the 6DOF capacity of the GISS.

5. Chapter 6 exploits the validated 6DOF capability of the GISS to describe behaviour of twin-ellipsoids migration in the shear flow. This chapter also reveals new physical insights responsible for hydrodynamic repulsion and attraction.

6. Chapter 7 validates the inviscid Euler equation mode in GISS against the classical Aref [10] problem of a chaotic motion of an asymmetric solid particle. This chapter also presents for the first time the influence of 3D solid geometry on the chaotic orbits tracked by the solids.

7. Chapter 8 summarises the conclusions drawn from this thesis work and recommends way forward.

Chapter 2
Literature Review

Literature on solid-fluid flows is vast. However, in this chapter literature concerning only flows tackled in this thesis were reviewed. These include flows around single solids at low Re_p, hydrodynamic interactions (wall-solid and solid-solid) and flows around single solids in inviscid flows. Both modelling (including analytical and numerical) and experiments are reviewed. A brief overview of numerical simulation techniques used to resolve solid-fluid flow systems is also presented.

2.1 Flow of a Single Solid (Particle) at Low Particle Reynolds Number

2.1.1 Stokes' Settling Problem

The most well-known solid-fluid coupling problem probably is the Stokes' settling problem [15] [16], named after Sir. George Gabriel Stokes who in 1851 explicitly deduced the frictional force (drag force) applied on a spherical solid particle in a viscous fluid at low particle Reynolds number (Re_p):

$$Re_p = \frac{\rho_f U_c L_c}{\mu} \tag{2.1}$$

Where ρ_f is the fluid density, μ is the dynamic viscosity of the fluid, U_c is the characteristic velocity of the fluid and L_c is the characteristic length of the solid particle.

Stokes solved the simplified the momentum equation of the NavierStokes equations:

$$\rho(\frac{\partial \mathbf{u}}{\partial t} + \mathbf{u} \cdot \nabla \mathbf{u}) = -\nabla p + \mu \nabla^2 \mathbf{u} + \mathbf{f} \tag{2.2}$$

to the Stokes Equations:

$$\mu \nabla^2 \mathbf{u} - \nabla p + \mathbf{f} = 0 \tag{2.3}$$

His conclusion is known as Stokes' Law:

$$F_{d0} = 6\pi\mu UR \tag{2.4}$$

Where F_{d0} is the drag force applied on the sphere particle, U is the travelling velocity of the sphere and R is the radius of the sphere. The flow at low particle Reynolds number ($Re_p \leq 1$) is therefore named after him as Stokes flow (also known as creeping flow). His simplifications were based on assumptions including: Re_p is assumed to be pseudo-zero so that the inertial effects can be neglected; the solid particle material is rigid so that its shape is non-deformable during the study; the fluid being studied is Newtonian so that the viscous stress is proportional to the local strain rate; the fluid domain is infinitely large and no boundary effect needs to be considered. These assumptions based on Stokes flow linearise the Navier-Stokes Equations and bring considerable simplifications [17] [18] (Eq. 2.3, Eq. 2.3). Within all those assumptions, the pseudo-zero Re_p assumption is the most critical one as the actual Re can never become zero unless there is no motion of fluid at all. Usually a very small Re_p ($\ll 1$) is considered to be a proper approximation to the assumption. The other assumptions are relatively easier to be satisfied in the practical situations [19] [20] when particle deformations and non-Newtonian effects are suitably weak and the particle is relatively small compared to the whole control domain.

During the development history of fluid dynamics, Stokes' Law has been studied extensively for more general situations. One important study is of Payne [21] who considered the effect of the shape of the solids. Payne provided the analytical solution for the particles of ellipsoidal shapes under these conditions: The shape of ellipsoid should be rotationally symmetric (with two of its axes being of equal size) and its polar axis of symmetry parallel to the flow direction. Under these conditions, the relation between drag force and the settling velocity of the ellipsoid can be analytically presented by applying a modification factor depending on the geometric aspect ratio ε (the ratio between the polar axis and the equatorial diameter) to the original Stokes' Law.

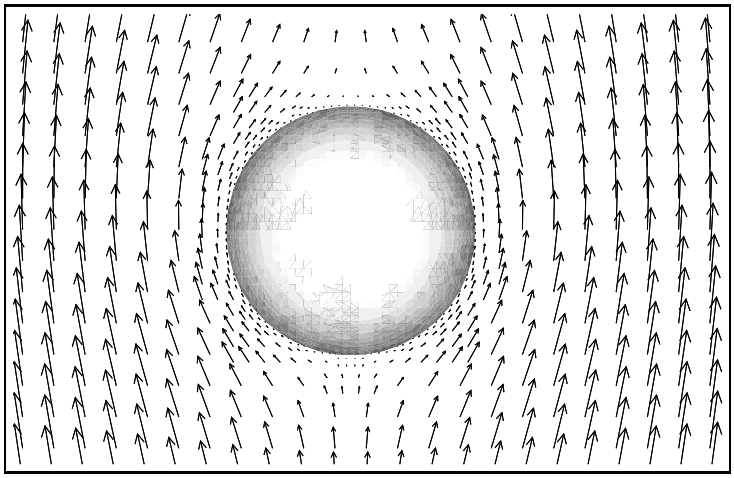

(a) Stand sphere particle in Stokes' flow

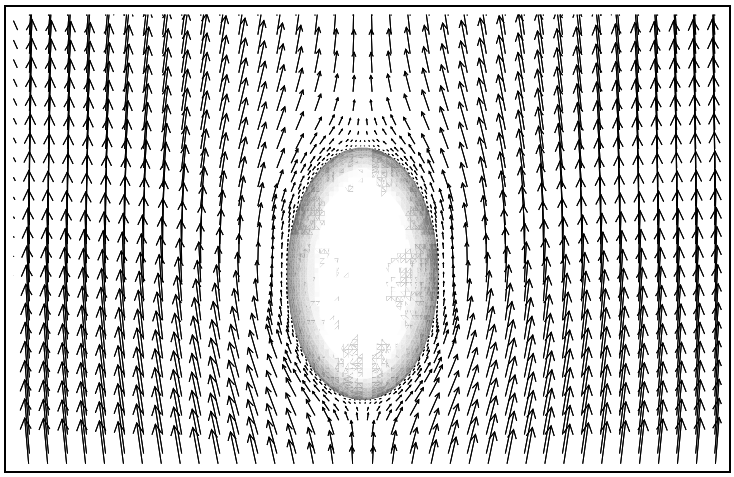

(b) Prolate ellipsoid particle in Stokes' flow

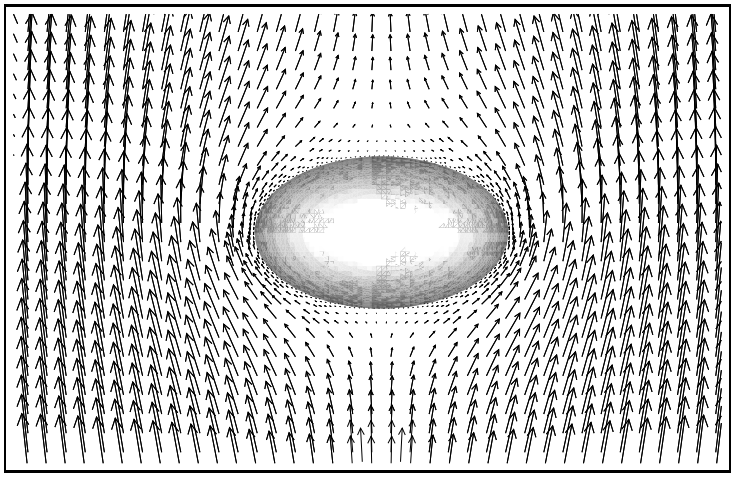

(c) Oblate ellipsoid particle in Stokes' flow

Figure 2.1: *Stokesian flows around solids of different geometries - A DNS solution by GISS.*

For prolate ellipsoid whose $\varepsilon > 1$, as shown in Fig. 2.1(b), the modified drag force is:

$$F_d(\varepsilon) = \frac{\frac{4}{3}(\varepsilon^2 - 1)}{\frac{2\varepsilon^2-1}{\sqrt{\varepsilon^2-1}} \ln(\varepsilon + \sqrt{\varepsilon^2 - 1}) - \varepsilon} F_{d0} \tag{2.5}$$

And for oblate ellipsoid whose $\varepsilon < 1$, as shown in Fig. 2.1(c), the modified drag force is:

$$F_d(\varepsilon) = \frac{\frac{4}{3}(1 - \varepsilon^2)}{\frac{1-2\varepsilon^2}{\sqrt{1-\varepsilon^2}} \arctan \frac{\sqrt{1-\varepsilon^2}}{\varepsilon} + \varepsilon} F_{d0} \tag{2.6}$$

where F_{d0} is the drag force on the sphere with same characteristic length (the diameter/axis perpendicular to the settling direction).

Besides the modification introduced by the particle geometry, the influence of the domain boundary was also systematically studied. The original Stokes' Law was derived with the assumption that the fluid domain should be infinitely large and no boundary effect needed to be considered. However, in many practical situations, the existence of the wall within finite distance to the particle can become an important source of an additional hydrodynamic force. Therefore in such situations the effects of those walls should be accounted in and necessary modifications should be applied to the Stokes' Law.

Lorentz [22] found that when a spherical particle moves towards to the wall, the Stokes' Law should be modified by a factor based on the ratio between the sphere radius and its instantaneous distance to the wall, yet he did not obtain the exact relation. Brenner [23] extended this study and provided the exact solution for this sort of problem where the spherical particles moves in a infinitely wide fluid domain and towards to or away from a rigid wall. In that study, the bounding aspect ratio λ is the sphere radius over the distance between the particle centre and the wall, as shown in Fig. 2.2(a). The modified drag force is:

$$F_{d1} = \left(1 + \frac{3}{4}\lambda + \frac{9}{16}\lambda^2 + \frac{19}{64}\lambda^3 + + \frac{93}{256}\lambda^4 + + \frac{387}{1024}\lambda^5 + ...\right) F_{d0} \tag{2.7}$$

Similar to the previous problem, the spherical particle motion parallel to a plane wall was comprehensively studied by Goldman [24] and Cox [25]. In that study, the bounding aspect ratio λ is also the sphere radius over the distance between the particle centre and the wall, as

shown in Fig. 2.2(b). The modified drag force is:

$$F_{d2} = \left(1 - \frac{9}{16}\lambda + \frac{1}{8}\lambda^3 - \frac{45}{256}\lambda^4 - \frac{1}{16}\lambda^5\right)^{-1} F_{d0} \tag{2.8}$$

Another classical study is the falling of a standard sphere particle in a circular cylinder tube. The direction of fall is along the axis of the cylinder tube whose wall is rigid and the flow remains stationary. To limit the possible variables, the length of the tube in the falling direction is assumed to be infinitely long so that only the influence of the radial wall can be considered. This problem was thoroughly studied by Haberman and Sayre [26] and the influence of the diameter ratio between the sphere particle and the cylinder tube were exactly provided. In that study, the bounding aspect ratio λ is the sphere radius over the cylinder radius, as shown in Fig. 2.2(c). The modified drag force is:

$$K_1 = \frac{1 - 0.75857\lambda^5}{1 - 2.1050\lambda + 2.0865\lambda^3 - 1.7068\lambda^5 + 0.72603\lambda^6} \tag{2.9}$$

$$K_2 = \frac{1 - \frac{2}{3}\lambda^2 - 0.20217\lambda^5}{1 - 2.1050\lambda + 2.0865\lambda^3 - 1.7068\lambda^5 + 0.72603\lambda^6} \tag{2.10}$$

$$F_{d3} = (UK_1 - VK_2)F_{d0} \tag{2.11}$$

Where U is the sphere velocity and V is the maximum flow velocity of Poiseuille flow in the cylinder tube.

2.1.2 Jeffery's Orbit Problem

The works discussed in the last section mainly concerned with the translational motion of a single particle at low Re. In this section, works concerning the rotation of immersed solids were reviewed briefly. Jeffery [14] was first to provide a thorough theoretical study on the rotation of a ellipsoid immersed in a viscous fluid. The ellipsoid in that study is neutrally buoyant which means that the density of the solid particle and the fluid around it are the same, as shown in Fig 2.3. The flow in that study was Newtonian fluid with a constant shear such that the Re_p of the flow is in the Stokes' regime. Jeffery successfully described the rotation of the ellipsoids with an analytical solution by neglecting solid's inertial effects,

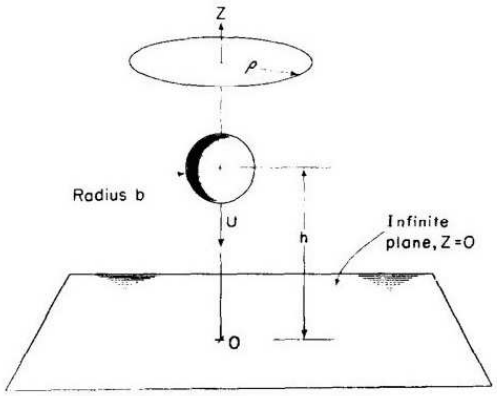

(a) Bouding of a plane wall at the settling direction [23]

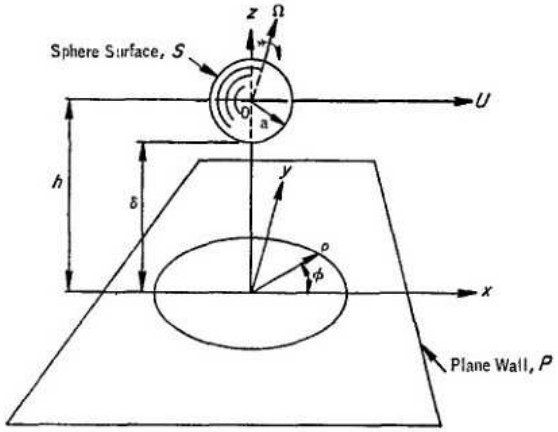

(b) Bouding of a plane wall parallel to the settling direction [24]

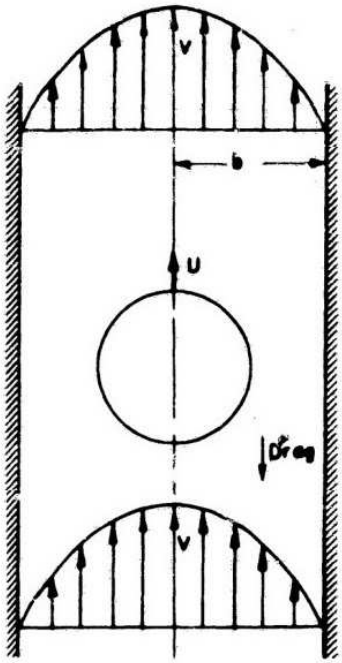

(c) Bounding of a cylinder tube [26]

Figure 2.2: *Three different bounding effect from the wall.*

Brownian motion and further employed an assumption that the ellipsoid should tend to adopt the motion corresponding to the least dissipation of energy, which means the ellipsoid was expected to eventually rotate with its polar axis along with the vortices axis of the shear. The presented motion pattern was named after him as Jeffery's orbits. The period of rotation were proven to be only dependent on the shape of the ellipsoid (in the form of geometric aspect ratio ε) and the scale of the pre-defined shear of the domain:

$$T_\varepsilon = \frac{2\pi(\varepsilon^2 + 1)}{\varepsilon\gamma} \tag{2.12}$$

However, if that additional assumption of least energy dissipation was not satisfied, the rotation patterns of ellipsoids would be dependent on their initial angular positions to the flow. Based on that, Harper and Chang [27] and Leal [28] also adopted perturbation theory to achieve the approximate solution for arbitrary three-dimensional body moving in the shear flow whose Re_p remained in the Stokes' regime.

Besides the theoretical studies, there are a number of relevant experimental works in the literatures. Taylor [29] [30] validated Jeffery's study with a series of experimental investigation. In his study, two possible moving patterns that follow Jeffery's "minimum energy dissipation hypothesis" were observed in the experiment:

- A prolate ellipsoid set its major axis parallel to the vortex lines that perpendicular to the plane of the undisturbed motion of fluid and then kept rotating with a constant angular velocity;
- An oblate ellipsoid set its equatorial diameter parallel to the vortex lines that perpendicular to the plane of the undisturbed motion of fluid and then kept rotating with a periodic variable angular velocity.

Suppose the velocity of the upper ($+y$) and lower wall ($-y$) was in $+x$ and x direction, then the axis of the shear is in z direction. If the minor axis of the prolate ellipsoid is just in z direction, according to Jeffery's equation, this is a special case where the prolate ellipsoid keeps rotating about the z axis at a fixed point(Fig. 2.3). However, if there is an angle between the rotation axis of the ellipsoid and the shear, the rotation axis would evolve towards

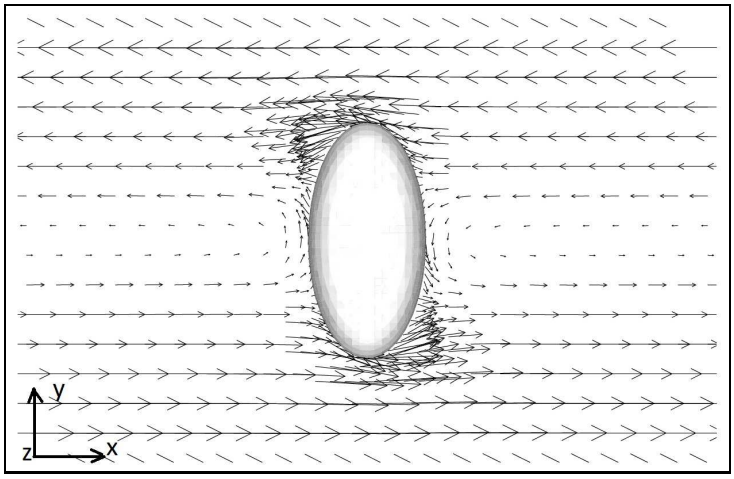

(a) t=0T

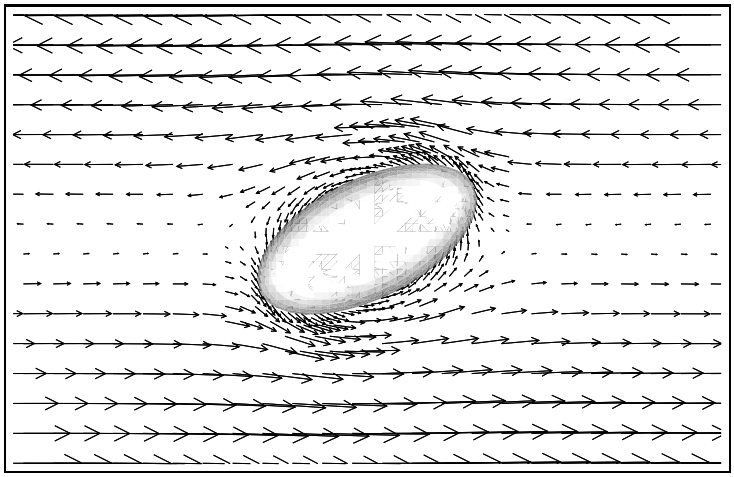

(b) t=0.1T

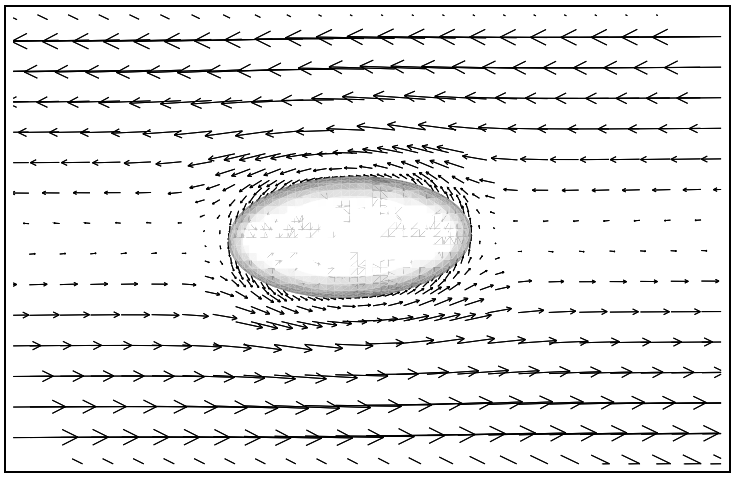

(c) t=0.25T

Figure 2.3: *Jeffery's Orbit Case A: The polar axis of the ellipsoid remains in the presented cross section.*

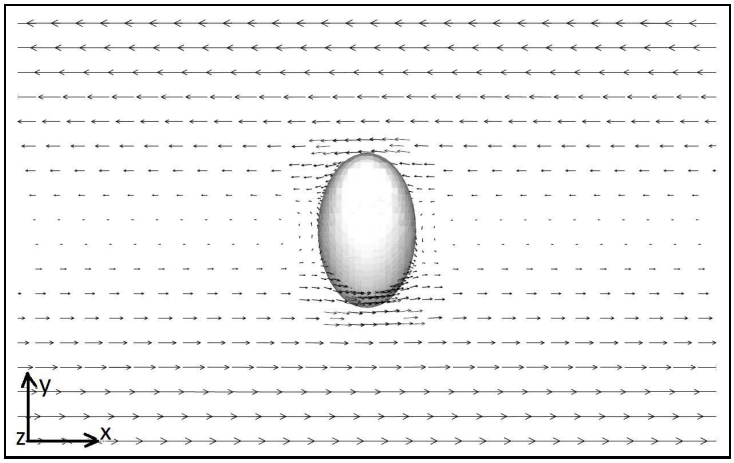

(a) t=0T

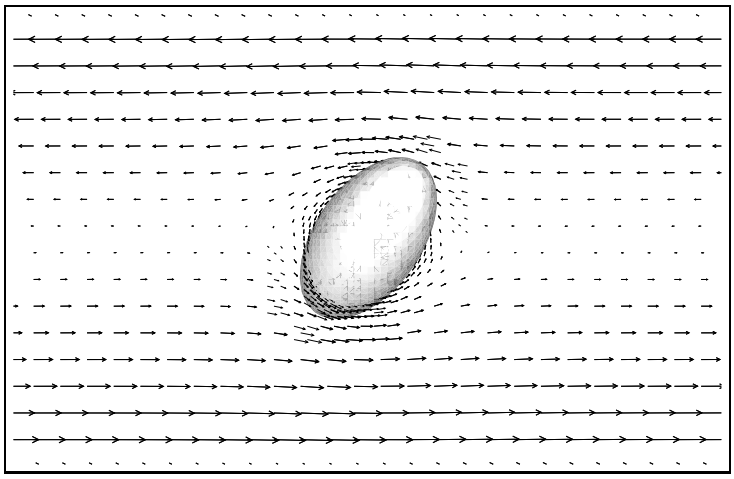

(b) t=0.25T

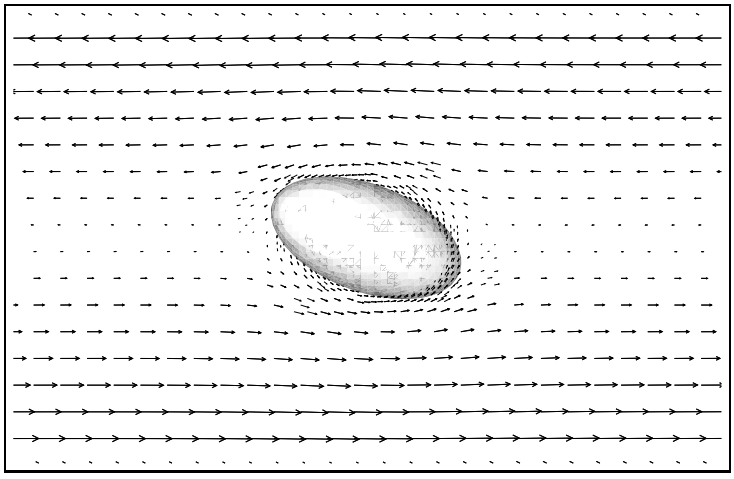

(c) t=0.5T

Figure 2.4: *Jeffery's Orbit Case B: The polar axis of the ellipsoid is initially not aligned with shear but subtends an angle with it. The simulation depicts evolution of this angle to align with the shear which is the configuration for least energy dissipation.*

eventually attaining the configuration with least energy dissipation (see Fig. 2.4), described before (Fig. 2.3).

Those experiments showed the strong influence of initial conditions on the time taken to achieve the period of rotation given by Eq. 2.12. For oblate ellipsoids not aligned with the direction of shear gradient take around 85 rotations to get to state of minimum energy dissipation. Misaligned prolate ellipsoids take around 370 rotations before stabilising to a rotational time period, as shown in Fig. 2.4. However, if the initial placement of the solid is in the direction of shear gradient, the work showed that the solids stabilise to the ideal Jeffery's orbit solution after a very fast initiative adjustment, as shown in Fig. 2.3. Sergre [31], Karnis, Goldsmith and Mason [32] [33] in their experimental studies also observed the axial migration of the ellipsoid in the Poiseuille flow and attributed that result to Magnus inertial effect. Besides the solids' migrations, they also reported the rotation behaviour of the prolate ellipsoid agreed quite well with the prediction of Jeffery's orbit theory when the Re_p was in the Stokes' regime.

Other extensive studies of Jeffery's orbits problem usually employ numerical methods and approach zero Re assumption via limiting $Re \leq 1$, just as in the Stokes' flow problems mentioned in Section. 2.1.1. Due to the limit of the computational resource, the early stage of the study was restricted to two dimensional (2D) simulations. Feng and Joseph [34], Feng et al. [35] used finite element method to validate Jeffery's orbits theorem at $Re \approx 1$ in 2D. Simulating the rotation of solids immersed in flow in three dimensions (3D) is a complex task, due to fact that the 3D flow governing equations need to solved simultaneously along with the solid motion governing equations (both translational and rotational momentum conservation) at every timestep. As the solid rotates it would cut across the numerical mesh in the flow domain dynamically which demands a careful choice of a timestep and efficient mesh adaptation strategies (refining the mesh close to the solid surfaces). This is essential to ensure the correct imposition of the no-slip boundary condition near the walls which in turn ensures that the calculation of viscous tensor around the solids is accurate at each timestep. Furthermore, in the conventional dynamic mesh adaptation (DMA) methods as the solid rotates and cuts across the numerical mesh of the flow domain the mesh elements close to the wall get skewed which would corrupt the simulation and introduce a high numerical error, like in Fig. 2.5.

Hence many methods other than DMA method have been developed, such as the immersed boundary method (IBM), distributed Lagrange-multiplier method (DLM), Lattice Boltzmann method (LBM) and so on. A review of these methods is presented in the following section. Ding and Aidun [36] reported a 3D numerical study with LBM to simulate the motion of a single oblate ellipsoid in Couette flow for $Re < 100$. However, it is necessary to note that their work only contained one rotational degree of freedom, which means that the ellipsoid could only rotate around a fixed axis in the direction of the shear and no other rotations and translations were available. In that study, it was reported that the 3D oblate ellipsoid would stop rotating when its Re_p surpassed a critical value (> 81). Yu, Phan-Thien and Tanner [37] employed the DLM method to study the ellipsoid rotation problem for $Re < 256$ and also observed the existence of the critical value for Re_p, yet the value was different with the simulation results of LBM. Huang [38] modified the LBM method based on Ladd [39] [40], Aidun, Lu and Ding [41] and Ding and Aidun's [36]) work, which came with improved phase interface treatment and rotations more than 1DOF, investigated the rotation of a single ellipsoid (oblate or prolate) in the shear flow. However, interestingly, the tumbling mode of ellipsoids in their simulation without any constraints did not follow the minimum energy dissipation hypothesis.

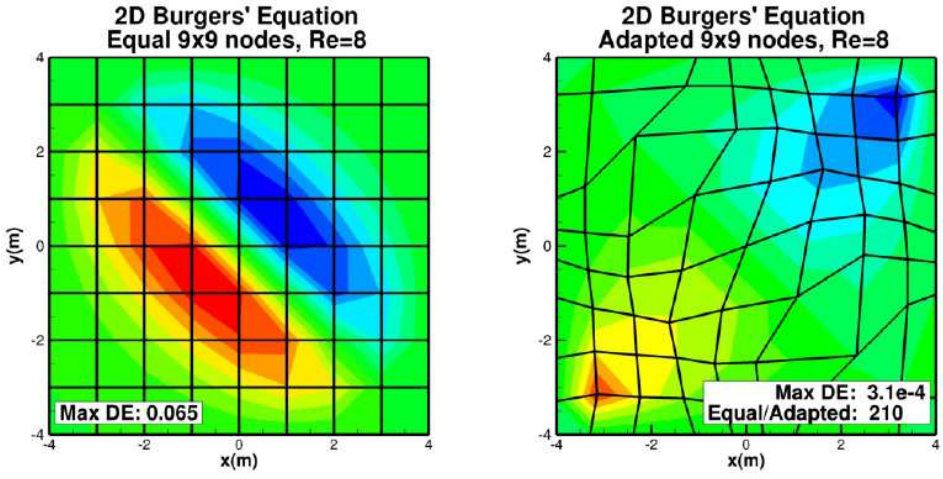

Figure 2.5: *An example of how the mesh quality affect the simulation accuracy. [4]*

2.2 Hydrodynamic Interactions

2.2.1 Solid-wall Interactions at Low Particle Reynolds Number

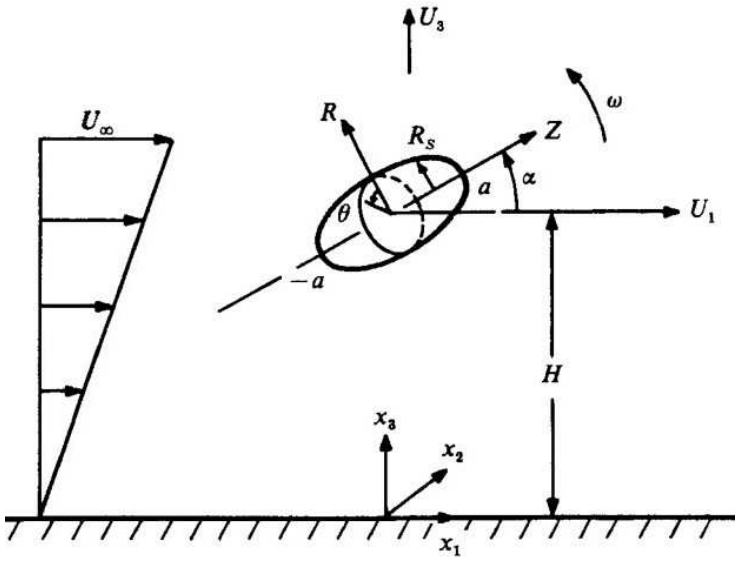

Figure 2.6: *Hsu and Ganatos' study: the migration of ellipsoid driven by the hydrodynamic interactions between wall and solid. [5]*

The studies in Section. 2.1 present the effect of hydrodynamic interactions between wall and solid in various circumstances and encourage in-depth study. It is important to point out that near any rigid and impenetrable wall, the strong influence of the no-slip boundary conditions ensures that the flow in the vicinity is at low Re_p and hence only such low Re_p problem is reviewed here briefly. Wakiya [42] employed the reflections method to study the motion of an ellipsoid parallel to a plane wall with different initial angles. This method was capable of providing accurate prediction to the reflected fields between distanced solids and walls where no-slip boundary conditions were achieved iteratively. However, the limitation of such a "distanced solid and boundary" required that the solid to be at least five times as long as the semi-major axis of the ellipsoid away from the boundary as shown in Fig. 2.6.

Kucaba-Pietal [43] used the boundary collocation method to study a torus close to a planar wall. This method was able to provide highly accurate results as it employed an infinite series of the integral of all the simply separable solutions in the appropriate coordinate system and satisfies no-slip boundary conditions on all the surfaces simultaneously instead of approach-

ing that iteratively. However, this method cannot handle the non-spherical solid with arbitrary initial angle. To handle more complicated solid geometries, Liron and Mochon [44], Liron and Shahar [45] used singularity method, which treat each solid body as a force singularity in the flow field and approximately satisfied the no-slip boundary conditions on the surface of bodies. The singularity method was also adopted in the Dabros' [46] study of rotation of prolate ellipsoid adjacent to a planar wall and Fan, Yuan and Wu's[47] study of prolate ellipsoid translating towards a planar wall. Boundary integral method was firstly introduced by Odqvist [48], which solved Stokes equations generally and expressed the flow field by an integral of a Green function over the boundary area (here major assumptions such as stokes flow ignore influence of inertial flows which may be important for correct lift predictions beyond the boundary layer region). This solution was utilized by Youngren and Acrivos [49] in their three-dimensional study of the creeping motion of an unbounded flow past an arbitrary isolated body. Later, Lewellen [50] improved this method by making more parameters accessible to study the hydrodynamic interaction between an infinitely long cylindrical tube and sphere of creeping motion. Hsu and Ganatos [5] further developed the boundary integral method to calculate the resistance tensor for any arbitrary body of revolution which is tumbling and adjacent to a planar wall at zero Reynolds limit. Their work showed a good agreement with the special case of a sphere moving parallel or perpendicular to a planar wall. The same solution were adopted later to calculate motion of an ellipsoid adjacent to an inclined plane [11].

A common theme in the above mentioned studies is that they avoid solving the Navier-Stokes equations in the entire domain. Though this is undoubtedly beneficial towards developing quick analytical solutions and numerically efficient methods, severe assumptions and approximations limit the validity of these solutions. With the fast growth of the computer power, many computational fluid dynamics (CFD) techniques were developed to specifically study these hydrodynamic interaction problems whilst employing the full description of Navier-Stokes equations. These are briefly reviewed in Section. 2.4.

2.2.2 Multi Solids Interactions at Low Particle Reynolds Number

In the previous sections, translational and rotational motion of only one single solid at low Re_p has been reviewed. However, the existence of another solid will doubtlessly affects the motion of the solid nearby. The hydrodynamic interaction between solids significantly affects the flow configuration by inducing a strong non-negligible two-way coupling between the motion of solids and the flow around them. Despite these hydrodynamic interactions being non-negligible, it is particularly difficult to quantify them.

Chen and Skalak [51] used the boundary collocation and truncated Fourier series solution to solve the problems of axis-symmetric Stokes flow past a periodic array of spheroidal particles placed at the centreline of an infinitely long circular cylinder. Here major assumptions such as Stokes flow ignore influence of inertial flows which may be important for correct lift predictions and more over axial symmetry ensures that 3d effects are totally ignored. The results show the relation among the drag and pressure drop, the spheroidal diameter and the spheroidal thickness and spacing. However, their study was limited to stationary cases. Tozeren [52] also used the same technique to study the problem of axis-symmetric creeping flow past a collection of spheroids at the centreline of an infinitely long circular cylinder. Fortes, et. al [53] designed a series of experiments to study the hydrodynamic interactions between multiple solids, and their results were later on used for validation by Hu and Joseph [54] in their two dimensional simulation work. Recently Martys [55] employed dissipative particle dynamics (DPD) technology to study the multiple solids system and observed the suppression of Jeffery's orbits.

2.3 Single Solid Flows in Inviscid Fluids

The aforementioned topics are mainly with the premise of low Re_p, where the viscous force of the flow is predominant and the inertia force of the flow may be neglected on some occasions. At higher Re_P, the inertial effects are non-negligible and the complete set of Navier-Stokes equations must be considered. Thus the problem would become much more complicated with increasing Re_p as the flow turns to be turbulent [56]. Only in very rare cases, the governing equations might have analytical solutions with certain approximations and assumptions. In

most situations, people has to study the problems by experiments or numerical simulations [57].

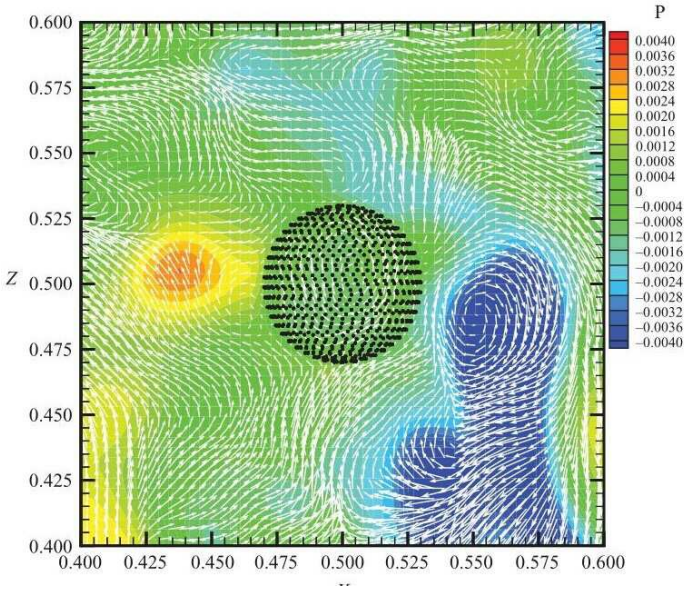

Figure 2.7: *Pressure contour and velocity vectors around a immersed solid particle in turbulent flow. [6]*

$$\rho\bar{u}_j\frac{\partial\bar{u}_i}{\partial x_j} = \frac{\partial}{\partial x_j}\left[-\bar{p}\delta_{ij} + \mu\left(\frac{\partial\bar{u}_i}{\partial x_j} + \frac{\partial\bar{u}_j}{\partial x_i}\right) - \rho\overline{u_i'u_j'}\right] + \rho\bar{f}_i \tag{2.13}$$

Simulating or predicting turbulent flows is complex and a highly computationally intensive given the necessity to be able to capture even the smallest of eddies. Thus several simplified models have been developed in order to resolve the Reynolds stresses ($\overline{u_i'u_j'}$) in the Reynolds Averaged Navier Stokes equations (Eq. 2.13) such as the Spalart-Allmaras model [58], $k-\varepsilon$ model [59], Reynolds stress model [60], Large eddy simulation model [61] and so on. Each of those turbulence models is based on assumptions related to modelling the turbulent transport of energy and hence come with their own advantages and limitations. Direct numerical simulations (DNS), without any turbulence modelling but solving the full Navier-Stokes equations directly, is no doubt the most accurate approach but demands tremendous computational resources. As the turbulence modelling itself can be a huge topic and our primary task is the solid-fluid flow, DNS is adopted in the current thesis work.

Having said this, an important advantage of the Gerris flow solver is its ability to resolve

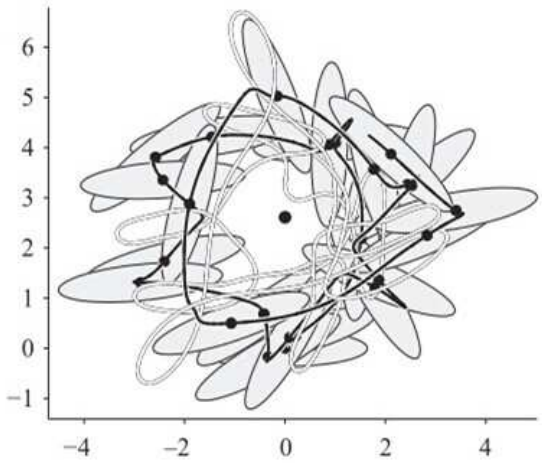

Figure 2.8: *Chaotic motion an ellipsoid in inviscid flow surrounding a vortex. [7]*

the Euler's equation for inviscid flows (as shown in Eq. 2.14) which is applicable to several practical situations when the viscous effect is insignificant compared to the inertial effect of the flow. In the early stage of the development fluid dynamics, the analytical studies based on inviscid flows helped build a series of important theories and applications [62]. This technique is widely utilized in the area of aerodynamic analysis of air vehicles where an inviscid analysis provides a fast estimate of the primary forces like drag and lift [63]. Euler's equations are also useful in estimating chaotic motions of suspended solids in inviscid environments - such as tracking orbits made by ash particles in air. However, it is necessary to aware that in reality only parts of the flow domain away from the solid boundary can be approximated to be inviscid. In the parts close to the solid boundary, viscous effects lead to the generation of the boundary layer [64] and the flow is no longer inviscid in the near-wall region.

$$\frac{\partial \mathbf{u}}{\partial t} + \mathbf{u} \cdot \nabla \mathbf{u} + \frac{1}{\rho} \nabla p = 0 \tag{2.14}$$

The problem discussed in Chapter 7 of this thesis work is one of those classical problems and has been studied for centuries: the motion of a solid through incompressible and inviscid flow. In 1752, d'Alembert proved that there is no drag force applied on the sphere in this problem with the potential flow theory [65] [66]. Later, Kirchhoff [67] showed that the motion of such solid fully immersed in an ideal fluid can be described by a set of ordinary differential equations that greatly simplified the problem which was originally involving an

infinite number of degrees of freedom (Eq. 2.15, Eq. 2.16).

$$\frac{d}{dt}\left(\frac{\partial T_{tot}}{\partial \mathbf{U}}\right) + \mathbf{\Omega} \times \frac{\partial T_{tot}}{\partial \mathbf{U}} = 0 \tag{2.15}$$

$$\frac{d}{dt}\left(\frac{\partial T_{tot}}{\partial \mathbf{\Omega}}\right) + \mathbf{\Omega} \times \frac{\partial T_{tot}}{\partial \mathbf{\Omega}} + \mathbf{U} \times \frac{\partial T_{tot}}{\partial \mathbf{U}} = 0 \tag{2.16}$$

After nearly a century, in 1982, Kozlov and Oniscenko [68] published an important paper which suggested the integrable conditions for the Kirchhoff's equations. They noted that unless those conditions were satisfied, the motion of the solid would become chaotic. Aref [10] provided a numerical evidence that the Kirchhoff's equations do have chaotic solutions. This chaotic features shown in Fig 2.8, even the vestiges of it due to the viscous effect, is of great scientific importance. Due to the complexity of the chaotic problem, most of the study were focused on 2D configurations [69] [70] [71] [72]. Fig. 2.8 presents one of those 2D studies. On the other hand, the 6DOF capacity of GISS developed in this thesis allow a comprehensive study of the 3D chaotic motion of solids immersed in the ideal flow, offers a powerful tool in this research direction.

2.4 Review of Simulation Techniques

2.4.1 Solid-Fluid Simulation Methods

The most popular simulation technique for the solid-fluid problems is the Eulerian continuum approach, which treats both solid and fluid as inter-penetrating mixtures and applies the continuum theory uniformly on them (Zhang and Prosperetti [73], Fan and Zhu [74], and Drew and Passman [75]). In this method, both solid or fluid phase behave like a homogeneous phase described by the field equations. An additional unknown term describing the interactions between the phases arises and has to be modelled to close the governing equations. Though with this approach it is difficult to understand the nature of detailed coupled interactions between the solids and the fluid, this method can be extremely efficient once the interaction terms are well modelled and therefore has been widely adopted in multiphase flow simulations.

Another widely accepted approach in solid-fluid simulation is the Lagrangian particle tracking method, where the fluid is governed by the continuum equations in a fixed control domain and described in the usual Eulerian way. In this method, motion of each solid particle is governed by the Newton's second law where the hydrodynamic forces applied on the solid are obtained from the existed knowledge. Separate models are used to describe one-way or two-way coupling. The one-way coupling model is usually adopted when the particle concentration is low and the influence of the solid existence is insignificant to the flow field. Alternatively the two-way coupling model should be chosen where a momentum exchange term is introduced into the governing equations to take account of the effects of the particle motion onto the fluid flow [76]. Andrews and O' Rourke [77] and Snider et al. [78] further developed this method by introducing a scheme that empirically modelled the inter-particle stress, which was usually neglected by either Eulerian continuum approach or usual Lagrangian particle tracking method.

The third approach to simulate the solid-fluid flow problems is through direct numerical simulations (DNS). This approach calculates all the coupled hydrodynamic forces affecting fluid flows laden with solids and allows calculation of the instantaneous motion of both fluid and solid. Therefore, it is may possibly be the only numerical tool that is capable of studying the non-linear dynamics of particle motion alongside ensuing flow instabilities and predicting complex outcomes of particle-particle and particle-wall interactions, such as the cluster formation and anisotropic micro-structures in Solid-Fluid systems. This thesis work has intensively studied two classical simplifications: neglecting the inertia (Stokes flow, very small Re_p) and neglecting the viscosity (inviscid flow, infinite large Re_p). Besides that, for more general problems with finite Re_p, several numerical methods have also been developed and these are discussed in the following section.

Johnson and Tezduya [79] reported their simulation of flow-particle interaction with 100 particles. Some commercial software, like EDEM, also claim they can handle flow-particle interaction. Different Eulerian approach has also been taken in the study of Sugiyama et al. [80].

2.4.2 DNS Methods for Solid-Fluid Problems

As discussed in Section. 2.1, the governing equations of flow can be simplified by neglecting the fluid inertia effect completely (Stokes flow) or by neglecting the viscous effect completely (inviscid flow). This strategy was also adopted in some DNS studies. For the Stokes flow case, Brady and Bossis [81] developed numerical techniques based on Stokesian dynamics and simulated the multi solids' motion successfully. The results could be utilized in the colloidal suspensions problem which follows the zero Re_p assumption. For the inviscid flow case, Sangani and Didwania [82] used the potential flow model to simulate the particles cross-stream alignment in fluidized systems.

Besides the simplified model, several numerical methods have been developed to study the Solid-Fluid problems under more general conditions. In the early DNS studies of hydrodynamic forces, conventional method was to use body-fitted or unstructured-grid methods. However, computational cost due to dense mesh requirement for complex geometry description and the transient re-meshing (Fig. 2.9a) at every time step for the moving solid boundary was prohibitively high. Tezduyar et al. [83] [84] adopted this method to study the flow with a drafting cylinder and obtained some results, yet the study also encountered the difficulties of this body-fitted method in handling the strong transient spatial domain changes due to a moving solid. These limitations inspired researchers to develop more advanced simulation techniques described below.

One method is the arbitrary LagrangianEulerian (ALE) method. This method is based on the combination of the fluid and particle momentum equations, and uses an unstructured,finite-element mesh to study movement of the particles. Hu and his co-workers [85] [54] firstly introduced this method to study two-dimensional behaviours of circular and elliptic cylinders sedimentation in a channel. He also studied the rotational mechanism of the circular cylinder settling close to a rigid wall using the same method [86]. Later he presented a study of multi circular particles at $Re = 100$. Feng et al. [87] [88] investigated the hydrodynamic interactions between circular or elliptical particles in various flow conditions, including sedimentation, Couette, and Poiseuille flows in Newtonian fluid, and sedimentation in Oldroyd-B fluid. On the other hand, Huang extended the study of the elliptic particles settling and coupling with some other flow conditions, like the viscous-elastic and shear-thinning fluids [89]

[90]. Patankar [91] also used this method to study the rheology of suspensions in various fluid conditions. Hu, et al. [92] also adopted ALE method to study the 3D tumbling and kissing motions of multi sphere particles.

Lattice Boltzmann method (LBM) is another very effective alternative CFD technique. In contrast to the usual CFD techniques that discretizes the macroscopic continuity equation of the fluid, LBM is a microscopic model built on mesoscopic kinetic equations of essential fluid particles which satisfy the macroscopic-averaged properties of the flow (Chen and Doolen [93]). LBM was extensively developed to simulate solid-fluid problems (Ladd [39] [40], Behrend [94], Aidun et al. [41], Qi [95] and more recently Krueger et al. [3]. Here, hydrodynamic forces and moments applied on solids were calculated based on the flow information from the flow simulation and then the particles' motion were determined by the Newton's second law. The principle of the LBM determines its natural compatibility the parallel simulations. Ladd [39]have simulated up to 32,000 suspending sphere particles in a three-dimensional study. A significant disadvantage of the LBM is the fow is not completely incompressible [96]. Besides, the solid in LBM is usually treated as a collection of grid-free points linked together [38], and a proper solid configuration asks excessive work on technical details [97] [98].

Another method is the distributed-Lagrange-multiplier method (DLM). An important feature of this method is the governing equations of the fluid are taking effect both inside and outside the solids boundary. The part of the fluid that overlaps the solid is constrained to the solid motion with a distributed Lagrange multiplier. This additional multiplier behaves as a general source term in the governing equations and is analogous to the pressure of the fluid as the constraint of incompressibility. The original idea of this method was initialized by Hyman [99]. Glowinski et al. [100] first introduced this method with the boundary constraint in a series of papers. Later, the DLM was further developed for the viscoelastic fluids (Singh et al. [101]).

The immersed boundary method (IBM) is the employed method in this thesis work. It was originally developed by Peskin [102] in his study of blood flow in vessels. After that, there have been several improvisations of the IBM for different applications and therefore this method now contains several variants. Some of these share similar features with the LBM

and DLM. A brief review of the IBM is presented in the following section.

2.4.3 Immersed Boundary Method

In the conventional approach of handling the solid-fluid problems, the fluid domain is partially occupied by the solid objects, which results in an irregular fluid domain. This limits the compatibility of a Cartesian mesh and normally an unstructured mesh is used which can be a combination of tetrahedral, prismatic and hexahedral elements. As the accuracy of any DNS method is highly dependent on the mesh quality [103], a non-uniform unstructured mesh can be a major source of error especially near the wall boundaries of the immersed solids. This gets exacerbated if there are suspensive solids results in the inability to predict formation of hydrodynamic clusters during flow (characterised by localised pockets of large volume fraction of solids within the domain). Further more, as in IBM these techniques also require mesh re-generation in every time step during the calculation in order to fit the latest solid position [104], quality control of unstructured meshes at every timestep becomes even more difficult [105].

IBM is a novel technique to solve the solid-fluid problem which can avoid unstructured mesh and repeating mesh generation. The concept was first introduced by Peskin [106] in his cardiac mechanism study with blood flow simulations, where the solid interface was elastic and the force applied by the boundary was computed by Hooke's law. Later on this technique was extended to rigid bodies by setting a huge value to the spring constant [102]. The interaction between the fluid and immersed solid was summarised as a source term in the governing equations. The basic idea of IBM is to force the immersed solid part to match the velocities of the local fluid. This fundamental idea inspired many variations, like the direct forcing approach [107], the immersed interface method [108], and the distributed Lagrange multiplier method [109], etc. These methods mainly differ on their treatment on the interface to satisfy the continuity equation and the no-slip boundary condition on the immersed solid wall.

IBM treats the solid objects and their effect as general source terms, which allows the fluid domain remaining its integrity. Therefore IBM naturally requires only Cartesian grids that greatly simplifies the mesh generation process [110], especially when the solid requires very

complex body-conformal mesh. What's more, the solver needs not to re-generate itself every time step when the solid is moving. With these advantages, much lower memories and computational costs can be assured. On the other hand, most existed IBM solvers are designed based on the premise of fixed Cartesian mesh with unified mesh resolution, which may abuse the computational resource if the simulation only need higher mesh resolution in limited part of the domain.

During this thesis work a fluid-solid DNS solver named the Gerris Immersed Solid Solver (GISS) based on a novel variant of the IBM has been developed. The GISS comprises a solid motion subsolver which resolves the solid momentum equations for translation and rotation (Eq. 3.21) and is smoothly coupled to the flow subsolver based on Gerris which solves the flow governing equations of mass and momentum conservation (Eq. 3.2). Gerris is an open source software originally developed by Popinet [13]. Gerris solves the fluid governing equations with an adaptive mesh projection method [111] [112]. On the solid-fluid interfaces, the solid boundaries are represented together by a volume fluid fraction and surface fluid fraction whose detail explanation can be found at Section 3.1.2. A fraction value of 1 means pure fluid, 0 means pure solid and values between 0 and 1 means the mixed cell on the solid-fluid interface. This variant of IBM is usually referred as "Cartesian grid method" or "embedded solid method" and was firstly proposed to study the ideal fluid with complex solid boundaries [113] [114]. It is also able to handle viscous flow with further development [10] [115]. Novel features of GISS have already been listed in Section 2.1. This special IBM helps to build another important feature of Gerris: the computational domain can be discretized by quadtree (in 2D) or octree(in 3D) cell [116] [117], which allows Gerris possessing the advantages from both conventional dynamic mesh adaptation method and IBM as shown in Fig 2.9c: A cell in the mesh will be automatically adapted by dividing the root cell to 4 (in 2D) or 8 (in 3D) leaf cells when necessary and meanwhile all the cells will always remain Cartesian. This "tree-structure adaptation" of the mesh is much simpler than the usual mesh adaptation based on body-conformal unstructured mesh (Fig 2.9a) resulting in reduced computational expense compared to those built on unified Cartesian mesh(Fig 2.9b).

Based on the aforementioned advantage of the mesh adaptation strategy, the GISS can theoretically handle as many solids as the computational resources allowed, while each of those

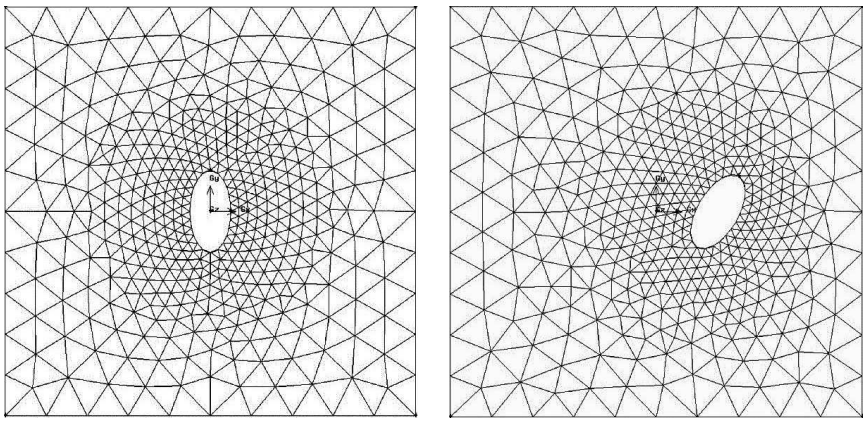

(a) Dynamic mesh adaptation

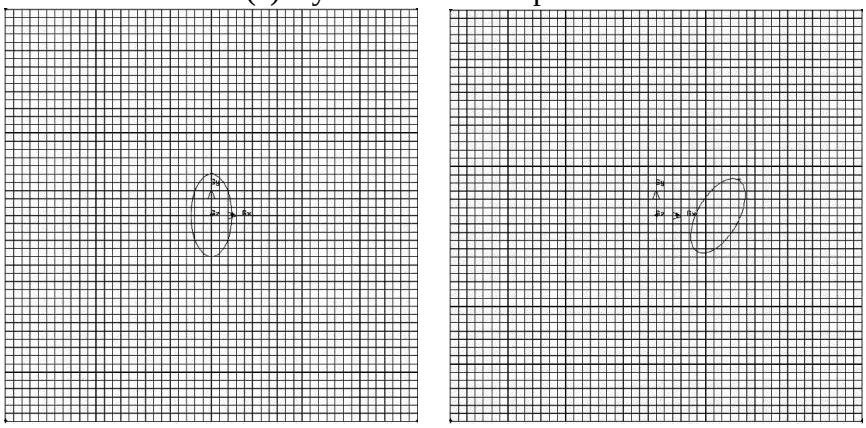

(b)Usual immersed boundary method

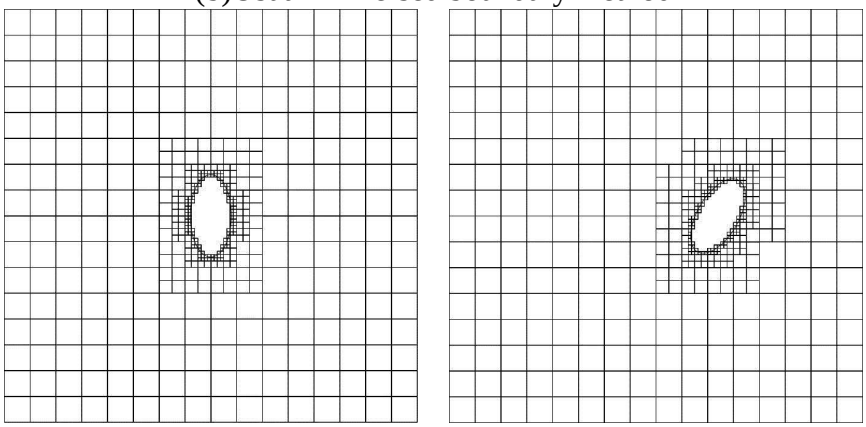

(c) Quadtree mesh adaptation in GISS

Mesh in one time step Mesh in next time step

(a) (b) are generated by commercial software(Gambit) and (c) is generated by Gerris.

Figure 2.9: *Comparison of different mesh strategies.*

solid particles can have its unique geometry and the mutual affects between fluid and solid with detail geometries characteristics are captured. This ability of GISS allows the simulation of the hydrodynamic interaction between solids with complex geometries, which can contribute to a finer model of the slurry flow simulation.

Chapter 3

GISS Methodology

As mentioned in Chapter 1, the Gerris Immersed Solid Solver (GISS) is a custom-built 3D DNS tool for solid-fluid flows that comprises two main subsolvers: the Gerris flow solver and the Immersed Solid (motion) solver. This chapter describes the numerical methodology used in both these solvers. It should be again emphasised that development and validation of the solver have been the key motives during the thesis work. While the flow solver is fully parallelisable, enhancing and optimising the parallelisability is beyond the scope of this work and is being dealt separately. The first version of the solver is aimed to be released as open source in February 2015.

3.1 Fluid Solver Provided by Gerris

The fluid solver in this thesis work is based on a highly parallelised and popular open source CFD package, Gerris (`http://gfs.sourceforge.net/wiki/index.php/Main_Page`). Gerris solves the partial differential equations with finite volume method. The value of variables are stored at the centre of each cell, while the value of the gradient of variables are calculated at the interface between cells, in favour of the Cartesian mesh employed by the solver. The solver has been originally created by Stéphane Popinet [13], research scientist at New Zealand's National Institute for Water and Atmospheric Research and originally at the Centre National de la Recherche Scientifique (CNRS) based at Université Pierre et Marie Curie (UPMC) in Paris, France. Over the years the flow solver has also been significantly extended by Prof. Stéphane Zaleski's group [118] [119] [120] from the Institut Jean le Rond d'Alembert at UPMC. The paragraphs below briefly describe the key elements of Gerris.

3.1.1 Fluid Solver by Projection Method

The governing equations for the fluid are the incompressible and Newtonian Navier-Stokes and continuity equations are built on an Eulerian specification of the flow field. In this description, the fluid is observed in a fixed frame of reference where the fluid flows as time passes. This is also the most common way to study the fluid behaviour in a given domain. The other class of specification, in contrast, is the Lagrangian description of the flow field. This description requires the observer following an individual fluid parcel while it moves through space and time [16]. This method is adopted by our moving solid solver described in Section 3.2.

In this thesis work, our study focusses on solid motion in incompressible Newtonian flow. The detail deduction of the Navier-Stokes equations can be found in every textbook of fluid dynamics such as Bird et al. [121]. As mentioned in Chapter 2, it is not possible to have an exact analytical solution of the full Navier-Stokes equation in 3D, therefore, a numerical solution is sought. The governing equations for the fluid are:

$$\nabla \cdot \mathbf{u} = 0 \tag{3.1}$$

$$\frac{\partial \mathbf{u}}{\partial t} + \mathbf{u} \cdot \nabla \mathbf{u} = -\frac{1}{\rho}\nabla p + \nu \nabla^2 \mathbf{u} + \mathbf{f_s} \tag{3.2}$$

Where Eq. 3.1 is the mass conservation equation (also known as the continuity equation), and Eq. 3.2 is the momentum conservation equation derived on the Newton's second law (also known as the equation of motion). In the above equations, $\mathbf{u} = (u, v, w)$ is the velocity vector, t is the time, $\nabla = (\partial/\partial x, \partial/\partial y, \partial/\partial z)$ is the vector differential operator and $\mathbf{f_s}$ is a general force term characterising the influence of the immersed solid.

Except the boundary conditions applied on the fluid domain which vary according to the situation, the boundary conditions applied on the solid-fluid interface in this thesis work were all set to no-slip, no-penetration condition indicating that the submerged solids are rigid and non-porous. This condition dictates the formulation of the general force term $\mathbf{F_s}$ in Eq. 3.2. Thus,

$$\mathbf{u}_f = \mathbf{u}_\Gamma \tag{3.3}$$

$$\nabla p \cdot \mathbf{n}_\Gamma = 0 \tag{3.4}$$

Here, Γ indicates the immersed solid region and f is the fluid domain region, as shown in Fig. 3.1.

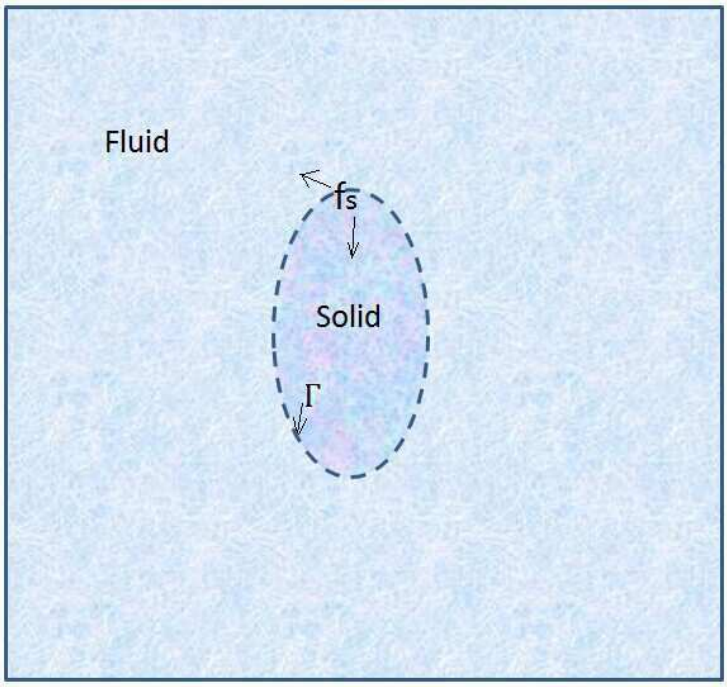

Figure 3.1: *A solid particle immersed in fluid.*

The Gerris fluid solver is based on a fractional-step projection method which is based on the theorem of Helmholtz-Hodge decomposition [122]. The theorem states that in a simply connected domain, any vector field $\mathbf{u}$ can be uniquely decomposed into a divergence-free (solenoidal) part $\mathbf{u}_{sol}$ and an irrotational part $\mathbf{u}_{irrot}$ [123]. To further illustrate the working process here, Eq. 3.1 and Eq. 3.2 can be re-rewritten in second-order, time-discrete semi-implicit forms. This section is mainly introducing the solver for the fluid domain. The strategy to take the effect of solid into account on the solid-fluid interface will be explained in Section 3.1.4.

$$\nabla \cdot \mathbf{u}^{n+1} = 0 \tag{3.5}$$

$$\frac{\mathbf{u}^{n+1} - \mathbf{u}^n}{\Delta t} + [(\mathbf{u} \cdot \nabla)\mathbf{u}]^n = -\frac{1}{\rho}\nabla p^{n+1/2} + \nu \nabla^2 \mathbf{u}^n \tag{3.6}$$

Here, the superscript n in $\mathbf{u}^n$ means the variable at the time point of $t = n\Delta t$. With the help

of an intermediate velocity field $\mathbf{u}^\star$, Eq. 3.6 can be divided into two equations:

$$\frac{\mathbf{u}^\star - \mathbf{u}^n}{\Delta t} + [(\mathbf{u}\cdot\nabla)\mathbf{u}]^n = \nu\nabla^2\mathbf{u}^n \tag{3.7}$$

$$\frac{\mathbf{u}^{n+1} - \mathbf{u}^\star}{\Delta t} = -\frac{1}{\rho}\nabla p^{n+1/2} \tag{3.8}$$

It is now possible to calculate the value of $\mathbf{u}^\star$ explicitly through Eq. 3.7 with the known velocity field $\mathbf{u}^n$, and with the help of Eq. 3.5, the following equation can be obtained by taking the divergence on both sides of the Eq. 3.8:

$$\nabla^2 p^{n+1/2} = \frac{\rho}{\Delta t}\nabla\cdot\mathbf{u}^\star \tag{3.9}$$

Eq. 3.9 is a typical Possion equation which can be solved to obtain the pressure field at $n+1/2$ time step. Substituting $\mathbf{u}^\star$ and $p^{n+1/2}$ back into Eq. 3.8, the velocity field can be calculated at the next time step $(n+1)$.

$$\mathbf{u}^{n+1} = \mathbf{u}^\star - \frac{\Delta t}{\rho}\nabla p^{n+1/2} \tag{3.10}$$

In practical calculation, both exact and approximate projections are processed to calculate the face and cell centred velocities.

3.1.2 Structured Mesh Representation for Both Solid and Fluid

In the Gerris fluid solver, the computational domain is spatially discretised with square (in 2D)/ cubic (in 3D) mesh elements which are hierarchically organised as a quadtree (in 2D)/ octree (in 3D) system. This technology is widely adopted computer graphics applications, and also in CFD studies (usually with structured hexahedral geometries) [124][117][116][125]. Fig. 3.2 shows an example of this spatial discretisation strategy. In the following discussion, each individual finite volume in the figure is refereed as a *cell*, whose length is denoted as Δx. Each cell may be further divided in to 4 (in 2D)/ 8 (in 3D) *children cells* and the original cell would be treated as a *parent cell*. The *root cell* is the base of the tree with no parent cell and its length L is defined at the beginning of the simulation. L is treated as a reference

length scale to further calculate the lengths of cells of each level. A *leaf cell* is a cell with no children. In this definition, only a Cartesian mesh exists and the size of cell can be described by its refinement level N, which is defined from zero for the root cell and increased to one when the cell is divided.

With this quadtree (in 2D)/ octree (in 3D) mesh adaptation strategy, Only Cartesian mesh is used in the solver, which makes the calculation of the gradient and the interpolation of the variables much simpler and more accurate than those with unstructured mesh. In addition, the tree adaptation system allows the mesh being refined at an exponential rate, which is very efficient, while maintaining the advantages guaranteed by the Cartesian mesh.

$$\Delta x = \frac{L}{2^N} \tag{3.11}$$

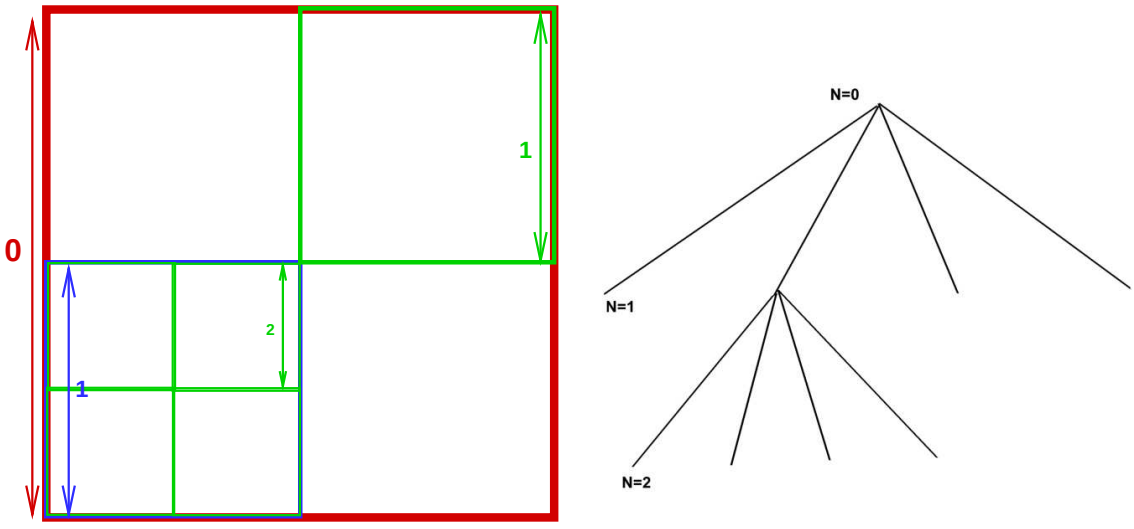

(a) (b)

Figure 3.2: *The quad tree mesh structure. The red cell has no parent cell thus it is the root cell and its length is L and it has 4 children cell. The green cell in the up-right corner has no children, so it is a leaf cell, so are the green cells in the down-left corner. The blue cell in down-left corner is the children cell of the root cell and is the parent cell of the green cell, so it is not a leaf cell.*

This kind of structured mesh in the fluid domain is usually not suitable to describe a compli-

cated solid geometry, where an unstructured body-conformal mesh is the conventional choice to satisfy the complex surface geometry of the solid objects. In order to maintain high efficiency and accuracy of the tree based structured mesh, the immersed boundary method is adopted here. Besides the fluid cells and solid cells, one more type, mixed cells are defined at where the mesh is cut by a solid boundary. In general, this solid boundary description can only capture the features of geometries whose scales are bigger than the mesh size. As a consequence, when a feature of the geometry is smaller than the mesh size, like a sharp angle, the solver cannot represent it with good accuracy limiting its application in some cases. In the IBM employed here, the following key definitions were adopted: a volume fraction a which is the ratio of the volume occupied by the fluid to the total volume of the cell, and the surface fraction s_d, which is ratio of the area occupied by the fluid to the total area on the cell surface in the direction d. For example, s_{x+} is the fluid surface fraction on the surface of positive x direction. With reference to Fig. 3.3(a) The area vector of the cut surfaces is thus defined as:

$$\mathbf{A} = (s_{x-} - s_{x+}, s_{y-} - s_{y+}) \cdot \Delta x \text{ in 2D} \tag{3.12}$$

where Δx is the size of the presented cell defined in Eq. 3.11. For example, In Fig .3.3(a), the side fluid fraction on the right side (s_{x-}) is 0, the side fluid fraction on the right side (s_{x+}) is 1, the side fluid fraction on the right side (s_{y-}) is 1, the side fluid fraction on the top side (s_{y+}) is 0. By Eq. 3.12:

$$\mathbf{A} = (s_{x-} - s_{x+}, s_{y-} - s_{y+}) \cdot \Delta x = (-1, -1)\Delta x \tag{3.13}$$

The direction of $(-1, -1)$ is pointed by the arrow in Fig .3.3(a), and the value of $\mathbf{A}$ is $\sqrt{2}\Delta x$, which is exactly the value of the approximated solid-fluid interface in the simulation.

Similar in general 3D case, the area vector would be

$$\mathbf{A} = (s_{x-} - s_{x+}, s_{y-} - s_{y+}, s_{z-} - s_{z+})\Delta x^2 \text{ in 3D} \tag{3.14}$$

As can be noted from above, the accuracy can be greatly improved by refining the mesh resolution, as shown in Fig. 3.3(b). In this thesis work, solid particles are described by the

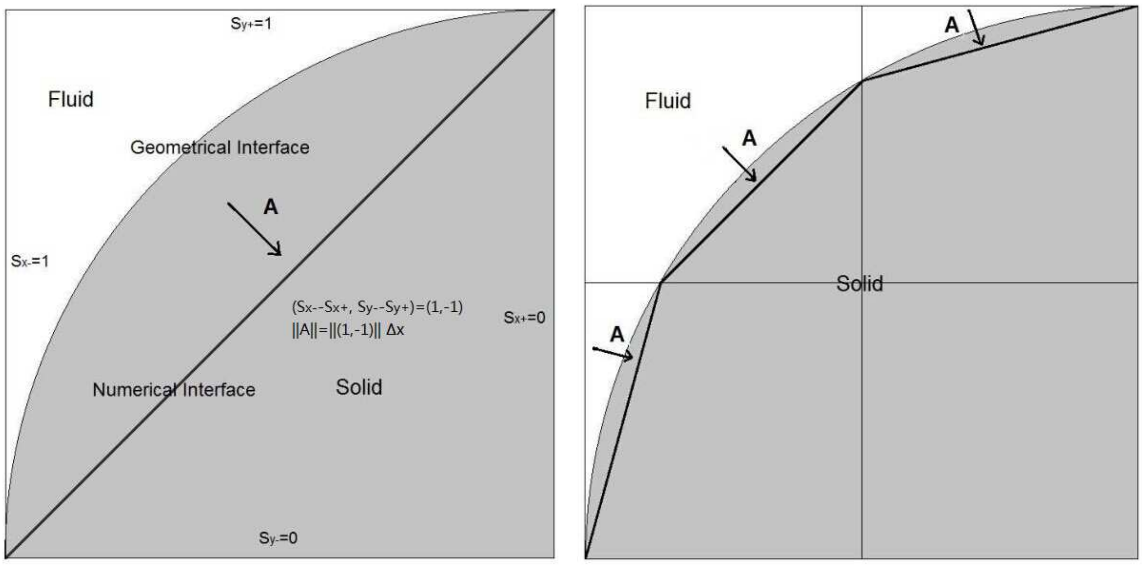

(a) Coarse mesh (b) Refined mesh

Figure 3.3: *Calculating surface area with fluid fractions.*

GNU Triangulated Surface (GTS) Library (`http://gts.sourceforge.net/`). It is an Open Source Free Software Library and able to efficiently provide boolean operations (intersection, union, difference) between curves (in 2D) or volumes (in 3D) for the surface and volume fractions based on an approach presented by Aftosmis et al. [126].

In order to process this tree based structured mesh system more efficiently, several constraints are applied. These constraints are (The numbers in the figure are the refinement level N):

1. The difference of the mesh refinement level, N, between neighbouring cells cannot be more than one.
2. The difference of N between diagonally neighbouring cells cannot be more than one.
3. The mesh refinement level N of all cells within a solid must be the same.

These constraints do sacrifice some flexibility of the discretisation by limiting mesh refinement in the flow (Constraints 1 and 2) and the solid domains (Constraints 3). But, these can greatly reduce the computational cost especially towards calculating gradients and fluxes as they allow very efficient access to the mesh information. This includes each cell's refinement level, the spatial coordinates and the index to their neighbouring cells which makes the

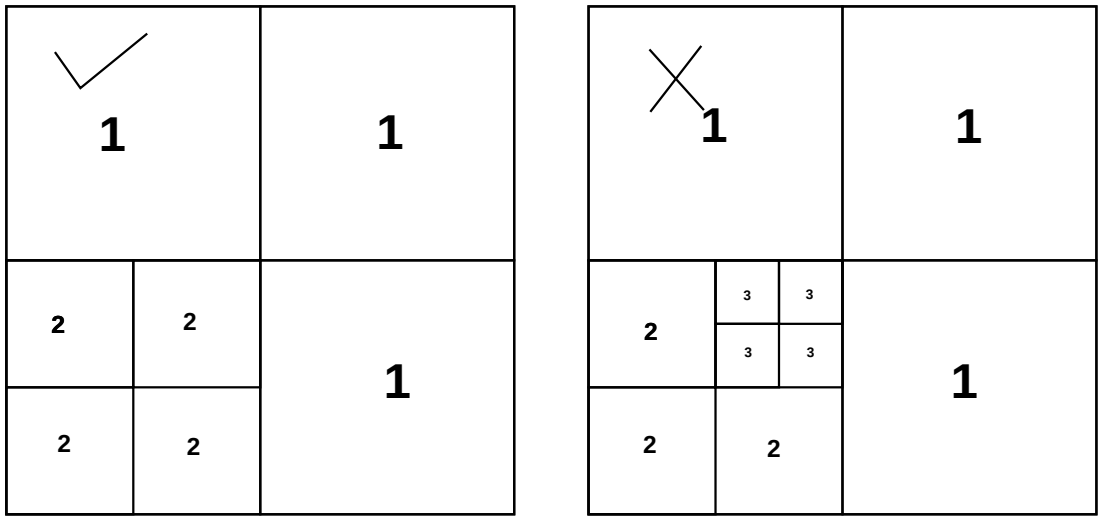

(a) Correct configuration (b) Incorrect configuration

Figure 3.4: *Constraint 1 - The difference of mesh refinement levels N between neighbouring cells cannot be more than 1.*

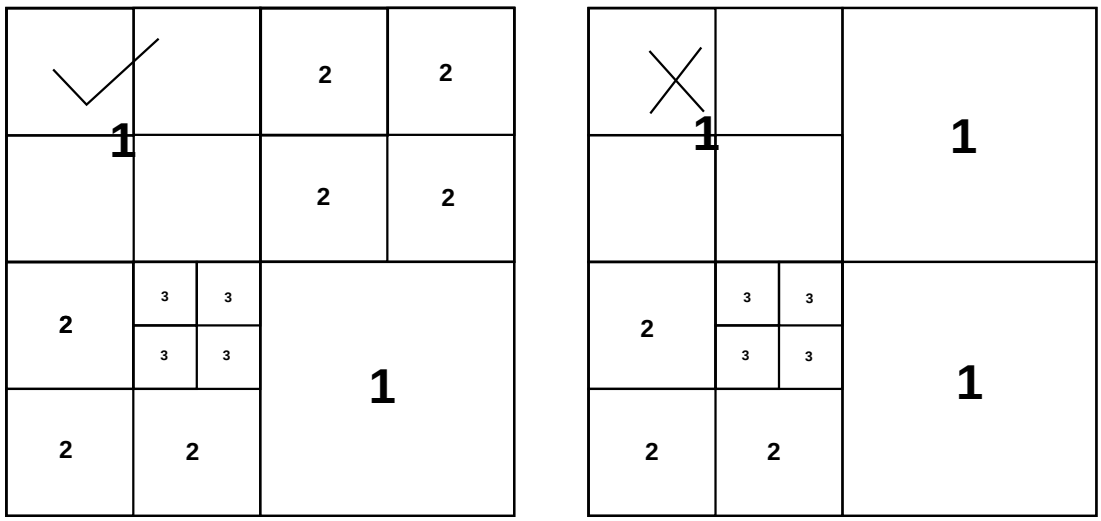

(a) Correct configuration (b) Incorrect configuration

Figure 3.5: *Constraint 2 - The difference of mesh refinement levels N between diagonally neighbouring cells cannot be more than 1.*

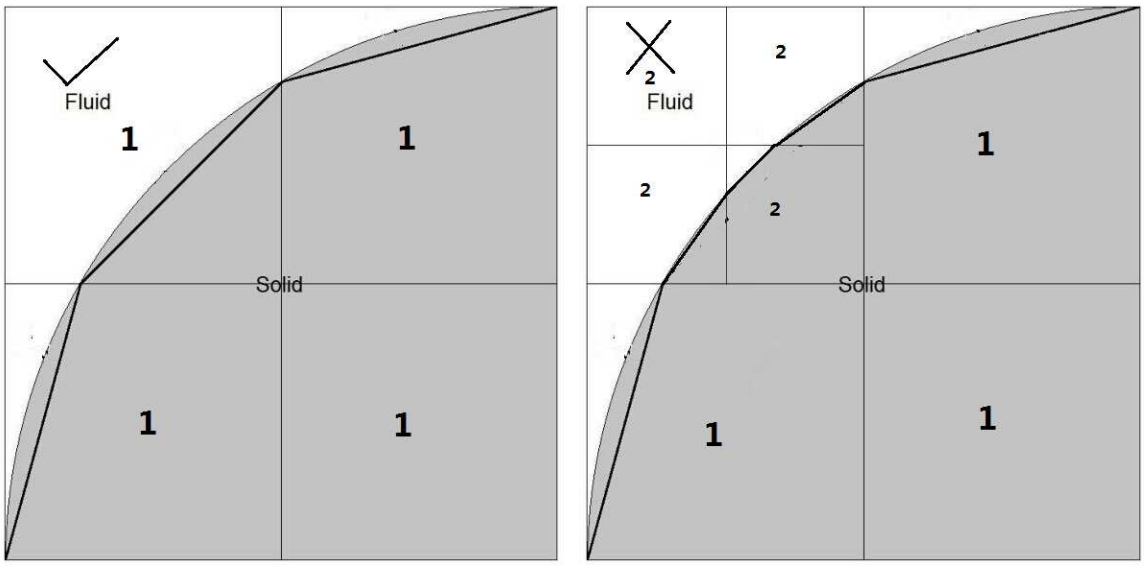

(a) Correct configuration (b) Incorrect configuration

Figure 3.6: *Constraint 3 - The mesh refinement level N of all cells within a solid must be the same.*

efficient traversal of the mesh possible. However, these constrains are not fundamentally necessary, to resolve them compromising with calculation efficiency can be a valuable extensive work, for example, allowing partially mesh refinement of the solid.

3.1.3 Adaptive Mesh Refinement

In order to ensure that body-force interaction term $\mathbf{f}_s$ in Eq. 3.2 is calculated accurately by correct imposition of the boundary conditions at the immersed solid walls (Eqs. 3.4 and 3.3 selective refining of the fluid mesh (known as adaptive mesh refinement) around the solid regions. The fluid mesh refines around the regions of the solid at every timestep.

The tree-based discretisation adopted in the Gerris solver is especially suitable for the adaptive mesh refinement. However, in the conventional solid mesh treatment where the body-conformal mesh is applied, a complicated solid geometry usually requires unstructured mesh and is not compatible with the tree-based discretisation strategy. The immersed boundary method employed here (described in the Section 3.1.2) uses a highly efficient quadtree (in 2D)/ octree (in 3D) mesh refinement.

In order to refine the mesh, a criterion ξ is set at the beginning of the simulation. This criterion varies with different simulation configurations and could be the norm (the scale of a variable) of the local vorticity vector, or the norm of the local pressure gradient, or the numerical approximation of the truncation error of the whole scheme [127][111], and so on. For example, the mesh can be refined when ξ satisfies with the condition defined by the vorticity in Eq. 3.15:

$$\frac{\Delta x \|\nabla \times \mathbf{u}\|}{\|\mathbf{u_{ref}}\|} > \xi \tag{3.15}$$

The judging process for whether to refine or not will increase about 5% computational cost, which is relatively small compared to the entire cost of the fluid solver.

At given timestep, firstly, the solver checks for every leaf cell for the criterion. Only those cells that satisfy the criterion will be refined. If necessary, their neighbouring cells will also be refined to fit the constraints mentioned in Section 3.1.2. Secondly, the solver will check on the parent cells of all the leaf cells, if they do not satisfy the criterion then those cells will be coarsened and become leaf cells. This adaptive mesh refinement process can be processed many times in one time step, but considering the flow evolution is usually slower than the frequency of mesh adaptation, usually refining mesh once is enough for most situations.

After the creation of the new cells, the variable values such as pressure and velocity vector need to be initialised in them. For the newly coarsened cells which are just merged into their original children cells, the volume weighted average of the values of those children cells is deemed enough. The flow quantities such as pressure and momentum can be exactly preserved through this approach. On the other hand, for the newly refined mesh, it is not as easy as to assign the value to the coarsened mesh. A *linear interpolation* is applied using the value and gradients of the cell being refined. This approach preserves the local conservation but introduces certain numerical errors. Higher-order interpolants, like polynomial interpolation or spline interpolation, may provide better accuracy here.

3.1.4 Solid - Fluid Coupling

Though Eq. 3.5 and Eq. 3.6 are described in the differential form, they are actually solved in the integral form during the simulation. Rewriting Eq. 3.9 to its integral form and applying

Gauss's theorem:

$$\oiint_A \nabla p \cdot \mathbf{n} \mathrm{d}A = \frac{\rho}{\Delta t} \iiint_V \nabla \cdot \mathbf{u}^\star \mathrm{d}V \tag{3.16}$$

Where A is the surface area of the cell and V is the volume of the cell. Unlike the conventional body conformal mesh technique which only needs to consider the fluid properties inside the mesh, the solid effect is also included when solving the governing equations. Including the fluid fraction to Eq. 3.16 and rewriting it to the discrete form,:

$$\sum_d s_d \nabla_d p = \frac{\rho \Delta x a}{\Delta t} \nabla \cdot \mathbf{u}^\star \tag{3.17}$$

Eq. 3.17 is the general form of the Possion equations solved by the Gerris (a is the fluid volume fraction of the cell). A similar treatment can be also applied on the diffusive term:

$$\iiint_V \nabla \cdot (\nabla u_d^n) dV = \oiint_A \nabla u_d^n \cdot \mathbf{n} dA \tag{3.18}$$

For the convective term and diffusive term of the governing equations, a conservative formulation can be used to evaluate them. Applying Gauss's theorem to the integral form of the advective term:

$$\iiint_V [(\mathbf{u} \cdot \nabla)\mathbf{u}]^n dV = \iiint_V [\nabla \cdot (\mathbf{u}\mathbf{u})]^n dV = \oiint_A \mathbf{u}^n (\mathbf{u}^n \cdot \mathbf{n}) dA \tag{3.19}$$

Combining Eq. 3.7 and Eq. 3.19,

$$a \Delta x \frac{\mathbf{u}^\star - \mathbf{u}^n}{\Delta t} = \nu \sum_d s_d \nabla_d \mathbf{u}^n - \sum_d s_d u_d^n u_d^n \mathbf{n}_d \tag{3.20}$$

Where u_d^n is the is the normal component of the velocity in direction d at time n. The value is obtained at the centre of the cell face. A Godunov procedure [128] based on Taylor series is employed here to calculate these values. The coupling processes would iterate several turns during each time step until the mass and momentum conservation of the governing equations are satisfied. Currently the completed simulation has reported that 5-10 iterations is necessary

in each step with proper simulation set up.

3.2 Solid Motion Solver

In this thesis work, the solid bodies are allowed to perform 6 degrees-of-freedom (6DOF) motions. This calculation is empowered by Open Dynamics Engine (ODE, `http://www.ode.org/`) which is an open source rigid body dynamics library with industrial quality (acceptable accuracy, wide extensibility and strong robustness) originally developed by Russell Smith[129]. The governing equations for the solid particles are based on Newton's second law built on a global coordinate system which will remain stationary during the simulation. In this thesis work, the global coordinate system used is the same as that for the flow solver. The solid governing equations based on conservation of translational and angular momentum are as follows.

$$m\frac{\mathrm{d}\mathbf{U_s}}{\mathrm{d}t} = \oiint_A \mathbf{f_s} \tag{3.21}$$

$$I\frac{\mathrm{d}\mathbf{\Omega_s}}{\mathrm{d}t} = \oiint_A \mathbf{r} \times \mathbf{f_s} \tag{3.22}$$

Here m is the mass of the solid particle and I is its moment of inertia. $\mathbf{f_s}$ is the hydrodynamic force applied by the fluid on the individual cell on the solid-liquid interface and r is the relative location of that individual cell to the mass centre of the solid particle. Note that $\mathbf{f_s}$ is also a term in the fluid momentum equation,(Eq 3.2) is the key coupling parameter between the flow and solid equations. Besides the global coordinate system, each solid particle has its own local coordinate system whose origin is located at the mass centre of the solid particle and move synchronously during the simulation. Eq. 3.22 is built on that local coordinate system. Though the input and output of the angles are described by Eulerian angle, the practical operation on the rotation are based on quaternions to avoid the "Gimbal lock"singularity that happens during rotation [130]. Gimbal lock is the loss of one degree of freedom in a 3D three-gimbal mechanism that occurs when the axes of two of the three gimbals are driven into a parallel configuration, "locking" the system into rotation in a degenerate two-dimensional

space. The conversion between them are as follows:

$$\begin{bmatrix} q_0 \\ q_1 \\ q_2 \\ q_3 \end{bmatrix} = \begin{bmatrix} \cos(e_x/2)\cos(e_y/2)\cos(e_z/2) + \sin(e_x/2)\sin(e_y/2)\sin(e_z/2) \\ \sin(e_x/2)\cos(e_y/2)\cos(e_z/2) - \cos(e_x/2)\sin(e_y/2)\sin(e_z/2) \\ \cos(e_x/2)\sin(e_y/2)\cos(e_z/2) + \sin(e_x/2)\cos(e_y/2)\sin(e_z/2) \\ \cos(e_x/2)\cos(e_y/2)\sin(e_z/2) - \sin(e_x/2)\sin(e_y/2)\cos(e_z/2) \end{bmatrix} \tag{3.23}$$

$$\begin{bmatrix} e_x \\ e_y \\ e_z \end{bmatrix} = \begin{bmatrix} \mathrm{atan2}[2(q_0q_1 + q_2q_3), 1 - 2(q_1^2 + q_2^2)] \\ \mathrm{asin}[2(q_0q_2 - q_3q_1)] \\ \mathrm{atan2}[2(q_0q_3 + q_1q_2), 1 - 2(q_2^2 + q3^2)] \end{bmatrix} \tag{3.24}$$

Here e_i denotes the rotation angle around the i axis of the local coordinate system. To calculate the force applied on each cell, it is essential to know the area and direction of the interface. With the interface direction determined by Eq. 3.12, Eq. 3.14 and the volume fraction of the fluid in the cell, the area of the interface can be uniquely determined. As previously shown in Fig. 3.3. The hydrodynamic force applied on the cell $\mathbf{F_s}$ can therefore be calculated by:

$$\mathbf{F_s} = \begin{bmatrix} A_x & A_y & A_z \end{bmatrix} \begin{bmatrix} p - 2\mu\frac{\partial u_x}{\partial x} & -\mu\left(\frac{\partial u_x}{\partial y} + \frac{\partial u_y}{\partial x}\right) & -\mu\left(\frac{\partial u_x}{\partial z} + \frac{\partial u_z}{\partial x}\right) \\ -\mu\left(\frac{\partial u_y}{\partial x} + \frac{\partial u_x}{\partial y}\right) & p - 2\mu\frac{\partial u_y}{\partial y} & -\mu\left(\frac{\partial u_y}{\partial z} + \frac{\partial u_z}{\partial y}\right) \\ -\mu\left(\frac{\partial u_z}{\partial x} + \frac{\partial u_x}{\partial z}\right) & -\mu\left(\frac{\partial u_z}{\partial y} + \frac{\partial u_y}{\partial z}\right) & p - 2\mu\frac{\partial u_z}{\partial z} \end{bmatrix} \tag{3.25}$$

where the second matrix in the right hand side of the equation is the stress tensor of the fluid.

Though ODE itself have already provided a series of solid objects template, none of them is adopted in this thesis work. As a consequence, during the simulation, the ODE is not taking care of the shape of solid particle, but only calculating the abstract motion based on the input parameters. This makes the solver highly flexible regarding the solid shape. The GISS can handle arbitrary solid geometry of varying deformability. It is also necessary to point out that the adoption of ODE is not an exclusive option that one can employ other more functional and accurate physics engine.

3.3 Simulation Environment

The computer used in this thesis work was provided by the VLX cluster of the University of Edinburgh, with Intel Xeon 16 cores processor and each cores has the maximum CPU speed of 2.6 GHz. The simulations was all carried on with single core, and its time depended highly on the configuration of each cases. Generally, for a case with one million meshes, it would take $5 \sim 8$ second to simulate a time step, therefore a case with 10,000 time steps, the simulation would take around a day. The simulations in Chapter 4 and Chapter 5 took about 8 hours to 72 hours to finish, based on their mesh resolution settings. For simulations with extended domains, like those in Chapter .6, the simulation need to take 5-7 days to complete.

Chapter 4
Single Solid Translation Motion at Low to Moderate Re

This chapter reports on basic validation studies of the GISS against experiments involving drag calculations around stationary or moving solids experiencing only translational motion. Calculations and validations against spherical and ellipsoidal immersed solids are specifically reported.

4.1 Drag Force on Stationary Solids

Though our GISS is capable of handling the 6DOF problems, it is still meaningful to start the validating the immersed boundary implementation against theoretical and experimental drag coefficients of stationary solids in flow. These kind of problems have been treated as a popular simplification of the particle moving problem at low Re_p, due to smaller computational resources required as one need not simulate the actual motion of slow moving solid particles. The simulations here could provide fundamental information of the inner composition of the hydrodynamic force, and can also suggest the error bounds of the GISS. These tests could also help determine proper simulation configurations, such as mesh resolution, domain scale and timestep requirement for subsequent moving solid simulations which would require much more computational resources.

4.1.1 Validation against Stokes' drag and Mesh Dependency Tests

In this section, the GISS is validated against the classical Stokes' drag. Note that while the flow field in this classical case can be determined analytically by the classical Stokes Law (see Appendix A), 3D DNS strategy is adopted here to simulate Stoke's law for 3D

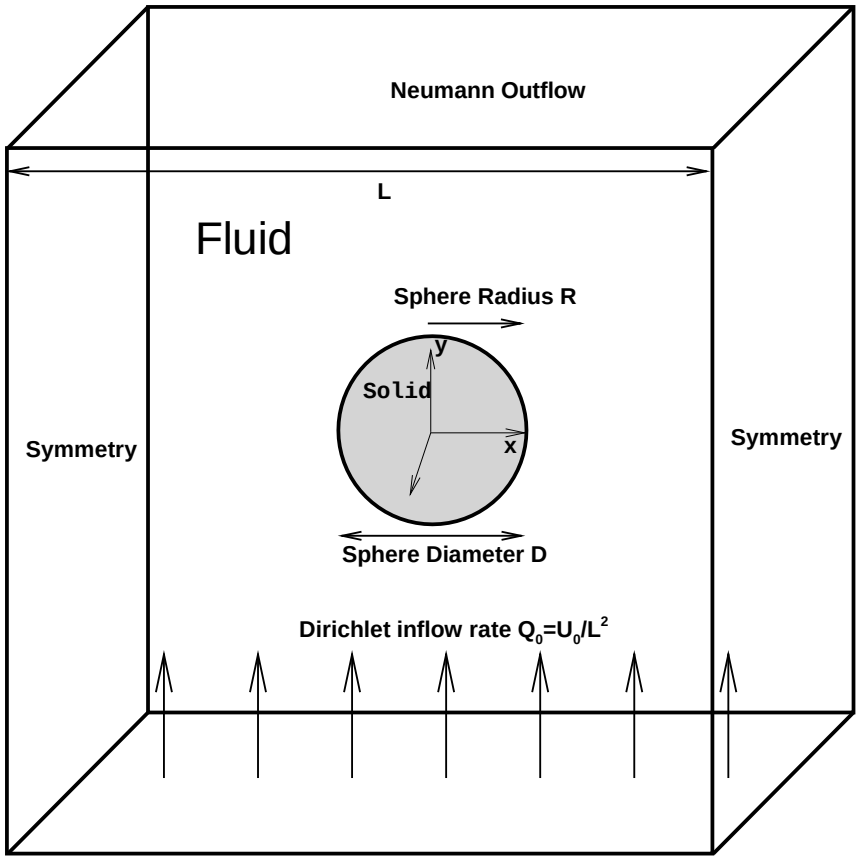

Figure 4.1: *Problem set-up for a fixed sphere in flow.*

sphere. As shown in Fig. 4.1, a rigid sphere solid is located at the centre of the computational domain with diameter D (radius R). A solid body of density ρ_s is submerged in a fluid of density ρ_f and viscosity μ_f. The boundary condition at the particle surface is the no-slip and no-penetration boundary conditions, which means the fluid velocity should exactly be zero (considering that the solid is fixed). The computational domain is a cube of side length L. A standard Dirichlet boundary condition (which specifies the values that a solution needs to take on along the boundary of the domain) of fluid inlet is placed at the bottom of the domain considering a constant inflow rate $\mathbf{Q_0}$ resulting in an average flow velocity $U_0 = Q_0/L^2$ perpendicular to the bottom surface. A standard Neumann outlet boundary condition (specifies the values that the derivative of a solution is to take on the boundary of the domain) is located at the top surface with local static pressure value and the gradient of

the velocity set to 0 on the surface normal direction of the boundary. The other four sides (right, left, front, back) are all set to being symmetry planes, also with the same definition as the free-slip wall boundary condition, where the gradient of all the variables is set to 0 on the surface normal direction of the boundary. The Reynolds number in this section can therefore be defined as:

$$Re_p = \frac{\rho_f U_0 D}{\mu} \tag{4.1}$$

By defining:

$$u^* = \frac{u}{U_0} \quad x_i^* = \frac{x_i}{D} \quad t^* = \frac{t}{t_0} = \frac{tU_0}{D} \quad p^* = \frac{p}{\rho U_0^2} \tag{4.2}$$

The dimensionless form of the momentum equations of Navier-Stokes equations can be obtained for the incompressible Newtonian fluid:

$$\frac{\partial \mathbf{u}^*}{\partial t^*} + \mathbf{u}^* \cdot \nabla \mathbf{u}^* = -\nabla p^* + \frac{1}{Re_p} \nabla^2 \mathbf{u}^* \tag{4.3}$$

The equation, Eq 4.3 reveals that the flow equations can be distinguished solely by Re_p. In this section, the flow falls in the Stoke's regime, which means $Re_p \ll 1$. The premise of the Stoke's regime results in the viscous term, $\frac{1}{Re_p}\nabla^2 \mathbf{u}^*$, being remarkably larger than the convective (inertial) term, $\mathbf{u}^* \cdot \nabla \mathbf{u}^*$, allowing us to neglect the convective term here. By assuming the flow to achieve a final stable state, the unsteady term $\frac{\partial \mathbf{u}^*}{\partial t^*}$ will also vanish thereby leading to a much simplified form:

$$\nabla p^* = \frac{1}{Re_p} \nabla^2 \mathbf{u}^* \tag{4.4}$$

For the aforementioned configuration of the problem, an analytical solution can be provided. By calculating the stress field around the sphere surface and integrating it, hydrodynamic force applied on the sphere by the fluid can be described as:

$$F_{hydro} = \underbrace{\frac{4}{3}\pi R^3 \rho_f g}_{buoyancy} + \underbrace{2\pi\mu U_0 R}_{F_{pressure}} + \underbrace{4\pi\mu U_0 R}_{F_{shear}} \tag{4.5}$$

In this section, neutrally buoyant solid sphere is studied, therefore $\rho_s = \rho_f$ here. With this condition, the buoyancy and the gravity neutralize each other. This allows us to concentrate only on the calculation of drag force caused by the flow. In order to reduce the computational cost, the body force term caused by the gravitational acceleration is set to 0 in the Eq. 4.3 to represent the neutral buoyancy condition, leaving only the drag force caused by the flow applied on the sphere which is known as "Stoke's Law":

$$F_{D0} = 6\pi\mu U_0 R \tag{4.6}$$

Its full derivation was first provided by Stokes in 1851[15] and later became the groundwork of many developments in fluid dynamics. For a clearer discussion, the subscript "0" is used to describe the theoretical solution of the drag force calculated based on the initial velocity U_0, and use F_d to represent the results obtained from experiments or simulations in the following discussion. The influence of F_D can also be described by the drag coefficient, which is defined as:

$$C_{D0} = \frac{F_{D0}}{\frac{1}{2}\rho_f U_0^2 A} = \frac{24}{Re_p} \tag{4.7}$$

where A is the cross sectional area of the sphere:

$$A = \frac{\pi D^2}{4} \tag{4.8}$$

Eq. 4.5 also shows that the pressure the shear stress together composing the overall F_d have a clear relation such that:

$$\lambda_f = \frac{F_{shear}}{F_{pressure}} = 2 \tag{4.9}$$

This inner correlation should be carefully tested. As a numerically lower pressure force and a numerically higher shear force may look like a correct result, while they may be actually incorrect. In order to enforce rigour, the pressure force and the shear force to their theoretical value is also compared separately to find out the real correct configuration for a validated simulation in the following discussion.

As mentioned before, the computational domain scale in this section is a cube of volume

L^3 and the characteristic length as the sphere diameter D. Thus the dimensionless size of the domain is $L^* = L/D$. For a mesh refinement level N, the smallest mesh size, $\Delta x_{MIN} = L/2^N$ surrounds the solid. In dimensionless terms, $\Delta x^*_{MIN} = \Delta x_{MIN}/D$. Thus the mesh resolution is defined as inverse of mesh size i.e. $M = 1/\Delta x^*_{MIN} = D/\Delta x_{MIN}$. In order to ensure the continuity of numerical error between the fluid and the solid domains, $\Delta x^*_{MIN}|_{fluid} = \Delta x^*|_{solid}$ where $\Delta x^*|_{solid}$ is the mesh defining the sphere. This is crucial to enforce the no-slip, no-penetration boundary condition on the walls of the solid. This also minimises error in calculation of the stress tensor around the solid and hence the drag and lift forces. During the simulation, the timestep is set to fulfil both Courant and viscous criteria such that :

$$\Delta t^* \leqq min\left(\frac{\Delta x_{MIN}}{U_0}\frac{U_0}{D}, \frac{\Delta x^2_{MIN}}{\nu}\frac{U_0}{D}\right) \implies \Delta t^* \leqq min\left(\frac{1}{M}, \frac{Re_p}{M^2}\right) \tag{4.10}$$

A mesh dependency test is essential for all numerical simulations. For this purpose, case with $Re_p = 0.1$ is selected to approach a pseudo-zero Re_p assumption of Stokes' Law. a domain scale of $L^* = 32$ is chosen at beginning (based on experience, would be validated later), and test the evolution of drag force (F^*_d) with increasing mesh resolution (which corresponds to finer mesh). The simulated dimensionless drag $F^*_d = F_d/F_{d0}$ is presented in Table. 4.1. The table shows that this dimensionless force is close to 1 at mesh resolutions with $\Delta x_{MIN} \ll D$, which means that the diameter of the sphere is much greater than the smallest mesh element in the fluid mesh around it. The result shows that while F^*_d is always marginally overpredicted at all mesh resolutions tested, it is closer to 1 at $M = 16$.

Recollecting that $F_{d}*$ is the sum of both the shear-force (F_{shear}) and pressure force ($F_{pressure}$), it is instructive to check if the equation 4.9 governing the force ratio λ_f is satisfied. It can be seen in Table. 4.1 that λ_f asymptotically approaches 2 with mesh resolution ($M > 32$) perfectly consistent with the analytical prediction. This indicates that with mesh resolutions smaller than 32, the shear force is severely over-predicted while the pressure force is under-predicted.

In order to ensure that the predicted drag force is purely generated by flow, it is necessary to limit all other possible interferences from the boundaries of the domain. The choice of

M	L^*	F_d^*	λ_f
8	32	1.06754	4.77976
16	32	1.05224	2.2307
32	32	1.08621	2.0244
64	32	1.1009	2.00141
16	2	2.93799	1.62847
16	4	1.56157	2.0078
16	8	1.22502	2.06147
16	16	1.10314	2.06812
16	32	1.05224	2.06817
16	64	1.0397	2.06917

Table 4.1: *Dimensionless drag force F_d^* and force composition ratio λ_f of different simulation cases.*

symmetry boundary condition for all the 6 sides of the fluid domain does help in this regard. However, this configuration may still not accurate enough to represent the feature of an infinitely large domain and the domain bounds will certainly affect the calculation of F_d. Applying periodic conditions is a also a reasonable compromise to achieve good results with less computational cost. However, a main purpose of this series of test is to find out the limit of our solver and to provide setting-up suggestions to the later simulations, thus the symmetric boundary condition is set on the bounding wall here.

Using the criteria of mesh resolution as determined from our mesh dependence study above, a careful examination is given towards the stability of our solver in handling symmetry boundary conditions. At symmetry boundaries, the gradient of any flow variable (such as $\phi = \mathbf{u}$ or p) in the normal direction to the plane must be 0, i.e. $\partial\phi/\partial\mathbf{n} = 0$. This means that the flow variable cannot vary in the direction perpendicular to the symmetry plane or in other words, for symmetry to be adhered the flow variable cannot be three-dimensional along the plane in consideration. Smaller domain sizes mean that the domain boundaries are too close to the solid body - where velocity and pressure fields are strong 3D functions of space and time and an imposition of symmetry conditions may lead to false smoothing of velocity and pressure fields in the vicinity of the solid body thereby causing an incorrect calculation of drag. The above result shows that when $M \geq 32$, the force composition is precisely simulated. When $M = 16$, the calculated and theoretical values of overall F_d and of λ_f differ by around 10%. Considering there is a very large domain to be simulated while maintaining the same mesh

resolution in this section, a mesh resolution $M = 16$ was chosen in this section. The idea is to check if domain size has influence in reducing the error for $M = 16$ case further. Table. 4.1 shows the influence of the domain scale on F_d. When $L^* \leq 16$, the errors on the predicted drag force F_d^* are exacerbated, and this influence decreases dramatically with the large L^*. Beyond $L^* \geq 16$, the results can safely be judged as reliable. The evolution of λ_f with the expanding domain scale is also presented in Table. 4.1 . It is worth mentioning that λ_f is under-predicted when the domain is narrow ($L^* \leq 8$) while the error in calculated F_D is only insignificant beyond $L^* \leq 32$. This suggests the influence of domain size on the calculations of shear and pressure forces in line with the arguments posed above.

The above discussion on mesh and domain scale dependency highlights the reliability of our GISS to simulate Stokes' flow using DNS in 3D. Fig. 4.2 presents the path-lines of a group of massless passive tracer randomly released in the domain. They are plotted on the xy plane when $L^* = 32$, $M = 32$ and $Re_p = 0.1$. Typical Stokes' flow behaviour can be found in the figure: only flow around the sphere is influenced and the fluid at certain distance away from the sphere is largely unaffected.

4.1.2 Validation against Experimental Results

In the previous section, the GISS against Stoke's theory at low Re_p is validated. In this section, the validation extends to the published experimental works, specifically at higher Re_p. When $1 < Re_p < 1000$, the flow falls in the transition regime and the drag coefficient can be calculated with empirical expressions [131]:

$$C_d = C_{d0} + \frac{4}{Re_p^{0.33}} \tag{4.11}$$

Besides the above analytical solution, the experimental result from Roos and Wilmarth's work [8] is adopted for validation. The set up of the experiment is sketched in Fig. 4.3. It consists of a $0.61m \times 0.61m \times 9.75m$ plywood and fibre glass towing channel and a linear air bearing track system that was able to provide a shock yet vibration-free linear motion. A loop of cable which could be driven at various speeds and directions by an electric motor drive unit

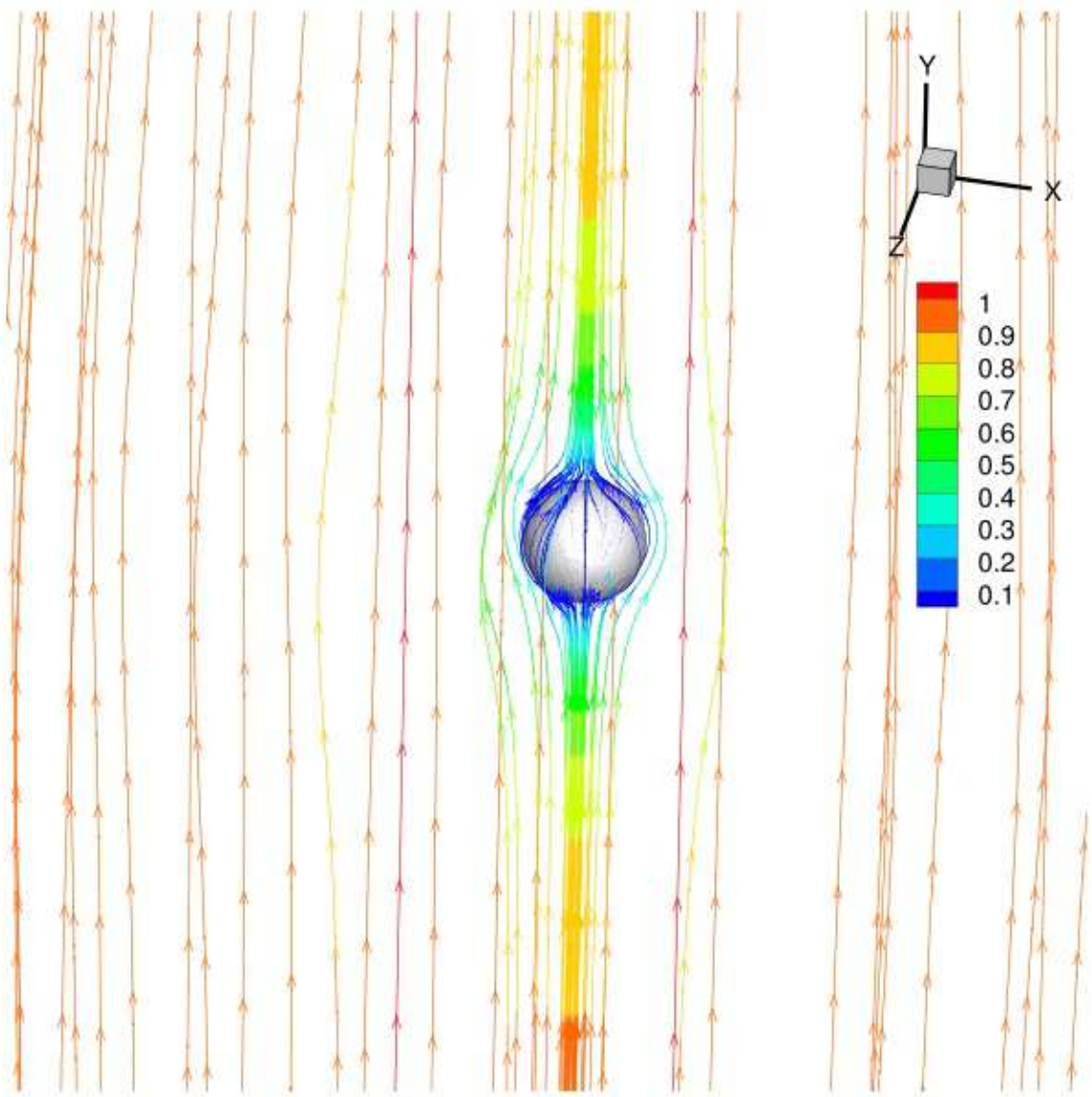

Figure 4.2: *Streamlines around a stationary solid sphere in Stoke's flow regime. Traces were disposed randomly in the domain and the colour of the streamlines represents the magnitude of velocity.*

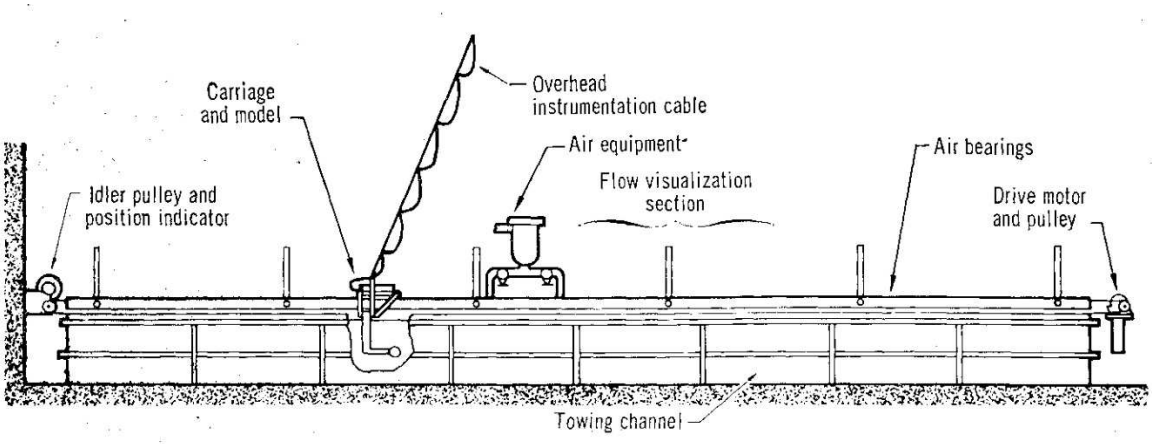

Figure 4.3: *Drag coefficient equipment. [8]*

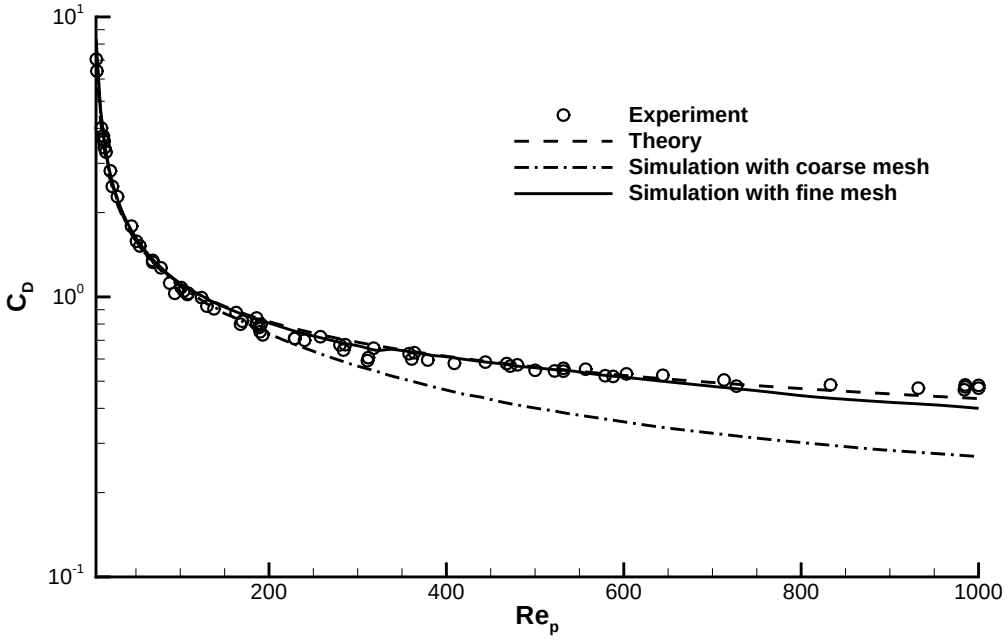

Figure 4.4: *Drag coefficient evolution with Re_p,$L^* = 40$ and $M = 12.8$.*

was adjacent to the horizontal tracking system. A strain-gauge-instrumented test model i.e. a sphere with $d = 7.62cm$ was suspended where a carriage was attached to the cable. The experiment measured the drag coefficient for $5 < Re_p < 100000$ and our focus is mainly the results in transition regime ($Re_p \leq 1000$).

Flow with higher Re_p requires greater mesh resolution to capture the detail of the flow structure, therefore two groups of simulations with different mesh resolution settings are processed here to test the mesh independence for flows extending to transitional regime: Group A with $M = 12.8$ and group B with $M = 25.6$. As shown in Fig. 4.4, the solver can provide accurate drag coefficient until $Re_p \leq 200$ at $M = 12.8$. As expected, a higher mesh resolution (at $M = 25.6$) predict accurate drag coefficients in a broader range of Re_p due to the ability to better predict the vortices in the wake structure.

The vortex contours shown in Fig. 4.5 are snapshots at late times. The figures have been truncated for clarity to simply depict the region influenced by the immersed solid sphere. Fig. 4.5(a) represents for the $Re_p = 0.1$ with mesh resolution of $M = 25.6$, Fig. 4.5(b) shows that even at these low $Re_p > 1$ the flow has already changed from being a smooth Stokes' flow regime as shown in Fig. 4.2. The vortex structure already begins to develop at $Re_p = 0.1$. Both Fig. 4.5(c) and Fig. 4.5(d) present vortices observed at $Re_p = 1000$ at mesh resolutions of $M = 25.6$ and $M = 12.8$, respectively. The expected flapping behaviour of the vortex was observed (the von Karman vortex) in Fig. 4.5(d) unlike the one shown in Fig. 4.5(c) which presents only an unrealistic smooth wake. The Strouhal number is used here to describe oscillating flow mechanisms:

$$S_t = \frac{fL_c}{U_c} \tag{4.12}$$

where f is the vortex shedding frequency. When $Re_p \sim 1000$, the previous experimental study had found that $S_t \sim 0.2$ [132], and the simulation result by GISS had $S_t \approx 0.25$ (only for Group B, the refined mesh, where the mesh resolution for the refined fluid region is $M = 25.6$, as large as the mesh resolution on the solid surface). This further verifies that the complicated flow structure with higher Reynolds number needs to be captured by higher mesh resolution.

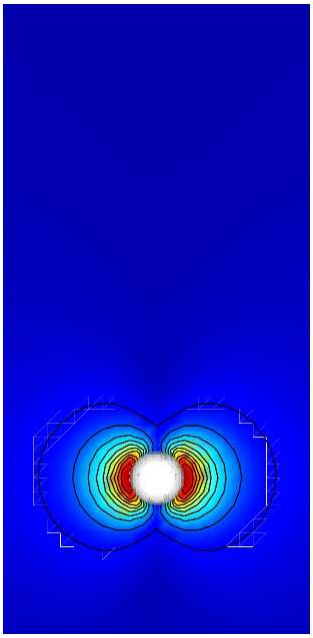

(a) Group B, $Re_p = 0.1$, predicted $C_D = 261$, $\varsigma = 8.6\%$

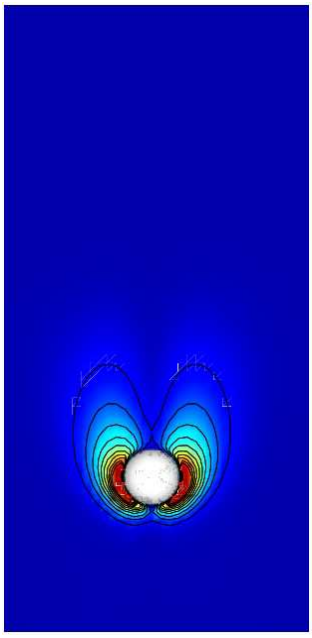

(b) Group B, $Re_p = 10$, predicted $C_D = 4.7$, $\varsigma = 11.9\%$

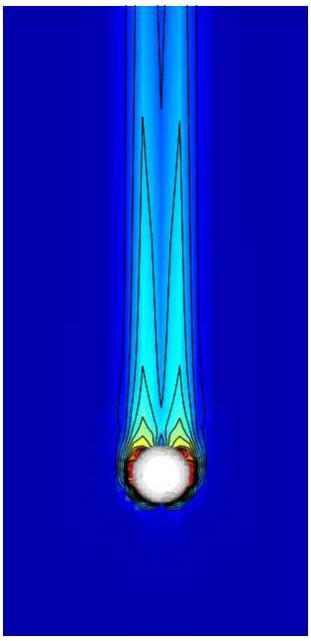

(c) Group A, $Re_p = 1000$, predicted $C_D = 0.4$, $\varsigma = 15.3\%$

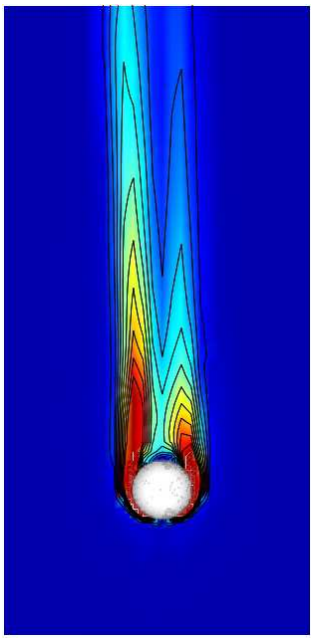

(d) Group B, $Re_p = 1000$, predicted $C_D = 0.269$, $\varsigma = 43\%$

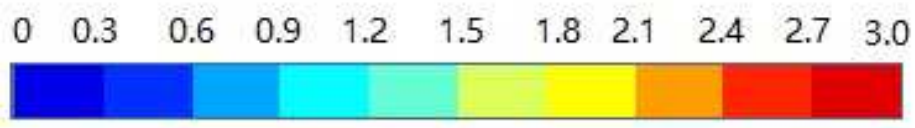

(e) Colour scale of vorticity

Figure 4.5: *The predicted vortex contours and drag coefficients at various Re_p and mesh resolutions. ς is the relative error of C_D, $M = 12.8$ for Group A, $M = 25.6$ for Group B. Flow is incoming from the bottom boundary.*

4.2 Terminal Velocity of Settling Solid

In the previous section, the competence of our solver in simulating the drag force applied on the stationary solid (where there was no movement of solid) has been validated. The validation also suggested simulation requirements to achieve accurate results. In this section, the information obtained from the last section would be utilized to simulate the moving body settling problem.

4.2.1 Validation against Stokes' Settling

The Stokes settling problem is derived based on the Stokes' law. As discussed in Section. 4.1.1, the F_d applied on a settling solid can be equivalent calculated as a stationary solid facing incoming flow. However, the neutral buoyancy condition on the solid is no longer applicable in this section. The ρ_s here is slightly larger than ρ_f and as a consequence, the gravity is larger than the buoyancy and their net effect can be defined as effective gravitational acceleration:

$$\mathbf{g}_{eff} = \frac{\rho_s - \rho_f}{\rho_s}\mathbf{g} \tag{4.13}$$

where g is the actual gravitational acceleration vector. At the initial stage of the settling, the F_d is smaller than the effective gravity and $\mathbf{g}_{eff}$ drives the solid to settle in the gravitational direction. When the solid achieves a terminal settling velocity, the magnitude of F_d is equal to that of the effective gravity and with the opposite direction. Defining this terminal settling velocity as U_t, the particle Reynolds number of this problem can be then defined as:

$$Re_p = \frac{\rho_f U_t D}{\mu} \tag{4.14}$$

As stated at the beginning of this section, $Re_p \ll 1$, and F_d can be calculated by Stokes' Law:

$$F_d = 6\pi\mu U_t R \tag{4.15}$$

By combining Eq. 4.13 and Eq. 4.15, U_t can be obtained:

$$U_{t0} = \frac{2}{9}\frac{\rho_s - \rho_f}{\mu} g R^2 \tag{4.16}$$

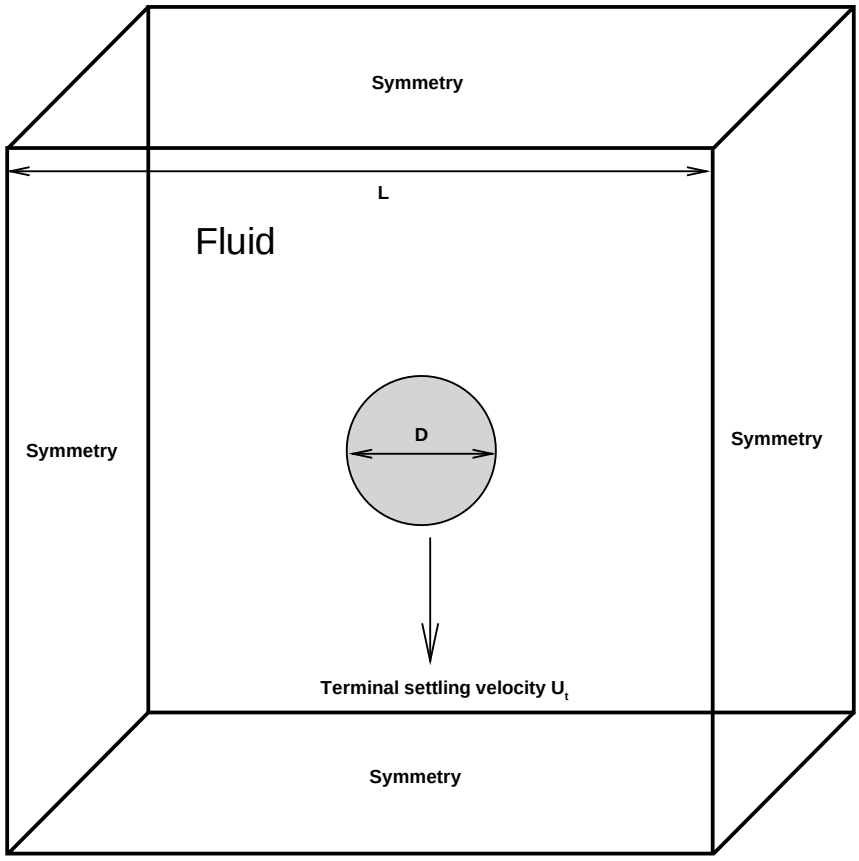

Figure 4.6: *Spheroid settling in stationary fluid.*

In order to make a general discussion, the results in this section would also be discussed in a dimensionless way, where:

$$U^* = \frac{U}{U_{t0}} \quad L^* = \frac{L}{D} \quad t^* = \frac{t}{t0} = \frac{tU_{t0}}{D} \tag{4.17}$$

In this simulation, the configuration is recommended by Section. 4.1.1. The mesh resolution M is set to 32. The domain is a cuboid composed by $L \times L \times L$ cube as shown in Fig. 4.6. The cube is also aligned in the gravitational direction, as the settling of the solid requires

longer domain scale in that direction. The span-wise domain scale L^* is set to 32, which is also recommended by the previous section. This large domain ensured that there are no boundary effects felt by the settling solid. In this simulation, there is no inflow or outflow for the fluid domain, so all six surfaces were set to symmetry boundaries. The evolution of the settling velocity is plotted on Fig. 4.7, and it shows that the dimensionless terminal settling velocity is approaches 1 on the figure, i.e. the simulated terminal velocity approaches the theoretical terminal velocity given by Eq. 4.16. The relative error ς of the simulation result in this case was 7.5%, and the simulated solid terminal settling velocity was slightly smaller than its theoretical value calculated by Eq. 4.16. This tendency of error is expected, as the domain sides would always enhance the drag force applied on the solid. Fig. 4.8 shows the massless stream tracers which were randomly released in the fluid domain and those tracers clearly illustrate the flow in the domain. Though the fluid close to the solid surface would move together with solid due to the no-slip boundary condition, the fluid near the domain sides and far away from the solid would translate in the opposite direction of the settling, as required by the mass conservation of the whole system. The consequence of this counter flow would make a larger relative settling velocity of the solid. A much larger domain farther away from the influence of the predicted vortices around the solid, would result in further reduction of error.

ε	λ_f	Ut by simulation	Ut by theory	ς
0.5	1.128339767	0.5176212	0.453927308	14.03%
0.6	1.315186501	0.6125444	0.545064645	12.38%
0.7	1.517535329	0.6975951	0.639520494	9.08%
0.8	1.730187654	0.7827975	0.737617199	6.13%
1	2.187050581	0.939133763	1	6.09%
1.5	3.478958845	1.267253041	1.361576	6.93%
2	4.975922585	1.540403008	1.661211014	7.27%
2.5	6.654731274	1.767218232	1.915636897	7.75%
3	8.51499176	1.959814191	2.136045694	8.25%

Table 4.2: *Terminal settling velocity Ut and drag composition λ_f of solid with of different geometry.*

The terminal velocity of a standard sphere is given by Eq. 4.16. As indicated in the literature review, this equation could be extended to account for more generalised geometries such as ellipsoids [21]. A general ellipsoid shown in Fig. 4.9 with semi-principal axes as a, b and

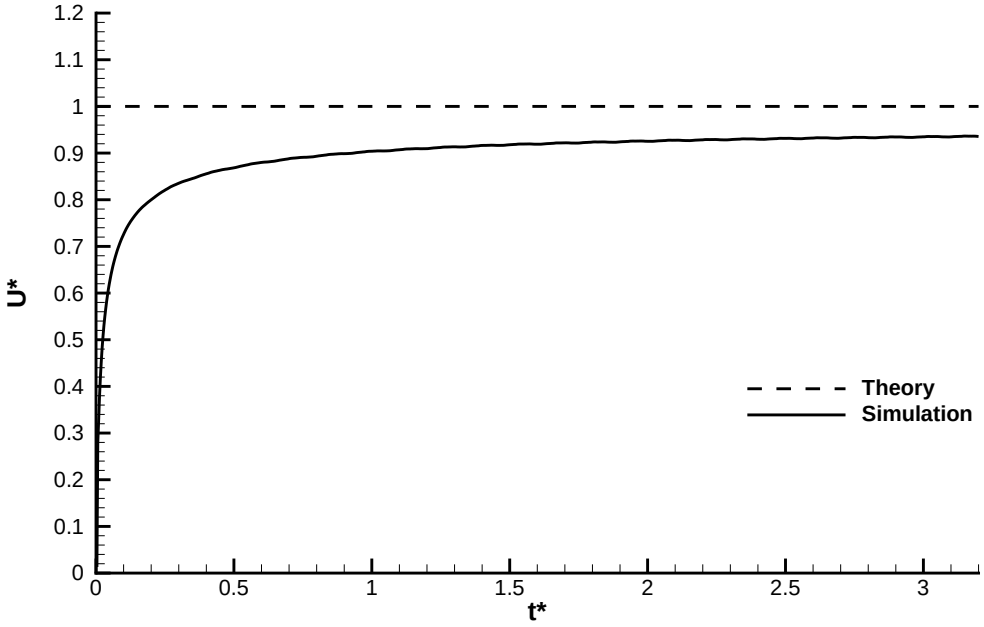

Figure 4.7: *Evolution of the settling velocity for* $Re_p = 0.1$, $L = 32$, $M = 32$, $\varsigma = 6.5\%$.

$c = a$ is considered. The geometry characteristic of the ellipsoid can be described by its geometric aspect ratio:

$$\varepsilon = \frac{a}{b} \tag{4.18}$$

Based on the solid settling direction, the characteristic length here is $2a$. Therefore the particle Reynolds number in this section can be defined as:

$$Re_p = \frac{2\rho_f U_t a}{\mu} \tag{4.19}$$

In this section, only cases where particle Reynolds number is in the Stokes regime ($Re_p < 1$) are considered. Consider a sphere with equivalent characteristic length $D = 2a$ settling with terminal settling velocity of U_{t0}, and defining its Stokes' drag force as F_{d0}. The drag force of a settling ellipsoid can be then described.

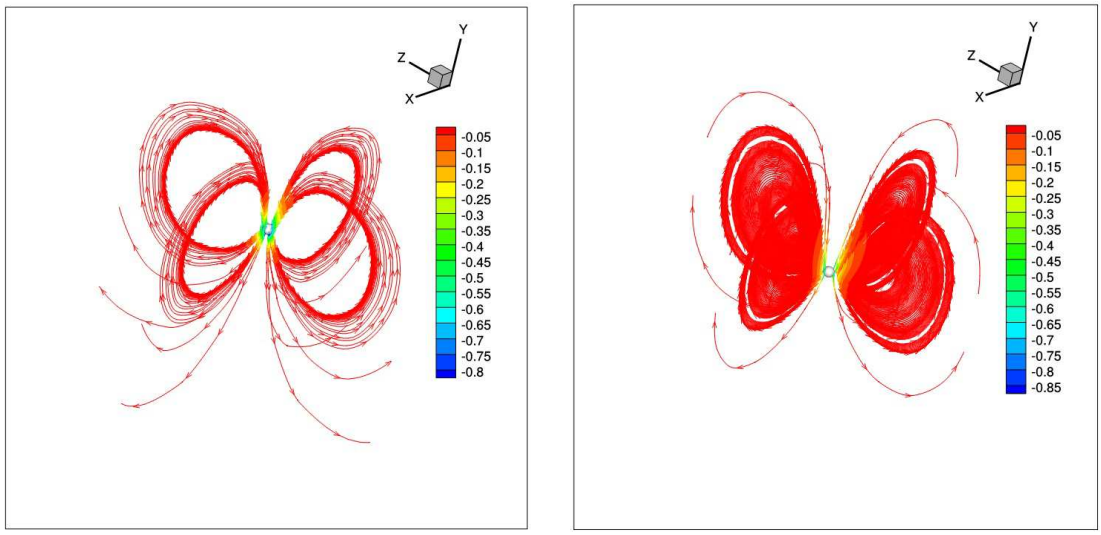

(a) $t^* = 0.1$ (b) $t^* = 0.3$

(c) $t^* = 0.5$ (d) $t^* = 7$

Figure 4.8: *Streamline for settling simulation. Traces were released randomly from the fluid domain and the colour of the streamlines represents the magnitude of velocity (dimensionless, -1 means the terminal settling velocity).*

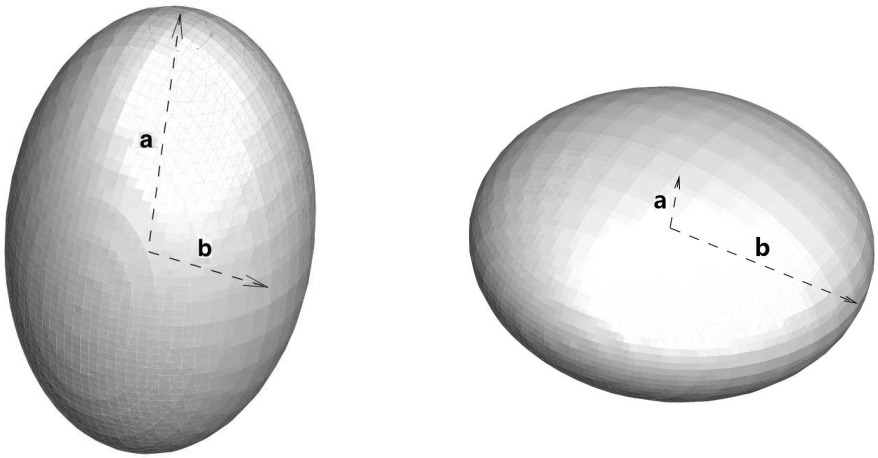

(a) Prolate ellipsoid (b) Oblate ellipsoid

Figure 4.9: *3D Ellipsoid settling in stationary fluid.*

Fro prolate ellipsoid ($\varepsilon > 1, a = c < b$): The drag force is

$$F_d(\varepsilon) = \frac{\frac{4}{3}(\varepsilon^2 - 1)}{\frac{2\varepsilon^2 - 1}{\sqrt{\varepsilon^2 - 1}} \ln(\varepsilon + \sqrt{\varepsilon^2 - 1}) - \varepsilon} F_{d0} \tag{4.20}$$

and the terminal settling velocity is:

$$U_t = \frac{3\varepsilon}{8} \left[\frac{2\varepsilon^2 - 1}{(\varepsilon^2 - 1)^{\frac{3}{2}}} \ln \frac{\varepsilon + \sqrt{\varepsilon^2 - 1}}{\varepsilon - \sqrt{\varepsilon^2 - 1}} - \frac{2\varepsilon}{\varepsilon^2 - 1} \right] U_{t0} \tag{4.21}$$

Fro oblate ellipsoid ($\varepsilon < 1, a = c > b$): The drag force is

$$F_d(\varepsilon) = \frac{\frac{4}{3}(1 - \varepsilon^2)}{\frac{1 - 2\varepsilon^2}{\sqrt{1 - \varepsilon^2}} \arctan \frac{\sqrt{1 - \varepsilon^2}}{\varepsilon} + \varepsilon} F_{d0} \tag{4.22}$$

and the terminal settling velocity is:

$$U_t(\varepsilon) = \frac{3\varepsilon}{8} \left[\frac{3 - 2\varepsilon^2}{(1 - \varepsilon^2)^{\frac{3}{2}}} \arctan \sqrt{1 - \varepsilon^2} - \frac{\varepsilon}{1 - \varepsilon^2} \right] U_{t0} \tag{4.23}$$

There are plenty of studies focused on the overall drag force applied on the ellipsoids [133] [134] [135], yet few of them studied the composition of the drag force. As studied in Sec-

tion. 4.1.1, the force composition ratio λ_f equals to 2 when the ellipsoid is exactly a special case, sphere. For ellipsoids, λ_f is expected to be changed, e.g., a oblate ellipsoid should experience more pressure force and have $\lambda_f < 2$ as it is more obstructive at the settling direction, while a prolate ellipsoid should experience less pressure force and have $\lambda_f > 2$ as it is more streamlined at the settling direction. This force composition is presented in Table. 4.2. The λ_f is expected to approach 0 when ε approaches 0 (a disk with face normal parallel to the settling direction) and to approach infinity when ε approaches infinity (a disk with face normal traverse to the settling direction). This tendency from the simulation result can be observed in Table. 4.2 and this information may provide meaningful suggestion when our solver is utilized in practical problems with complex shaped solids. Further, our 3D DNS results also show that at these low Re_p there is hardly any rotational motion of the solid - which is expected. The azimuthal component of velocity (not shown here) is always very close to zero.

Besides the drag force, the settling velocities for ellipsoids of different shapes are also compared. For an ellipsoid with its polar axis parallel to the settling direction, the U_t was non-dimensionalized by the terminal settling velocity of the sphere(U_{t0}) and is presented in Table. 4.2. The simulations have shown general competence in handling these settling problems with different geometry characteristics. The error increases when the solid became "less" spherical as the increased geometrical complexity of the solid demands greater mesh resolution for both the solid and fluid domains.

4.2.2 Validation against Settling Experiments

Besides the simulation of Stokes' flow regime, our simulation are also compared with experimental results reported by Mordant [9]. They had different spheres settling with different Reynolds number in a $1.1m(length) \times 0.75m(width) \times 0.65m(height)$ tank filled with water. Fig. 4.10 presents the set up of their experiment. 4 sets of their experiments were chosen to compare with our 3D DNS, two of them were with beads made of glass, the other two were made of steel. The specifications of the beads and the fluid, the terminal velocity and the Re_p are presented in Table. 4.3, where the superscript "exp"means experiment and "sim" means simulation. At the beginning of the experiment, the bead was held by tweezers below the

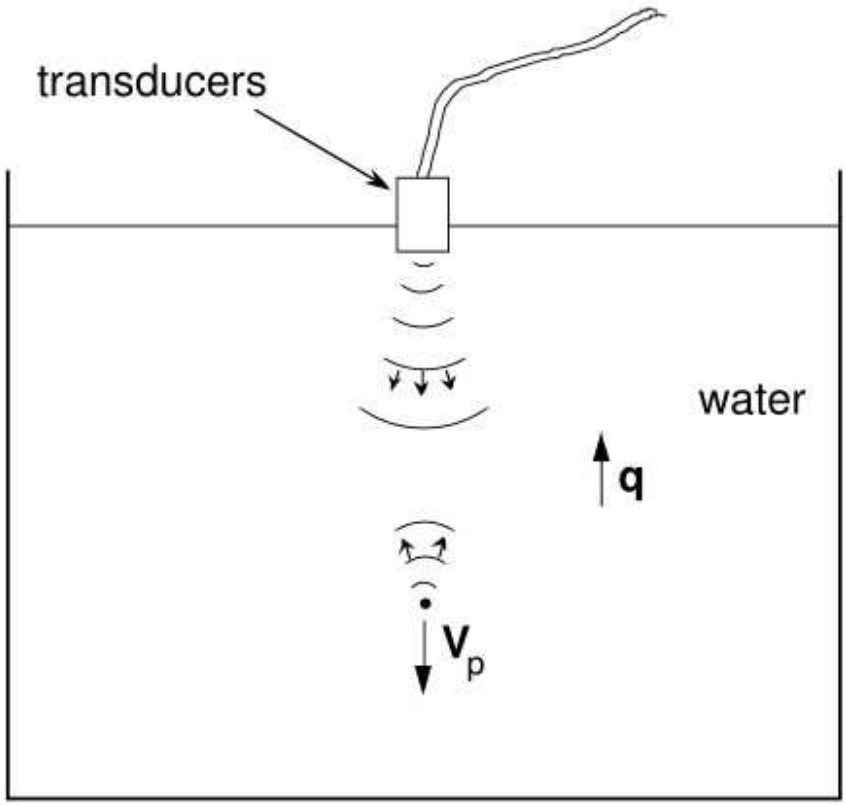

Figure 4.10: *Settling equipment used by Mordant. [9]*

transducer and released without initial momentum. The initial condition for the experiment were such that the beads were only expected settle vertically and without rotation.

The domain scale $L^* = 32$ and in the settling direction the length is extended to $2L^*$ to allow fully developed settling process. Other geometric and flow parameters strictly follow the set up of the experiments. The Re_p of the cases chosen fall in the transition regime, whose C_d can be approximately calculated by Eq. 4.11. By introducing this modified drag coefficient to Eq. 4.16, the theoretical terminal settling velocity for transition regime can be approximately predicted by:

$$U_t^0 = \sqrt{\frac{d\left(\rho_s - \rho_f\right) g Re_p}{3\rho_f \left(6 + Re_p^{0.67}\right)}} \tag{4.24}$$

General speaking, in all these 4 set of comparison study, our 3D DNS solver has shown good agreement with both the theoretical predictions and experiments. The maximum relative error

$d(mm)$	material	$\rho_s(kg/m^3)$	Re_p	$U_t^0(m/s)$	$U_t^{exp}(m/s)$	$U_t^{sim}(m/s)$
0.5	glass	2560	41	0.0761	0.0741	0.0741
0.8	steel	7850	280	0.318	0.316	0.313
1.5	glass	2560	360	0.219	0.218	0.219
1	steel	7710	430	0.383	0.383	0.383

Table 4.3: *Mordant's [9] experiment configuration.*

is 4.3% for the case of $Re_p = 360$ here and for the other cases the relative error is around 2%. Except for the case of $Re_p = 41$, the evolution of the settling velocity for all other 3 cases are also well simulated, as shown in Fig. 4.12, 4.13 and 4.14. In these simulations, the result shows that the rotation of the solid is negligible ($< 5°$).

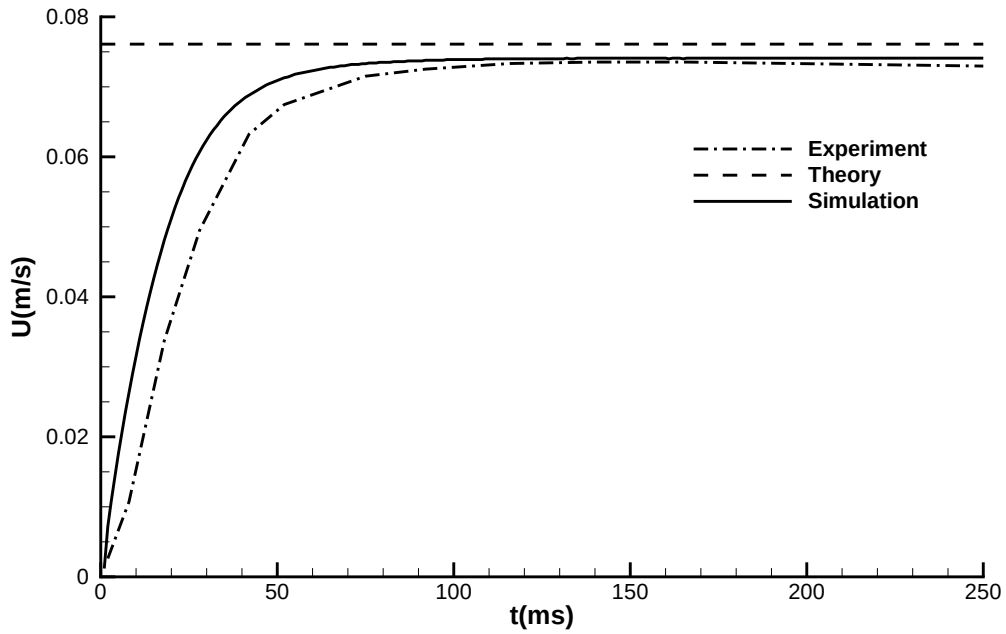

Figure 4.11: $Re_p = 41$, *glass.*

4.3 Conclusion

In this chapter, the GISS has been firstly validated by simulating the drag force applied on a fixed solid when Reynolds number is very small ($\ll 1$). The theoretical result of this problem

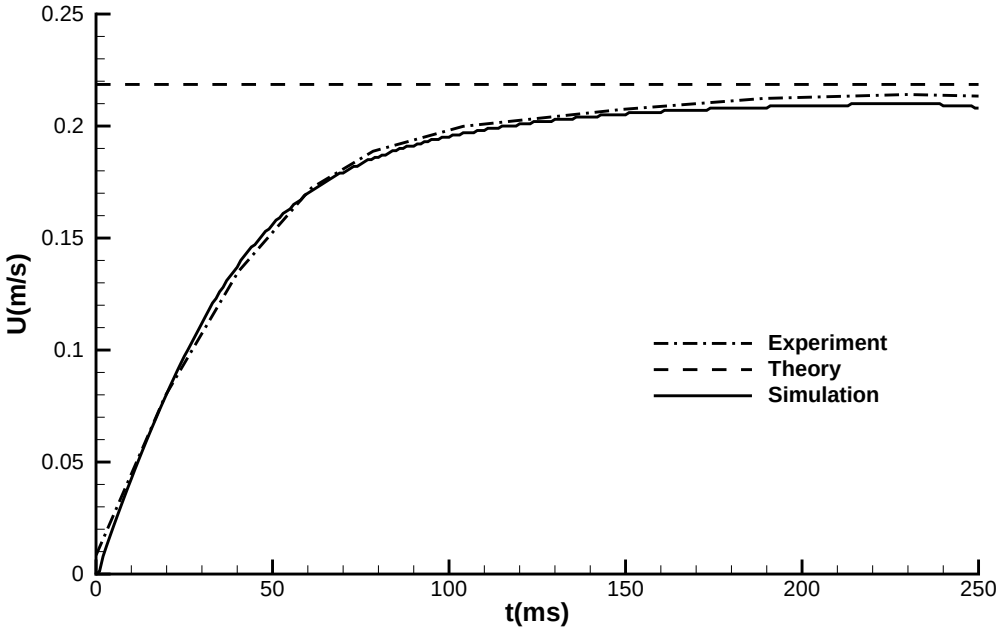

Figure 4.12: $Re_p = 360$, *glass.*

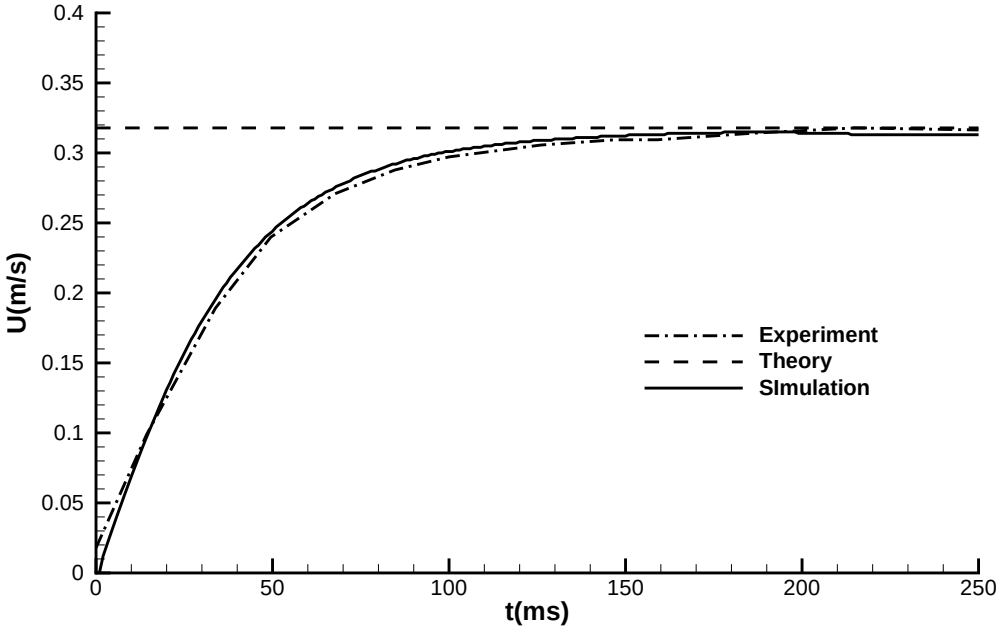

Figure 4.13: $Re_p = 280$, *steel.*

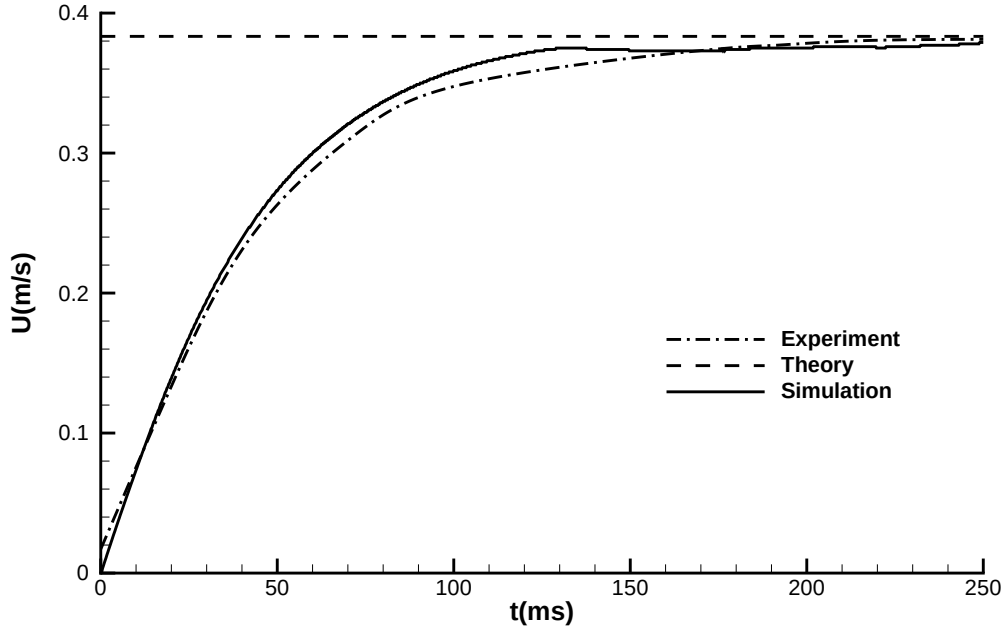

Figure 4.14: $Re_p = 430$, *steel.*

was provided by the Stokes' law. The solver was tested for mesh independence and domain-size dependency test, and criteria have been established. A detail study of the drag force composition was also presented in order to rigorously check the shear force and the pressure force components. To extend the study, our simulation was also compared with an experiment which covered a range of Reynold numbers from 5 to 1000. The comparison showed with proper mesh resolution, our solver can be reliable not only in Stokes' flow regime, but also in transition regime.

With the configuration suggested by the fixed solid, our 6DOF solver was then utilized to simulate the settling problem. The solid with different geometry characteristic (sphere, prolate ellipsoids, oblate ellipsoids) were validated them against the theoretical solutions/approximations. After that, the numerical result was compared with experiment with a extended scope of Reynolds number. The solver showed general competence in all these studies.

Chapter 5
Single Ellipsoid Coupled-6DOF Motion at Low to Moderate Re_p

This chapter reports on validation tests on the GISS against benchmark cases involving rotational motion alone and those involving both translational and rotational motion. Crucial parameters to compare and analyse include period of rotation of the ellipsoid and the lift experienced when the ellipsoid moves closer to the wall.

5.1 Ellipsoid Rotation in the Shear Flow

In the previous chapter, the GISS was validated against the fixed and settling solid problem. Though only the translational behaviour were focused in those problems, it is worth mentioning that in the validations of settling problems, all solids were also free to rotate during the simulation, therefore the potential influence of rotation were also captured by our 6 DOF solver. In this chapter, the study will be extended to rotation-dominant problems to validate our solver in a wider scope.

5.1.1 Validation against Jeffery's Orbits

Jeffery [14] derived the analytical solution for motion of a single neutrally buoyant ellipsoid in shear flow under the hypothesis that the ellipsoid tend to adopt positions with least energy dissipation (see Appendix B). The orbit made by the solid under these conditions is called as the *Jeffery's orbit*. At low Reynolds numbers when the effects of inertia are negligible, the solution was confirmed by several related experiments [30]. In this section, solutions obtained from our 3D DNS are compared against this analytical solution. Orientations of the ellipsoid and time periods of rotation will be predicted and compared against theoretical

results. Our setup contains a neutrally buoyant ellipsoid subjected to a Couette flow with constant shear rate (γ) in a channel. The channel is bounded by walls at the top and bottom moving with constant velocity but in opposite directions. The boundaries in the streamwise and spanwise directions are periodic, as shown in Fig. 5.1.

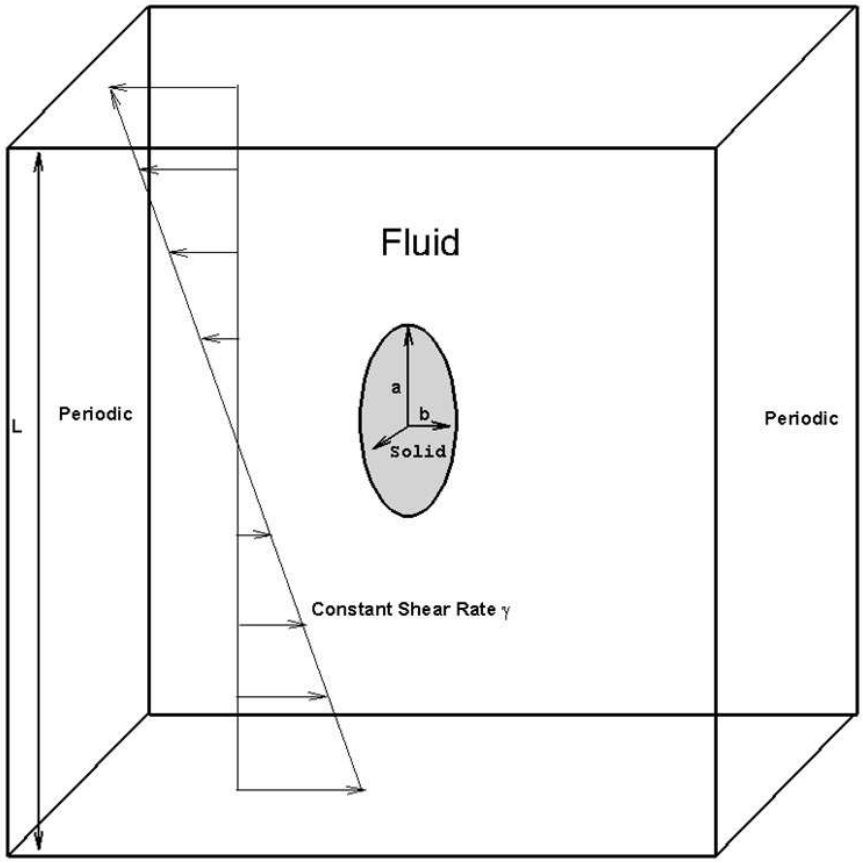

Figure 5.1: *Problem set-up for the Jeffery's orbit problem of a neutrally buoyant ellipsoid rotating in a Couette flow with shear rate γ. The axes are x (streamwise), y (cross-stream) and z (transverse.)*

Given a neutrally buoyant solid-fluid system ($\rho_s = \rho_f$) where the possible influence of gravity can be neglected. The solid is a rotationally symmetric ellipsoid whose length of polar axis is $2a$ and the diameter of the equatorial circle is $2b$. Hence the characteristic of the ellipsoid shape can be described by its geometric aspect ratio:

$$\varepsilon = \frac{a}{b} \tag{5.1}$$

Note that $\varepsilon = 1$ is a special case when the ellipsoid becomes a sphere. The characteristic length (D) for this problem is the diameter of the sphere, or the length of major axis of the ellipsoid. The characteristic velocity for this problem can be given by the applied shear rate and the characteristic lengthscale, $U_0 = \gamma D$. Thus, the particle Reynolds number can therefore be defined as:

$$Re_p = \frac{\rho_f \gamma D^2}{\mu} \begin{cases} D = 2a & \varepsilon > 1 \quad \text{prolate ellipsoid} \\ D = 2b & \varepsilon < 1 \quad \text{oblate ellipsoid} \end{cases} \tag{5.2}$$

According to Jeffery [14], when the $Re_p \ll 1$, a sphere ($\varepsilon = 1$) would rotate with constant angular speed, which is:

$$\Omega = \frac{\gamma}{2} \tag{5.3}$$

Thus the rotation period for a sphere ($\varepsilon = 1$) would be:

$$T_1 = \frac{4\pi}{\gamma} \tag{5.4}$$

If $\varepsilon \neq 1$, the solid body is an ellipsoid and its geometry would influence the ellipsoid rotation, based on Jeffery's study [14] :

$$T_\varepsilon = \frac{\varepsilon^2 + 1}{2\varepsilon} T_1 \tag{5.5}$$

And the evolution of rotation can be described by:

$$\theta(t) = \arctan\left(\varepsilon \tan \frac{2\pi t}{T_\varepsilon}\right) \tag{5.6}$$

A complete conclusion including the influence of all three axis and initial angles, with the detail derivation, can be found at Jeffery's original paper[14].

With a significant rotational aspect, this case demands enabling complete 6DOF solid rotation in response to flow. In order that this rotational aspect of the GISS is tested for numerical accuracy, a mesh dependency test is firstly performed. A typical prolate ellipsoid with $\varepsilon = 2$ was selected and validated against Eq. 5.6 and 5.6. The domain scale L^*, which was non-

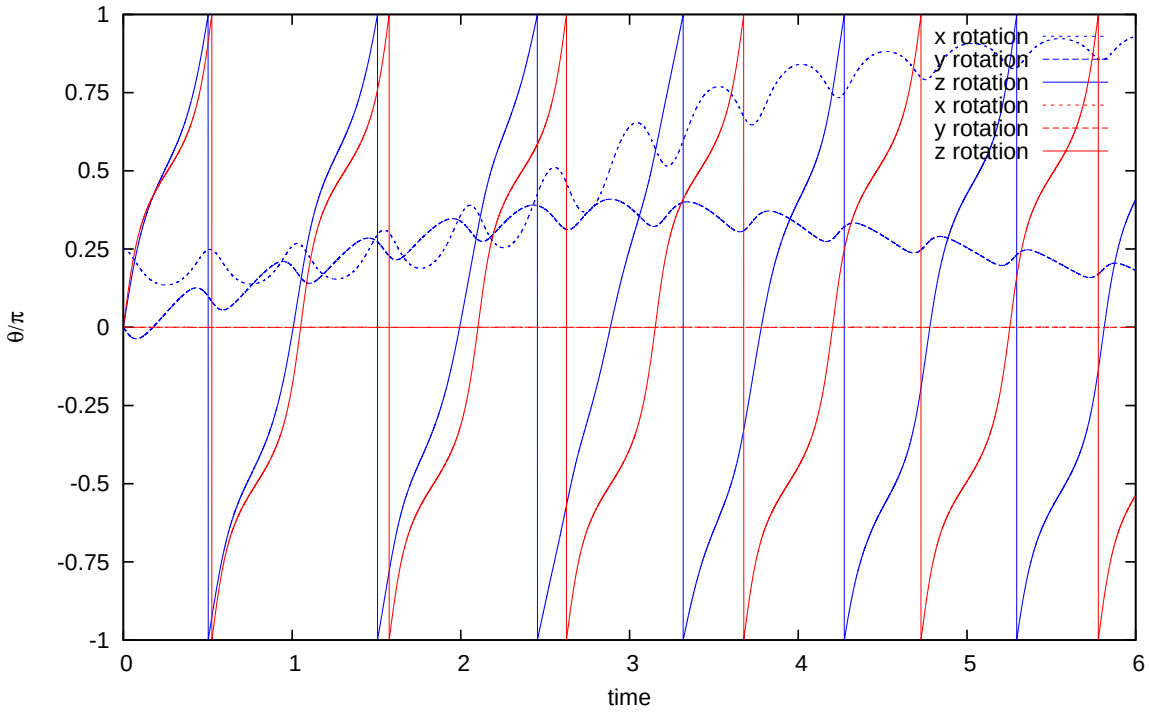

Figure 5.2: *Rotation around three axis ($\varepsilon = 2$, $Re_p = 0.1$, $L^* = 4$, $M = 16$), simulated by GISS.*
Red line for case A: The rotation axis of ellipsoid is same as the shear axis.
Blue line for case B: The rotation axis of ellipsoid is with an initial angle to the shear axis.

dimensionalized by D, was set to 4. Re_p was set to 0.1 to approximate the premise of $Re_p \ll 1$.

For such a set-up the predicted rotation process is depicted in the introduction (Fig. 2.3). It can also be seen from Fig. 2.4 that though the solver predicts rotation well, the period of rotation stabilises after several cycles depending on the initial conditions, an initial condition where the solid is aligned with the shear stabilises faster than the one which is not aligned with imposed shear. A detailed comparison is provided in Fig. 5.2, where case A is for solid initially aligned along shear ($\theta_x = \theta_y = \theta_z = 0$, as shown in Fig. 5.1) and case B is for solid with initial alignment not along shear ($\theta_x = \pi/4$, $\theta_y = \theta_z = 0$). the main rotation (around z axis) of two cases can be clearly observed to be different at the beginning but after several

tumbling the differences between their rotation period tends to be stable which suggest the rotation of case B is approaching the situation of case A. Rotation around the axis other than the shear direction is also observed, which exactly matches the behaviours described by Jeffery and Taylor's work [14] [30].

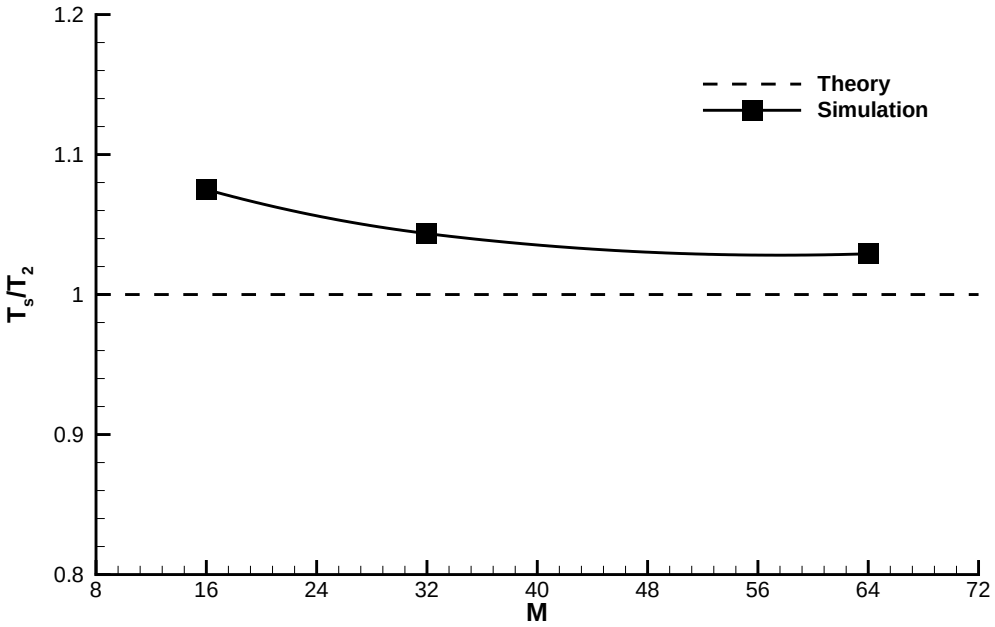

Figure 5.3: *Dimensionless rotation period for ellipsoids ($\varepsilon = 2$, $Re_p = 0.1$, $L^* = 4$) with increasing mesh resolution M.*

In Fig. 5.3, T_s is the 'stabilised' rotation period which can be obtained from the simulation, which is non-dimensionalized by its relevant analytical rotation period T_2 calculated from Eq. 5.5. Similar to Section. 4.1.1, the dimensionless mesh resolution for a prolate ellipsoid is $M = 1/\Delta x^* = D/\Delta x$. The figure also shows that the rotation period can be well predicted with limited error. Even with the coarsest mesh ($M = 16$) in this group of validation tests, the relative error of the rotation period was still less than 8%, and this relative error reduces with mesh refinement. In the current study when $M = 64$ the relative error was reduced to 2.9% and it still tends to reduce as presented in Fig. 5.3, thus a further reduced relative error can be expected.

On the other hand, the Jeffery's analytical solution is based on the assumption that the domain

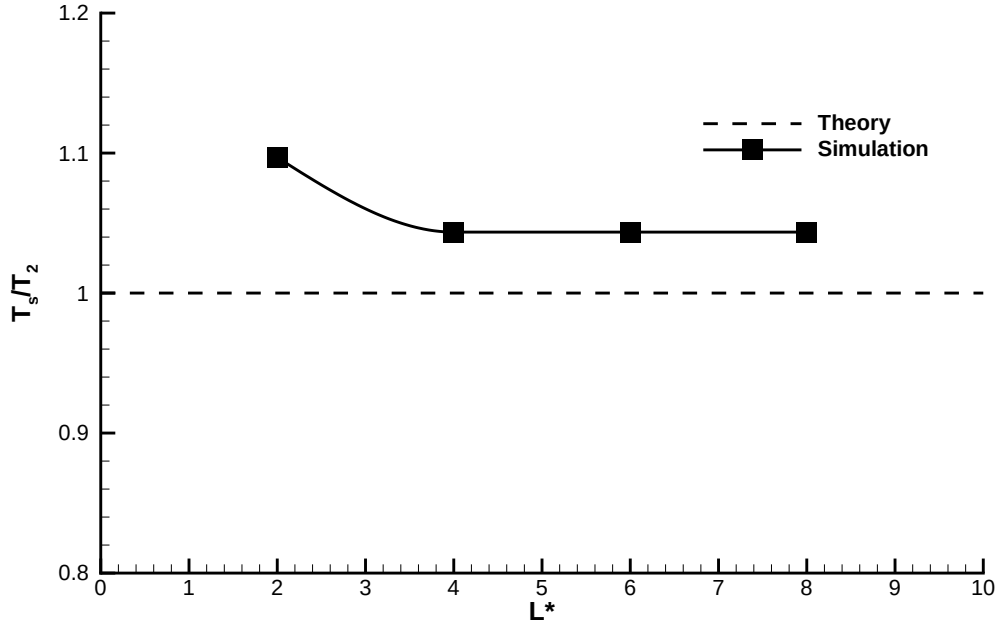

Figure 5.4: *Rotation period of ellipsoids ($\varepsilon = 2$, $Re_p = 0.1$, $M = 16$) with increasing domain scale L^*.*

is infinitely large such that walls don't affect the motion of the solid. Therefore, it is necessary to find out the limit of the domain scale that fits the theory requirement. In this domain scale dependency test, $\varepsilon = 2$, $Re_p = 0.1$ and $M = 16$. Fig. 5.4 plots the rotation period against the domain scale L^*. It can be seen that the rotation would not be affected by the domain scale unless the L^* is too small (< 4). A further study of the rotation process is plotted in Fig. 5.5. Here the angle of rotation is plotted against the dimensionless time $t^* = t/T_2$. The figure shows that by enlarging the computational domain, the rotation period approaches the theoretical value. The figure also shows that our solver can well simulate the detail process of the rotation (the acceleration, and deceleration caused by the ellipsoid geometry during the rotation) and provides important benchmarks for subsequent studies.

In the previous validation, our tests were focused on an ellipsoid with same geometry ($\varepsilon = 2$) and the results suggested requirements for mesh-resolution and domain sizes to obtain reliable simulation results. Here, the study can be extended to ellipsoids with different geometries. Fig. 5.6 plots the rotation period against the aspect ratio of the ellipsoid. When ε changes

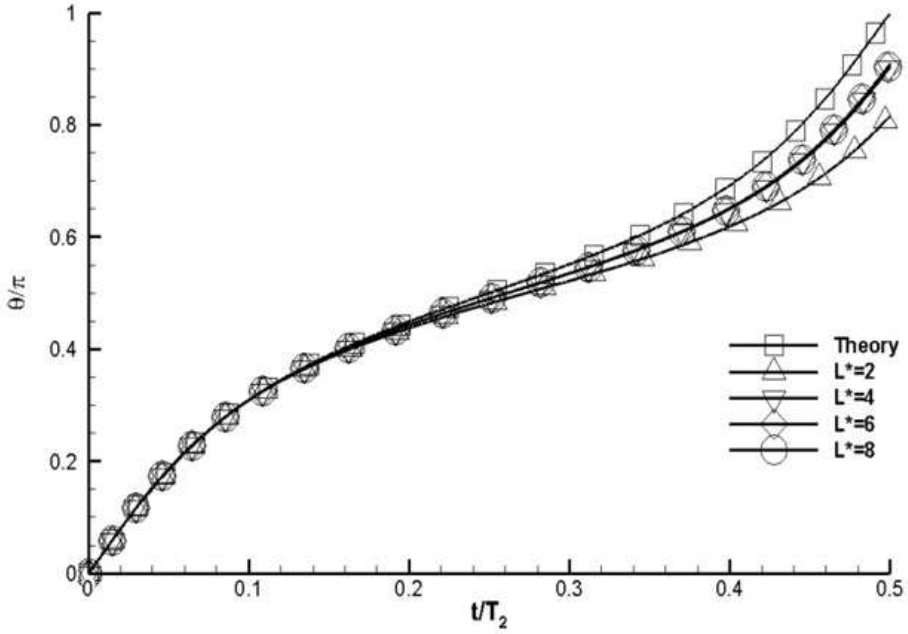

Figure 5.5: *Rotation curves of ellipsoids ($\varepsilon = 2$, $Re_p = 0.1$, $M = 16$) for various domain scale L^*.*

from 0.6 to 2, the ellipsoid become less "oblate" and finally approaching a sphere at $\varepsilon = 1$. The rotation period here is non-dimensionalized by T_1 (the rotation period of a sphere). It is shown that rotation period is a strong function of ε. The error increases when the ellipsoid becomes "less" spherical, as the increasing geometrical complexity requires higher mesh resolution.

A critical limitation was detected through simulations, when $\varepsilon \leq 0.5$ the solid ellipsoid experiences significant irregular oscillation (both translational and rotational thereby increasing the rotation period. These irregular oscillations could only be suppressed by limiting the DOF of the ellipsoid such that only the rotational DOF in the plane of γ is available. Only then a regular rotation can be obtained whose period could be predicted by Eq. 5.5. This suggests poor resolution of viscous tensor in planes perpendicular to the shear. For highly oblate ellipsoids, this necessitates higher mesh resolutions in the solid domain and mesh refinements in the fluid domain. While these irregular oscillations may not be significant when $\varepsilon > 0.5$, their cumulative error during the period of rotation may be the main source of error between

DNS and theoretical results. But despite this error for highly oblate ellipsoids the period of rotation stabilises after several rotations, thereby confirming the Jeffery's hypothesis that "The ellipsoid will tend to adopt that motion which, of all the motions possible under the approximated equations, corresponds to the least dissipation of energy".

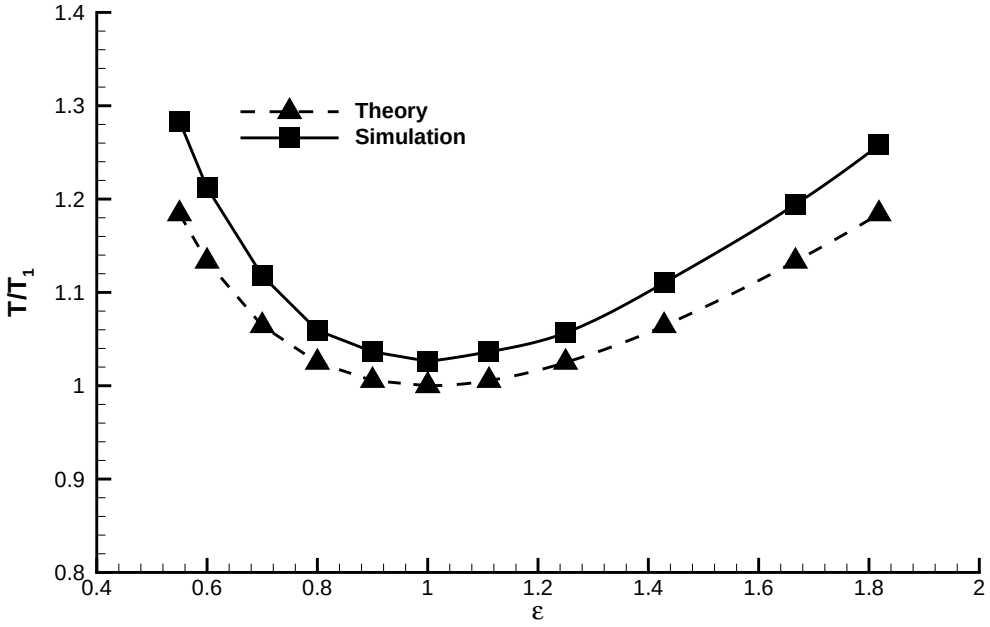

Figure 5.6: *Rotation period for ellipsoids ($Re_p = 0.1$, $M = 16$, $L^* = 4$) with varying ε. For prolate ellipsoid, $\varepsilon > 1$, for oblate ellipsoid, $\varepsilon < 1$.*

A similar behaviour is also noted in Fig. 5.6, where the rotation period of different ellipsoid is plotted. When ε changes from 1 to 2, the solid becomes more and more "prolate" and when ε reduces from 1 to 0.5, the solid becomes more and more "oblate", these changes also require higher mesh resolution to fully capture more complex geometrical shape. As the mesh resolution was fixed in this validation, the error was expected to increase when ε was larger. Fig. 5.3 shows that by increasing the mesh resolution, the error of simulation can be greatly reduced. A better performance of the simulation can be expected with increased mesh resolution here. Generally speaking, the overall tendency of the evolution of the rotation period with ε was well predicted in Fig. 5.6. Fig. 5.7 shows the detail process of the rotation of prolate ellipsoids with different ε. Both angle and time were non-dimensionalized by one cycle. The rotation procedure were predicted accurately with current configurations, proving

the ability of our full DNS GISS to predict solid body rotation using the full Navier-Stokes equations at low Re_p. Fig. 5.6 also shows that the simulated T is always overestimated compared to the theory, which means the motion of the ellipsoid is damped than the analytical result. The similar phenomenon is also reported in the settling simulation of Chapter .4, where the terminal settling velocity is also always slower than the analytical result. Considering the general tendency of overestimating the hydrodynamic resistance, these errors are expected.

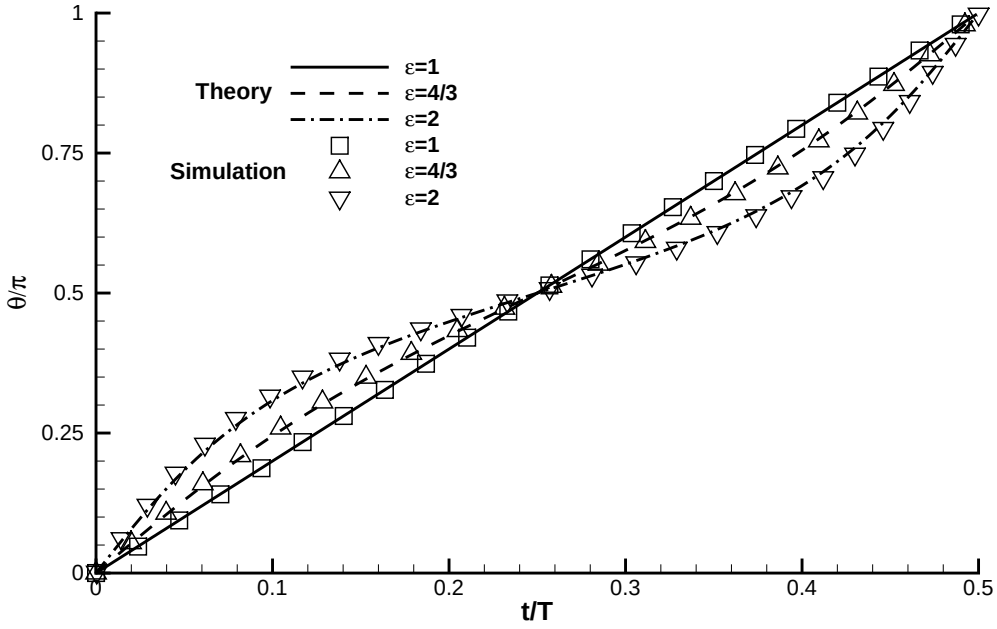

Figure 5.7: *Rotation curve of different prolate ellipsoids $Re_p = 0.1$, $M = 16$, $L^* = 4$.*

5.1.2 Rotation at Moderate $\mathbf{Re_p}$

Besides the validation for Jeffery's orbits problem where $Re_p \ll 1$, it is also interesting to check when inertial effects of flow are significant. Aidun [41] and Huang [38] studied this problem numerically using a lattice-Boltzmann method and summarised an equation describing the relation between the rotation period and the Reynolds number:

$$T^{Re_p} = T^0 \left(1 - \frac{Re_p}{Re_c}\right)^{-\frac{1}{2}} \tag{5.7}$$

Here the supper script of T^{Re_p} represents the rotation period at particles Reynolds number Re_p thus T^0 is the rotation period of the ellipsoid when $Re_p = 0$. Note that T^0 can be calculated by Eq. 5.5. A critical Reynolds number Re_c was reported when the oblate ellipsoid stopped rotating. As discussed in the last section, the oblate ellipsoid cannot remain simple rotation in our simulation when $\varepsilon \leq 0.5$ if the solid was prescribed a 6DOF using our solver. And in the LBM simulations of Huang [38], the translational motion was suppressed too. Therefore, to aid comparison at our current mesh resolutions, the translational DOF of the ellipsoid is limited and compared our simulation result with Eq. 5.7 in Fig. 5.8.

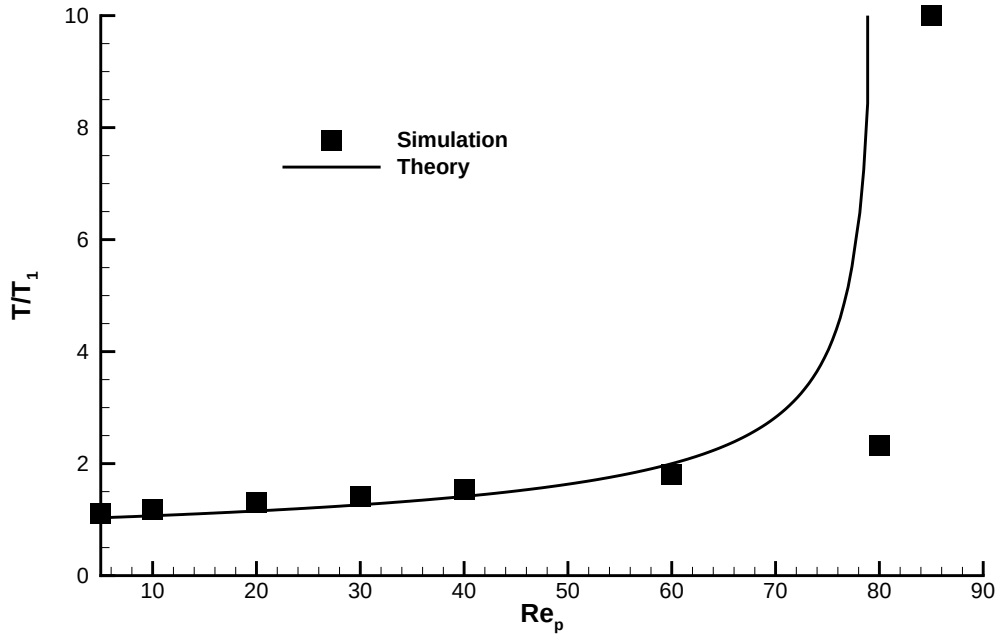

Figure 5.8: *Rotation period of oblate ellipsoid evolving with Re_p.*

A good agreement can be found between the relation described by Eq. 5.7 and our simulations. The Re_c was reported as 80 in the referenced paper in their LBM simulation and the solid curve was drawn based on that. The simulation also shows that $Re_c = 90$, after which the oblate ellipsoid solid stopped rotating. Considering the limitations of our solver in relation to mesh resolution, this level of difference is expected (note that the simulations were conducted at maximum possible mesh resolution for a single-core processor. This will albeit be significantly improved once our solver is fully parallelised - however, this is beyond the

scope of this work). However, the above study dealt with rotation of oblate ellipsoids with

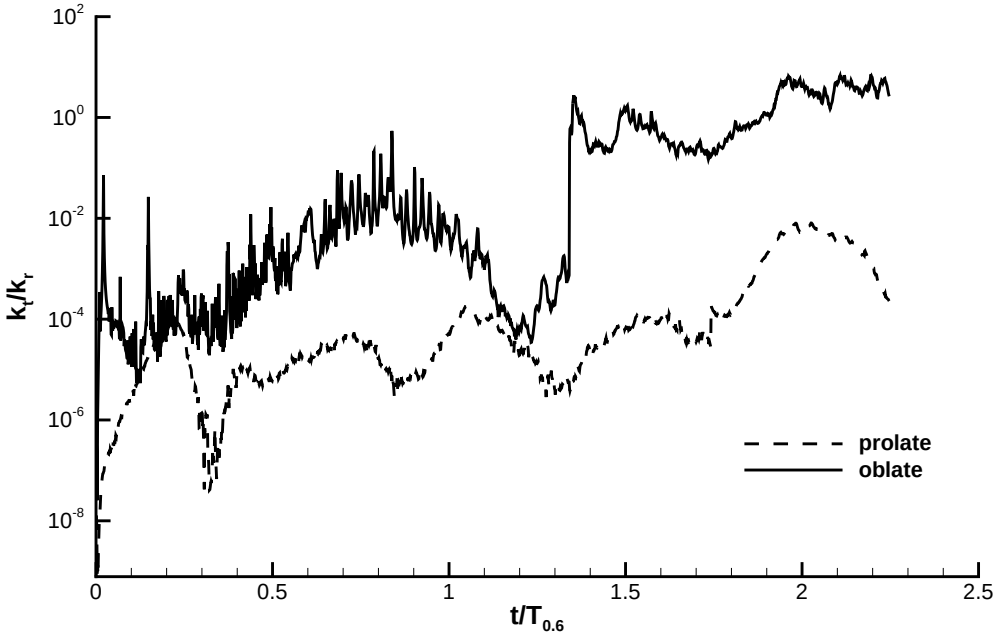

Figure 5.9: *Kinematic energy aspect ratio of prolate and oblate ellipsoid with same ε.*

limited DOF. When an oblate ellipsoid is simulated with full DOF and when Re_p increases, things are much different. The rotation occurs not only in the direction of the shear flow, but also in other directions and the current study does not suggest this is a truth or a fluctuation introduced by numerical errors. With further increase of Re_p, an oblate ellipsoid may even leave its initial location. The rotation periods for prolate ellipsoids with Re_p are also presented. As a comparison to its oblate counterpart, the $\varepsilon = 1/0.6 = 1.66$ for the prolate ellipsoid (Fig. 5.10). The simulation shows that the prolate ellipsoid could still remain at its initial position and just rotate under the effect of the shear flow.

Since the oblate ellipsoid cannot remain simple rotation in the shear flow direction, it is meaningless to compare its motion with that of a prolate ellipsoid solely on the basis of rotational periods. However, to aid our analysis an energy aspect ratio E is introduced as the ratio between translational kinetic energy and rotational kinetic energy.

$$E = \frac{k_t}{k_r} = \frac{0.5m|\mathbf{u}|^2}{0.5I|\mathbf{\Omega}|^2} \tag{5.8}$$

Here, m and I are the mass and moment of inertia of the solid ellipsoid, respectively. Vectors $\mathbf{u}$ and $\mathbf{\Omega}$ represent the translational velocity and angular velocity experienced by the ellipsoid. For an ellipsoid with an aspect ratio of ε, the moment of inertia is:

$$\begin{aligned} I_a &= 0.2m(b^2+c^2) = 0.4m\varepsilon^2 a^2 \\ I_b &= 0.2m(a^2+c^2) = 0.2m(1+\varepsilon^2)a^2 \\ I_c &= 0.2m(a^2+b^2) = 0.2m(1+\varepsilon^2)a^2 \end{aligned} \tag{5.9}$$

Substituting Eq 5.9 in Eq 5.8 :

$$E = \frac{5|\mathbf{u}|^2}{a^2(2\varepsilon^2, 1+\varepsilon^2, 1+\varepsilon^2)\cdot(\Omega_a^2, \Omega_b^2, \Omega_c^2)} \tag{5.10}$$

Fig. 5.9 presents the evolution of the energy ratio E with time for both prolate and oblate ellipsoid when $Re_p = 400$. The vertical axis is in log scale and the result shows the translational energy of an oblate ellipsoid is at least two orders of magnitude (~ 100 times) larger than for a prolate ellipsoid.

In the current scope of Re_p, the relation between the rotation period of prolate ellipsoid has been given by:

$$T^{Re_p} = T^0\left[1 + \left(\frac{Re_p}{1000}\right)^{0.5}\right] \tag{5.11}$$

This is just an approximation in the range of Re_p and ε studied in this work and a detailed study will be needed to develop a generalised relation.

As shown in Fig. 5.10 the rotation period of prolate ellipsoid increases smoothly with Re_p largely following the relation described in Eq. 5.11. Fig. 5.11 also suggests that when the projection area of the ellipsoid in stream-wise direction achieved its biggest value (the first and the last ellipsoids in the figure), the ellipsoid with higher Re_p rotated faster than those with smaller Re_p. When the projection area achieved its minimum value (the middle ellipsoid in the figure), the ellipsoid with bigger Re_p rotated relatively slower than the one with smaller Re_p.

Both pressure and shear stresses contribute to the hydrodynamic force applied on the solid and

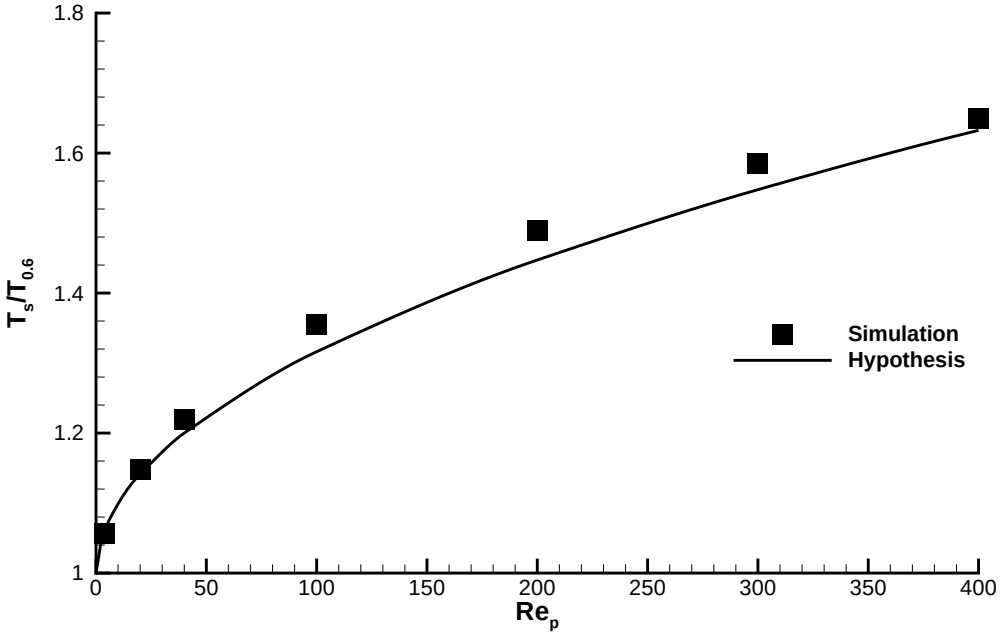

Figure 5.10: *Rotation period of prolate ellipsoid evolving with Re_p at $\varepsilon = 1.66$, $M = 16$, $L^* = 4$.*

hence torques caused experienced by the solid. One can decompose the torque into a normal torque, $\mathscr{T}_n$, which is due to forces normal to the surface of the ellipsoid and a tangential torque $\mathscr{T}_t$, which is due to forces tangent to the surface of the ellipsoid. Thus,

$$\mathscr{T} = \mathscr{T}_n + \mathscr{T}_t = \oint_A (\mathbf{F_s} \cdot \mathbf{n}) \times \mathbf{r} dA + \oint_A (\mathbf{F_s} \cdot \mathbf{t}) \times \mathbf{r} dA \tag{5.12}$$

Here, F_s is the stress tensor described by Eq. 3.25, $\mathbf{n}$ and $\mathbf{t}$ are the normal and tangent unit vectors, respectively, to the infinitesimal solid surface area dA and $\mathbf{r}$ is the radial (vector) position of the area dA with respect to the centre of solid.

This torque composition is presented in Fig. 5.12. The net value of these two torques maintains the rotation of the ellipsoid. The torque caused by normal forces such as pressure ($\mathscr{T}_n$) are considered, torque caused by tangential forces such as shear stresses ($\mathscr{T}_n$), and their overall torque ($\mathscr{T}$) separately for $Re_p = 10$ and 100 in Fig. 5.12(a) and 5.12(b). For a neutrally buoyant ellipsoid performing Jeffery's orbits, it is necessary that the ellipsoid simply rotates about a fixed point with minimal translation. The normal and tangential torques are expected

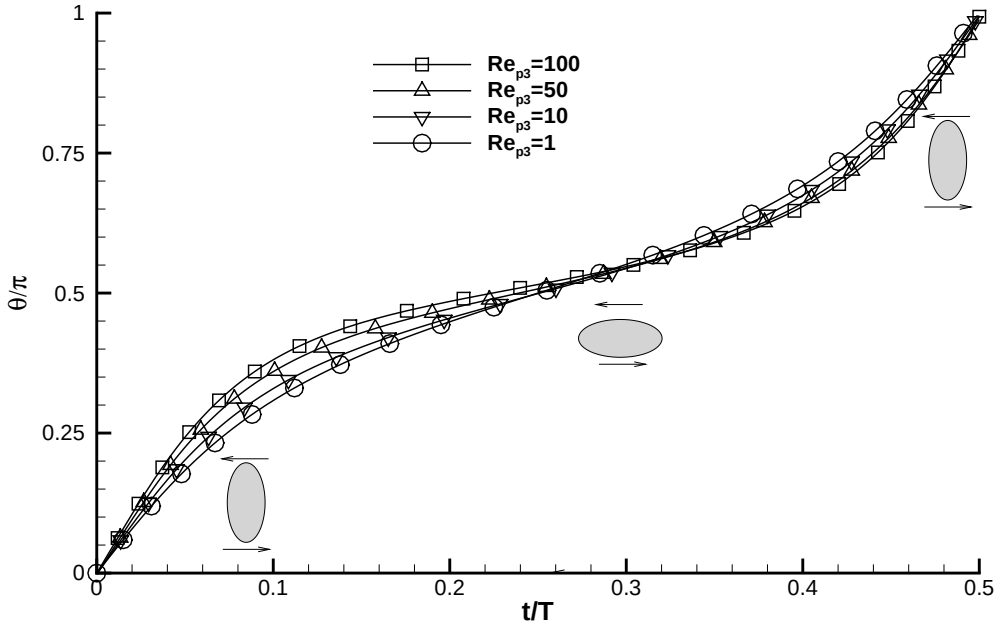

Figure 5.11: *Rotation of ellipsoid at different Re_p at $\varepsilon = 1.66$ and $M = 16$.*

to nearly cancel out each other in order to stabilize the rotation of the ellipsoid. The result shows that for when Re_p grows, the magnitude of net $\mathscr{T}$ becomes even comparable relative to $\mathscr{T}_n$ and $\mathscr{T}_t$, indicating the possible fluctuation of the particle becomes more difficult to be balanced and hard to fulfil the Jeffery's conditions. Actually, as reported before, for the oblate ellipsoid case which is more sensitive to the developing of $\mathscr{T}$ (as they are more obstructive to the flow), their Jeffery's orbit has been broken up when $Re_p > 90$ and with 6DOF motion. The result also shows that when Re_p increases, the $\mathscr{T}$ decreases, suggesting a smaller angular impulse and the extension of the rotation period, as shown in Fig. 5.11. However, it is interesting to note that the decrease in magnitude of both $\mathscr{T}_n$ and $\mathscr{T}_t$ (about 500% drop) is much more greater than that of $\mathscr{T}$ (about 25% drop). The reason of this insignificant decrease T_a with much smaller T_p and T_s is the phase difference. It is observed that the phase difference between $\mathscr{T}_n$ and $\mathscr{T}_t$ enlarges while the Re_p increases, maintaining nearly same level of rotation with much smaller stress tensor field.

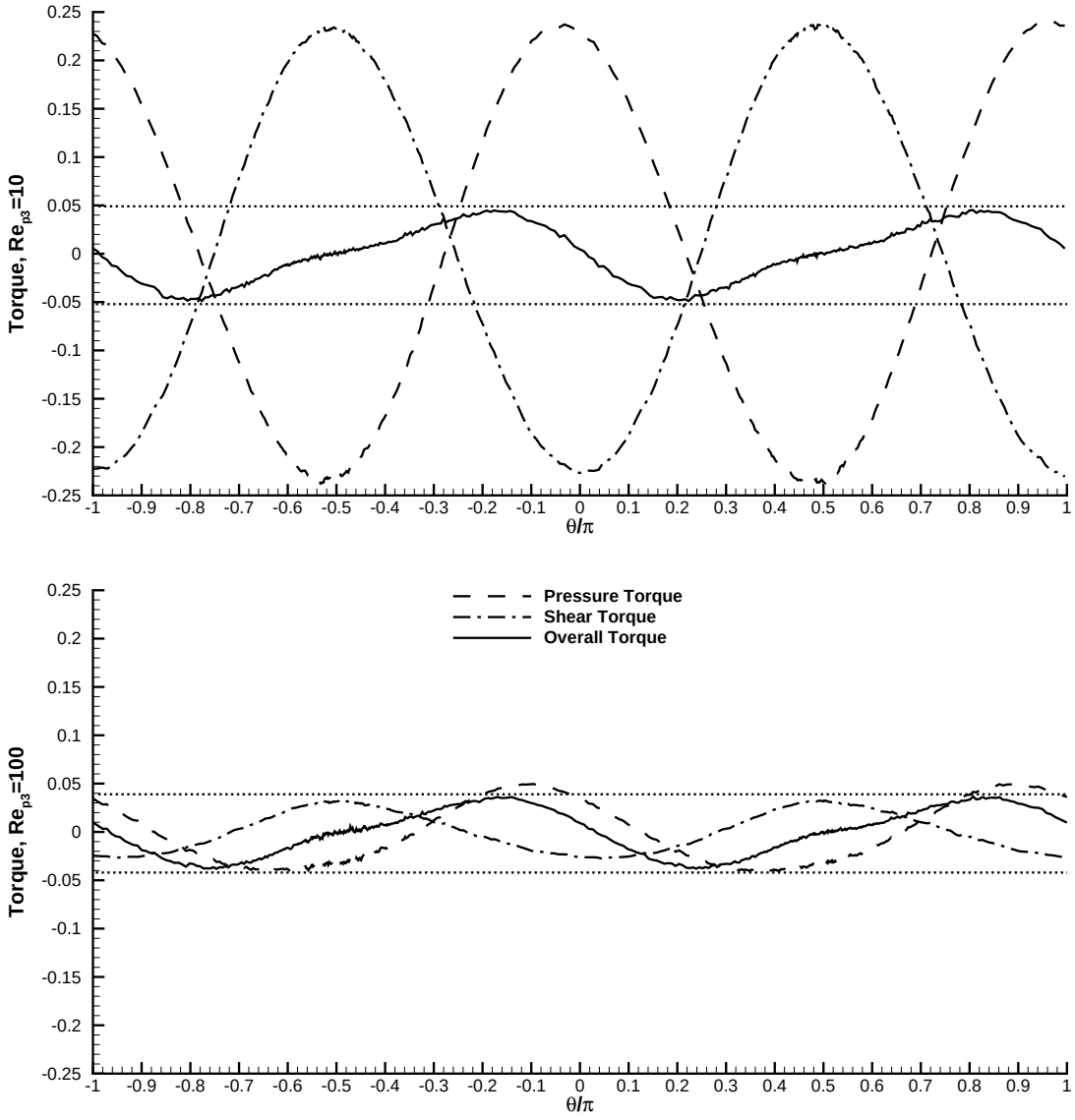

Figure 5.12: *Torque composition for neutrally buoyant ellipsoids at a)* $Re_p = 10$ *and b)* $Re_p = 100$.

5.2 The Rotation and Migration of An Ellipsoid Near Wall

In the sections above, the GISS has been validated separately for cases where either translational or the rotational motion of the solid is dominant. In this section, a 3D ellipsoid near a wall when subjected to flow is studied, experiences both translational and rotational motion simultaneously. Care is taken to calculate the hydrodynamic interaction between the wall and solid and validate this interaction against theoretical predictions. This is a particularly difficult problem - as it is necessary to ensure sufficient mesh resolution to capture the spatio-temporal evolution of the hydrodynamic interaction in 3D.

5.2.1 The Influence of Initial To-Wall Distance

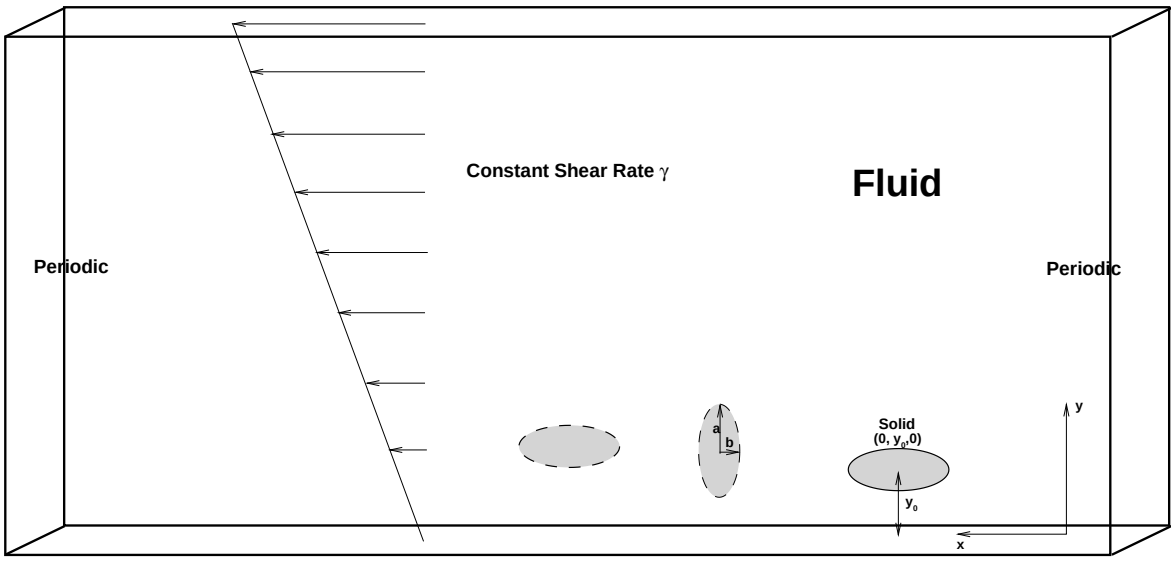

Figure 5.13: *Ellipsoid with both rotation and translation in the shear flow.*

Considering a flow configuration shown in Fig. 5.13 where the top wall of the domain has a constant velocity, and the bottom wall stationary. The boundary conditions for the other sides are periodic. The relative movement between the walls generates a constant shear rate γ in the entire fluid domain. The shear flow assumption close to the wall represents laminar sublayer region within the boundary layer. A neutrally buoyant and prolate ellipsoid whose $a = c = \frac{1}{2}b$ is placed such that its centre is at a distance of y_0 to the bottom wall. The initial angular position θ_0 of the ellipsoid is described by the angle between the major of the ellipsoid

and the x axis. For example, the initial angular position of the ellipsoid (in solid line) shown in Fig. 5.13 is $\pi/2$ which subsequently evolves as the solid tumbles from right to left. As seen before, Re_p could be defined based on either translational behaviour or rotational behaviour:

Reynolds number	Characteristic Velocity	Characteristic length
$Re_{pt} = \dfrac{2\rho_f \gamma y a}{\mu}$	γy	$2a$
$Re_{pr} = \dfrac{4\rho_f \gamma a^2}{\mu}$	$2\gamma a$	$2a$

(5.13)

In this study, since the ellipsoids were generally not too far away from the bottom wall, both these definitions fall in the same order of magnitude. In this work, we choose $Re_p = Re_{pr}$.

Hsu and Ganatos [11] have studied this problem with a zero-drag motion assumption, which is valid for cases where dispersed small ellipsoids are carried along by the fluid. This assumption requires nearly stationary flow, therefore Re_p should be very close to 0. Considering that the to-wall distance y would not be too large ($y^*_{max} = 2$), in the following simulation $Re_p = 0.1$.

To simplify the problem, Hsu and Ganatos only studied the 2D motion of a ellipsoid in the xy plane as the problem should be symmetric to this plane. By modifying the force coefficient based on the to-wall distance, the horizontal and vertical velocity and the rotation speed could be calculated using a boundary integral method with a high degree of accuracy. The results were then interpolated into Fourier series shown in Eq. 5.14:

$$\begin{aligned} -U^*_s &= a_0 + a_2 \cos 2\theta + a_4 \cos 4\theta + a_6 \cos 6\theta \\ -U^*_y &= b_2 \sin 2\theta + b_4 \sin 4\theta + b_6 \sin 6\theta + b_8 \sin 8\theta \end{aligned} \tag{5.14}$$

Here, U_s is the slip velocity which is the difference between the solid velocity and the local fluid velocity in x direction, and U_y is the solid velocity in y direction (and also the slip velocity in y direction, as the fluid velocity in y direction is 0). The velocity is non-dimensionalized by the initial local fluid velocity, which is γy_0 and the displacement is non-dimensionalized

by the half major b:

$$U_s^* = \frac{U_x - \gamma y}{\gamma y_0} \quad U_y^* = \frac{U_y}{\gamma y_0}$$
$$x^* = \frac{x}{a} \qquad y^* = \frac{y}{a} \tag{5.15}$$

y_0/a	a_0	a_2	a_4	a_6
1.1	0.0673	-0.0195	-0.0071	0.0014
1.3	0.0386	-0.0074	-0.0045	0.0004
1.5	0.0249	-0.0032	-0.0031	0.0002
2.0	0.0106	-0.0011	-0.0015	0

Table 5.1: *The coefficients of U_s^*. [11]*

y_0/a	b_2	b_4	b_6	b_8
1.1	-0.03209	0.02233	-0.00480	0.00123
1.3	-0.01496	0.01004	-0.00118	0.00017
1.5	-0.00833	0.00571	-0.00043	0.00006
2.0	-0.00284	0.00216	-0.00008	0

Table 5.2: *The coefficients of U_y^*. [11]*

Results of a typical simulation (with $Re_p = 0.1$, $M = 16$, $y_0^* = 1.1$) are presented in Fig. 5.16. The choice of mesh resolution used is dictated by our previous studies for translation and rotation.

Fig. 5.14 plots the slip velocity against the orientation of the ellipsoid and Fig. 5.15 plots the vertical velocity against the angle of the ellipsoid. It is very clear in both figures, when $y_0^* = 1.5,\ 2$, which means the ellipsoid is relatively far away from the bottom wall and hence experiencing less influence from the wall, our simulation can give nearly same prediction with Hsu and Ganatos' [11] result. When $y_0^* = 1.1,\ 1.3$, our 3D simulation is very close to the theoretical curve of Eq. 5.14 at the beginning and then discrepancies gradually increase. A reasonable explanation the hydrodynamic force caused by the boundary effect will inevitably change the to-wall distance of the solid dynamically. When the ellipsoid is relatively close to the bottom wall, this change of location will greatly affect the force applied on the ellipsoid. However, this influence is neglected in the zero-drag motion hypothesis used to develop the analytical solution of Eq. 5.14. Our results also show that the hydrodynamic interaction

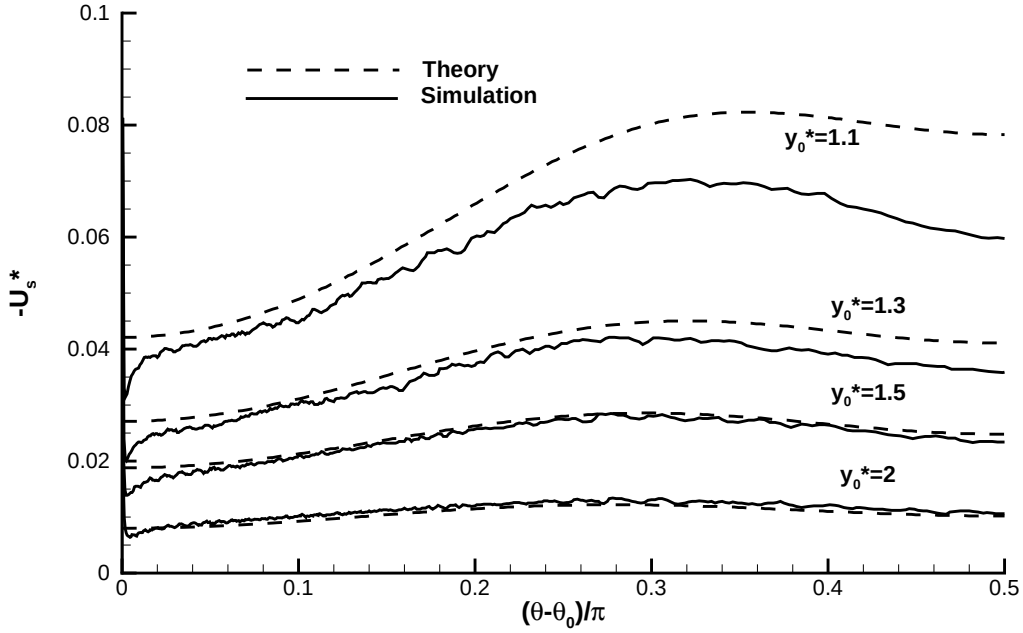

Figure 5.14: *The slip velocity of the solid as a function of initial to-wall distance. The parameter values are $Re_p = 0.1$, $M = 16$. The theoretical prediction is obtained from Eq. 5.14.*

between the wall and the solid is highest when the distance between them is the smallest. Thus a solid close to the wall under flow will be pushed towards the bulk - indicating hydrodynamic repulsion. The lift experienced by the solid comprises the following parts:

- Shear induced lift: when the difference in shear on either side of the solid causes it to spin. There is an associated force perpendicular to the direction of fluid motion which causes the ellipsoids to roll down the shear gradient. The force originates from inertia effects in the fluid surrounding the ellipsoid [136]. Note that under the assumption of a zero-drag hypothesis these inertial forces are neglected in the analytical formulation but included in the 3D DNS. Further more during the tumbling motion of the ellipsoid near the wall - y_0 is minimum whenever the major axis is perpendicular to the wall ($\theta = \pi/2$) and maximum when the major axis is parallel to the wall ($\theta = 0$). This will lead to a discrepancy between the results when the inertial forces in the fluid are high enough to induce a finite non-zero drag, which could be the case during the tumbling

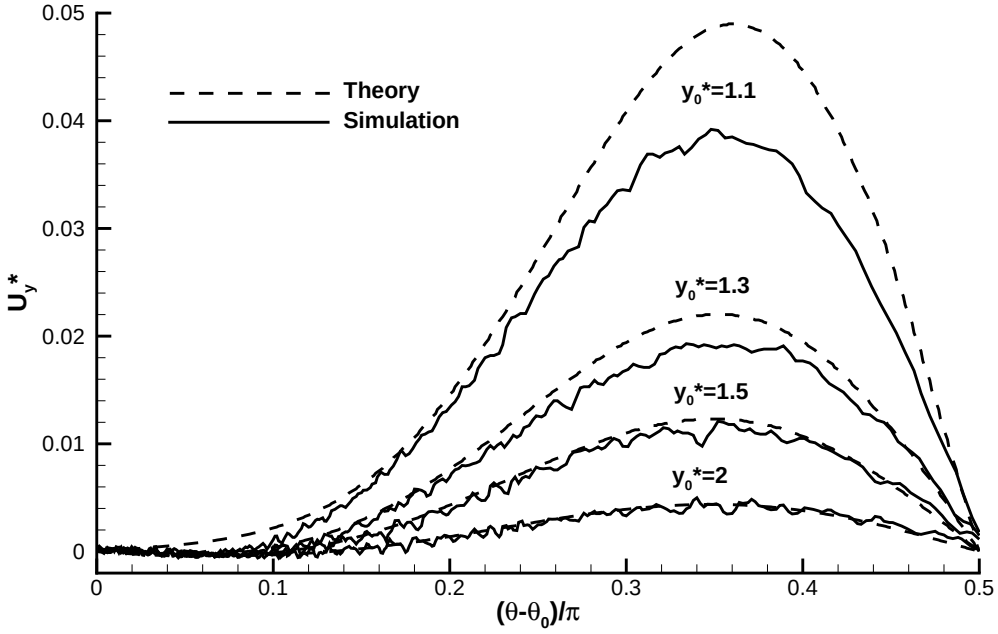

Figure 5.15: *The vertical velocity of the ellipsoid as a function of initial to-wall distance. The parameter values are $Re_p = 0.1$, $M = 16$. The theoretical prediction is obtained from Eq. 5.14.*

motion of the ellipsoid. It can also be seen from the Fig. 5.14 that the discrepancy is the highest the point of maximum velocity - indicating the failure of the analytical model when inertial effects are highest.

- Wall induced inertial lift forces: A number of different inertial forces are present on a ellipsoid near a wall or an ellipsoid touching a wall. All these forces are directed away from the wall leading to motion of the ellipsoid away from the wall. These include lift on a non-spinning ellipsoid near a wall [137], lift on a spinning ellipsoid near a wall (called the Magnus effect), and lift on a ellipsoid touching the wall [138]. In the cases considered here, the spinning ellipsoid never touches the wall - thus the Magnus lift is the most prominent lift force.

Actually, an extended study shows with increasing ($Re_p \geq 1$), the vertical migration would be significant strengthened, as shown in Fig. 5.17. Thus, the result proved that our GISS can predict the horizontal and vertical migration of a neutrally buoyant ellipsoid which is fully

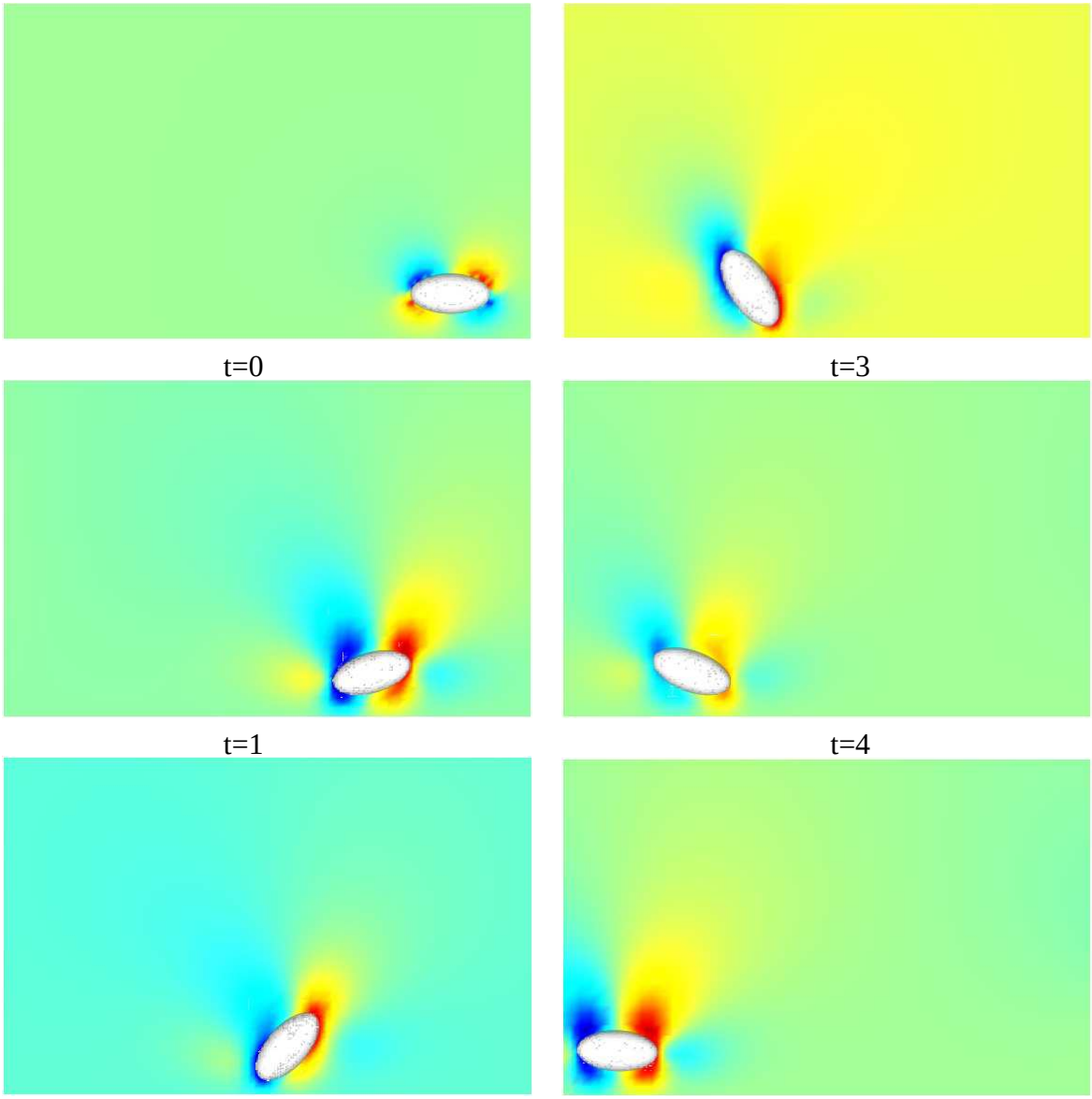

Figure 5.16: *The process of tumbling, both translation and rotation. Follow figures chronologically from top left to bottom right. The contour shows the vertical velocity ($Re_p = 0.1$, $M = 16$, $y_0^* = 1.1$).*

validated at near-zero shear cases against theory of Hsu and Ganatos [11].

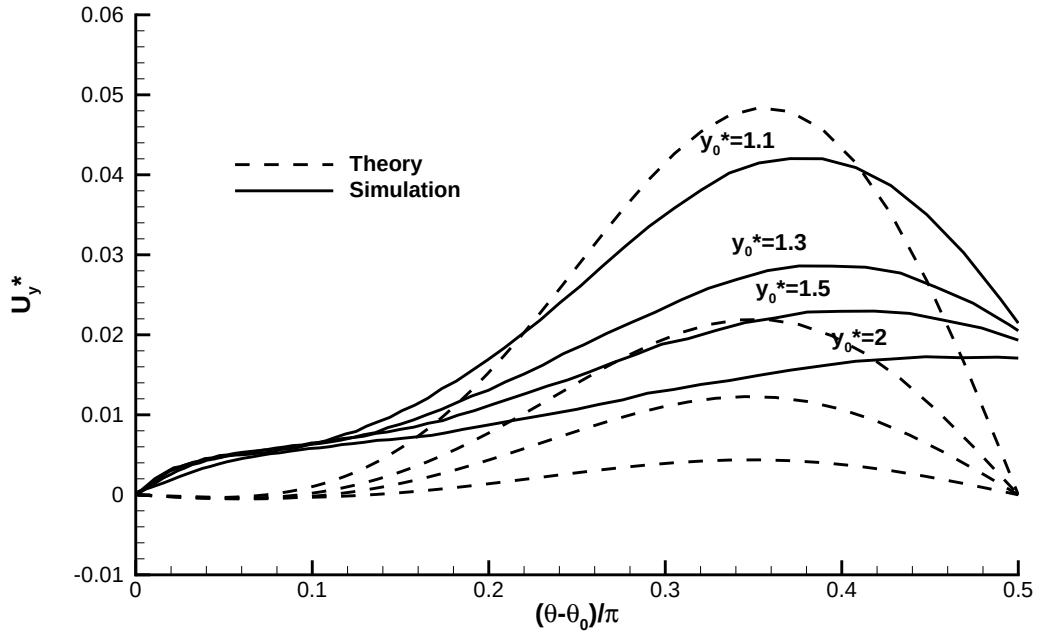

Figure 5.17: *The vertical velocity of the ellipsoid as a function of initial to-wall distance. The parameter values are $Re_p = 1$, $M = 16$. The theoretical prediction is obtained from Eq. 5.14.*

It is interesting to find out that in Fig. 5.15, after half-rotation ($\theta = \pi$) when the major axis b of the prolate ellipsoid is parallel to the x axis again (as in the initial condition when $\theta = 0$), the U_y* returns to 0, no matter how large the ellipsoid initial to-wall distance is. However, the peak of U_y* does not happen when the major axis aligns with the x axis ($\theta = \pi/2$) but slightly later. It is noteworthy that critical angular position at maximum U_y^* and the zero U_y^* are same in all four simulations, implying that the critical angular position is not a function of the initial to-wall distance of the ellipsoids.

The hydrodynamic interaction not only affects the migration of the ellipsoid, but also its rotation behaviour. As shown in Fig. 5.18, T^* is the actual ellipsoid rotation period scaled by the theoretical value given by Eq. 5.5, and is plotted against the initial vertical to-wall distance of the ellipsoid y_0^*. It is easy to note from the figure that when the ellipsoid is initially far from the bottom wall ($y_0^* = 2$), its rotation period increases by about 7% of the theoretical

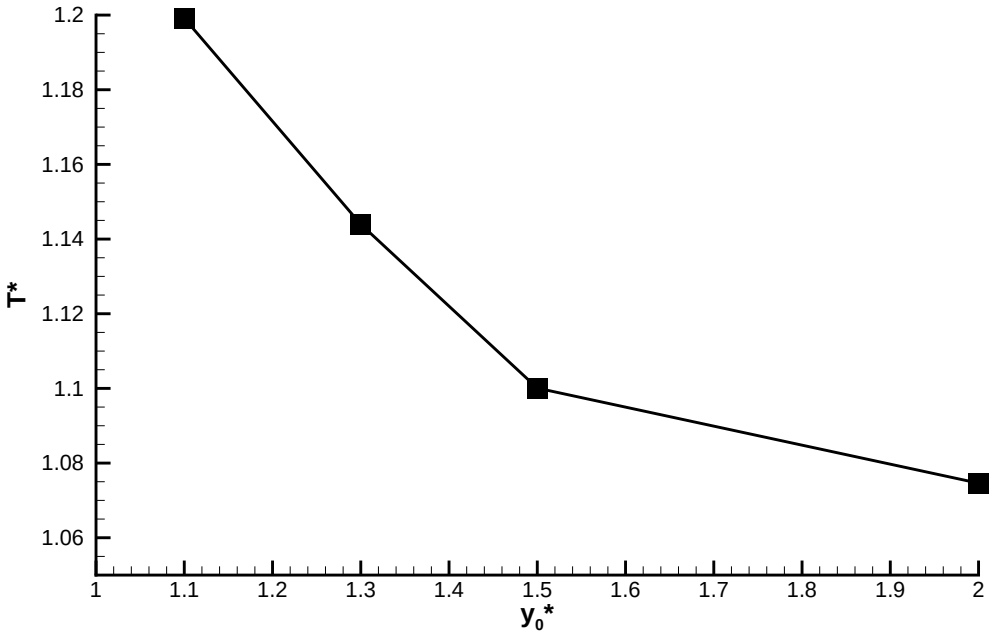

Figure 5.18: *The rotation period evolution with initial to-wall distance y_0^* ($Re_p = 0.1$, $\varepsilon = 2$, $M = 16$).*

value predicted by Eq. 5.5, which is insignificant as the original error of the rotation period is about 5% as presented in Section 5.1.1. However, when the initial to-wall distance of the ellipsoid is relatively close ($y_0^* = 1.1, 1.3, 1.5$), the rotation period of the ellipsoid increases. Interestingly, this result contradicts with the one shown in Fig. 5.5, where the rotation period of the ellipsoid decreases as it is closely bounded by walls perpendicular to the streamwise direction. This difference indicates the complex hydrodynamic interaction caused by the asymmetric bounding effect of a single wall against the one that is symmetrically bounded by walls.

5.2.2 The Influence of The Ellipsoid Geometry

In Section 5.2.1, an ellipsoid with a fixed geometry (aspect ratio, $\varepsilon = 2$) was studied with various initial to-wall distance ($y_0^* = 1.1, 1.3, 1.5, 2$). In this section, the influence of ellipsoid geometry is discussed with fixing the initial to-wall distance at $y_0^* = 1.25$. Here ε varies from 1 (standard sphere) to 4 (very thin ellipsoid). The Re_p is limited to 0.1 in these simulations.

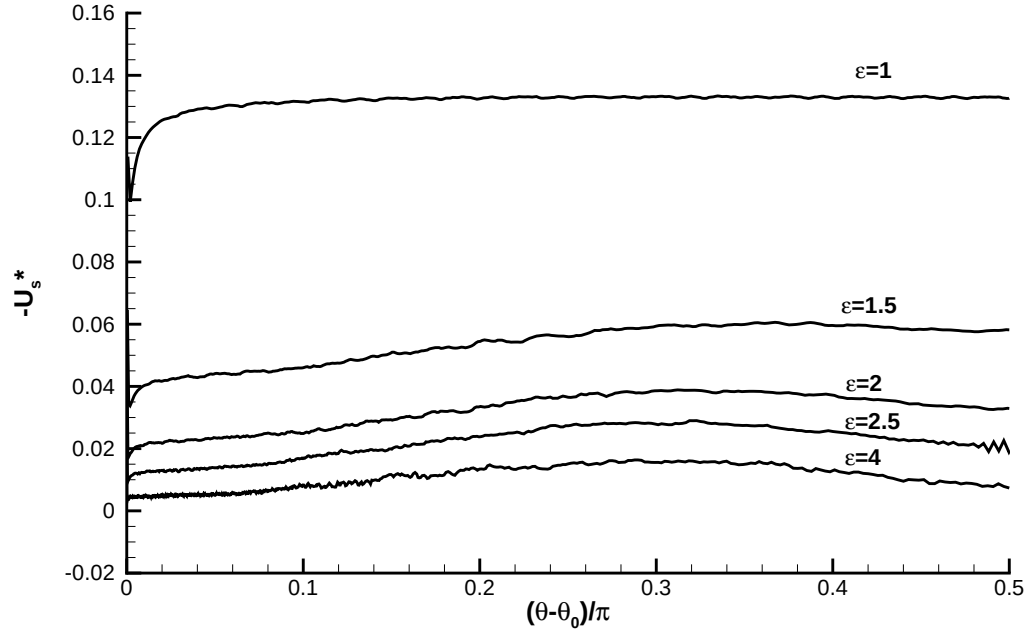

Figure 5.19: *Horizontal slip velocities of ellipsoids with different geometry as a function of orientation. Parameter values are $Re = 0.1$ and $y_0 = 1.25$.*

Fig. 5.19 shows the evolution of slip velocities of (ellipsoids of varying geometry) during the tumbling motion (depicted by the orientation angle). It can be seen that horizontal migration decreases with increasing ε and the standard sphere ($\varepsilon = 1$) experiencing the highest horizontal migration. This is expected given that ellipsoids respond to the inertia of the fluid by tumbling motion - so that the surface area perpendicular to the flow changes with orientation giving rise to both vertical and horizontal migration. Smooth geometries like spheres, on the other hand do not tumble (though they may rotate due to the fact that surface area perpendicular to flow is always constant and the inertia that the fluid imposes on them is mainly used to translate in the horizontal direction.

Fig. 5.19 shows the evolution of vertical velocities of ellipsoids with different geometry during the tumbling motion (depicted by the orientation angle). Here, amongst all the geometries the standard sphere ($\varepsilon = 1$) exhibits poorest vertical migration. However, unlike the horizontal migration velocity, the vertical migration velocity exhibits a non-monotonic dependence on ε. The vertical migration velocity increases with ε (as ellipsoid becomes ”thinner”) until

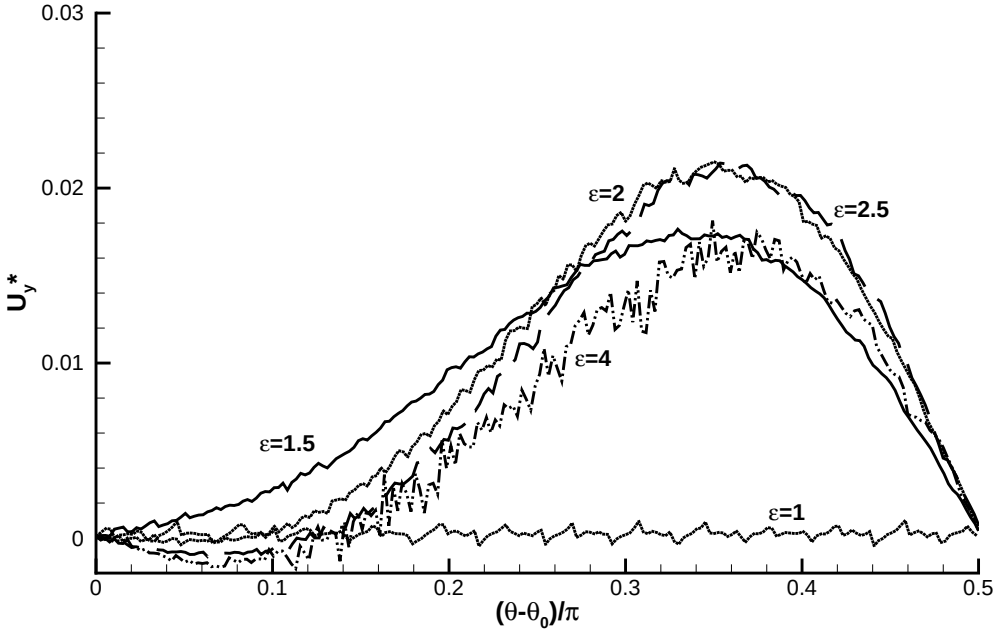

Figure 5.20: *Vertical velocities of ellipsoids with different geometry as a function of orientation. Parameter values are $Re = 0.1$ and $y_0^* = 1.25$.*

$\varepsilon \leq 2$ and then decreases, suggesting an optimum ellipsoidal geometry for maximum vertical migration.

In addition to the above validation for ellipsoids, GISS has also been tested for simulating migration of dense spheres in Poisuelle flow. These have been validated against published results of Yu et al. [139]. The results are shown in Appendix D.

5.2.3 The Influence of The Initial Angular Position

In all previous validations and studies, the ellipsoids were released with the initial angular position $\theta_0 = 0$ (the major axis of ellipsoids is parallel to the streamwise direction). In this section, the effect of initial angular position on migration pattern of the ellipsoids is studied.

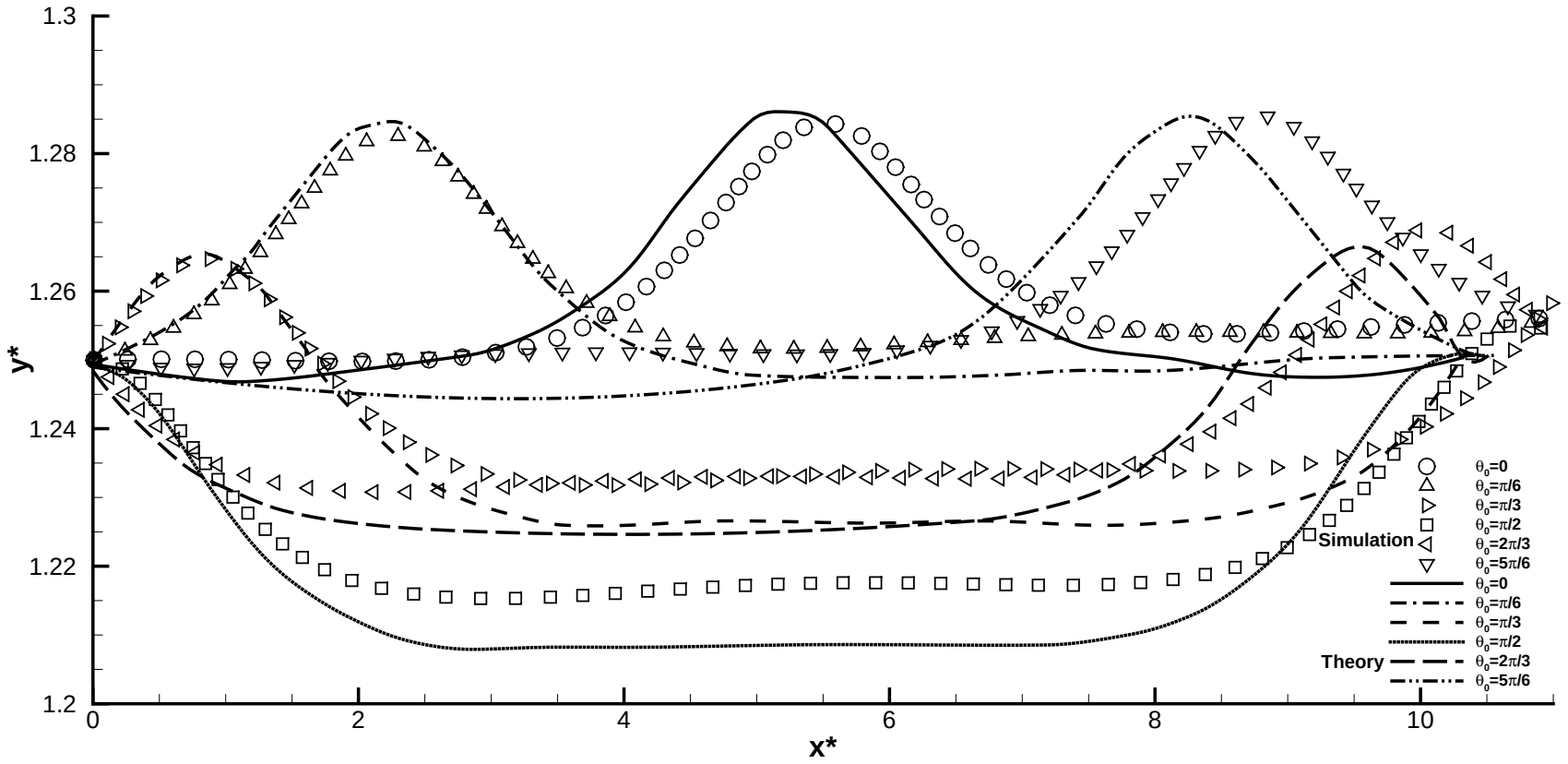

Figure 5.21: *The migration of a neutrally buoyant ellipsoid with different θ_0 in shear flow near the wall.*

Results presented in in Fig. 5.21 concern with a group of simulations located at $y_0^* = 1.25$ and ellipsoidal geometry ($\varepsilon = a/b = 0.5$). The ellipsoids are released at $\theta_0 = 0$,$\pi/6$, $\pi/3$, $\pi/2$, $2\pi/3$, $5\pi/6$. Half circle of the rotations are presented in the figure. Based on the theoretical prediction of Hsu and Ganatos' study [11], all the ellipsoids are expected to return to their initial vertical position after half-period of rotation under the pseudo zero Reynolds number assumption. To approximately simulate this behaviour, the Re_p in these 6 validations has been set to 0.1. As the Re_p here was still slightly larger than 0, a tiny disagreement is expected, which is also seen in the figure. Despite this slight difference, our simulation showed a general agreement with the Hsu and Ganatos' study [11].

Fig. 5.21 shows that the migration orbit of ellipsoid with initial angular position of $\theta_0 = \pi/3$ is same as that with initial angular position of $\theta_0 = 2\pi/3$, and the migration orbit tracked by an ellipsoid with initial angular position of $\theta_0 = \pi/6$ is same as that with initial angular position of $\theta_0 = 5\pi/6$. It is easy to realise that $\pi/3$ and $\pi/3$ are symmetric of $\pi/2$, as well as $\pi/6$ and $5\pi/6$. As a conclusion, the migration pattern should be categorized on the base of same maximum/minimum migration, like the case of $\theta_0 = \pi/3$ and $\theta_0 = 2\pi/3$, they are actually in one pattern, but with a phase lag. Besides, the upward migrations of the ellipsoid were better predicted while the downward migration had considerable yet constant error, which also accorded with the conclusion in the previous paragraph.

5.3 Conclusion

In this chapter, the rotational compatibility of our solver were firstly validated by comparing our simulation result with the theoretical conclusion of the Jeffery's orbits theorem at low particle Reynolds number ($Re_p \ll 1$). Mesh dependency and domain dependency tests determined the necessary numerical mesh and domain criteria for minimising numerical errors. A further test of the ellipsoid rotation at moderate Re_p ($1 \leq Re_p \leq 100$) determined a critical Re_p where the solid stops rotating. The calculated critical Re_p predicted by GISS is 90, which closely matches with the one recently predicted by Huang's[38] LBM simulation result (80).

Despite the general stable results for prolate ellipsoids, the oblate ellipsoids depicted a complex numerical behaviour, which may due to a more complicated vortex-particle interaction.

The rotation of the ellipsoid would always correspond to an extra local vortex, and the more streamlines-like geometry of the prolate ellipsoid lead to a much less disturbance than the oblate one, which behaves more like an obstacle to the flow field. This more complicated vortex-particle interaction calls for very fine mesh. In our current studies, the oblate ellipsoids could not be simulated with 6DOF at the maximum mesh resolutions possible for single-core processing and the translational DOF had to switch off to obtain rotation-only simulation data. The predicted rotation data for the oblate ellipsoids matches with the theory.

These comprehensive validations of the translational and rotational abilities of our GISS in Chapter 4 and Section 5.1, gives us confidence to solver for cases where both translation and rotation exist. The solver was also validated against Hsu and Ganatos study [11] where both translation and rotation take prominence. These simulations also suggested the relation between the migration and the geometry of solids. A standard sphere had the smallest vertical migration performance but the highest horizontal migration. On the other hand, ellipsoids showed a non-monotonic dependence on migration - predicting an optimum geometry for maximum vertical migration.

Chapter 6
Hydrodynamic Interaction Between Twin Particles

In Chapters. 4 and Chapter. 5, the translational and rotational behaviour of a solid particle have been thoroughly validated and several parametric analyses been discussed. Those single solid problems establish the foundation of handling more complicated problems involving multiple solids. The competence shown by the GISS to predict those single solid migration problems gives us confidence in using the solver towards understanding hydrodynamic behaviour between two solids. In this chapter, our studies are extended to account for two immersed solids in shear flow. As this work focusses only on pure hydrodynamic interactions between solids (before collision), no collision model is introduced. The simulation is stopped when the solid surfaces come within a distance less than half the minimum grid spacing.

6.1 Problem Setup

The computational domain is very similar to the set-up of the Jeffery's Orbit problem in Section 5.1. A rectangular fluid domain is defined with vertical dimension of L, which is 4 times the characteristic length $2a$(corresponding to the major axis of the immersed ellipsoids). The upper and lower boundaries are no-slip walls with same speed but opposite in direction giving a constant shear rate γ. The boundaries at the streamwise and spanwise direction are periodic. Here, instead of a single ellipsoid located in the centre of the fluid domain, two geometrically identical ellipsoids are located symmetrically away at a distance $D_i/2$ from the centre of the fluid domain. Thus the initial distance between the solids D_i. Same as in Chapter 5, the geometry of the solid is defined by their half major axis (also the polar axis) a and half minor axis $b(= c)$ giving a geometric aspect ratio $\varepsilon = a/b$. The particle Reynold's number is given by Eq. 5.2 and the rotational period T_ε is given by Eq. 5.5. In this chapter,

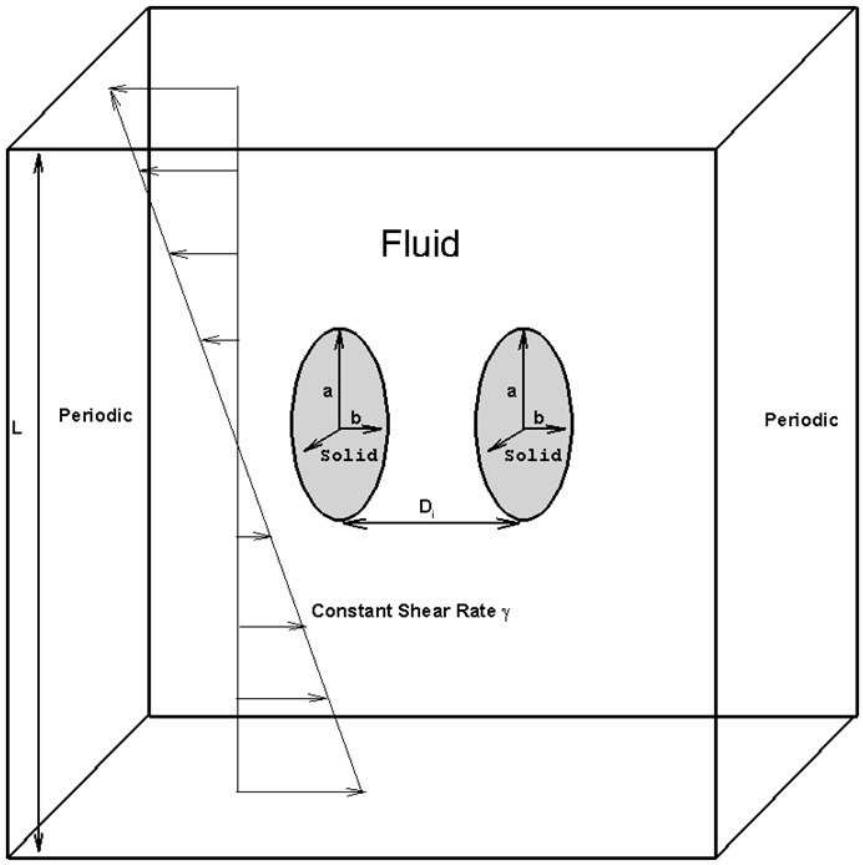

Figure 6.1: *Multi solids embedded in shear flow.*

all the lengths are scaled by the characteristic length of the elliposid $2a$, and time t^* is scaled by T_ε. Only interactions between identical standard sphere and prolate ellipsoids are studied in this chapter. The influence of D_i^*, ε and Re_p on the hydrodynamic interaction is discussed in the following sections.

6.2 Influence of Initial Inter-solid Separation Distance at Low Re_p

In this study, $Re_p = 1$. If a single neutrally buoyant solid is placed in a shear flow, it would simply rotate following Jeffery's orbit predicted by Eq. 5.5 devoid of any translation. When

another solid is placed close to it, the hydrodynamic effect between them would play a role depending on the extent of initial separation distance. Also, as shown in Section 5.2.2, the hydrodynamic effect is also dependent on the geometry of the ellipsoid. In order to make a comprehensive discussion, the effect of separation distance and geometry would be studied coherently.

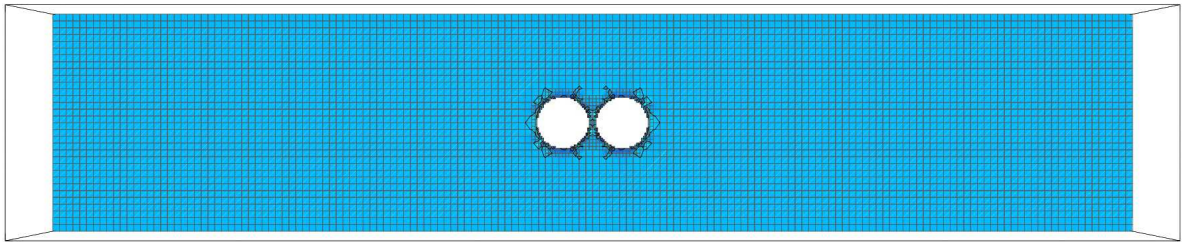

(a) $t^* = 0$

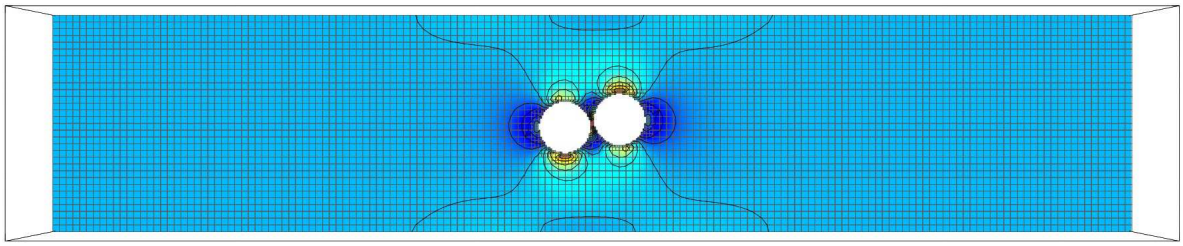

(b) $t^* \approx 0.255$

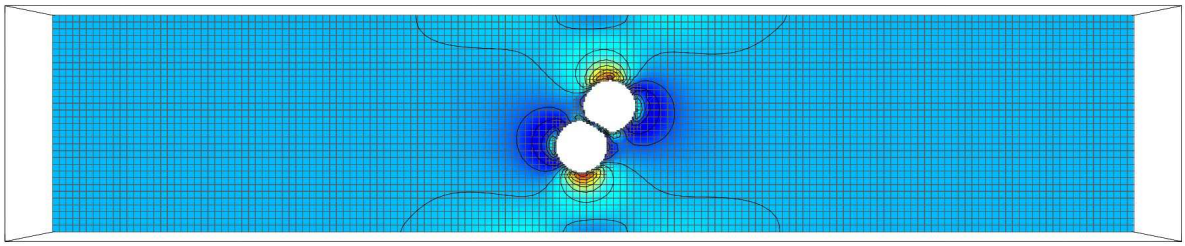

(c) $t^* \approx 0.510$

Figure 6.2: $Re_p = 1, \varepsilon = 1, L^* = 4, D_i^* = 1.1$, *Contour shows the vorticity profile.*

Fig. 6.2 demonstrates the case for two identical spheres placed of dimensionless diameter $d^* = 1$ next to each other in a channel subjected to shear flow. The dimensionless initial distance between the solid centres is $D_i^* = 1.1$, which means the closest surface distance between the two spheres is merely one tenth of the sphere diameter at $t^* = 0$. It must also be noted that initially the centres of the solids are in the plane of zero-velocity (the top wall has a velocity $-U_0$ and the bottom wall at a velocity $+U_0$, thus the centre is at zero velocity). The figure shows that at $t^* \approx 0.255$, the left particle is slightly lower than its initial position

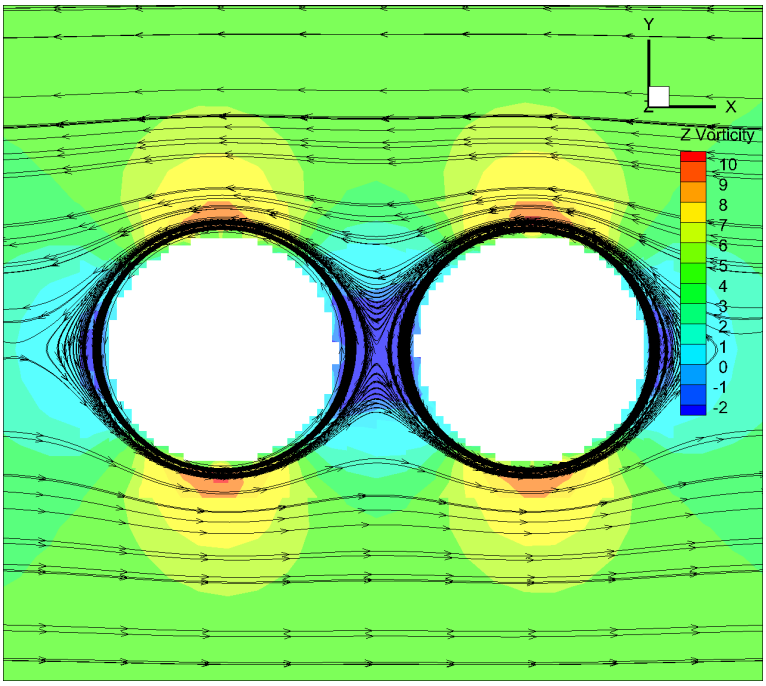

(a) 2D view of Z=0 plane

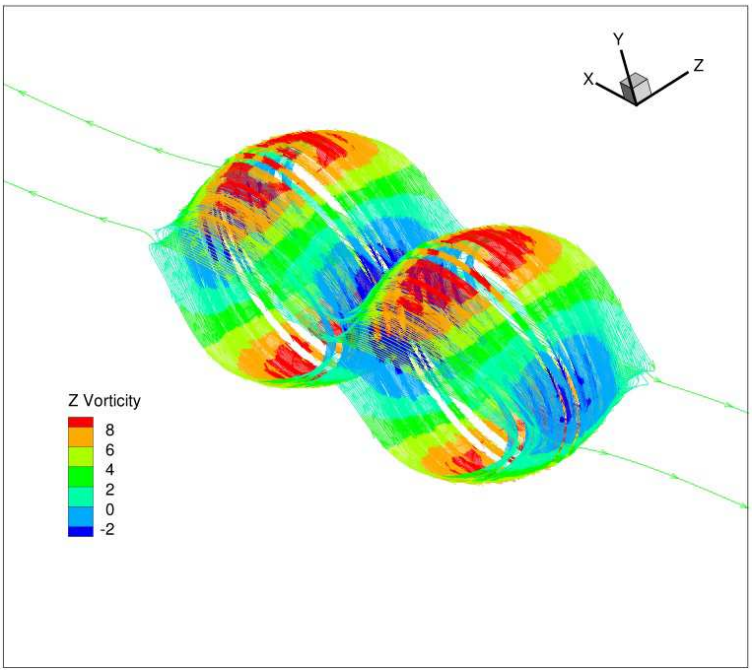

(b) 3D view

Figure 6.3: *Z Vorticity field and streamlines between separating spherical solid-pairs, steam tracers are released at the etcetera region between particles (*$\varepsilon = 1, Re_p = 1, D_i^* = 1.4, t^* = 0.01$*).*

in the region of positive velocity and the right one is slightly higher in the region of negative velocity. The left solid experiences two forces, one towards the $-y$ and the other towards $+x$ leading to a resulting counter-clockwise motion of the left solid. The right solid, on the other hand, experiences motion in the $+y$ and $+x$ direction, leading to a counter-clockwise motion too for the right solid as shown in Fig. 6.6.

For the attraction case, two moving solids are engulfed in one vortex and their trajectories show that they rotate about the domain centre as they approach each other. However, it is important to keep in mind that both these motions represent "point reflection" or "central symmetry" and do not represent "reflection/flow symmetry". Thus the central YZ plane or any plane should not be approximated as a symmetry boundary condition. At $t^* \approx 0.510$, the point reflected motion of both these spheres result in the spheres getting closer, eventually leading to a collision. As no collision model is applied in this study, the simulation was stopped before collision happened. Plotting of the vorticity contours shows that there is a one vortex which engulfs both the solids, as shown in Fig. 6.3(b), indicating the reason for clustering or "hydrodynamic attraction" of solids. This vortex is in counter-clockwise direction - in the same direction as the rotation of individual spheres, as well as the background shear γ.

In Fig. 6.2(c), slight deformation of both solids is observed. This picture is captured when the solids are just going to collide. As mentioned at the beginning of this chapter, no collision model is included in the current GISS, this deformation is purely a numerical error when the solid interfaces are very close to each other. We stop the simulation at this point.

However, our simulations show that the particles do not always cluster. For example, when the initial distance between the sphere centres, $D_i^* = 2$, which means that the closest surface distance between two particles is as long as the sphere diameter, the results show a strong hydrodynamic repulsion, completely reverse of the result when $D_i^* = 1.1$. As shown in Fig. 6.4, at $t \approx 0.955$, the left solid is slightly higher than its initial position in the region of negative velocity and the right solid is slightly lower in the positive of negative velocity (reverse of the case when $D_i^* = 1.1$ which resulted in clustering). The left solid experiences two forces, one towards the $+y$ and the other towards $-x$ leading to a resulting clockwise motion of the left solid, but directed away from the domain centre. The right solid, on the other hand, experiences motion in the $-y$ and $+x$ direction, leading to a clockwise motion

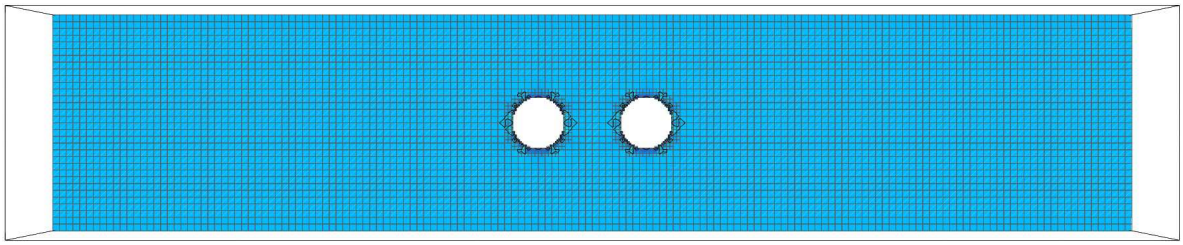

(a) $D_i = 2, t^* = 0$

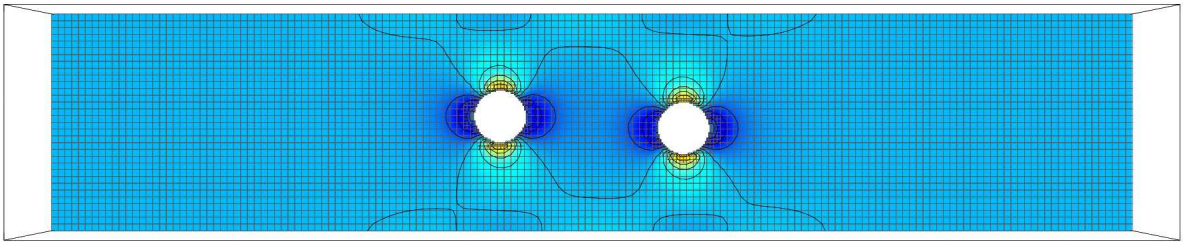

(b) $D_i = 2, t^* \approx 0.955$

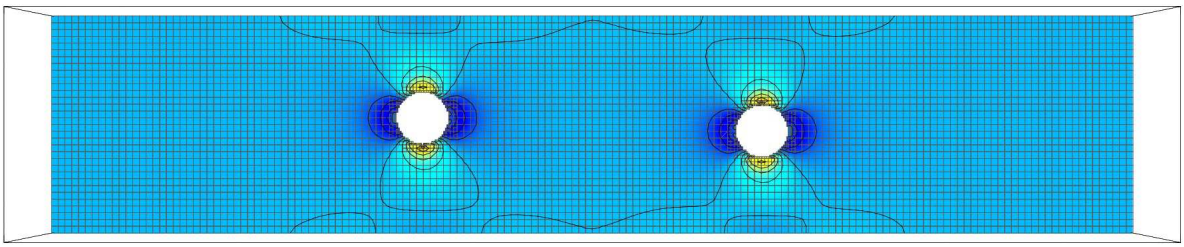

(c) $D_i = 2, t^* \approx 1.911$

Figure 6.4: $Re_p = 1, \varepsilon = 1, L^* = 4, D_i^* = 2$
Contour line shows the vorticity profile.

too but directed away from the centre as shown in Fig. 6.6. In consequence, they eventually separate away from each other - indicating hydrodynamic repulsion. Just as in the case of clustering, the system exhibited point reflection.

Fig. 6.6 presents the evolution of solid trajectories at various D_i^*. The particles were all released at $y^* = 0$ but at different x^*. In the figure, the trajectories in the $(+x)$ plane belong to the right solid and those in the $(-x)$ plane belong to the right solid. A general direction of motion is also shown: when $D_i^* \geq 1.4$ the solids move away from domain centre (hydrodynamic repulsion) and for cases with $D_i^* < 1.4$ the solids move towards the domain centre (hydrodynamic attraction). As no collision model has been introduced, the simulation was stopped when two particles nearly "touched" each other. In order to further investigate the migrating behaviour, evolution of the vertical and horizontal slip velocity of the right solid

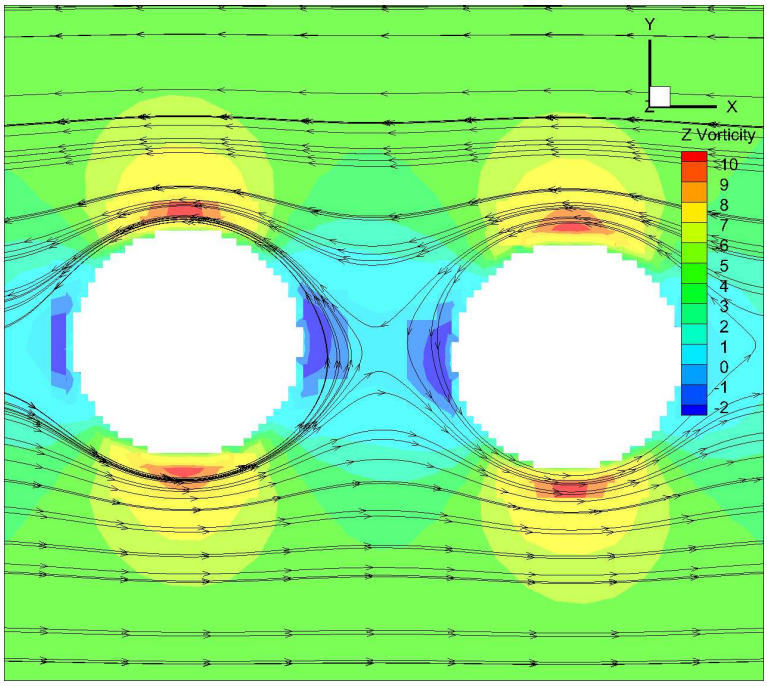

(a) 2D view of Z=0 plane

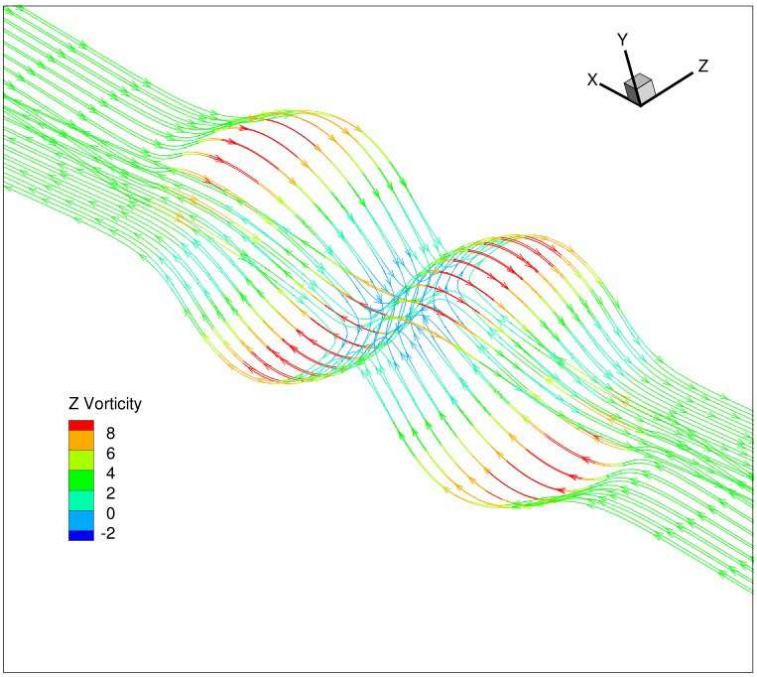

(b) 3D view

Figure 6.5: *Z Vorticity field and streamlines between separating spherical solid-pairs, stream tracers are released randomly at the entire domain* ($\varepsilon = 1, Re_p = 1, D_i^* = 2.0, t^* = 0.01$)*.*

particle have been presented in sections below. The definitions of the dimensionless migrating velocities and location are as in Eq. 5.15.

The simulations results indicate that it is reasonable to expect a critical initial distance, when the hydrodynamic repulsion and attraction effects cancel each other. However, it is difficult to exactly predict this critical D_i^* given numerical errors which make the system inherently unstable. So, at present, the critical D_i^* could only be estimated and its value is between 1.3 and 1.4. Again, given that the motion of these two solids are always point reflections, only the data concerning the right solid is plotted, henceforth.

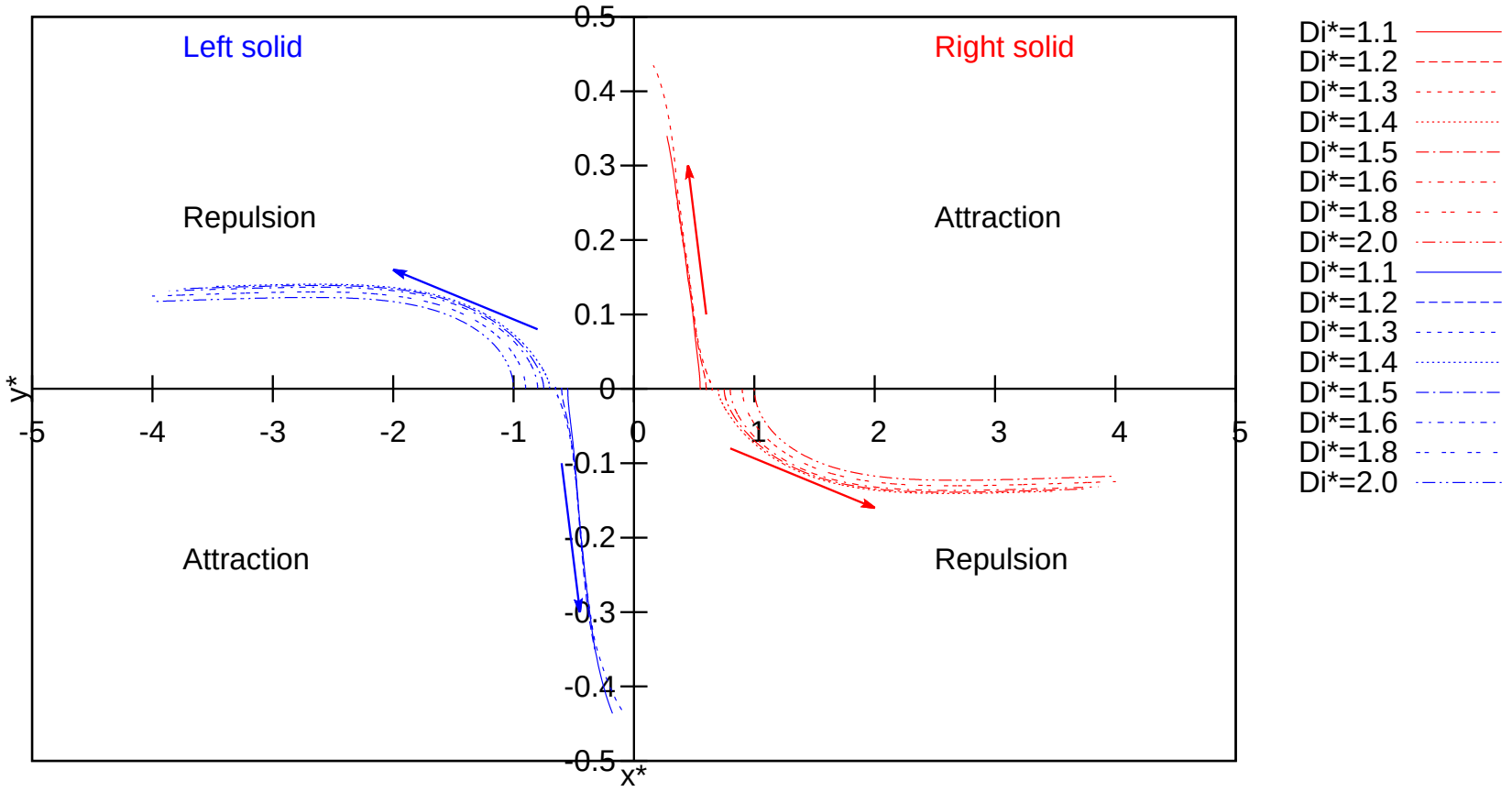

Figure 6.6: *Solid trajectories (black for right solid and) with different* D_i^* *at* $\varepsilon = 1, Re_p = 1, M = 16$.

Fig. 6.3 and Fig. 6.5 show the vorticity field and streamlines around the solid particles. When the initial distance between solid particles is close, as shown in Fig. 6.3(a), the streamlines show that a well-defined boundary layer exists around both the solid bodies and for clustering cases these boundary layers are in close proximity to each other. The boundary layer thickness is defined as $\delta_0 = \delta_{0l} = \delta_{0r}$ where subscripts l and r indicate left and right solids, respectively. This means that the solids are nearly tangent to each other with surface separation distance, $S \sim 2\delta_0$. Moreover the both the solids spin in counter-clockwise direction ($\Omega = \Omega_r = \Omega_l$) and the no-slip boundary condition ensures that the maximum velocity in the thin boundary layer region is $u_{bl} = R\Omega$ where R is the radius of the solid (for spheres $R = a = b$). It must be noted that the direction of the boundary layer velocities for the left and right solids are in opposite directions - thereby cancelling out each other. Action of the boundary layer ensures that the fluid is constantly exiting the thin tangential region - which keeps bringing the solids closer. Given that this is a 3D domain, there is hardly any flow area between this tangential region for the fluid to pass through. This tangential region becomes the region of highest flow resistance and most fluid bypasses this region - thereby flowing around both the solids as the streamlines indicate. This generates an overall vortex engulfing both the bodies - thereby creating a hydrodynamic clustering effect region. In such a case, when considering the clustering twin-solids system can be studied as an entity, the migration of the twin solids, can be treated as the counter-clockwise rotation around the the centre of the two solids, which also exactly reflects the influence of the background shear γ. When the initial distance between solid particles is not close enough, as shown in Fig. 6.5 , where $D_i^* = 1.4$, a region can be observed with weaker vorticity locate just between the two stronger vorticity regions near the solid surface.

At greater initial separation distances, as shown in Fig. 6.5(a) the minimum surface separation distance $S >> 2\delta 0$. This ensures that the boundary layer velocities is insufficient to drain away the fluid in the tangential region. This results in a vortex counter-rotating to the solid spin between the two solids. This vortex prevents the boundary layers from interacting favourably to induce “attraction” causing hydrodynamic repulsion. The 3D view of the streamline in Fig. 6.3(b) and Fig. 6.5(b) also demonstrate how the streamlines around the twin particles system behave for separating case.

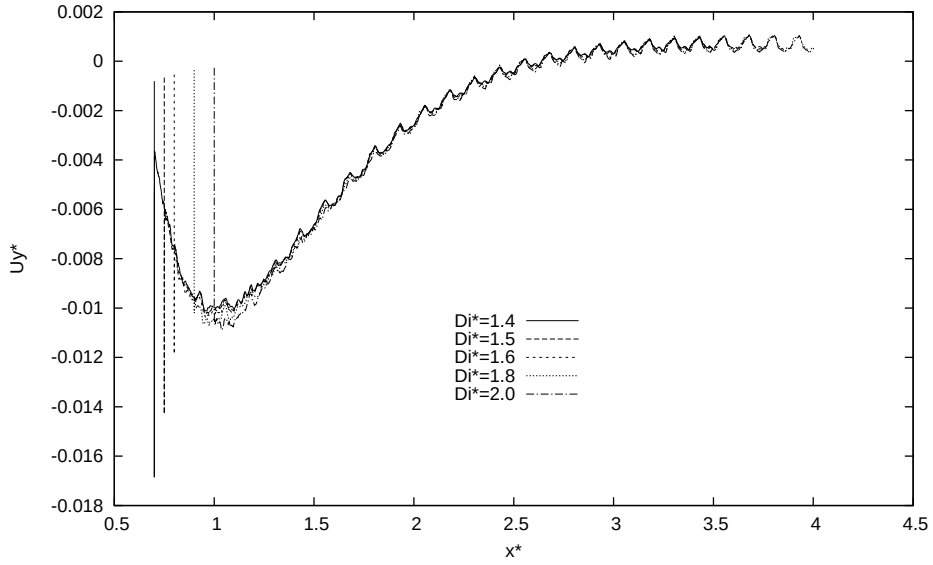

(a) hydrodynamic repulsion

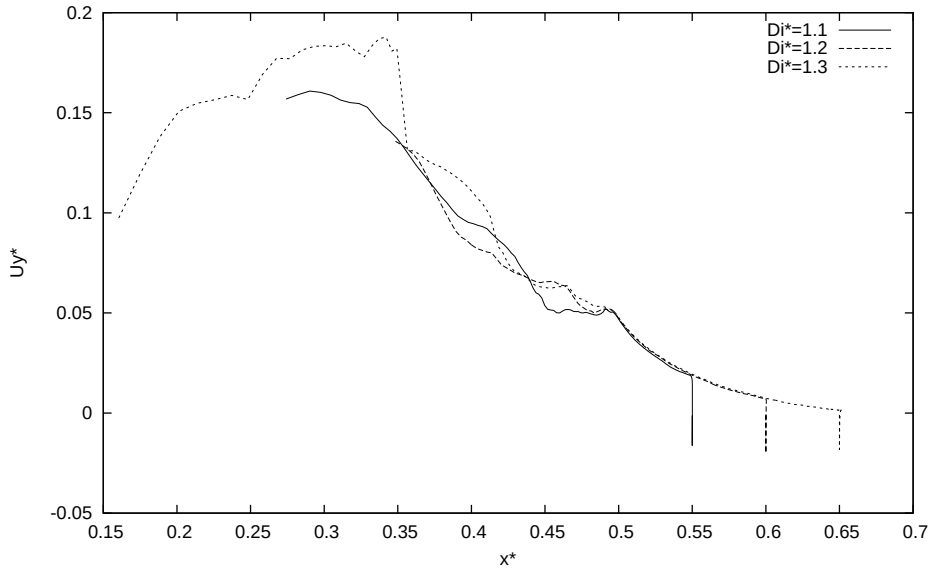

(b) hydrodynamic attraction

Figure 6.7: *Spatial evolution of vertical migration velocities for the right solid experiencing hydrodynamic repulsion/attraction at different D_i^* ($\varepsilon = 1, Re_p = 1$).*

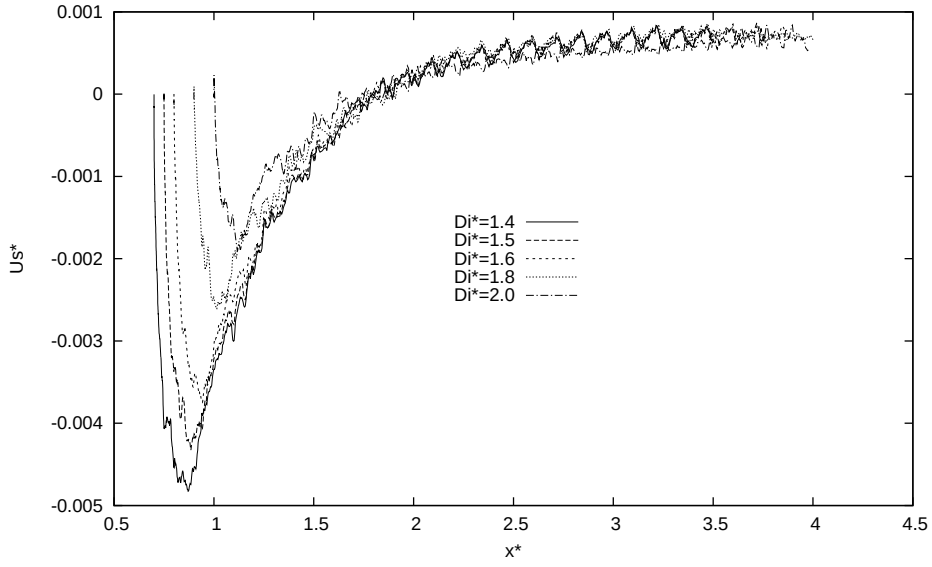

(a) hydrodynamic repulsion

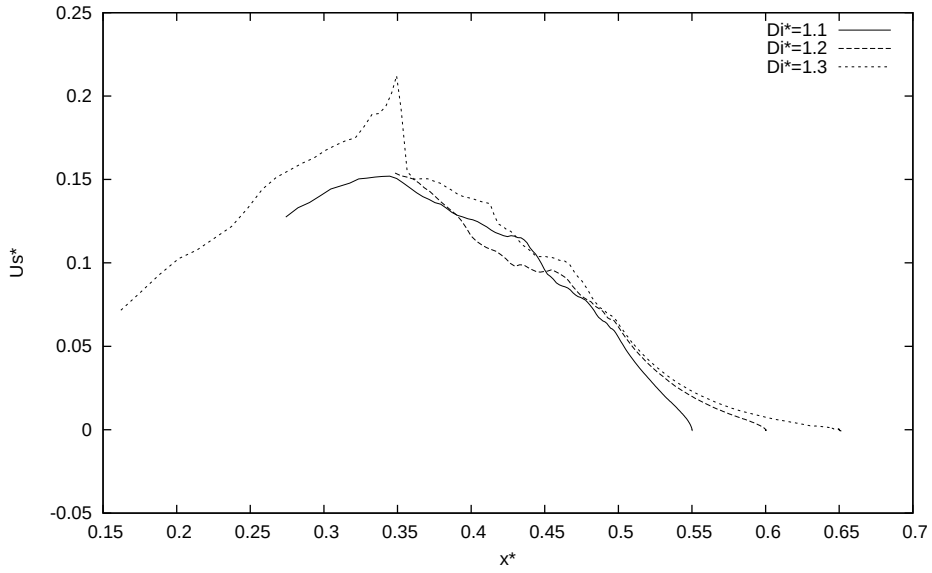

(b) hydrodynamic attraction

Figure 6.8: *Spatial evolution of horizontal migration velocities for the right solid experiencing hydrodynamic repulsion/attraction at different D_i^* ($\varepsilon = 1, Re_p = 1$).*

Fig. 6.7 shows the spatial evolution of vertical migration velocities as a function of initial separation distance, D_i^*. The figure shows that despite different D_i^*, the solids show nearly identical vertical velocities after an initial transient, indicating that vertical migration velocity is not a strong function of D_i^*. Fig. 6.7(a) also shows that the location where the separating solid particles achieve their maximum norm of vertical migration velocity corresponds to $2D$. On the other hand, for the collision cases, Fig. 6.7(b) shows that the magnitude of the vertical migration is significantly greater than those separation cases, which is clearly due to the strong hydrodynamic interactions when the particles are very close.

The U_s^* in Eq. 5.15 describes the horizontal migrating velocity of the solid particles relative to the local fluid. Fig. 6.8 shows the spatial evolution of the horizontal migration velocities as a function of D_i^* for solid-pairs experiencing hydrodynamic repulsion. Even here the result shows that the horizontal velocity after the initial transient is not a function of D_i^*. However, in the initial transient phase, a negative U_s^* captured by our simulation suggests an opposite effect, implying that the initial hydrodynamic effect prevents the solids from separating, and this effect monotonically decreased with the increasing particle distance. For the collision case, the magnitude of the migration is also much larger than those separating cases, as well as vertical migration velocity.

Fig. 6.9 and Fig. 6.10 depict evolution of vertical and horizontal migration velocities with the angular position of the solids. These figures show that the vertical velocities did influence the angular velocity of the solid spheres - higher velocities corresponding to faster spins. However, given the solids considered were spheres, the effects of solid spins on the flow field were small and only a one-way coupling i.e. flow impacting the angular velocity is seen, the same pattern is also observed in Fig. 6.9(b) and Fig. 6.10(b) with fewer rotations captured as the simulation stopped when particles' collision happened.

6.3 Influence of Ellipsoid Geometries at Low Re_p

Section. 6.2 focused on the migration behaviours of standard spheres. Section. 5.2.2 also proved that a standard sphere is a special case of a general ellipsoid which has an aspect ratio of unity. Therefore, in this section, more general shape would be discussed. The solid

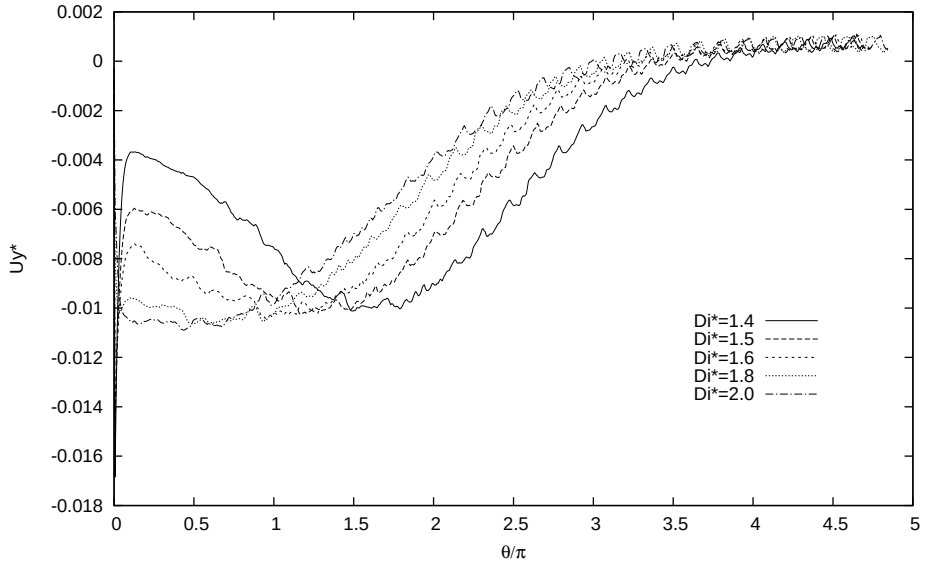

(a) hydrodynamic repulsion

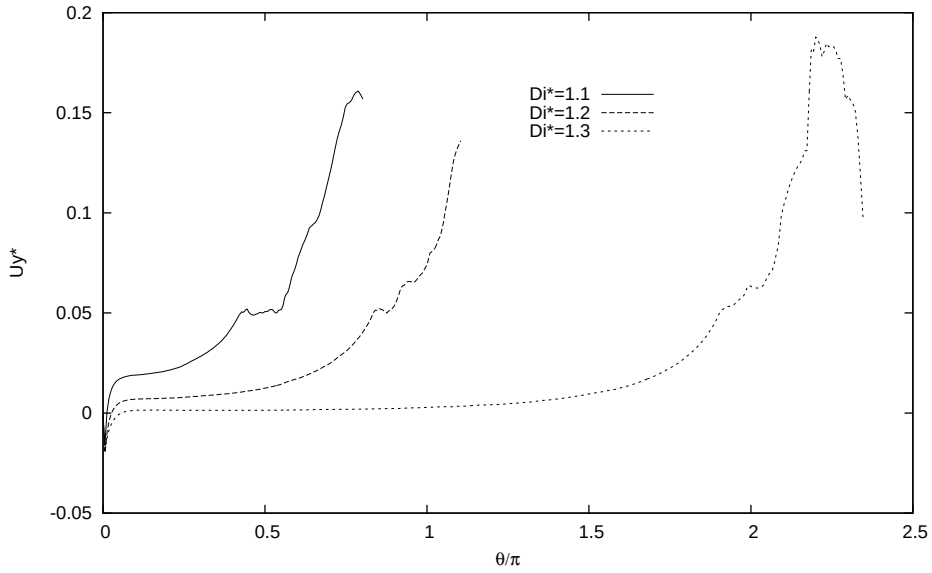

(b) hydrodynamic attraction

Figure 6.9: *Angular evolution of vertical migration velocities for the right solid experiencing hydrodynamic repulsion/attraction at different D_i^* ($\varepsilon = 1, Re_p = 1$).*

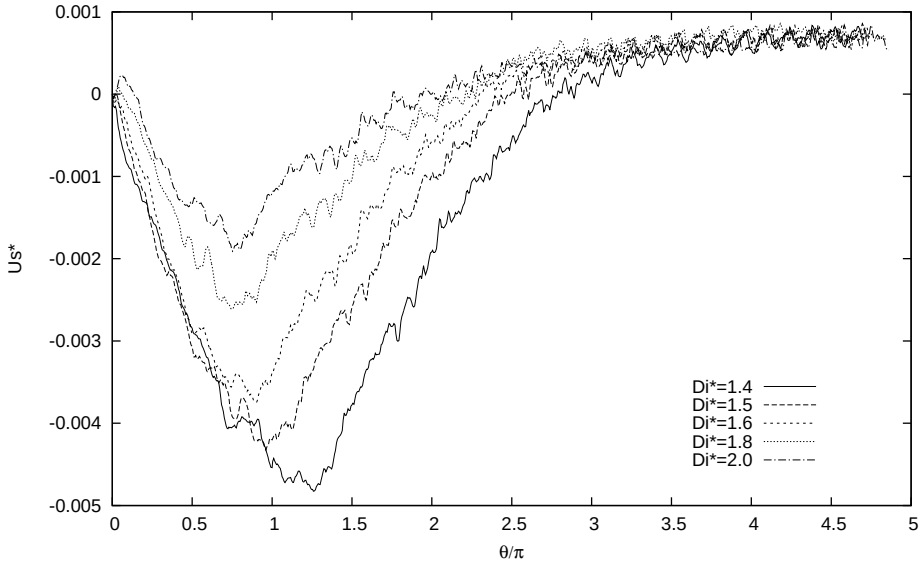

(a) hydrodynamic repulsion

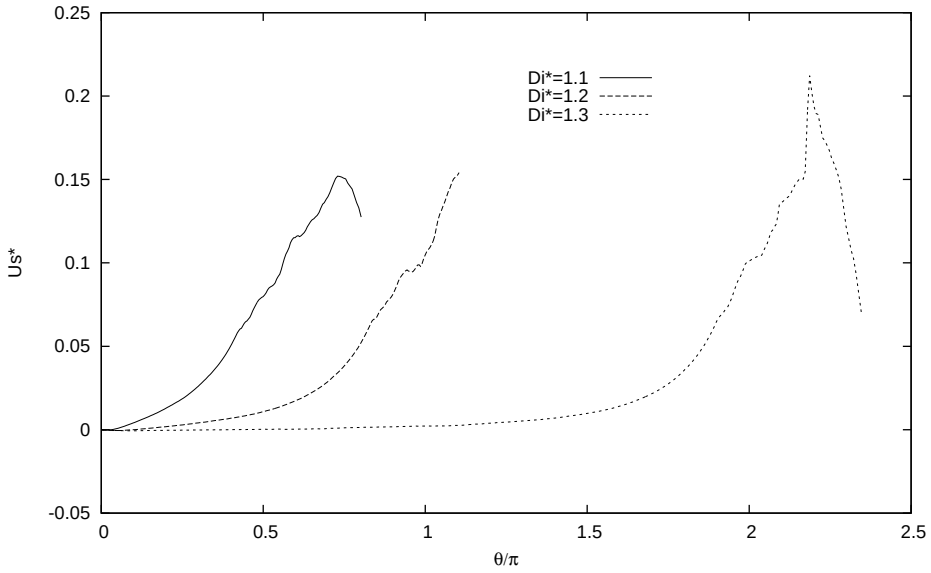

(b) hydrodynamic attraction

Figure 6.10: *Angular evolution of horizontal migration velocities for the right solid experiencing hydrodynamic repulsion/attraction at different D_i^* ($\varepsilon = 1, Re_p = 1$).*

particles considered here are prolate ellipsoids with $\varepsilon = 2$. The definitions of characteristic length scale ($2a$), velocity scale ($2\gamma a$), domain scale ($L^* = 4$) and $Re_p = 1$ remain the same as in Section 6.2.

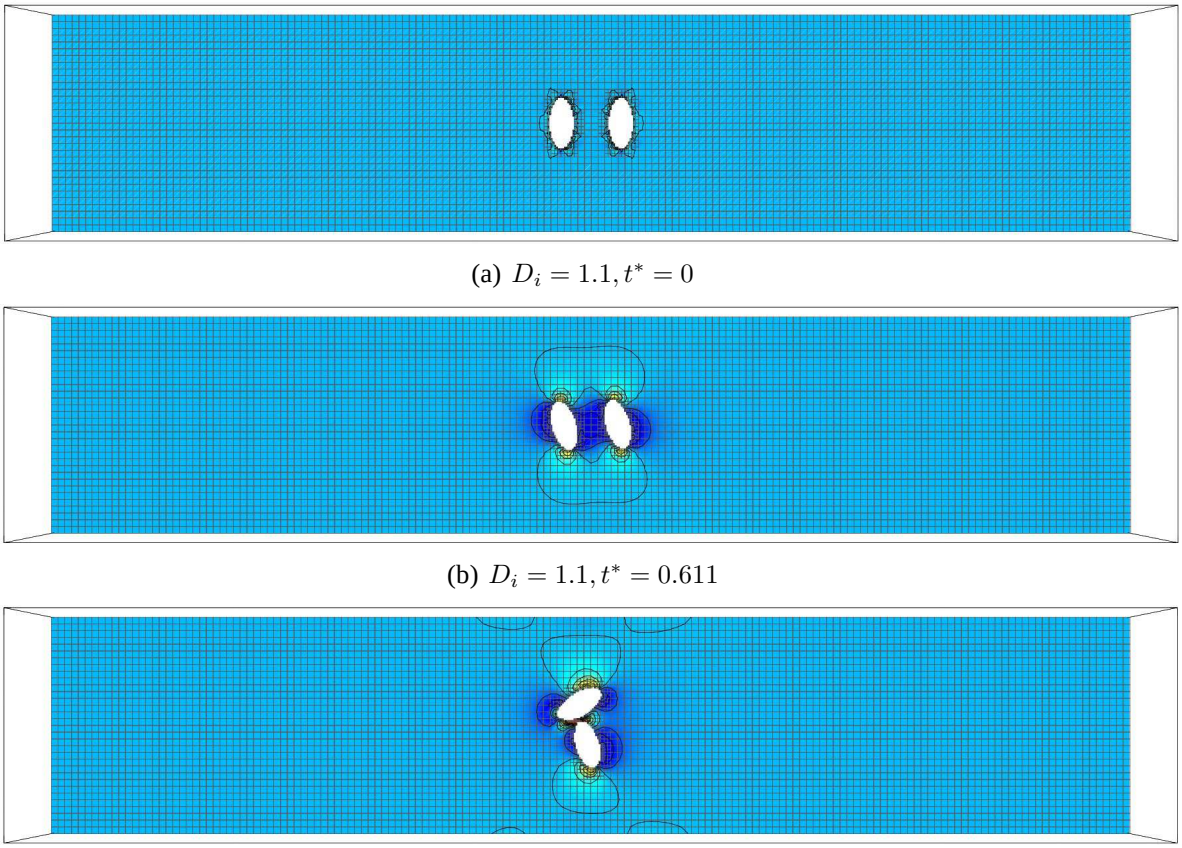

(a) $D_i = 1.1, t^* = 0$

(b) $D_i = 1.1, t^* = 0.611$

(c) $D_i = 1.1, t^* = 1.222$

Figure 6.11: $Re_p = 1, \varepsilon = 2, L^* = 4, D_i^* = 1.1$
Contour line shows the vorticity profile.

In the simulation shown in Fig. 6.11, the geometric aspect ratio $\varepsilon = 2$, which means the major axis is two times longer than the minor. The dimensionless initial distance D_i^* between the centres of two particles is 1.1, making their closest surface distance one-tenth of the ellipsoid major (as in the case for spheres in Fig 6.2). Fig. 6.11 shows that with this configuration, the prolate ellipsoid particles also hydrodynamically cluster exhibiting point reflection behaviour. Further on, the two ellipsoids solids even climbed over each other and therefore exchanged their relative horizontal position, showing a tumbling cluster.

Fig. 6.12 shows the trajectories of the ellipsoid particle centre for case of $\varepsilon = 2$. The result shows that the trajectories are very similar to those shown in Fig 6.6. As with spheres, it is confirmed there is a critical initial separation distance below which clustering occurs and above which separation occurs. For $\varepsilon = 2$, the result shows the distance is between 1.1 and 1.2 (for spheres it was between 1.3 and 1.4). These results indicate that the criteria for clustering is also shape-dependent.

Fig. 6.13 and Fig. 6.14 show the vertical and horizontal migrating velocity, respectively of the right ellipsoid solid with $\varepsilon = 2$. For case of $\varepsilon = 2$, Fig. 6.13 shows that the curves for the vertical migration velocity for simulations with different D_i^* collapsed on each other beyond a spatial point, very similar to the simulations of $\varepsilon = 1$ shown in Fig. 6.7. However, as the rotational (tumbling) behaviour is more prominent for the ellipsoids, strong oscillations can be observed around the main curve in Fig. 6.13. Several spikes are observed from Fig. 6.13 and each of them correlates to a starting simulation with different initial D_i^*. A strong impulse happens at the beginning of the simulation to adjust the initial stationary ellipsoid with the background flow velocity, which yields those spikes. The fluctuations are more prominent in the horizontal migration velocities, as seen in Fig. 6.14.

Fig. 6.15 and 6.16 plot the migration velocities of the solids against their angular positions. Unlike the cases of standard sphere particles, the velocities of ellipsoid solids are strong functions of their angular position. This influence increases with increasing ε (narrower ellipsoids, not shown here).

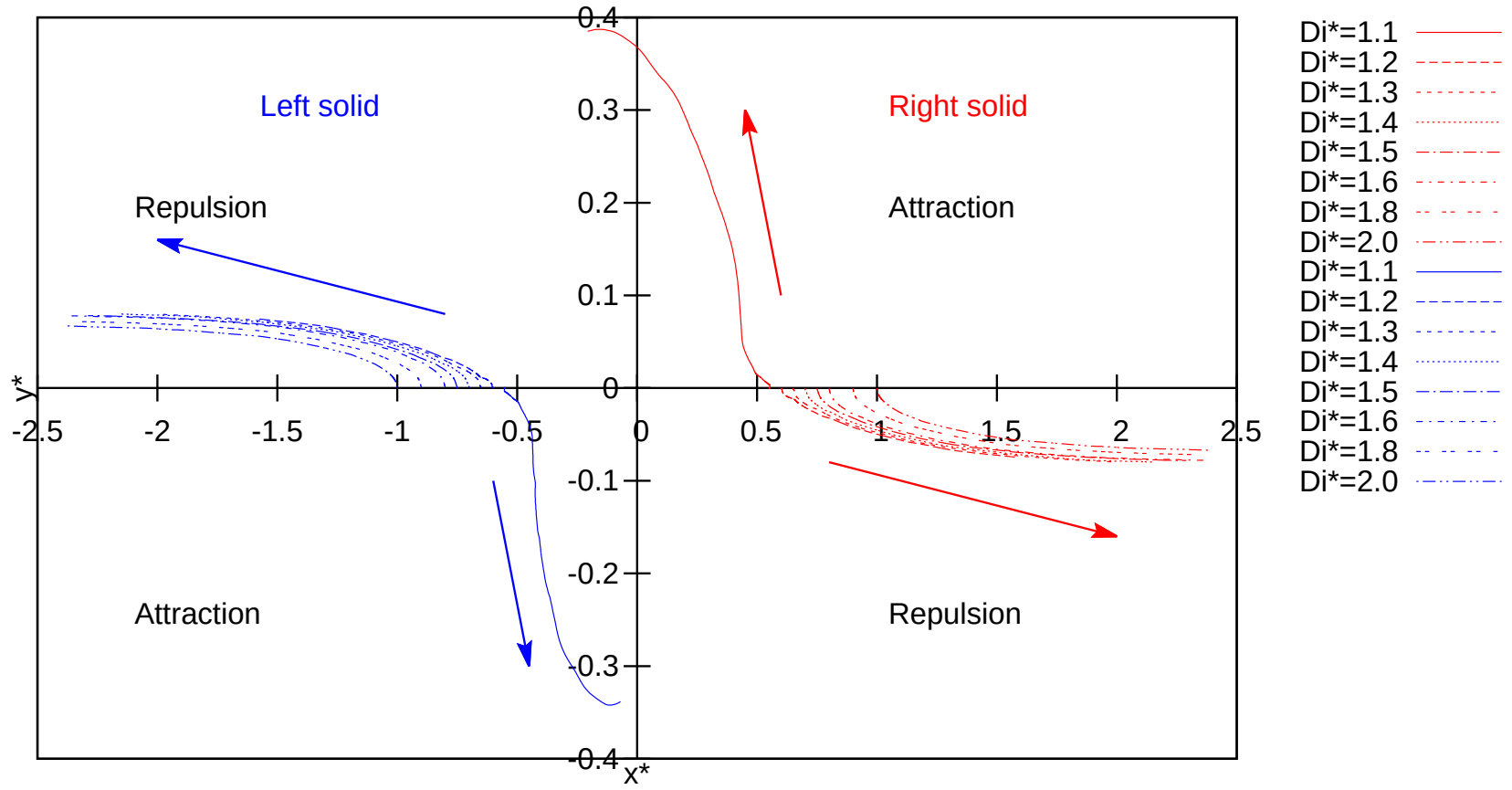

Figure 6.12: *Particle trajectories with different* D_i^* *(*$\varepsilon = 2, Re_p = 1$*).*

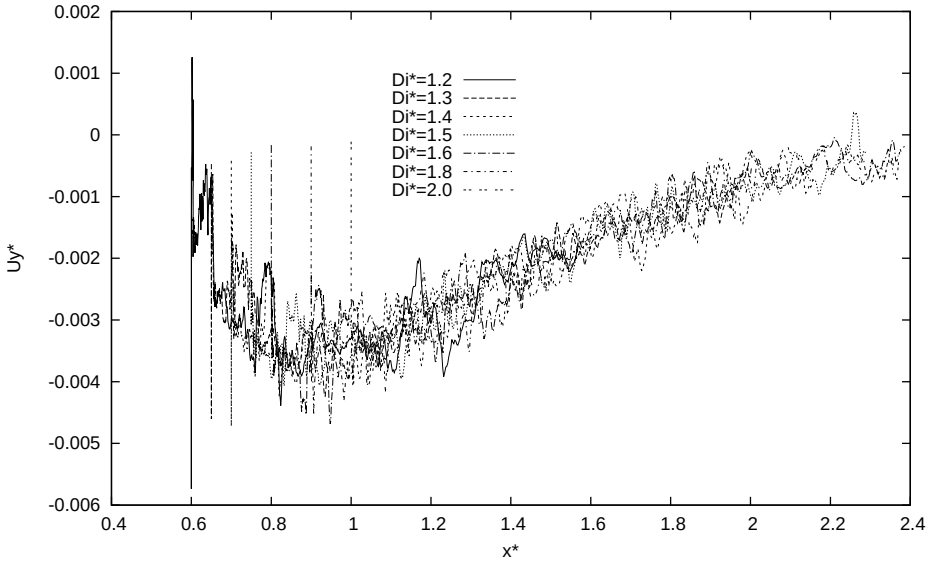

Figure 6.13: *Spatial evolution of vertical migration velocities for the right solid experiencing hydrodynamic repulsion with different D_i^* ($\varepsilon = 2, Re_p = 1$).*

As in the case of spheres, Figs 6.17 and 6.18 show clustering behaviour if their separation distance $S \sim 2\delta_0$. However it must be noted that the boundary layer velocity in a spinning ellipsoid is a strong function of the geometry - $u_{bla} = a\Omega$ at the edges of the major axis and $u_{blb} = b\Omega$ at the edges of the minor axis. Therefore, $u_{bla} > u_{blb}$ explaining the periodic behaviour of velocities in the Figures above as the ellipsoid spins. This also means that the boundary layer thickness is not uniform around the ellipsoid, $\delta_{0a} < \delta_{0b}$. This will result in a complex clustering behaviour - with separation distances smaller when major axes face each other and separation distances large when minor axes face each other.

6.4 The Influence of Re_p

In this section, the influence of the particle Reynolds number Re_p on the relative motion of the solids is reported. The geometric aspect ratio is fixed to $\varepsilon = 2$. Re_p grows to 2. All other simulation parameters remain unchanged.

Fig. 6.19 shows that the behaviour at $Re_p = 2$ is qualitatively similar to that for $Re_p = 1$

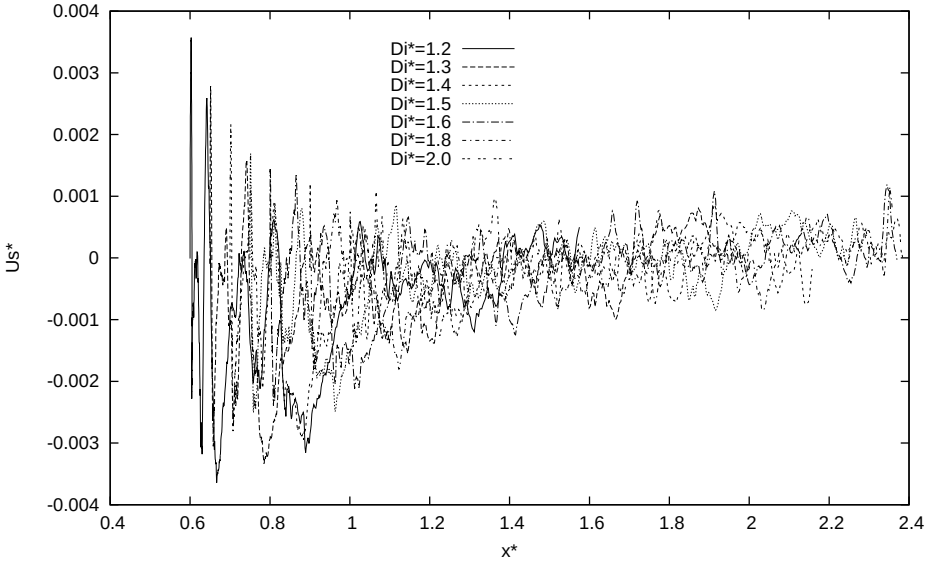

Figure 6.14: *Spatial evolution of horizontal migration velocities for the right solid experiencing hydrodynamic repulsion with different D_i^* ($\varepsilon = 2, Re_p = 1$).*

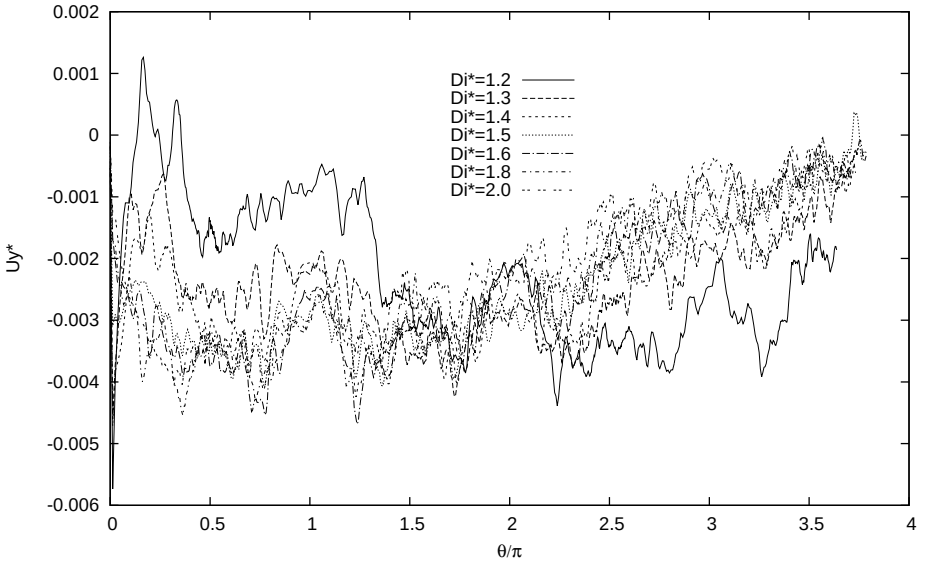

Figure 6.15: *Angular evolution of vertical migration velocities for the right solid experiencing hydrodynamic repulsion with different D_i^* ($\varepsilon = 2, Re_p = 1$).*

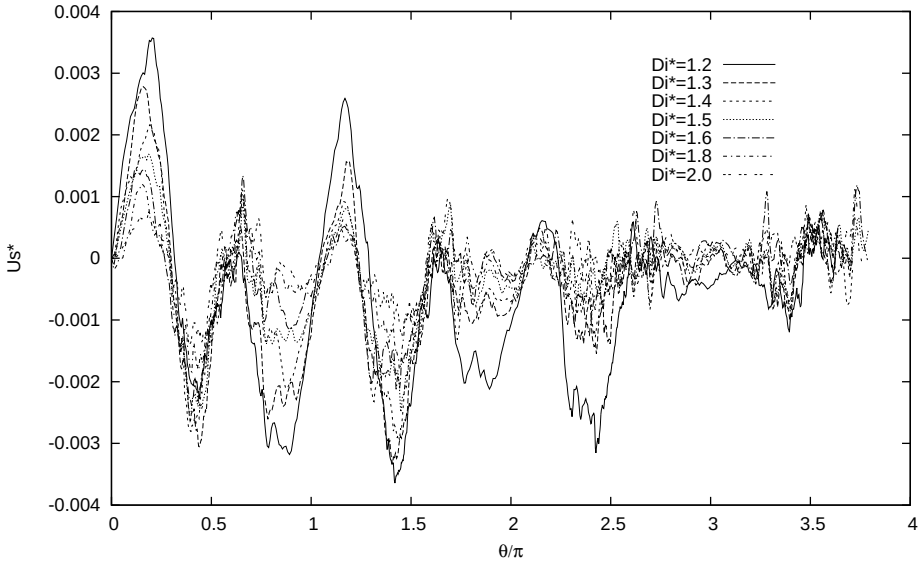

Figure 6.16: *Angular evolution of horizontal migration velocities for the right solid experiencing hydrodynamic repulsion with different D_i^* ($\varepsilon = 2, Re_p = 1$).*

(shown in Fig 6.11). Particle trajectories and migration velocities in horizontal and vertical direction are also qualitatively similar to those presented in Section 6.3.

However even at the same initial placement distance, the clustering is delayed. This is expected because high Re_p results in thinner boundary layers around the bodies, thus for a higher Re_p one needs a smaller separation distance for the boundary layers on the two solids to interact. So as demonstrated in this case, at $Re_p = 2$, the clustering starts to accelerate only when the solids are close enough for their respective boundary layers to interact. The Prandtl's Boundary Layer Equations (or the reduced Navier-Stokes equations under boundary-layer/lubrication approximation) [140] suggests along the boundary, the advective term and diffusive term of the momentum equation (Eq. 3.2) should with same order of magnitude (See Appendix C):

$$\delta_0 \sim O(\frac{1}{\sqrt{Re_c}}) \tag{6.1}$$

where Re_c is defined by u_c and l_c. Since in this section u_c is triggered by the rotation of the solid, it has the same magnitude of the solid surface linear velocity $2\gamma a$, and l_c is where boundary layer thickness δ_0 developed at the solid surface, Re_c is expected to be with the

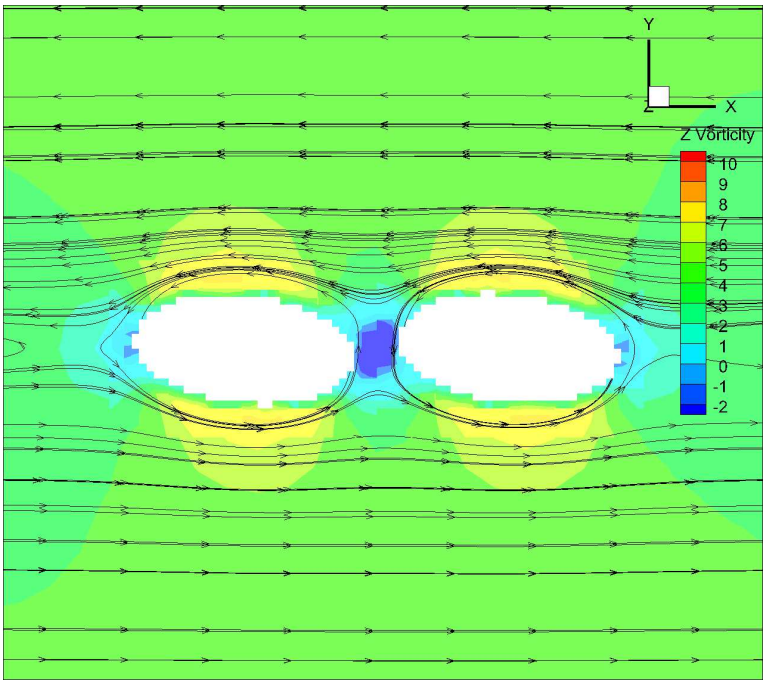

(a) 2D view of Z=0 plane

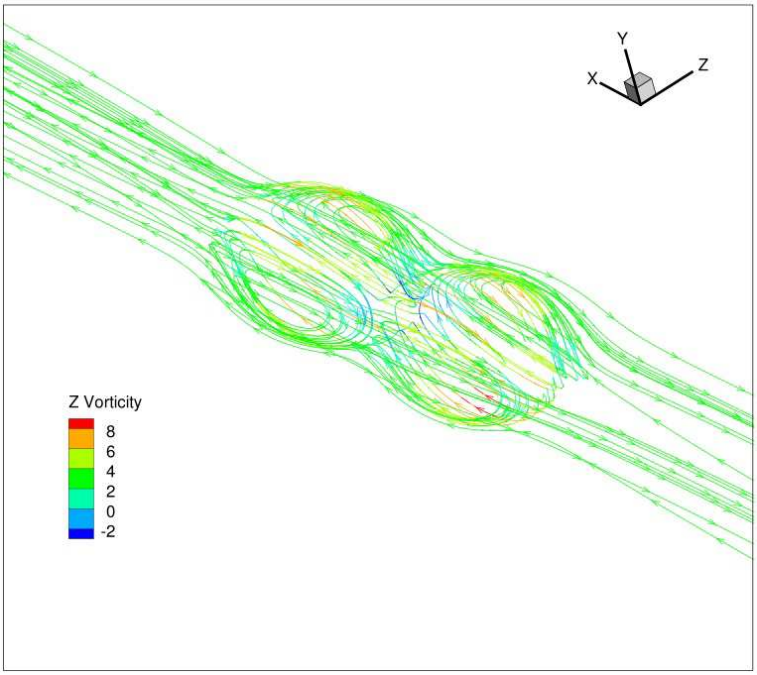

(b) 3D view

Figure 6.17: *Z Vorticity field and streamlines between clustering ellipsoid-pairs, stream tracers are released randomly at the entire domain ($\varepsilon = 2, Re_p = 1, D_i^* = 1.1$).*

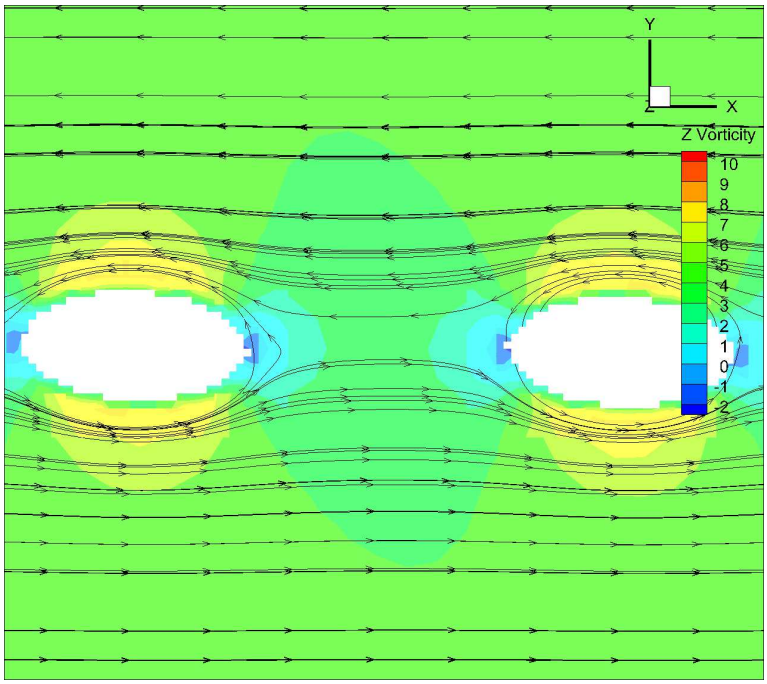

(a) 2D view of Z=0 plane

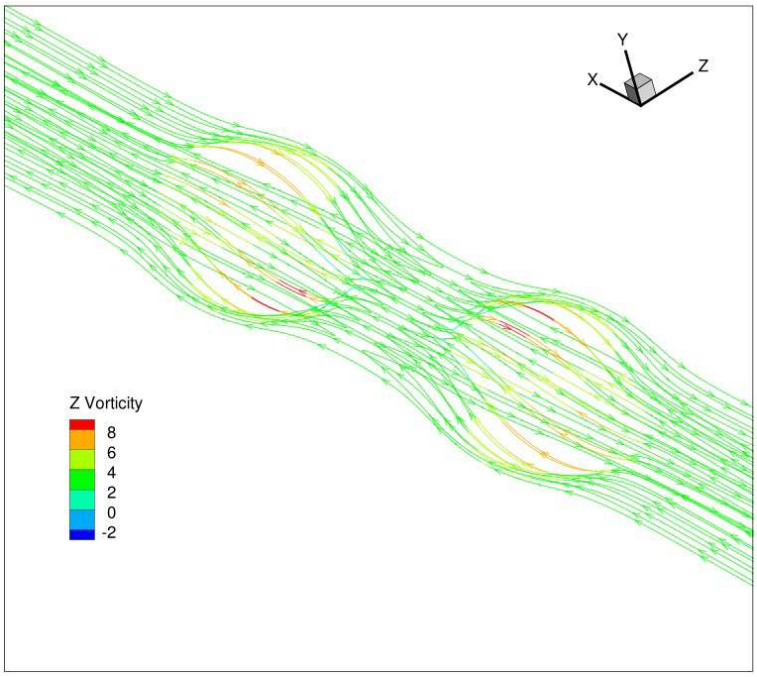

(b) 3D view

Figure 6.18: *Z Vorticity field and streamlines between separating ellipsoid-pairs, stream tracers are released randomly at the entire domain ($\varepsilon = 2, Re_p = 1, D_i^* = 2.0$).*

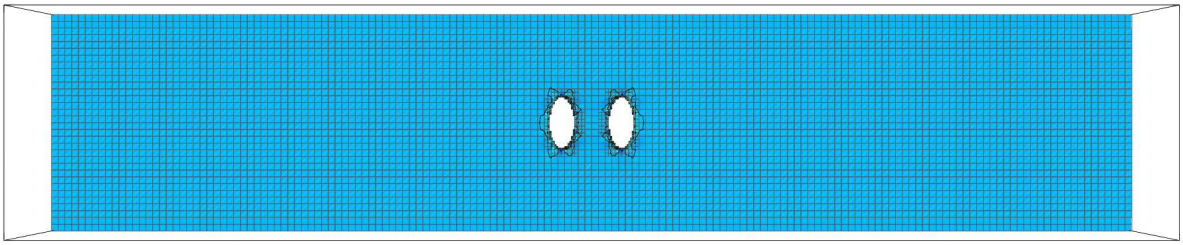

(a) $D_i = 1.1, t^* = 0$

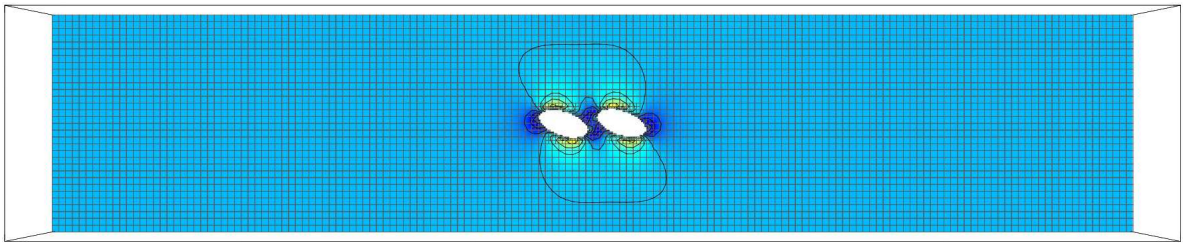

(b) $D_i = 1.1, t^* = 0.764$

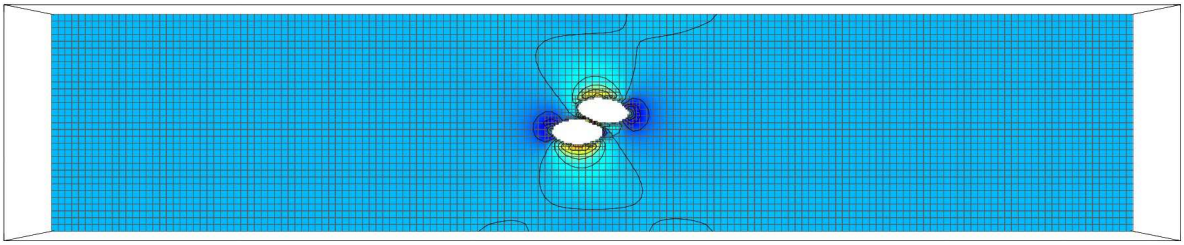

(c) $D_i = 1.1, t^* = 1.528$

Figure 6.19: $Re_p = 2, \varepsilon = 2, L^* = 4, D_i^* = 2$
Contour line shows the vorticity profile.

same magnitude of Re_p in this study, thus:

$$\delta_0 \sim O(\frac{1}{\sqrt{Re_p}}) \tag{6.2}$$

The equation provides an general scale of the boundary layer thickness corresponding to the Re_p, and the actual value could be obtained from the simulation results.

Eq. 6.2 indicates that for solids to hydrodynamic clustering at high Re_p, their separation distance $S \sim \delta_0$ must drop - which means that an extremely high mesh resolution is needed. Dimensionless boundary layer thickness and critical surface separation distance for clustering as predicted by our solver are presented in Table. 6.1 at $Re_p = 1$ and 2 for standard sphere. These are difficult 3D simulations because mesh refinement around the solids must be high

Re_p	S reported by simualtions	δ_0 between solids
1	between $0.3 \sim 0.4$	0.3
2	between $0.2 \sim 0.3$	0.22
4	around 0.2	0.16

Table 6.1: *Relation among Re_p, S and δ_0, S is measured from the simulation data at the distance from the solid surface to where the flow rate equals to 99% of the pre-set background flow rate.*

enough to predict the boundary layers at the these very small separation distances accurately. Currently, several simulations at various Re_p are being conducted to understand the role of boundary layer around the solids towards their hydrodynamic clustering behaviour. Owing to their high computational requirements, these simulations are still ongoing and the results will be reported in article 2 of Appendix A currently under preparation for submission to Physics of Fluids. These results will also verify whether the above hypothesis holds good. It must also be noted that only hydrodynamic interactions has been discussed in this thesis. However in reality - in applications like flows of hydrate solids or understanding micro-PIV applications, the so-called short-range and long-range electrostatic forces come into play as the solid-bodies come closer to each other or to the wall. In this thesis - these effects are not studied and solely concentrate on hydrodynamic forces.

6.5 Conclusion

In this chapter, the behaviour of two closely placed neutrally buoyant solids under shear flow has been studied. The mesh resolution, time step and the domain scale determined in Chapter. 4 and Chapter. 5 were used.

The result shows that the solids may either experience hydrodynamic repulsion (leading to separation) or hydrodynamic attraction (leading to clustering) depending upon their initial separation distance. The result also shows that the solids under this configuration exhibit point reflection. A detailed study of horizontal and vertical migration velocities suggest a highly complex behaviour depending on the geometry of the solids - the velocity fields show higher fluctuations for higher aspect ratios. The period of fluctuation frequency corresponds to the period of the spinning ellipsoid - with every half period either the lateral or longitudinal

axis is perpendicular to the streamwise direction. For the standard sphere particles, the spin of the solids would not affect the surface area normal to the streamwise direction, thus no fluctuations were exhibited.

The DNS results show that when the separation distance between the solid surfaces is within the order of boundary layer thickness - hydrodynamic attraction/clustering occurs, otherwise hydrodynamic repulsion occurs. It was noted that during hydrodynamic attraction - a single vortex engulfs the solids and these solids move as a cluster. During repulsion - a vortex (rotating in an opposite sense to the spinning solids) exists in the region between the solids causing the solids to separate out. At higher Re_p the minimum distance needed for clustering decreases. The separation distance is thus hypothesised to be $S \sim O(Re^{-0.5})$.

Chapter 7

Chaotic Motion of Ellipsoid in Inviscid Flow

Previous chapters dealt with flows of solids immersed in viscous fluids with a finite Reynolds numbers. In this chapter, the applicability of the GISS is tested by extending our study to understand solid motion in an inviscid fluid, where the Reynolds number is infinitely large. As the target of GISS is to provide a solid-fluid coupling solver, the validation case should focus on those problems where the flow can be certainly solved, which are either the low Reynold problems as discussed in previous chapters, or the inviscid flow problems in this chapter, where the momentum equation of the Navier-Stokes equations (Eq. 3.2) can be simplified to:

$$\frac{\partial \mathbf{u}}{\partial t} + \mathbf{u} \cdot \nabla \mathbf{u} = -\frac{1}{\rho} \nabla p + \mathbf{f_s} \tag{7.1}$$

A particular module for solving the inviscid flow problem is provided by the Gerris solver.

On the other hand, Kirchhoff [67] simplified the inviscid Euler's equations to a set of ordinary differential equations. Kozlove and Oniscenko [68] later found the integrable conditions for the Kirchhoff's equations and pointed out the possibility of particles tracking chaotic motions. Aref [10] provided the numerical evidence that the Kirchhoff's equations do have chaotic solutions, yet his work only proved the possible existence of the chaotic motion, the actual conditions needed to trigger this chaotic motion has been an unsolved question. Therefore, in order to effectively test our GISS for inviscid problems, there are two objectives in this chapter: i) to validate the chaotic motion of solids in an inviscid fluid, and ii) seek to identify the triggers for chaotic motion.

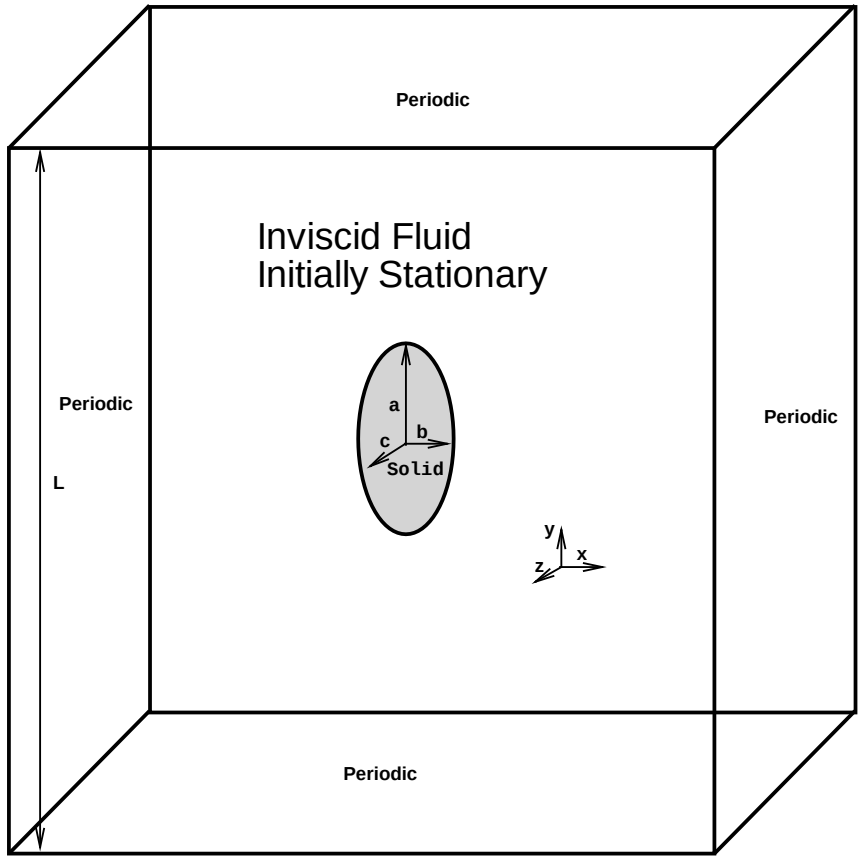

Figure 7.1: *Initial set up of the ellipsoid in Aref's study [10]. Neutrally buoyant general ellipsoid with aspect ratio $a : b : c$ in an inviscid fluid with an initial translational velocity U_0 in the xy plane and and an initial angular velocity Ω_0 at the z plane.*

7.1 Chaotic Motion of a General Ellipsoid in Inviscid or Viscous Flow

Fig 7.1 shows the setup of Aref's problem [10] concerns with a neutrally buoyant general ellipsoid ($a \neq b \neq c$) in an inviscid fluid. The domain size is $L = 512a$ and all sides of the domain are periodic. Such a large domain is chosen to ensure that the solid has enough space to track the orbits even under chaos. The highest mesh resolution was set as $M = 32\Delta x$ around the solid surface and adaptive mesh refinement ensures that the flow around it adequately captured. The ellipsoidal solid was given an initial velocity U_0 and angular velocity Ω_0 whose direction are perpendicular to each other as proposed by Aref [10]. This is

akin to setting up a *point vortex* in the domain in plane XY. Note that the dot product of the momentum and angular momentum is zero. The objective is to study the motion tracked by such an ellipsoid and to check for conditions of chaos. The results were outputted at $t^* = 10$, where t^* is the dimensionless time characterised by U_0 and $2a$.

At this point, it is helpful to recollect the generalised vorticity equations for both viscous and inviscid flows, respectively:

$$\frac{d\boldsymbol{\omega}}{dt} = \frac{\partial \boldsymbol{\omega}}{\partial t} + \mathbf{u} \cdot \nabla \boldsymbol{\omega} = \boldsymbol{\omega} \cdot \nabla \mathbf{u} + \nu \nabla^2 \boldsymbol{\omega} \tag{7.2}$$

thus:

$$\frac{d\boldsymbol{\omega}}{dt} = \boldsymbol{\omega} \cdot \nabla \mathbf{u} \text{ under inviscid conditions} \tag{7.3}$$

Here, $\boldsymbol{\omega} = \nabla \times \mathbf{u}$ is the vorticity vector. From Eq. 7.3, for an inviscid flow if the flow is irrotational ($\boldsymbol{\omega} = 0$) everywhere at the initial instant, it remains irrotational through out. Thus, in order to prevent such irrotationality - a point vortex is set up at an initial instant. Under these conditions Eq. 7.3 shows that without viscosity, vorticity can be amplified and advected but there is no mechanism to generate/dissipate it. The point vortex causes the vorticity to be finite in the system for all time.

A marker point located on a vertex of the ellipsoid is selected where the distance to the ellipsoid centre is a. The coordinates of the trajectories relative to the solid centre can be written as:

$$\mathbf{X_r} = \mathbf{X_p} - \mathbf{X_c} \tag{7.4}$$

where the $\mathbf{X_r}$ is the relative position vector plotted in the figure, $\mathbf{X_p}$ is the position vector of the marker point in the global frame and $\mathbf{X_c}$ is the position vector of the solid centre in the global frame. Hence, plotting $\mathbf{X_c}$ show the trajectory of the particle centre moving in the fluid, and plotting $\mathbf{X_r}$ shows the orbit of the marker point relative to the solid centre itself, representing the orientation of the solid. These vectors as solutions of the equations give an immediate view of how the orientation and position of the ellipsoid changes as it moves through the fluid. Aref [10] provided four possible result of marker point orbit for ellipsoid with $a : b : c = 1 : 0.8 : 0.6$ moving in an inviscid fluid and is shown in Fig. 7.2.

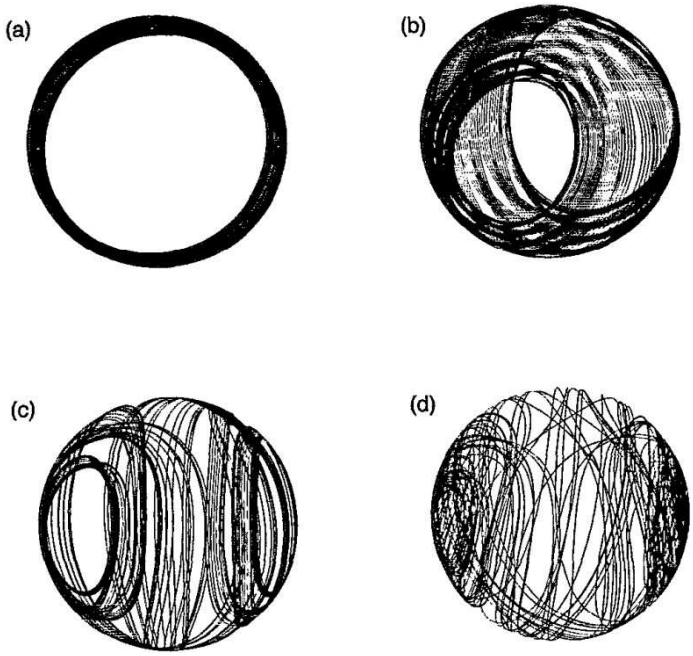

Figure 7.2: *Orientation of a neutrally buoyant general ellipsoid (with $a : b : c = 1 : 0.8 : 0.6$) moving in an inviscid fluid predicted Aref's study [10]. The corresponding E for the a, b, c, d is 1, 2, 5, 10 in this thesis work.*

In our study, the only different initial condition between different cases is the ratio between translational kinetic energy, k_t and the rotational kinetic energy k_r, which is the energy aspect ratio E defined in Section 5.1 (see Eq. 5.8).

Fig. 7.3 presents the orbit of the marker point on a general ellipsoid at different energy ratios $E = k_t/k_r$ by plotting $\mathbf{X_r}$. As the GISS uses a volume fraction to describe the solid boundary, the orientation of the ellipsoid is exhibits a jittery "zig-zag" behaviour which smooths out with increased solid mesh density - however, the actual curve should be smoother. It can be clearly seen that the orbit of the marker point is a smooth circle at initial conditions for which the rotational kinetic energy exactly matches the translational kinetic energy i.e. $E = 1$, as shown in of Fig. 7.2(a). When $E > 1$, as shown in the Fig. 7.3(b) 7.3(c) whose $E = 2, 5$, it can be seen that the orbit of the marker point becomes more irregular. Further increase in the energy ratio especially when $E \geq 8$ (Fig. 7.3(d) and beyond), the orbits of the marker point become less predictable which can be roughly categorised a chaotic regime. In this chaotic regime, a small increase in E leads to a totally different result. These results shown in Fig 7.3 validate the performance of the GISS against Aref's results in Fig. 7.2 [10].

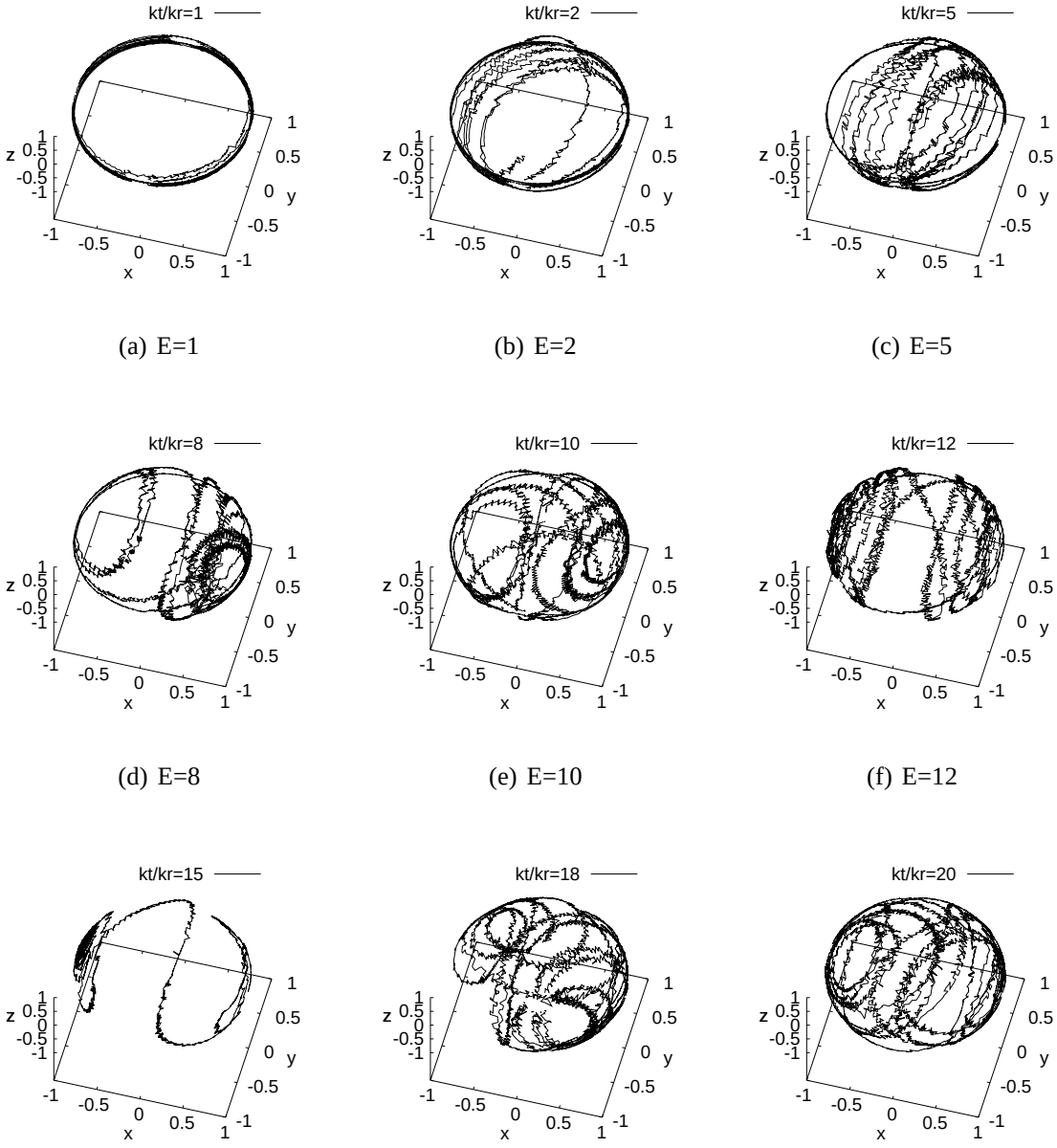

(a) E=1 (b) E=2 (c) E=5

(d) E=8 (e) E=10 (f) E=12

(g) E=15 (h) E=18 (i) E=20

Figure 7.3: *Orbit of the marker point on an ellipsoid with aspect ratio* $a : b : c = 1 : 0.8 : 0.6$ *in an inviscid fluid at different energy ratios* E.

In real fluids, viscosity would damp the motion of the solid and suppress chaotic behaviour. However, it is instructive to characterise the lower limit of viscosity when the ellipsoid trajectory re-exhibits chaos. The solid Reynolds number, Re_p, is defined by the characteristic length scale being the major axis and characteristic velocity being the translational velocity of the solid. Considering that the velocity of the solid evolves during the simulation, this Re_p can be treated as an initial condition. It must be kept in mind that given our definition of Re_p, a higher Re_p corresponds to either large diameter solid or a low viscosity fluid around. The chaotic motion of the solid is essentially dependant on the accurate resolution of flow immediately around the body and the exact imposition of the no-slip boundary condition. Our mesh adaptation strategy has ensured that the mesh is sufficiently resolved in the immediate vicinity of the solid. The result shows that a mesh resolution of $M = 32$ is sufficient for the exact imposition of no-slip conditions on the solid and full resolution of the viscous stress tensor around it. A series of mesh dependency test have also been applied to assure the accuracy of the simulation at high Re_p. Also, though the error introduced by high Re_p would be indeed an important factor affects the simulation results, yet the result for the high Re_p cases here could still work as valuable references.

Fig. 7.4 shows simulations with $Re_p = 1000$ at energy ratios same as in the inviscid fluid simulations (Fig. 7.3). It can be clearly seen that no chaotic motion of the ellipsoid is predicted for $1 \leq E \leq 20$, which is on expected lines at this low Re_p. On the other hand, ellipsoid motion predicted at $Re_p = 100,000$ shown in Fig. 7.5 is similar to that of an inviscid fluid shown in Fig. 7.3 with chaotic motion predicted when $k_t/k_r > 1$ and the degree of chaos increased with E.

The standard deviation of the angular velocity vector $\boldsymbol{\sigma_\Omega}$ over the simulation period is introduced to quantitatively analyse this chaotic motion. As the degree of chaos increases in a system, i.e. as the orbit tracked by the ellipsoid becomes more and more chaotic, such a standard deviation should also rise. It is defined as,

$$\boldsymbol{\sigma_\Omega} = \sqrt{\sigma(\Omega_x)^2 + \sigma(\Omega_y)^2 + \sigma(\Omega_z)^2} \tag{7.5}$$

where $\sigma(\Omega_i)$ is the standard deviation of i-component of the angular velocity over the time

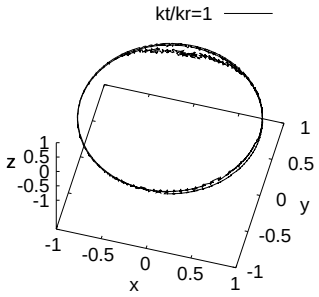

(a) E=1

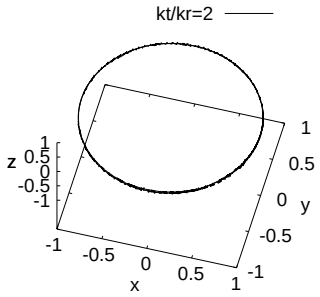

(b) E=2

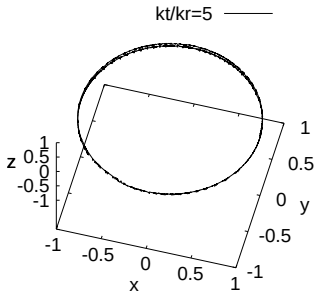

(c) E=5

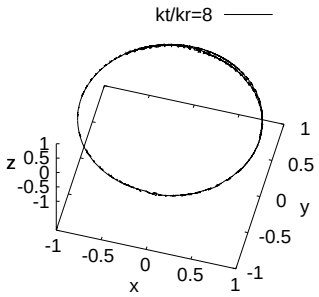

(d) E=8

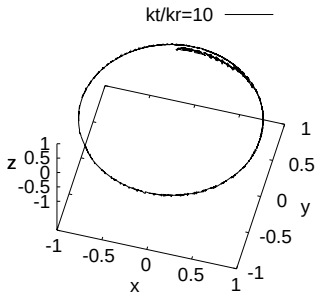

(e) E=10

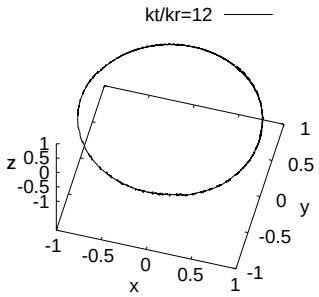

(f) E=12

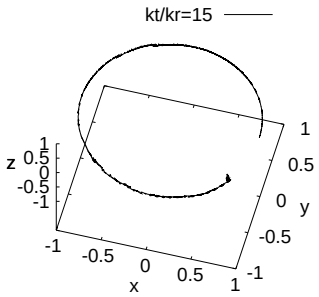

(g) E=15

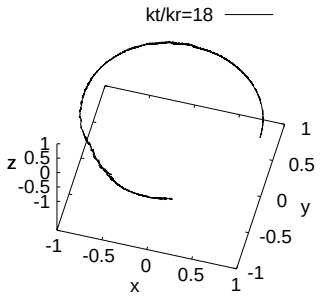

(h) E=18

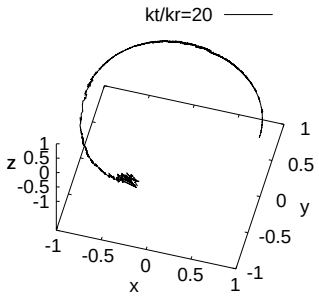

(i) E=20

Figure 7.4: *Orbit of the marker point on a neutrally buoyant ellipsoid with aspect ratio* $a : b : c = 1 : 0.8 : 0.6$ *at* $Re_p = 1000$ *at different energy ratios* E.

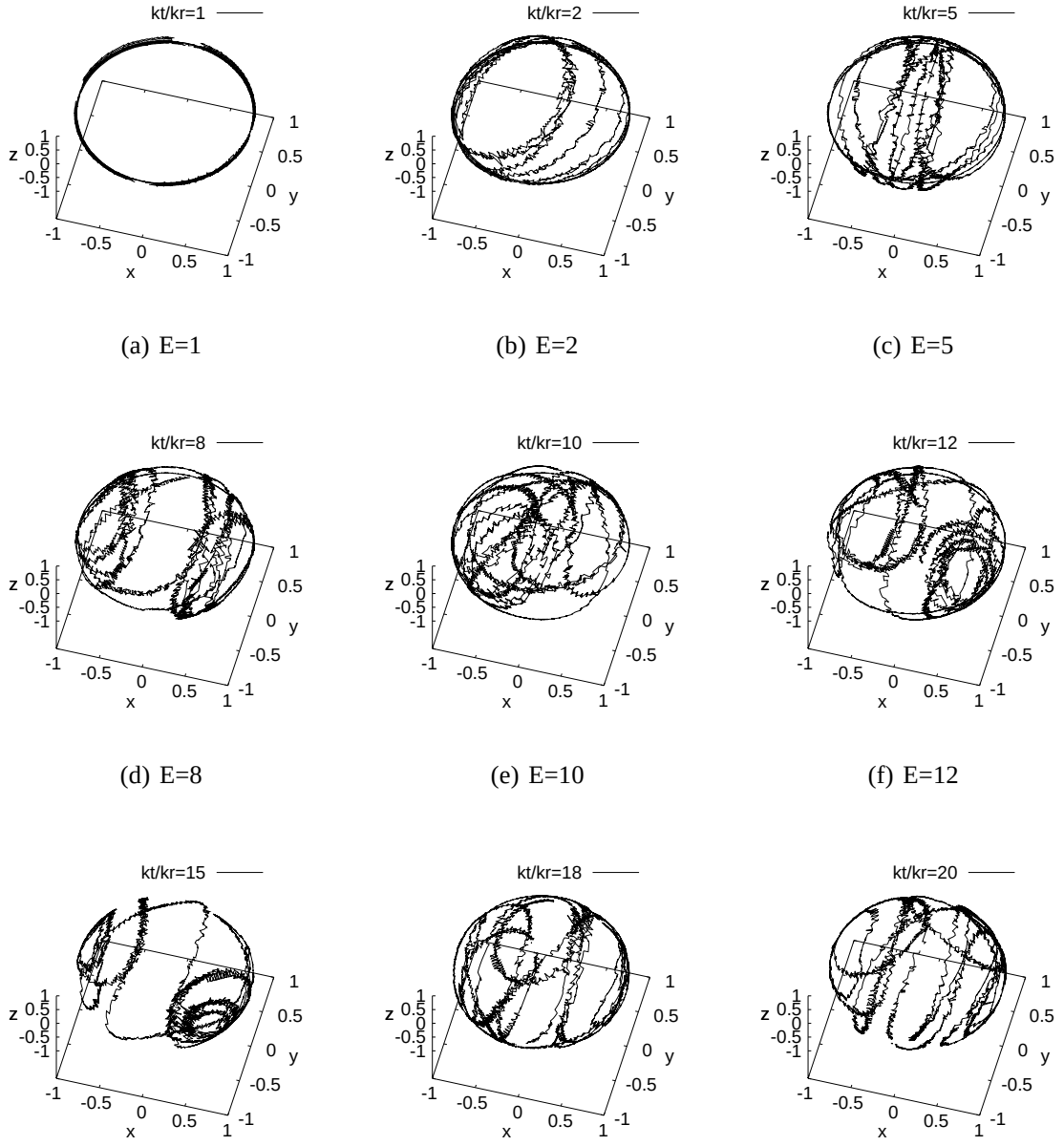

(a) E=1 (b) E=2 (c) E=5

(d) E=8 (e) E=10 (f) E=12

(g) E=15 (h) E=18 (i) E=20

Figure 7.5: *Orbit of the marker point on a neutrally buoyant ellipsoid with aspect ratio* $a : b : c = 1 : 0.8 : 0.6$ *at* $Re_p = 100000$ *at different energy ratios* E.

period of the simulation calculated as:

$$\sigma(\Omega_i) = \sqrt{\frac{1}{N}\sum_{j=1}^{N}\left(\Omega_{ij} - \overline{\Omega}_i\right)^2} \tag{7.6}$$

Here, $\overline{\Omega}_i$ is the time-averaged i-component of the angular velocity over the period of the simulation:

$$\overline{\Omega}_i = \frac{1}{t_s}\int_0^{t_s} \Omega_i dt \tag{7.7}$$

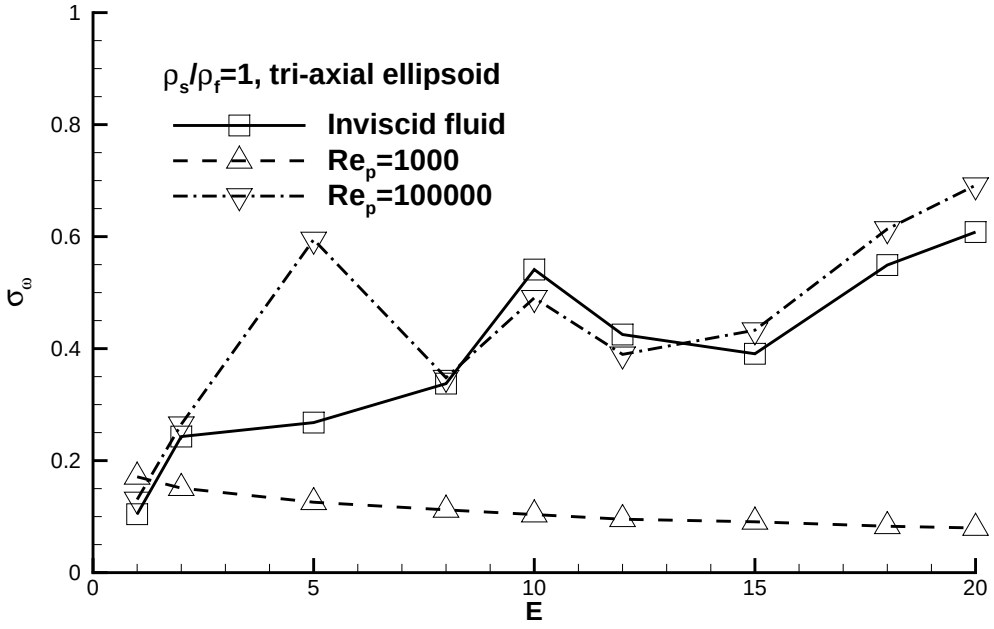

Figure 7.6: *The standard deviation of the angular velocity vector $\boldsymbol{\sigma_\Omega}$ against energy ratio, $E = k_t/k_r$, for cases with a neutrally buoyant ellipsoid of the same geometry at different Re_p.*

Fig. 7.6 plots the $\boldsymbol{\sigma_\Omega}$ against E at various Re_p. It can be easily observed that for cases with big enough E to cause chaos, the value of σ_ω keeps increasing. This is prominent in the inviscid case (Fig. 7.3) and when $Re_p = 100000$ (Fig, 7.5). But, when $Re_p = 1000$ (Fig. 7.4) which exhibits remarkably regular orbits standard deviation is consistently small. This indicates that the key dampening factors for chaos are fluid viscosity and low E which can be induced by initial conditions with high rotational momentum (or low translational momentum).

7.2 Chaotic Motion of General Ellipsoids Denser Than the Fluid

When the density of the ellipsoid is larger than the density of the fluid ($\rho_s/\rho_f > 1$), under conditions of no gravity, the only effect on the flow is due to the acceleration/deceleration of the body. This is called as the virtual mass effect. It must be noted that the virtual mass effect is already present for neutrally buoyant solids. For systems with a finite density ratio there is a factor greater than 1 multiplying the virtual mass force. This simply acts as a source term in the momentum equation. The simulation result shows that this virtual mass force acts to suppress the chaotic motion of the solid at increasing density ratios.

Fig. 7.7 and 7.8 show the orbits of the marker point on a heavier ellipsoid with density ratios $\rho_s/\rho_f = 2$ and $\rho_s/\rho_f = 3$, respectively. All other parameter values are the same as in Fig. 7.3. When comparing the simulation outputs, the density ratio shows its influence in a simple and direct manner. In Fig. 7.3, where $\rho_s/\rho_f = 1$, the solid motion is significantly chaotic when $E = k_t/k_r \geq 2$ whereas in Fig. 7.7 when $\rho_s/\rho_f = 2$ chaos is seen after $E \geq 5$. In Fig. 7.8, when $\rho_s/\rho_f = 3$, chaos is seen after $k_t/k_r \geq 8$. The results indicate that chaos is indeed suppressed at higher density ratios due to the effect of virtual mass.

Fig. 7.9 plots σ_Ω against the E for simulations with different ρ_s/ρ_f. Based on the results from Fig. 7.9 and **the orbits** presented in Fig. 7.3, 7.7 and 7.8, it shows that when $\sigma_\omega > 0.2$, the motion of particle becomes obviously chaotic. Fig. 7.9 also suggests that though it is more difficult for the case with higher ρ_s/ρ_f to become chaotic, once it passed the threshold ρ_s/ρ_f, the chaotic behaviour of it can catch, or becomes even larger than the other two cases, whose motion of particle are less likely to become chaotic. For example, when $k_t/k_r = 5$, the motion of particle with $\rho_s/\rho_f = 2$ behaves most chaotically, and when $k_t/k_r = 20$, the motion of particle with $\rho_s/\rho_f = 3$ behaves most chaotically.

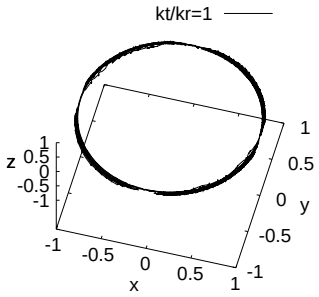

(a) E=1

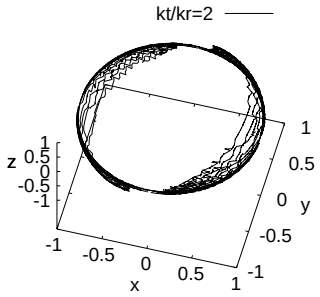

(b) E=2

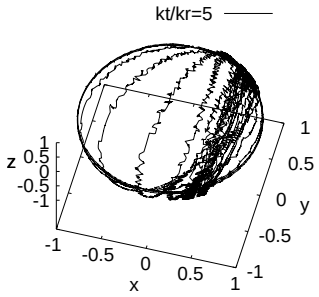

(c) E=5

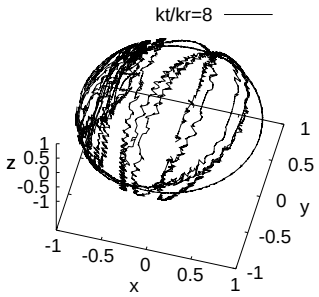

(d) E=8

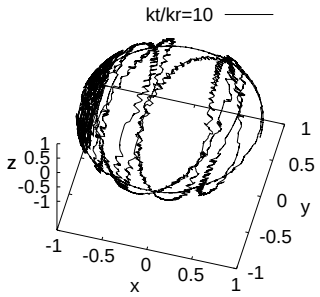

(e) E=10

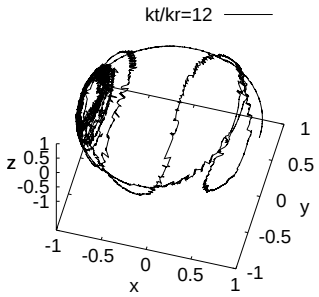

(f) E=12

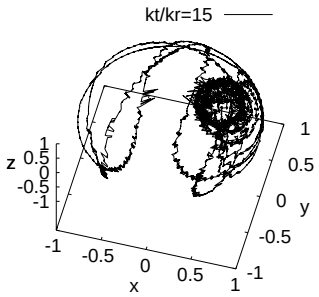

(g) E=15

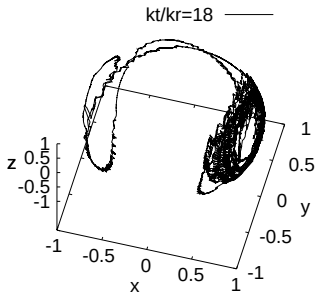

(h) E=18

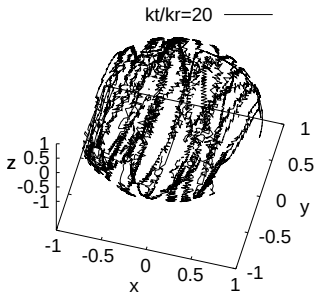

(i) E=20

Figure 7.7: *Orbit of the marker point on a heavier ellipsoid with* $\rho_s/\rho_f = 2$*,* $a : b : c = 1 : 0.8 : 0.6$ *in an inviscid fluid at different energy ratios* E*.*

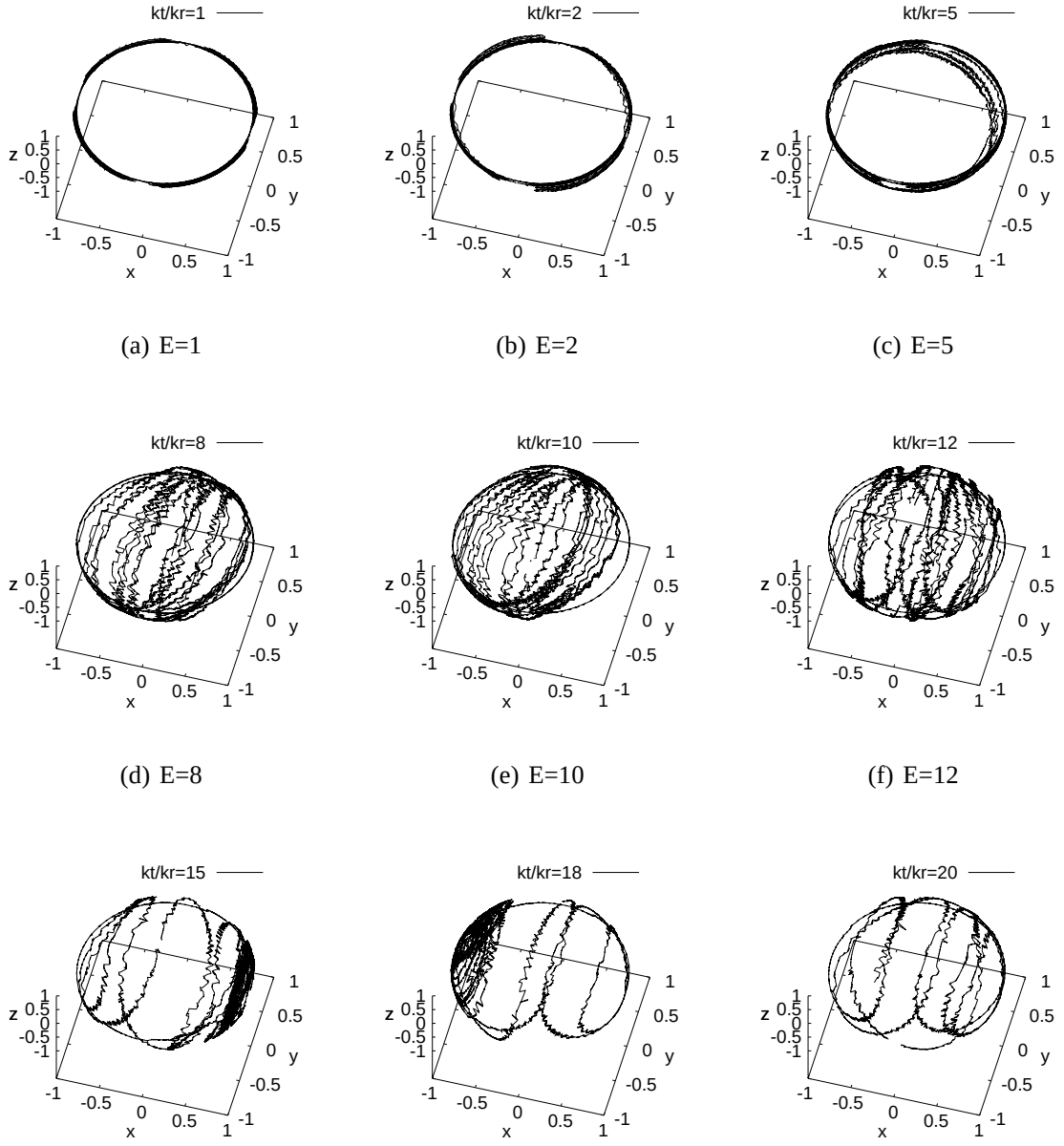

(a) E=1 (b) E=2 (c) E=5

(d) E=8 (e) E=10 (f) E=12

(g) E=15 (h) E=18 (i) E=20

Figure 7.8: *Orbit of the marker point on a heavier ellipsoid with* $\rho_s/\rho_f = 3$*,* $a : b : c = 1 : 0.8 : 0.6$ *in an inviscid fluid at different energy ratios* E*.*

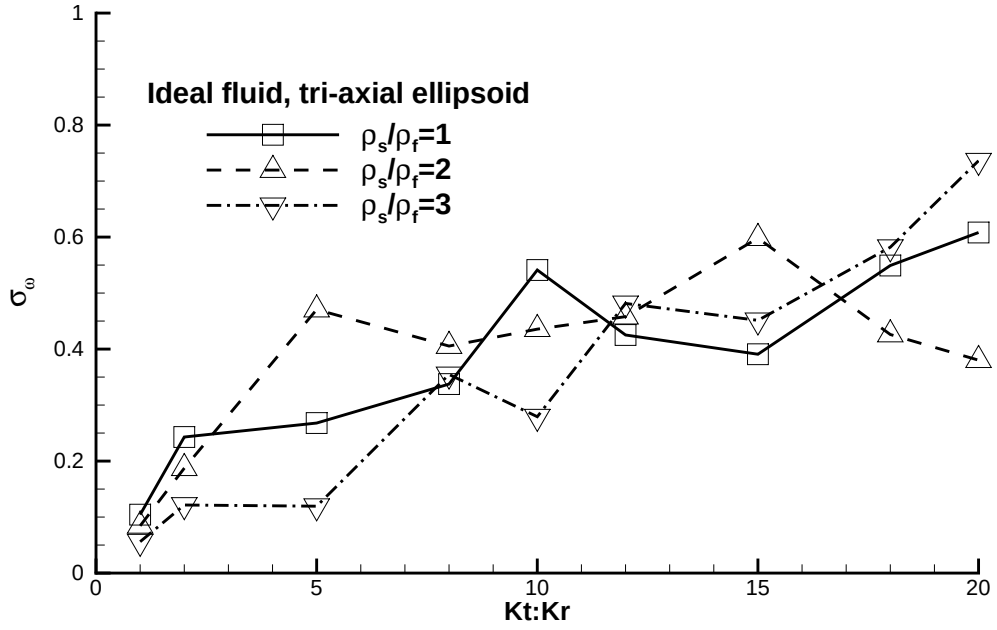

Figure 7.9: *The standard deviation of the angular velocity vector $\boldsymbol{\sigma_\Omega}$ against energy ratio, $E = k_t/k_r$, for cases with ellipsoid of same geometry but different density moving in the inviscid flow.*

7.3 Chaotic Motion of particles with different geometries

The geometry of the solids is found to have a significant influence on the orbits of the marker point tracked. In Section 7.3, the orbits tracked by a standard sphere ($a : b : c = 1 : 1 : 1$) are compared against those tracked by a prolate ellipsoid with $a : b : c = 1 : 0.7 : 0.7$.

Fig. 7.10 shows the orbits of the marker point tracked by a neutrally buoyant prolate ellipsoid and Fig. 7.11 shows the orbits of the marker point tracked by a neutrally buoyant sphere. Fig. 7.10 shows that the motion pattern developed with increasing E for prolate ellipsoid is similar (but not identical) to that of a tri-axial ellipsoid ($a : b : c = 1 : 0.8 : 0.6$)shown in Fig. 7.3. The orbit of a prolate ellipsoid becomes more chaotic with increasing E. As for the standard sphere, it is easy to notice in Fig. 7.11 that the trajectories plotted are constrained with in a well defined circular region (corresponding to the initial condition of angular and translational velocity). This is because the angular momentum of a standard sphere is not significantly impacted by its orientation (angular position of the marker point with respect to

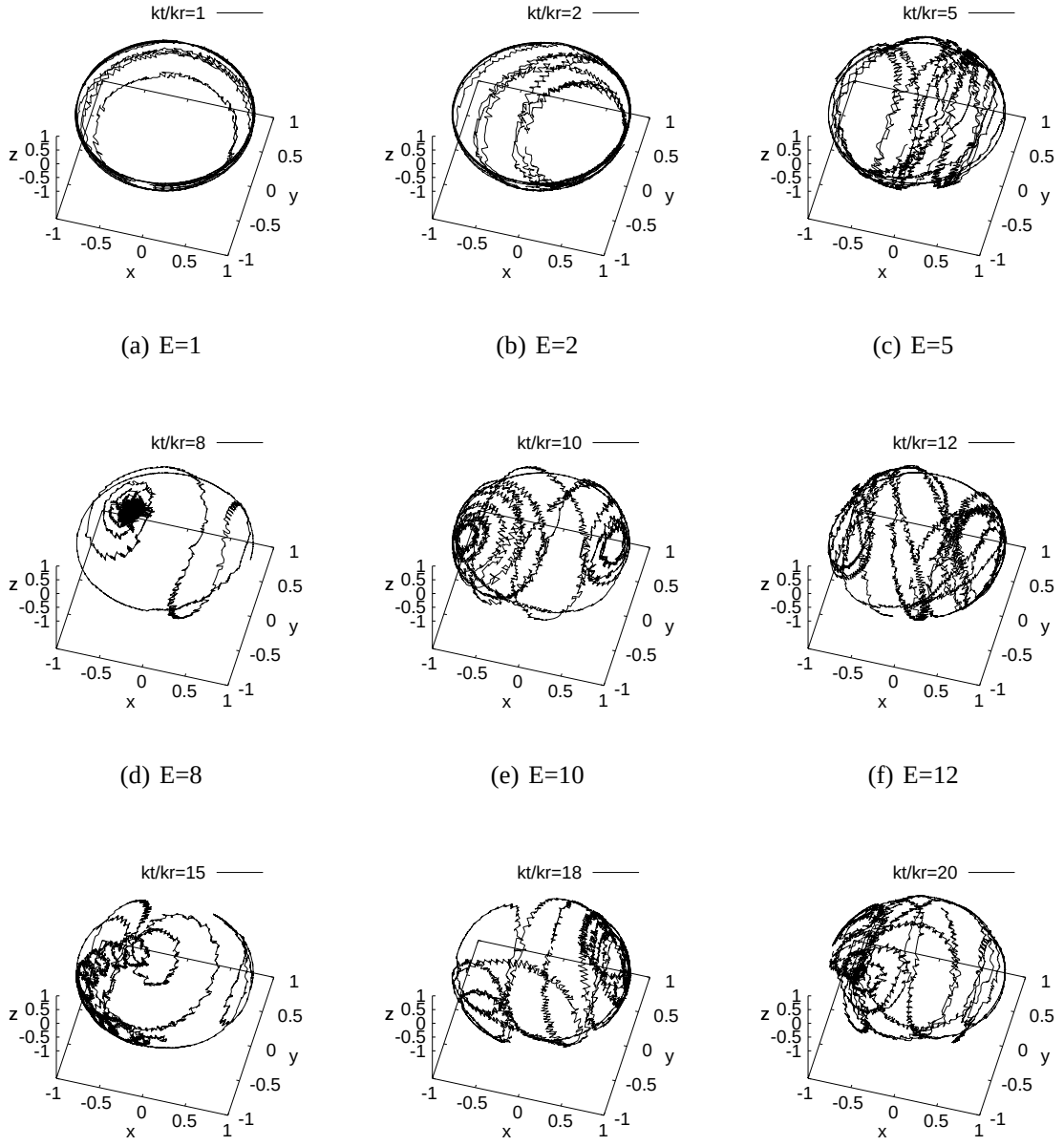

(a) E=1 (b) E=2 (c) E=5

(d) E=8 (e) E=10 (f) E=12

(g) E=15 (h) E=18 (i) E=20

Figure 7.10: *Orbit of the marker point on a neutrally buoyant ellipsoid with* $a : b : c = 1 : 0.7 : 0.7$ *in an inviscid fluid at different energy ratios* E*.*

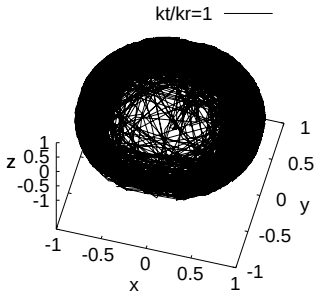

(a) E=1

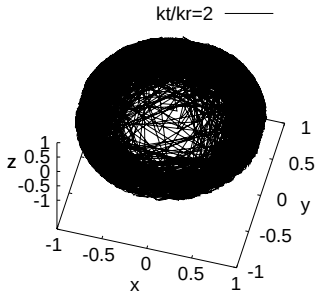

(b) E=2

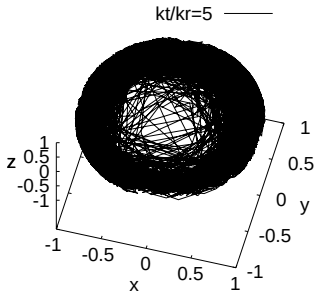

(c) E=5

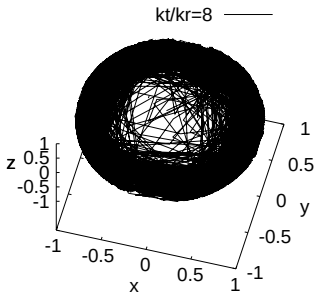

(d) E=8

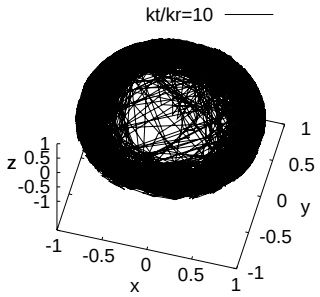

(e) E=10

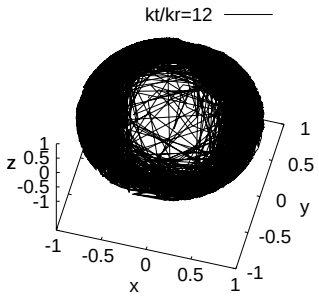

(f) E=12

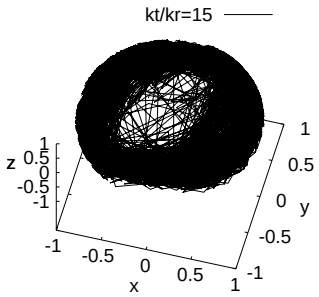

(g) E=15

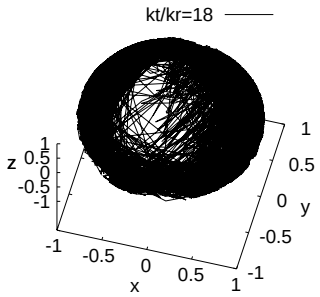

(h) E=18

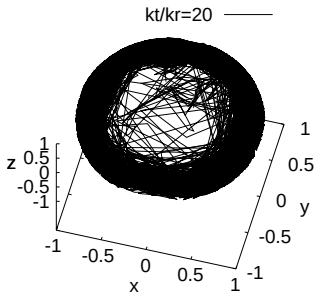

(i) E=20

Figure 7.11: *Orbit of the marker point on a neutrally buoyant sphere in an inviscid fluid at different energy ratios E.*

the solid centre), unlike ellipsoids.

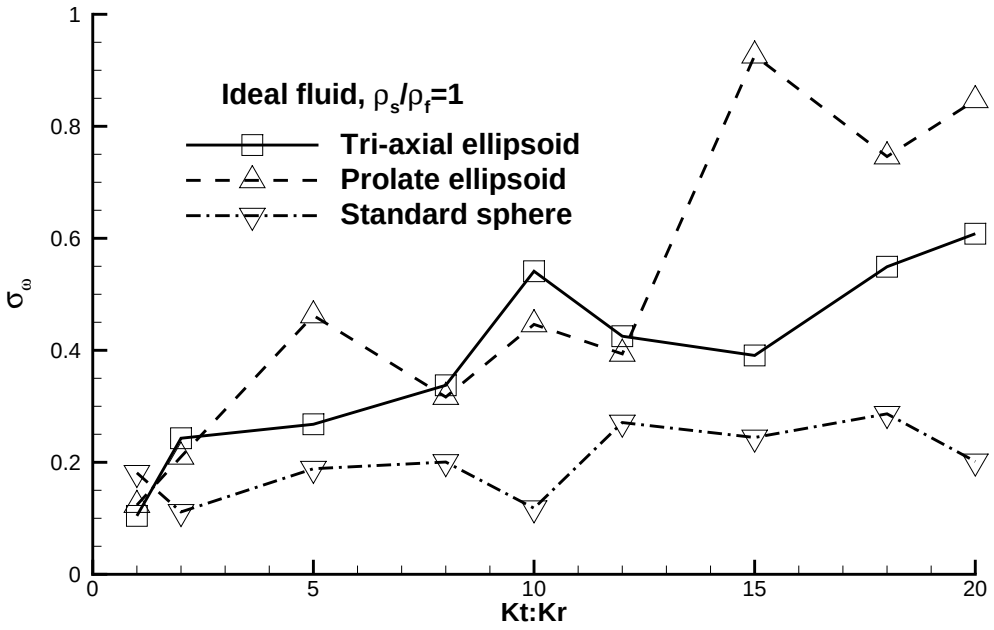

Figure 7.12: *The standard deviation of the angular velocity vector $\boldsymbol{\sigma_\Omega}$ against energy ratio, $E = k_t/k_r$, for cases with neutrally buoyant solids of different moving in the inviscid flow.*

Fig. 7.12 plots the σ_ω against E for simulations shown in Figs. 7.10 and 7.11. These figures show that very obviously a standard sphere exhibits the lowest chaotic behaviour (for the cases considered).

7.4 The Centroid Trajectory of The Solids Under Different Simulation Conditions

Fig. 7.14-7.17 show the trajectories of the solid centroids of all the aforementioned simulations in the global frame. These trajectories depict another point of view to observe the chaotic motion of the solid concerned. As is expected the centroid trajectories show a similar dependence with the energy ratio E as before. For the simulations with low Re_p (Fig .7.15(a)), the figure shows when the kinetic energy aspect ratio E gradually changes, the cen-

troid trajectory of the solids also develops gradually with apparently similar pattern, yet for simulations with inviscid flow (Fig .7.14), or very high Re_p (Fig .7.15(b)), it is difficult to conclude any similar pattern of the centroid trajectory for the solids with different initial E. The chaotic pattern is also reported for the denser solids (Fig .7.16) and prolate ellipsoid (Fig .7.17(a)), but cannot be found for the simulations of standard spheres (Fig .7.17(b)), which also agrees with the results in Section. 7.3.

7.5 Measuring Chaos by Lyapunov Exponent

The theoretical description of the solid motion in this chapter was given by Kirchhoff [67] and in terms of both linear velocity vector ($\mathbf{U}$) referred to the global coordinate system and angular velocity vector ($\mathbf{\Omega}$) referred to the local coordinate system:

$$\frac{d}{dt}\left(\frac{\partial k_{tot}}{\partial \mathbf{U}}\right) + \mathbf{\Omega} \times \frac{\partial k_{tot}}{\partial \mathbf{U}} = 0 \tag{7.8}$$

$$\frac{d}{dt}\left(\frac{\partial k_{tot}}{\partial \mathbf{\Omega}}\right) + \mathbf{\Omega} \times \frac{\partial k_{tot}}{\partial \mathbf{\Omega}} + \mathbf{U} \times \frac{\partial k_{tot}}{\partial \mathbf{U}} = 0 \tag{7.9}$$

Where k_{tot} is the total kinetic energy of the solid body and the surrounding fluid. Both $\mathbf{U}$ and $\mathbf{\Omega}$ are three dimensional and therefore Eq .7.8 and Eq .7.9 constitute a system of 6 coupled ordinary differential equations. A chaotic behaviour represented by the orientation the solid has been plotted and discussed in the previous sections. Hence in this section, the discussion focuses on the chaotic behaviour presented by the motion of the solid centroid.

A common definition for chaotic behaviour is, by introducing a slight disturbance to the initial condition, the result will become quite different and unpredictable. A measurement based on this description is:

$$\lambda_L = \lim_{\Delta t \to \infty} \frac{1}{\Delta t} \ln \frac{|\Delta \mathbf{x}(t_0 + \Delta t)|}{|\Delta \mathbf{x}(t_0)|} \tag{7.10}$$

where λ_L is the Lyapunov exponent [141]. In this study, $\Delta \mathbf{x}(t_0)$ is the difference of position of centroid at time t_0 for the two examined simulations in each group:

$$|\Delta \mathbf{x}(t_0)| = |\mathbf{x_1}(t_0) - \mathbf{x_2}(t_0)| \tag{7.11}$$

where:

$$\mathbf{x_1}(t_0) = (0, 0, 0) \quad \mathbf{x_2}(t_0) = (0.05, 0, 0) \tag{7.12}$$

$\Delta\mathbf{x}(t_0 + \Delta t)$ is the difference of position of centroid at time $t_0 + \Delta t$.

$$|\Delta\mathbf{x}(t_0 + \Delta t)| = |\mathbf{x_1}(t_0 + \Delta t) - \mathbf{x_2}(t_0 + \Delta t)| \tag{7.13}$$

Based on its definition, when $\lambda_L < 0$, the system turns to be damping and dissipative, when $\lambda_L = 0$, the system is conservative and in a steady state mode, and when $\lambda_L > 0$, the system is unstable and chaotic.

In this study, two identical group are chosen. In Group A, the flow is inviscid and E=20, and in Group B, $Re_p = 1000$ and E=20. Ideally the $|\Delta\mathbf{x}(t_0)|$ is expected to be infinite large and $|\Delta\mathbf{x}(t_0)|$ is expected to be infinite small. There are two set of simulation in each group, and the only difference between these two set is there initial centroid location (dimensionless), one is $(0, 0, 0)$ and the other one is $(0.05, 0, 0)$. The initial location difference is 5% of the characteristic length scale of the solid, which is consider to be reasonable "slight" initial disturbance. The λ_L is calculated for each group and plotted against the simulation time t.

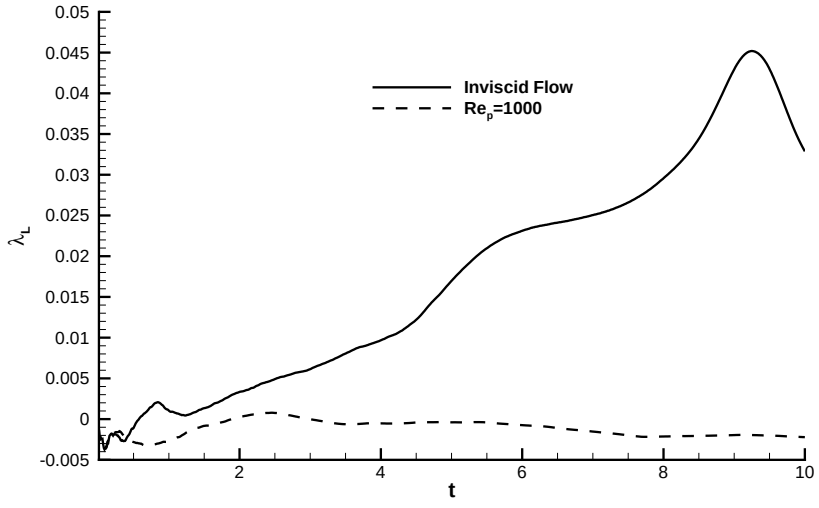

Figure 7.13: *Lyapunov exponent developing with simulation time. Solid line for inviscid flow and dash line for* $Re_p = 1000$.

In order to achieve a better approximation for the maximal Lyapunov exponent, Δt in Eq .7.10 is expected to be infinite large, which is however impractical to achieve in either experiments or CFD simulations, therefore, the λ_L is plotted here against the evolution of the time t. The evolution of λ_L presented in Fig .7.13 leads to the same conclusion as discussed before. When the flow is inviscid, $\lambda_L > 0$ and the system appears to be chaotic, and when $Re_p = 1000$, $\lambda_L < 0$ and the motion of both solid and fluid are damped by the viscous force.

The method to calculate λ_L has the similar form as the one suggested in Wolf's work [142] except the exponent was calculated by $\log_2$ in his work but by $\ln$ in Eq .7.10. Since the λ_L for the trajectory of the solid centroid is plotted against the evolution of the simulation time, it is unlikely to be false positive in this certain aspect. However, Rössler's study also suggested that this method is based on trajectory of only one fiducial variable but fails to take advantage of all the available data. Additional calculation of the Lyapunov spectrum with all affecting factors will provide a thorough observation of the chaotic behaviours of the solids and make more reliable judgements.

It is necessary to point out that in order to quantify the overall chaotic behaviour of the system, a set of Lyapunov spectrum with all dimension in the system need to be considered, which requires a huge amount of calculation. However the purpose of this section is to provide an qualitative evidence of the chaos, which can be satisfied by a single positive Lyapunov characteristic exponent. The scale of maximal λ_L of the examples listed in Rosenstein's studies [143] varies from 0.09 to 1.5, where ours is about 0.05. In the references, $\lambda_L = 1.5$ comes from Lorenz's study [144] of turbulence flow modelling and $\lambda_L = 0.09$ comes from Rössler's study [145] of continuous chaos after Lorenz's work. The governing equations of both Lorenz and Rössler's study are modelled from the Navier-Stokes equations in order to study the chaotic behaviour of the flow as this chapter. However, as indicated before, the Lyapunov characteristic exponent provided in this section is not the maximal one, therefore comparing their absolute value has no significant meaning until the full Lyapunov spectrum is calculated and the maximal Lyapunov exponent is obtained in the further work.

7.6 Conclusion

In this chapter, our study was extended to the possible chaotic motion of a general ellipsoid under the influence of a point vortex. The GISS implementation was firstly validated against the Aref problem [10]. It is confirmed that the energy ratio $E = k_t/k_r$ plays an important role in the chaotic motion of the solid through fluid. When E is relatively small, the particle motion tends to be regular circular orbit dictated by the point vortex - this is more demonstrated for viscous fluids. The degree of chaos increases with increasing E. Our simulations show that increasing fluid viscosity or solid density plays a strong role in dampening chaos. The result also shows that departure from a spherical geometry also increases chaos.

It is necessary to mention that a low σ_Ω is merely a sufficient condition yet not a necessary condition, which means a low σ_Ω will indeed represent the case with less chaotic pattern, but a high σ_Ω may not necessary represent a chaotic case, for example, periodic motion. Therefore a better approach to describe the chaotic properties of these simulations will be part of the future work.

In this study, for Re_p=1000, since gradually developing pattern is observed, the non-chaotic motion is confirmed. For inviscid flow case, comparing to Re_p=1000, there are more confidences to declare that is chaotic. A study with less differed initial conditions will help to define the chaotic pattern better in the future work. For Re_p=100000, turbulence may also contribute to the chaotic motion of the solid, yet the mesh is probably not resolving turbulent vortices with the current mesh resolution, therefore a further study will help to locate the actual threshold of the chaotic motion.

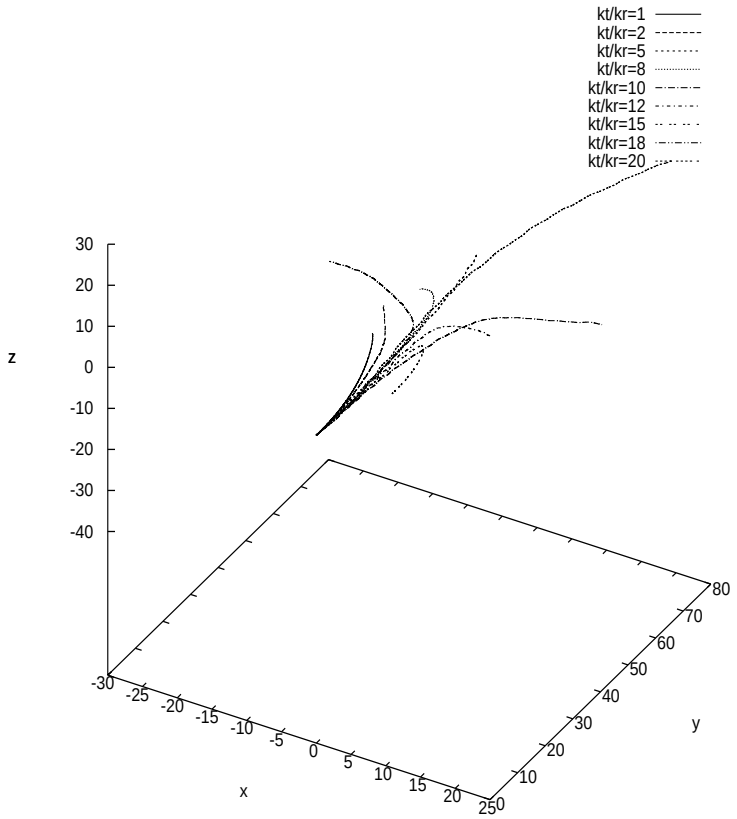

Figure 7.14: *The centroid trajectory of the solids,* $a : b : c = 1 : 0.8 : 0.6$*,* $\rho_s/\rho_f = 1$*, inviscid fluid.*

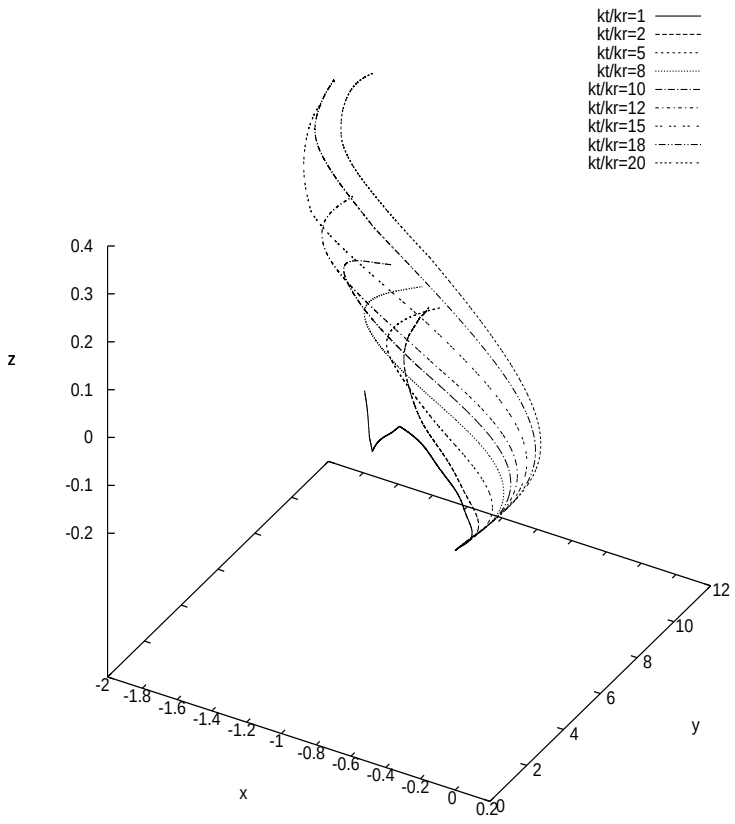

(a) $Re_p = 1000$

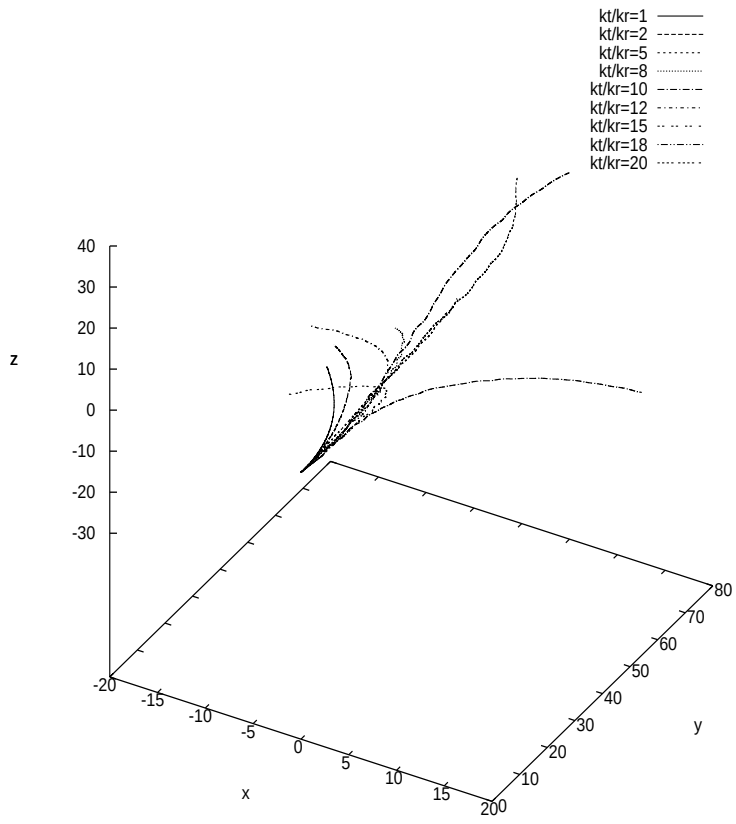

(b) $Re_p = 100000$

Figure 7.15: *The centroid trajectory of the solids,* $a : b : c = 1 : 0.8 : 0.6$*,* $\rho_s/\rho_f = 1$*,* $\rho_s/\rho_f = 1$*, at different* Re_p*.*

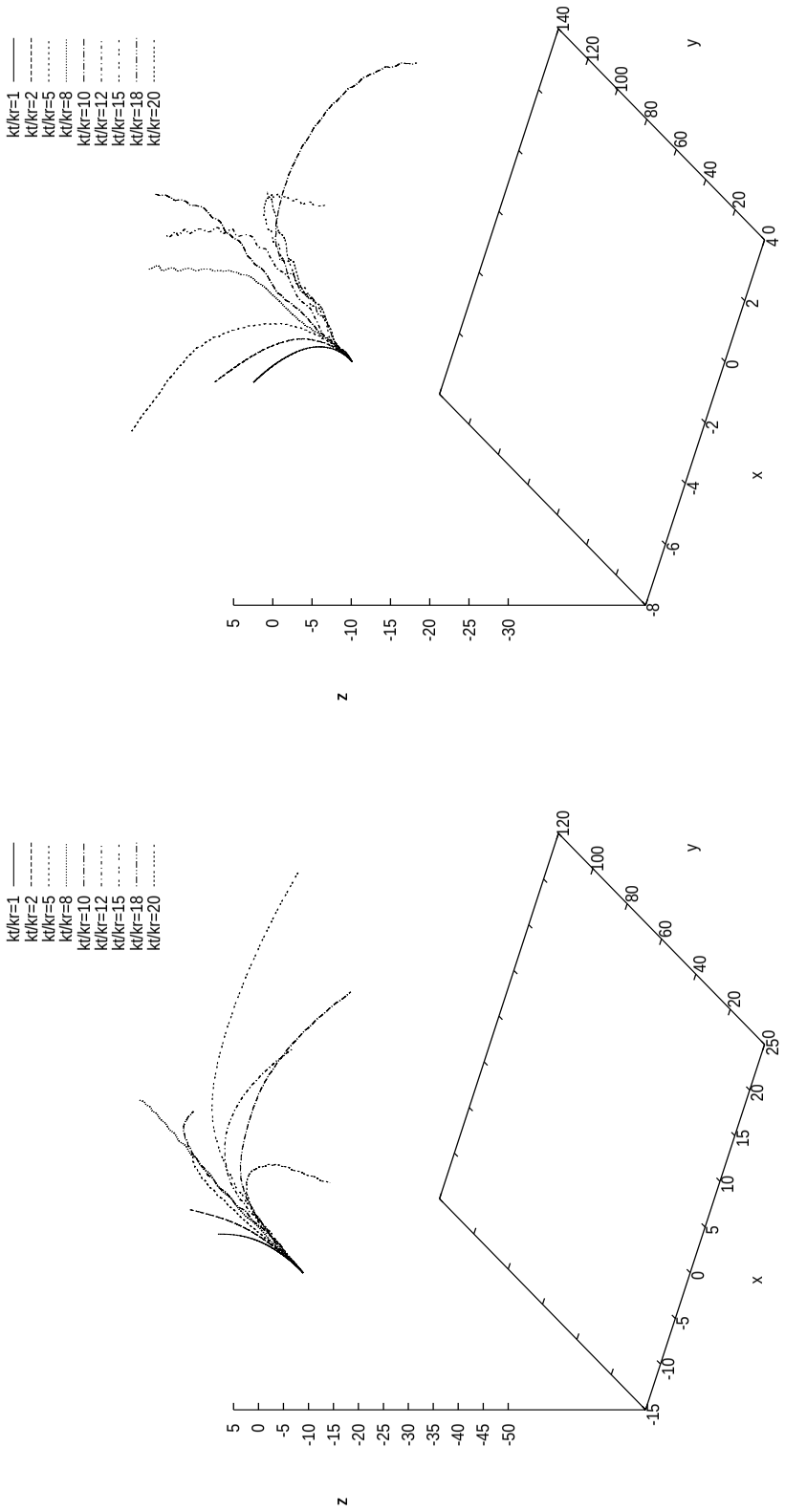

(a) $\rho_s/\rho_f = 2$ (b) $\rho_s/\rho_f = 3$

Figure 7.16: *The centroid trajectory of the solids,* $a : b : c = 1 : 0.8 : 0.6$*, inviscid fluid, with different density ratio.*

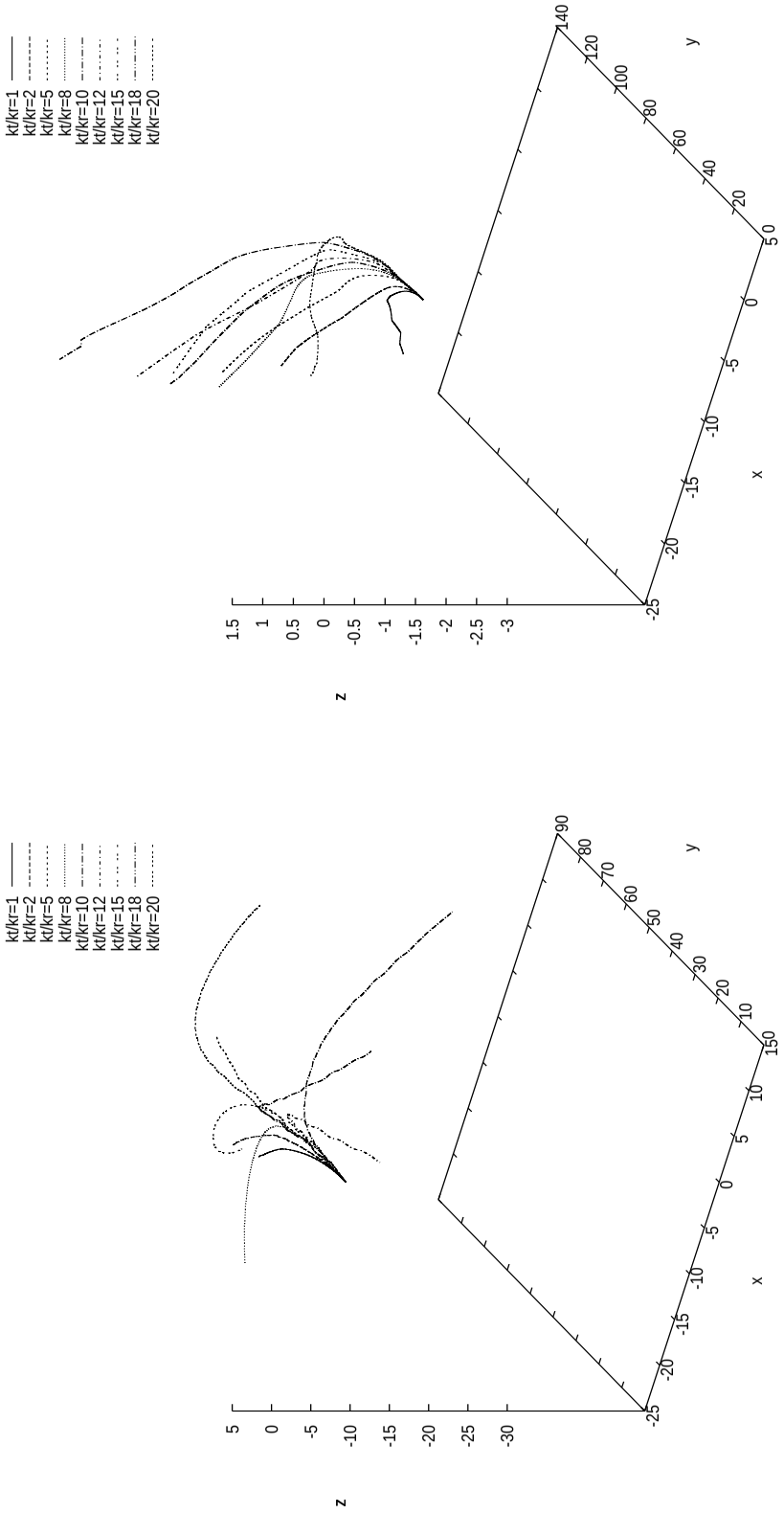

(a) $a : b : c = 1 : 0.7 : 0.7$

(b) $a : b : c = 1 : 1 : 1$

Figure 7.17: *The centroid trajectory of the solids, $\rho_s/\rho_f = 1$, inviscid fluid, with different geometry.*

Chapter 8
Conclusions and Recommendations for Future work

8.1 Conclusions

In this thesis work, a bespoke and a novel 3D DNS solver for solid-fluid flows called the Gerris Immersed Solid Solver (GISS) has been developed. The solver allows for arbitrary number of solids, arbitrary solid geometries, 6DOF motions of solids and complete resolution of coupled solid-fluid interactions. The solver adopts a novel variant of immersed boundary method and allows for dynamic Quad/Oct-tree structured mesh adaptation. This mesh adaptation technique is highly efficient and robust comparing to the conventional dynamic mesh adaptation method. The GISS comprises a solid motion subsolver and a fluid subsolver based on Gerris. While the fluid subsolver is optimised for full parallelisation, the solid motion subsolver is not (parallelising the solid motion subsolver is beyond the scope of this work). The thesis focusses on the rigorous validation of the GISS with key theoretical and experimental results involving translational and rotational motions of solids under flow. First, GISS is validated against cases where only one of these motions is dominant. Then the Solver is validated against cases where both motions are important, which is the full test of the 6DOF capability. The thesis also reports on high resolution DNS results revealing new hydrodynamic behaviour of solid-fluid flows - especially as a function of geometry, initial conditions and boundary layer development. The solver is targeted to be opensourced in February 2015.

Refer to the research target enumerated in Section .1.2, this thesis work has revealed:

1. Chapter. 4 validates the GISS for translational motion of single solids. Key tests include those against theory (Stokes' law and its variants), experiments measuring the drag coefficient on a fixed sphere and the settling velocity of spheres. The validation

tests considered cover a wide range of Re_p from 0.1 to 1000. The results obtained from GISS agreed not only in Stokes' flow regime, but also with experiments performed in transition regime. The drag force composition was investigated in detail and benchmark numerical parameters such as mesh resolution, mesh adaptation and timestep size were obtained. These benchmark values ensure correct imposition of no-slip and no-penetration boundary conditions on the walls of immersed solids and avoid miscalculation of the viscous stress tensor around the immersed solid.

2. The first section Chapter. 5 validates the GISS for rotational motion of single solids. The results from GISS (in 6DOF mode) agreed with the theoretical predictions of the Jeffery's orbits [14] for low Re_p. The rotation periods of ellipsoids at moderate Re_p ($1 \sim 100$) also agree with LBM simulation results [38]. The GISS simulations showed that for prolate ellipsoids, the rotation period increased smoothly with increasing Re_p in agreement with expectations. Though GISS performed well with moderately oblate ellipsoids, highly oblate ellipsoids demonstrated numerical vibrations (wobbling) which reduced with increased mesh resolution but making the computation very expensive. The problem was alleviated by switching off the translational DOF. However, the obtained rotation results for the oblate ellipsoids still agreed well with the theory and LBM simulation results: The GISS predictions of rotational period agree with Jeffery's orbits theorem at low Re_p and the solver also predicts that rotation period tends to infinite at a critical Re_P around 80.

3. In the second section Chapter. 5, the rigorous validation of the GISS against key theories and experiments for translational and rotational solid motion was utilized together towards exploiting the solver's capabilities towards understanding cases where both rotational and translational motions are dominant. These include Hsu and Ganatos' study [11] on wall-solid interactions. The GISS results demonstrated a very good agreement with the predicted lift forces near the wall at the limit of zero Re_p. The solver also demonstrated the effect of solid geometry on wall-solid interactions for the first time. The results showed that while a standard sphere has the poorest migration (both in the horizontal and vertical directions, a thinner ellipsoid exhibits an enhanced horizontal migration. The results also demonstrate an optimum geometry solid geometry (between

that of a sphere and a thin ellipsoid) for highest vertical migration near the wall.

4. Chapter. 6 reports how GISS uses all the features validated (i.e. translation, rotation, migration) in Chapters. 4 and 5 to understand hydrodynamic interactions between a pair of solids, revealing several phenomena for the first time.

   - Hydrodynamic interaction between the solids during shear flow can lead towards either hydrodynamic attraction or repulsion, based on the initial placement. The interaction force is a strong function of distance between the solids, geometry of the solids, and the Re_p.
   - When the distance between the solids is below a critical distance (around twice the boundary layer thickness) there is almost no flow between the solids and most flow is directed around both the solids. This eventually results in twin-solid system to be engulfed in one vortex leading to clustering (hydrodynamic attraction).
   - When the solids are placed at greater distances, flow from outside is able to easily pass into the gap between the solids and generates a vortex counter-rotating to the solids. This results in separation (hydrodynamic repulsion).
   - The current hypothesis suggests that the threshold solid distance of the aforementioned phenomena corresponds to the boundary layer thickness. It is observed that with growing Re_p that solids need to be closer to trigger the hydrodynamic attraction.

5. While all previous studies mostly concerned with low Re_p, Chapter. 7 focusses on the possible chaotic motion of solid under inviscid or high Re_p flow, as predicted by Aref [10]. The GISS Simulations reveal that energy ratio, E, between rotational and translational energies plays a critical role in triggering chaotic motion of solid through fluid. The simulation results also revealed that the solid motion tends to be regular when E is relatively small and that propensity for the solid to exhibit chaos increases with E. The simulations also showed the damping effect of viscosity on the chaotic motion of solid when $Re_p = 1000$. It is also revealed that chaos is also a strong function of geometry - chaos increases as geometries are more and more non-spherical.

The rigorous analysis of above studies demonstrates that the GISS is capable enough to handle complex problems concerning multiple immersed solids of arbitrary shape and number. Already there have been more than 12 pre-release requests over the past two-years from researchers in this field, indicating a growing need for such rigorous DNS solver suites. As mentioned, GISS is due to be released with an open source public license in February 2015.

8.2 Recommendations for Future Work

As mentioned earlier, the base frame of GISS, Gerris flow solver, supports extensive parallelisation. However, the immersed solid solver is not yet compatible for parallelisation. Thus, one extension of the GISS in plain sight is the full parallelisation of the GISS. This is essential in-order to access high grid resolutions necessary at high Reynolds number and also when handling flows with high solid volume fraction - such as slurries. Given that GISS does not require an individual mesh for the solid - both solid and fluid phases are described by the same variables - the most difficult technical problem concerns with processing the solid governing equations in parallel alongside flow equations. An idea may be to pre-allocate and segregate processors for fluid and for solid computation, with data gathering at each timestep on a mother processor. However - this would need extensive optimisation towards improving performance of the solver.

Besides, the collision model between the solids can also extend the application range of GISS. In the cases being studied so far, the hydrodynamic interaction between solids prevents collisions to happen. However, for some cases in Chapter. 6 simulations has to be stopped before collisions happen. One option to solve this problem is by introducing the collision models, like one presented by Glowinski [100] in the GISS. Theoretically, GISS has no additional limitation for the numbers of solid particles except the computational resources, with proper collision models added and the the calculation simplified, the GISS is expected to be able to handle simulations involving 6DOF motion of thousands of solid particles.

The flexibility of solid description in GISS also allows the further study on the deformable solids. Actually, during the development of the current GISS, significant effort was made to apply proper constraint to maintain the solid to be rigid. With a proper predefined deforming

rules, the GISS can simulate solids both moving and deforming simultaneously. This is a very essential feature that make the study of complex fluids with deformable solids (such as red blood cells in plasma) possible.

The GISS can also be extended to account for effects of heat transport - this is particularly useful to study the behaviour of micro-PIV particles in highly confined systems such as heated capillaries or sessile droplets. This is also important for systems where thermal gradients in solid-fluid suspensions induce separation based on particle properties. Preliminary testing of such systems in GISS has already shown promise.

Besides, the current studies of the hydrodynamic attraction/repulsion between solids and the solid chaotic motion in viscid flow are still in a relatively preliminary stage, more validation will help to quantify and analysis the detail mechanism of those phenomenons.

Appendix A
Derivation of Stokes' Law

Stokes' Law is the fundamental formulation describing forces over a settling particle. There are many ways to derive it, here it is derived by using stream functions. Consider a sphere, with radius R, located in an incompressible fluid with dynamic viscosity μ, density ρ, and an attack velocity U_0 from "far field'. When its particle Reynolds number is very small:

$$Re_p = \frac{2\rho U_0 R}{\mu} \ll 1 \tag{A.1}$$

The momentum equation of the incompressible governing equations of flow:

$$\rho\left(\frac{\partial \mathbf{u}}{\partial t} + \mathbf{u}\cdot\nabla\mathbf{u}\right) = -\nabla p + \mu\nabla^2\mathbf{u} \tag{A.2}$$

can be simplified by neglecting the advective inertial forces in Stokes' flow regime:

$$-\nabla p + \mu\nabla^2\mathbf{u} = 0 \tag{A.3}$$

Define a stream function $\Psi(r,\theta)$ under the spherical coordinate system:

$$u_r = \frac{1}{r^2\sin\theta}\frac{\partial\Psi}{\partial\theta} \tag{A.4}$$

$$u_\theta = -\frac{1}{r\sin\theta}\frac{\partial\Psi}{\partial r} \tag{A.5}$$

And rewrite Eq. A.3 with Eq. A.4:

$$\frac{\partial p}{\partial r} = \frac{\mu}{r^2\sin\theta}\frac{\partial(\Upsilon\Psi)}{\partial\theta} \quad , \quad \frac{\partial p}{\partial\theta} = -\frac{\mu}{r\sin\theta}\frac{\partial(\Upsilon\Psi)}{\partial r} \tag{A.6}$$

where Υ is differential operator defined as:

$$\Upsilon = \frac{\partial^2}{\partial r^2} + \frac{\sin\theta}{r^2}\frac{\partial}{\partial\theta}\left[\frac{1}{\sin\theta}\frac{\partial}{\partial\theta}\right] \tag{A.7}$$

Eliminating p between two momentum equations in Eq. A.6:

$$\Upsilon^2\Psi = 0 \tag{A.8}$$

Eq. A.8 can be solved by including the boundary condition:

$$u_r = 0, \qquad u_\theta = 0, \qquad \text{at solid surface} \tag{A.9}$$

$$u_r = U_0\cos\theta, \quad u_\theta = -U_0\sin\theta, \quad \text{at "far field"} \tag{A.10}$$

Therefore the analytical stream function for Stokes flow is:

$$\Psi(r,\theta) = U_0\left[\frac{R^3}{4r} - \frac{3Rr}{4} + \frac{r^2}{2}\right]\sin^2\theta \tag{A.11}$$

and the solution for the fluid variables are:

$$u_r = U_0\left[\frac{R^3}{2r^3} - \frac{3R}{2r} + 1\right]\cos\theta \tag{A.12}$$

$$u_\theta = U_0\left[\frac{R^3}{4r^3} + \frac{3R}{4r} - 1\right]\sin\theta \tag{A.13}$$

$$p = -\left[\frac{3R\mu U_0}{2r^2}\right]\cos\theta \tag{A.14}$$

In the calculation, p is the normal stress and the shear stress is:

$$\tau_{r\theta} = -\mu\left[r\frac{\partial}{\partial r}\left(\frac{u_\theta}{r}\right) + \frac{1}{r}\left(\frac{\partial u_r}{\partial\theta}\right)\right] \tag{A.15}$$

And then force applied on the sphere can be then integrated:

$$F_{pressure} = 2\pi R^2\int_0^\pi p\sin\theta\cos\theta\mathrm{d}\theta = 2\pi R\mu U_0 \tag{A.16}$$

$$F_{shear} = 2\pi R^2\int_0^\pi \tau_{r\theta}\sin^2\theta\mathrm{d}\theta = 4\pi R\mu U_0 \tag{A.17}$$

The overall drag applied on the sphere, known as Stokes' Law, which is:

$$F_d = F_{pressure} + F_{shear} = 6\pi R\mu U_0 \tag{A.18}$$

And therefore the terminal settling velocity of a solid sphere with density ρ_s can be obtained based on the balance among the buoyancy, gravity and drag:

$$U_t = \frac{2(\rho_s - \rho_f)gR^2}{9\mu} \tag{A.19}$$

Appendix B

Derivation of Jeffrey Equation

This brief derivation for simplified cases of this thesis has been provided by Gavze [146], the complete version can be found in Jeffrey's original work [14]. Considering an ellipsoid, with half major c, half minor a, rotational symmetric to the major axis, and the geometric aspect ratio ε. The rotation equation in an inertial coordinate system is:

$$\frac{\mathrm{d}}{\mathrm{d}t}(\mathbf{I}\cdot\boldsymbol{\Omega}) = -\nu\boldsymbol{\Theta}\cdot\boldsymbol{\Omega} + \nu\mathbf{N} \tag{B.1}$$

Here $\mathbf{I}$ is the inertia tensor, $\boldsymbol{\Theta}$ is the rotation, ν is the kinematic viscosity, $\boldsymbol{\Omega}$ is the angular velocity and $\mathbf{N}$ is the torque applied on the particle by the fluid. The advective inertial forces can be neglected when the particle Reynolds number is very small that allow the simplification on Eq. B.1:

$$\boldsymbol{\Omega} = \boldsymbol{\Theta}^{-1}\mathbf{N} \tag{B.2}$$

The torque $\mathbf{N}$ acting on a solid immersed in a flow is given by:

$$\mathbf{N} = \boldsymbol{\Theta}\cdot\hat{\mathcal{L}}\cdot(\hat{\mathcal{D}}\times\mathbf{u}) \tag{B.3}$$

where $\hat{\mathcal{L}}$ is a linear operator and $\hat{\mathcal{D}}$ is a first-order differential operator, both of which depend on the particle geometry. $\mathbf{u}$ is the fluid velocity field. Combining Eq. B.2 and B.3 leads to

$$\boldsymbol{\Omega} = \mathcal{L}\cdot\mathbf{g} \quad , \quad \mathbf{g} = (\mathcal{D}\times\mathbf{u}) \tag{B.4}$$

It is convenient to normalize the operator $\hat{\mathcal{L}}$ and $\hat{\mathcal{D}}$ with respect to the half major c:

$$\mathcal{L} = c^2\hat{\mathcal{L}} \quad , \quad \mathcal{D} = \frac{1}{c^2}\hat{\mathcal{D}} \tag{B.5}$$

Define the body coordinate system (x', y', z') whose z' axis is parallel to the major axis. In such coordinate system, there is a diagonal matrix $\mathcal{L}$ whose elements are:

$$\mathcal{L}'_{11} = \mathcal{L}'_{22} = \frac{1}{1+\varepsilon^2} \quad , \quad \mathcal{L}'_{33} = \frac{1}{2\varepsilon^2} \tag{B.6}$$

and for $\mathcal{D}$:

$$\mathcal{D}' = \bar{i}\varepsilon^2 \frac{\partial}{\partial x'} + \bar{j}\varepsilon^2 \frac{\partial}{\partial y'} + \bar{k}\frac{\partial}{\partial z'} \tag{B.7}$$

where $\bar{i}$, $\bar{j}$, $\bar{k}$ are unit vectors in the x', y', z' directions in the body coordinate system. Transforming $\mathcal{L}'$ back to the laboratory coordinate system with the coordinate transformation $\mathcal{A}$, i.e. $\mathcal{L} = \mathcal{A}\mathcal{L}'\mathcal{A}^T$ and noting that $\mathcal{A}_{i3} = x_i$ where $\mathbf{x}$ is the orientation vector of the solid major axis in the laboratory system. The following expression for $\mathcal{L}$ can be obtained in tensor form:

$$\mathcal{L}_{ij} = \frac{1}{1+\varepsilon^2}\delta_{ij} + \frac{1}{2\varepsilon^2}\frac{1-\varepsilon^2}{1+\varepsilon^2}x_i x_j \tag{B.8}$$

where δ_{ij} is the Dirac delta function. Substituting Eq. B.8 in Eq. B.4, the angular velocity $\mathbf{\Omega}$ of the solid can be then obtained:

$$\Omega_i = \frac{1}{1+\varepsilon^2}g_i + \frac{1}{2\varepsilon^2}\frac{1-\varepsilon^2}{1+\varepsilon^2}x_i x_j g_j \tag{B.9}$$

In the Jeffrey orbit case, the problem is restricted to linear flow fields determined by the gradient tensor $\mathbf{\Gamma}$:

$$u_i = \Gamma_{ij} x_j \tag{B.10}$$

The tensor Γ_{ij} can be decomposed into the symmetric strain tensor Γ^s_{ij} and the antisymmetric rotation tensor Γ^r_{ij}, therefore:

$$\Gamma^S_{ij} = \frac{1}{2}\left[\Gamma_{ij} + \Gamma_{ji}\right] \tag{B.11}$$

$$\Gamma^R_{ik} = \frac{1}{2}\left[\Gamma_{ik} - \Gamma_{ki}\right] = \frac{1}{2}\epsilon_{ijk}\omega_j \tag{B.12}$$

where ω is the vorticity:

$$\omega_j = \epsilon_{ijk}\frac{\partial u_k}{\partial x_j} = \epsilon_{ijk}\Gamma^R_{kj} \tag{B.13}$$

To obtain g, $\mathcal{D}$ is represented in tensor form. In the body coordinate system:

$$\mathcal{D}'_n = \mathcal{M}'_{nj}\frac{\partial}{\partial x'_j} \quad , \quad \mathcal{M}'_{nj} = \varepsilon^2\delta_{nj} + (1-\varepsilon^2)\delta_{n3}\delta_{j3} \tag{B.14}$$

In the laboratory coordinate system:

$$\mathcal{D}_i = \mathcal{M}_{ik}\frac{\partial}{\partial x_k} \quad , \quad \mathcal{M}_{ik} = \varepsilon^2\delta_{ik} + (1-\varepsilon^2)x_i x_k \tag{B.15}$$

Then:

$$g_i = \varepsilon^2\omega_i + \epsilon_{ijk}(1-\varepsilon^2)\Gamma_{kn}x_j x_n \tag{B.16}$$

And together with Eq. B.9:

$$\frac{\mathrm{d}\mathbf{x}}{\mathrm{d}t} = \mathbf{\Omega}\times\mathbf{x} = \frac{1}{1+\varepsilon^2}\mathbf{g}\times\mathbf{x} \tag{B.17}$$

Eq .B.17 can be rewritten to Jeffrey equation after some manipulations:

$$\frac{\mathrm{d}x_i}{\mathrm{d}t} = \frac{1}{2}(\omega\times\mathbf{x})_i + \frac{1+\varepsilon^2}{1-\varepsilon^2}[\Gamma^S_{ij}x_j - x_j\Gamma^S_{jk}x_j x_k] \tag{B.18}$$

Eq. B.18 consists of two parts. The first two terms on the right-hand side of the equation change the orientation and the magnitude of the orientation vector. The third, nonlinear term, acts to restore the magnitude to unity. It is therefore convenient to write the right-hand side of the equation as a sum of the linear and the nonlinear parts:

$$\varsigma\frac{\mathrm{d}x_i}{\mathrm{d}t} = \mathcal{J}_{ij}x_j - x_i(x,\Gamma^S x) = g_i(x) \tag{B.19}$$

$$\mathcal{J}_{ij} = \Gamma^S_{ij} + \varsigma\Gamma^R_{ij} \tag{B.20}$$

$$\varsigma = \frac{1+\varepsilon^2}{1-\varepsilon^2} \tag{B.21}$$

Here x_i are the Cartesian coordinates of the symmetry (major) axis and its orbit motion around the solid centre is so called Jeffrey Orbit.

Appendix C

Derivation of Prandtl's Boundary Layer Equations Over a Solid

The Prandtl's Boundary Layer Equations (or the reduced Navier-Stokes equations under boundary-layer/lubrication approximation) [140] suggest that along the boundary layer, the advective term and diffusive term of the momentum equation (Eq. C.1) should with same order of magnitude:

$$\rho\left(\frac{\partial \mathbf{u}}{\partial t}+\mathbf{u}\cdot\nabla\mathbf{u}\right)=-\nabla p+\mu\nabla^2\mathbf{u} \tag{C.1}$$

For convenience, a 2D steady case is taken for example here. Rewrite Eq. C.1 along the normal and tangential direction of the boundary surface, there is:

$$u_n\frac{\partial u_t}{\partial x_n}+u_t\frac{\partial u_t}{\partial x_t}=-\frac{\partial p}{\partial x_n}+\nu\left(\frac{\partial^2 u_t}{\partial x_n^2}+\frac{\partial^2 u_t}{\partial x_t^2}\right) \tag{C.2}$$

Where the subnote t represents variables along the boundary direction and n represents

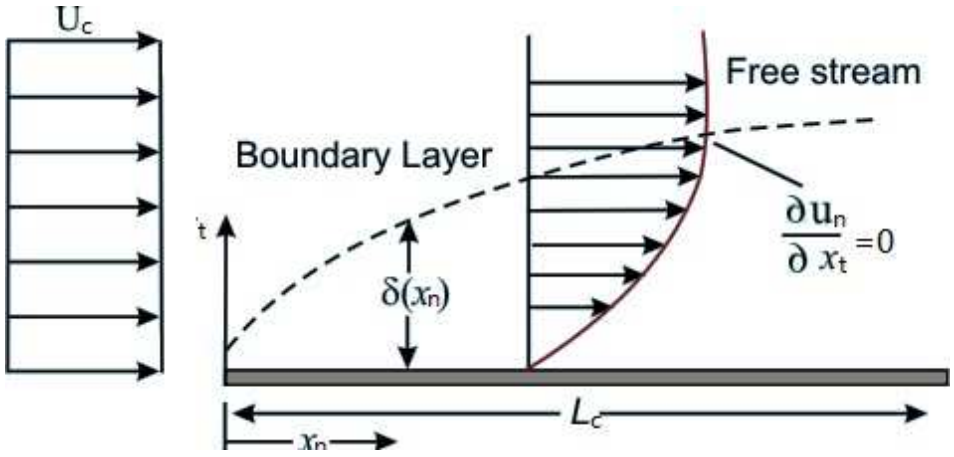

Figure C.1: *Boundary layer development.*

variables at the normal direction of the boundary. Given the characteristic velocity U_c, the

boundary layer δ_0 related to position L_c. Due to the definition of the boundary layer in Fig. C.1, there is:

$$O\left(u_t\frac{\partial u_t}{\partial x_t}\right) \sim O\left(\frac{U_c^2}{L_c}\right) \quad \text{from the second term in the left hand side of Eq. C.2} \tag{C.3}$$

and

$$O\left(\nu\frac{\partial^2 u_t}{\partial x_n^2}\right) \sim O\left(\nu\frac{U_c}{\delta_o^2}\right) \quad \text{from the third term in the right hand side of Eq. C.2} \tag{C.4}$$

Based on Eq. C.2, there is:

$$O\left(u_t\frac{\partial u_t}{\partial x_t}\right) \sim O\left(\nu\frac{\partial^2 u_t}{\partial x_n^2}\right) \tag{C.5}$$

Combining Eq. C.3, C.4, C.5:

$$O\left(\frac{U_c^2}{L_c}\right) \sim O\left(\nu\frac{U_c}{\delta_o^2}\right) \tag{C.6}$$

By rewriting Eq. C.3, the relation between the boundary layer thickness δ_c and the flow Reynolds number $Re_c(= U_c L_c/\nu)$ can be obtained:

$$\delta_c \sim O(\frac{1}{\sqrt{Re_c}}) \tag{C.7}$$

Appendix D
Migration of a Sphere in Poiseuille flow

This appendix shows a validation work comparing with Yu's distributed Lagrange multiplie (DLM) simulation work [139]. In this study, a sphere with radius a is settling in a vertical tube with radius $A = 4a$. A upward Poiseuille flow is applied in the tube, with maximum velocity U_m in the central of the tube and 0 at the tube wall, thus the velocity profile is defined by:

$$U(r) = U_m \left[1 - \left(\frac{r}{A}\right)^2\right] \tag{D.1}$$

Where r here is the distance to the central axis of the tube. The Pipe Reynolds number here is:

$$Re_f = \frac{\rho A U_m}{\mu} = 100 \tag{D.2}$$

The solid sphere is slightly denser than the fluid, therefore it will settle at the gravitational direction relative to the flow, its Stokes free-fall velocity U_t^* can be obtained from Eq .A.19. Here the supernote $*$ is used to indicate that it is a expected value, not the real settling velocity in the study.

A velocity ratio is defined by:

$$\lambda_v = \frac{U_t^*}{U_m} \tag{D.3}$$

And the solid density is expected to change with λ_v:

$$\rho_s = \frac{9\mu\lambda_v U_m}{2ga^2} + \rho_f \tag{D.4}$$

In this study, the sphere is released at $r/A = 0.4$ and its density is defined through λ_v. The mesh resolution $M = 16$ is suggested by the validation work in Chapter. 4. Cases of $\lambda_v = 0.1$, 0.2, 0.3, 0.4, 0.5 have been tested. For all cases expect $\lambda_v = 0.1$, our simulation results show a good agreement with Yu's result [139], and the GISS is able to successfully

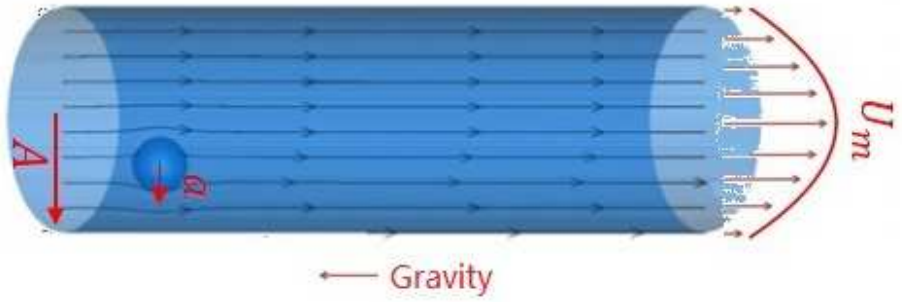

Figure D.1: *Simulation set up.*

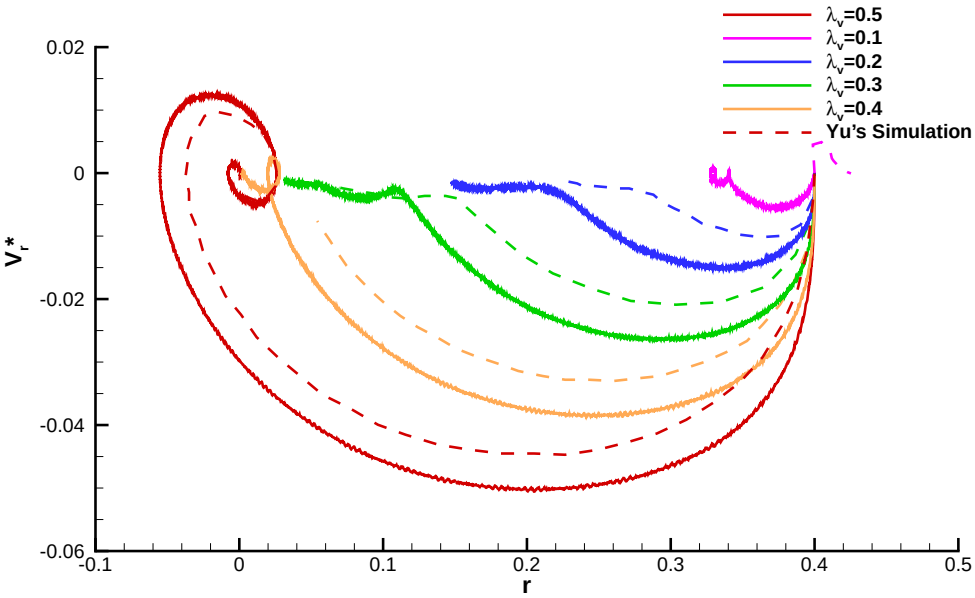

Figure D.2: *Radical migration velocity with different* λ_v.

capture the sphere revolution around tube axis (the curve for $\lambda_v = 0.5$ goes from $r > 0$ to $r < 0$ and then back to $r > 0$). This is yet another validation of GISS for cases where solids can both translate and rotate.

Appendix E
Publications and Research Outputs From This Thesis

1) P. Shui, S. Popinet and P. Valluri “Gerris Immersed Solid Solver (GISS) - A bespoke Solid-Fluid 3D DNS Solver,” to be distributed as OpenSource in February 2015.

2) P. Shui, S. Popinet, R. Govindarajan and P. Valluri “Chaotic motion of general ellipsoids in flows,” to be submitted to *Journal of Fluid Mechanics*.

3) P. Shui, P. Valluri, S. Popinet and R. Govindarajan, “Hydrodynamic interactions between two immersed solids,” to be submitted to *Physics of Fluids*.

4) P. Shui, S. Popinet, P. Valluri and R. Govindarajan, “Direct numerical simulation study of hydrodynamic interactions between immersed solids and wall during flow,” Accepted for IUTAM Proceedings, Hyderabad, India, 8-11 December, 2014.

5) P. Shui, S. Popinet, P. Valluri and R. Govindarajan, “Chaotic orbits tracked by a 3D asymmetric immersed solid at high Reynolds numbers using a novel Gerris-Immersed Solid (DNS) Solver,” 67th Annual Meeting of APS-DFD, San Francisco, California, 2325 November, 2014.

6) P. Shui and P. Valluri, “Solid particle migration in heated Couette flow,” First Therma POWER Symposium, Shanghai, China, 18-20 August, 2014.

7) P. Shui, S. Popinet and P. Valluri, “Direct Numerical Simulations of Solid-Fluid Flows Using a Variant of immersed boundary method in Gerris,” 66th Annual Meeting of APS-DFD, Pittsburgh, Pennsylvania, 24-26 November, 2013.

8) P. Shui, “6 degrees-of-freedom solid-fluid solver with immersed boundary method,” ChemEngDayUK 2013, London, UK, 25-26 March, 2013.

9) P. Shui, S. Popinet, P. Valluri, S. Zaleski and M. Crapper, “Solid-Fluid flows using a variant of Immersed Boundary method in Gerris,” 65th Annual Meeting of APS-DFD, San Diego, California, 18-20 November, 2012.

References

[1] S. SPT Group, "Olga solids management." Online publishment.

[2] Z. Wang, J. Fan, and K. Luo, "Combined multi-direct forcing and immersed boundary method for simulating flows with moving particles," *International Journal of Multiphase Flow*, vol. 34, no. 3, pp. 283–302, 2008.

[3] T. Krüger, M. Gross, D. Raabe, and F. Varnik, "Crossover from tumbling to tank-treading-like motion in dense simulated suspensions of red blood cells," *Soft Matter*, vol. 9, no. 37, pp. 9008–9015, 2013.

[4] C. Roy, "Discretization error." Workshop, May / June 2012.

[5] R. Hsu and P. Ganatos, "The motion of a rigid body in viscous fluid bounded by a plane wall," *Journal of Fluid Mechanics*, vol. 207, pp. 29–72, 1989.

[6] F. Lucci, A. Ferrante, and S. Elghobashi, "Modulation of isotropic turbulence by particles of taylor length-scale size," *Journal of Fluid Mechanics*, vol. 650, pp. 5–55, 2010.

[7] J. Roenby and H. Aref, "Chaos in body-vortex interactions," *Royal Society of London Proceedings Series A*, vol. 466, pp. 1871–1891, 2010.

[8] F. W. Roos and W. W. Willmarth, "Some experimental results on sphere and disk drag," *AIAA Journal*, vol. 9, no. 2, pp. 285–291, 1971.

[9] N. Mordant and J.-F. Pinton, "Velocity measurement of a settling sphere," *The European Physical Journal B-Condensed Matter and Complex Systems*, vol. 18, no. 2, pp. 343–352, 2000.

[10] H. Aref and S. W. Jones, "Chaotic motion of a solid through ideal fluid," *Physics of Fluids A: Fluid Dynamics (1989-1993)*, vol. 5, no. 12, pp. 3026–3028, 1993.

[11] R. Hsu and P. Ganatos, "Gravitational and zero-drag motion of a spheroid adjacent to an inclined plane at low reynolds number," *Journal of Fluid Mechanics*, vol. 268, pp. 267–292, 1994.

[12] A. Askounis, K. Sefiane, V. Koutsos, and M. E. Shanahan, "The effect of evaporation kinetics on nanoparticle structuring within contact line deposits of volatile drops," *Colloids and Surfaces A: Physicochemical and Engineering Aspects*, vol. 441, pp. 855–866, 2014.

[13] S. Popinet, "Gerris: a tree-based adaptive solver for the incompressible euler equations in complex geometries," *Journal of Computational Physics*, vol. 190, no. 2, pp. 572–600, 2003.

[14] G. B. Jeffery, "The motion of ellipsoidal particles immersed in a viscous fluid," *Proceedings of the Royal Society of London. Series A, Containing papers of a mathematical and physical character*, vol. 102, no. 715, pp. 161–179, 1922.

[15] G. G. Stokes, *On the effect of the internal friction of fluids on the motion of pendulums*, vol. 9. Pitt Press, 1851.

[16] H. Lamb, *Hydrodynamics*. Cambridge university press, 1993.

[17] L. G. Leal, *Advanced transport phenomena: fluid mechanics and convective transport processes*. Cambridge University Press, 2007.

[18] R. W. Fox, A. T. McDonald, and P. J. Pritchard, *Introduction to fluid mechanics*, vol. 5. John Wiley & Sons New York, 1998.

[19] D. B. Dusenbery, *Living at micro scale: the unexpected physics of being small*. Harvard University Press, 2009.

[20] B. J. Kirby, *Micro-and nanoscale fluid mechanics: transport in microfluidic devices*. Cambridge University Press, 2010.

[21] L. E. Payne and W. H. Pell, "The stokes flow problem for a class of axially symmetric bodies," *Journal of Fluid Mechanics*, vol. 7, no. 04, pp. 529–549, 1960.

[22] H. A. Lorentz, "A general theorem concerning the motion of a viscous fluid and a few consequences derived from it.," in *Abhandl.Theor.Phys.*, vol. 1, (Leibzig), 1907.

[23] H. Brenner, "The slow motion of a sphere through a viscous fluid towards a plane surface," *Chemical Engineering Science*, vol. 16, no. 3, pp. 242–251, 1961.

[24] A. J. Goldman, R. G. Cox, and H. Brenner, "Slow viscous motion of a sphere parallel to a plane wall motion through a quiescent fluid," *Chemical Engineering Science*, vol. 22, no. 4, pp. 637–651, 1967.

[25] R. G. Cox and H. Brenner, "The slow motion of a sphere through a viscous fluid towards a plane surfacei small gap widths, including inertial effects," *Chemical Engineering Science*, vol. 22, no. 12, pp. 1753–1777, 1967.

[26] W. L. Haberman and R. M. Sayre, "Motion of rigid and fluid spheres in stationary and moving liquids inside cylindrical tubes," tech. rep., DTIC Document, 1958.

[27] E. Y. Harper and I.-D. Chang, "Maximum dissipation resulting from lift in a slow viscous shear flow," *Journal of Fluid Mechanics*, vol. 33, no. 02, pp. 209–225, 1968.

[28] L. G. Leal, "The slow motion of slender rod-like particles in a second-order fluid," *Journal of Fluid Mechanics*, vol. 69, no. 02, pp. 305–337, 1975.

[29] G. I. Taylor, "Experiments on the motion of solid bodies in rotating fluids," *Proceedings of the Royal Society of London. Series A, Containing Papers of a Mathematical and Physical Character*, vol. 104, no. 725, pp. 213–218, 1923.

[30] G. I. Taylor, "The motion of ellipsoidal particles in a viscous fluid," *Proceedings of the Royal Society of London. Series A*, vol. 103, no. 720, pp. 58–61, 1923.

[31] G. Segre, "Radial particle displacements in poiseuille flow of suspensions," *Nature*, vol. 189, pp. 209–210, 1961.

[32] H. L. Goldsmith and S. G. Mason, "Axial migration of particles in poiseuille flow," *Nature*, vol. 190, pp. 1095–1096, 1961.

[33] A. Karnis, H. L. Goldsmith, and S. G. Mason, "Axial migration of particles in poiseuille flow," *Nature*, vol. 200, pp. 159–160, 1963.

[34] J. Feng and D. D. Joseph, "The unsteady motion of solid bodies in creeping flows," *Journal of Fluid Mechanics*, vol. 303, pp. 83–102, 1995.

[35] J. Feng, P. Y. Huang, and D. D. Joseph, "Dynamic simulation of the motion of capsules in pipelines," *Journal of Fluid Mechanics*, vol. 286, pp. 201–227, 1995.

[36] E.-J. Ding and C. K. Aidun, "The dynamics and scaling law for particles suspended in shear flow with inertia," *Journal of Fluid Mechanics*, vol. 423, pp. 317–344, 2000.

[37] Z. Yu, N. Phan-Thien, and R. I. Tanner, "Rotation of a spheroid in a couette flow at moderate reynolds numbers," *Physical Review E*, vol. 76, no. 2, p. 026310, 2007.

[38] H. Huang, X. Yang, M. Krafczyk, and X.-Y. Lu, "Rotation of spheroidal particles in couette flows," *Journal of Fluid Mechanics*, vol. 692, pp. 369–394, 2012.

[39] A. J. C. Ladd, "Numerical simulations of particulate suspensions via a discretized boltzmann equation. part 1. theoretical foundation," *Journal of Fluid Mechanics*, vol. 271, pp. 285–309, 1994.

[40] A. J. C. Ladd, "Numerical simulations of particulate suspensions via a discretized boltzmann equation. part 2. numerical results," *Journal of Fluid Mechanics*, vol. 271, pp. 311–339, 1994.

[41] C. K. Aidun, Y. Lu, and E.-J. Ding, "Direct analysis of particulate suspensions with inertia using the discrete boltzmann equation," *Journal of Fluid Mechanics*, vol. 373, pp. 287–311, 1998.

[42] S. Wakiya, "Effect of a submerged object on a slow viscous flow," *Res Rep Fac Eng Niigata Univ Jpn*, vol. 10, pp. 15–24, 1961.

[43] A. Kucaba-Pietal, "Nonaxisymmetric stokes flow past a torus in the presence of a wall," *Archives of Mechanics*, vol. 38, no. 5-6, pp. 647–663, 1986.

[44] N. Liron and S. Mochon, "Stokes flow for a stokeslet between two parallel flat plates," *Journal of Engineering Mathematics*, vol. 10, no. 4, pp. 287–303, 1976.

[45] N. Liron and R. Shahar, "Stokes flow due to a stokeslet in a pipe," *Journal of Fluid Mechanics*, vol. 86, no. 04, pp. 727–744, 1978.

[46] T. Dabros, "A singularity method for calculating hydrodynamic forces and particle velocities in low-reynolds number flows," *Journal of Fluid Mechanics*, vol. 156, no. 1, p. 1, 1985.

[47] Y. Fan and W. W.-Y., "The stokes flow of an arbitrary prolate axisymmetric body towards an infinite plane wall," *Applied Mathematics and Mechanics*, vol. 8, no. 1, pp. 17–30, 1987.

[48] F. G. K. Odqvist, "On the boundary value problems in hydrodynamics of viscous fluids," *Math. Z*, vol. 32, pp. 329–375, 1930.

[49] G. K. Youngren and A. Acrivos, "Stokes flow past a particle of arbitrary shape: a numerical method of solution," *Journal of fluid Mechanics*, vol. 69, no. 02, pp. 377–403, 1975.

[50] P. C. Lewellen, T. A. Hatton, and E. N. Lightfoot, "Transient diffusion and reaction in solids immersed in poorly-stirred fluidsi: Numerical aspects," *Chemical Engineering Science*, vol. 37, no. 9, pp. 1325–1336, 1982.

[51] T. C. Chen and R. Skalak, "Stokes flow in a cylindrical tube containing a line of spheroidal particles," *Applied Scientific Research*, vol. 22, no. 1, pp. 403–441, 1970.

[52] H. Tözeren, "Boundary integral equation method for some stokes problems," *International Journal for Numerical Methods in Fluids*, vol. 4, no. 2, pp. 159–170, 1984.

[53] A. F. Fortes, D. D. Joseph, and T. S. Lundgren, "Nonlinear mechanics of fluidization of beds of spherical particles," *Journal of Fluid Mechanics*, vol. 177, pp. 467–483, 1987.

[54] H. H. Hu, D. D. Joseph, and M. J. Crochet, "Direct simulation of fluid particle motions," *Theoretical and Computational Fluid Dynamics*, vol. 3, no. 5, pp. 285–306, 1992.

[55] N. S. Martys, "Study of a dissipative particle dynamics based approach for modeling suspensions," *Journal of Rheology (1978-present)*, vol. 49, no. 2, pp. 401–424, 2005.

[56] A. N. Kolmogorov, "The local structure of turbulence in incompressible viscous fluid for very large reynolds numbers," in *Dokl. Akad. Nauk SSSR*, vol. 30, pp. 299–303, 1941.

[57] U. Frisch, *Turbulence: the legacy of AN Kolmogorov*. Cambridge university press, 1995.

[58] P. Spalart and S. Allmaras, "A one-equation turbulence model for aerodynamic flows," tech. rep., American Institute of Aeronautics and Astronautics, 1992.

[59] B. E. Launder and D. Spalding, "The numerical computation of turbulent flows," *Computer methods in applied mechanics and engineering*, vol. 3, no. 2, pp. 269–289, 1974.

[60] B. E. Launder, G. J. Reece, and W. Rodi, "Progress in the development of a reynolds-stress turbulence closure," *Journal of fluid mechanics*, vol. 68, no. 03, pp. 537–566, 1975.

[61] J. Smagorinsky, "General circulation experiments with the primitive equations: I. the basic experiment*," *Monthly weather review*, vol. 91, no. 3, pp. 99–164, 1963.

[62] M. Feistauer, *Mathematical methods in fluid dynamics*. Chapman & Hall/CRC, 1993.

[63] E. Arian and S. Ta'asan, "Analysis of the hessian for aerodynamic optimization: Inviscid flow," *Computers & fluids*, vol. 28, no. 7, pp. 853–877, 1999.

[64] H. Schlichting, K. Gersten, and K. Gersten, *Boundary-layer theory*. Springer, 2000.

[65] J. L.-R. d'Alembert, *Essai d'une nouvelle theorie de la resistance des fluides.-Paris, David l'aine 1752*. David l'aîné, 1752.

[66] K. Stewartson, "D'alembert's paradox," *SIAM review*, vol. 23, no. 3, pp. 308–343, 1981.

[67] G. Kirchhoff, *Vorlesungen über mathematische Physik*. BG Teubner, 1883.

[68] V. V. Kozlov and D. A. Onishchenko, "Nonintegrability of kirchhoff's equations," in *Sov. Math. Dokl*, vol. 26, pp. 495–498, 1982.

[69] B. N. Shashikanth, J. E. Marsden, J. W. Burdick, and S. D. Kelly, "The hamiltonian structure of a two-dimensional rigid circular cylinder interacting dynamically with n point vortices," *Physics of Fluids (1994-present)*, vol. 14, no. 3, pp. 1214–1227, 2002.

[70] B. Shashikanth, "Poisson brackets for the dynamically interacting system of a 2d rigid cylinder and n point vortices: the case of arbitrary smooth cylinder shapes," *Regul. Chaotic Dyn*, vol. 10, no. 1, pp. 1–14, 2005.

[71] A. V. Borisov, I. S. Mamaev, and S. M. Ramodanov, "Motion of a circular cylinder and n point vortices in a perfect fluid," *Regular and chaotic dynamics*, vol. 8, no. 4, pp. 449–462, 2003.

[72] A. V. Borisov, I. S. Mamaev, and S. M. Ramodanov, "Dynamic interaction of point vortices and a two-dimensional cylinder," *Journal of mathematical physics*, vol. 48, no. 6, p. 065403, 2007.

[73] D. Z. Zhang and A. Prosperetti, "Averaged equations for inviscid disperse two-phase flow," *Journal of Fluid Mechanics*, vol. 267, pp. 185–219, 1994.

[74] L.-S. Fan and C. Zhu, *Principles of gas-solid flows*. Cambridge University Press, 2005.

[75] D. A. Drew and S. L. Passman, *Theory of multicomponent fluids*. Springer, 1999.

[76] J. B. McLaughlin, "Numerical computation of particles-turbulence interaction," *International journal of multiphase flow*, vol. 20, pp. 211–232, 1994.

[77] M. J. Andrews and P. J. O'rourke, "The multiphase particle-in-cell (mp-pic) method for dense particulate flows," *International Journal of Multiphase Flow*, vol. 22, no. 2, pp. 379–402, 1996.

[78] D. M. Snider and P. J. O. M. J. Andrews, "Sediment flow in inclined vessels calculated using a multiphase particle-in-cell model for dense particle flows," *International Journal of Multiphase Flow*, vol. 24, no. 8, pp. 1359–1382, 1998.

[79] A. A. Johnson and T. E. Tezduyar, "3d simulation of fluid-particle interactions with the number of particles reaching 100," *Computer Methods in Applied Mechanics and Engineering*, vol. 145, no. 3, pp. 301–321, 1997.

[80] K. Sugiyama, S. Ii, S. Takeuchi, S. Takagi, and Y. Matsumoto, "A full eulerian finite difference approach for solving fluid–structure coupling problems," *Journal of Computational Physics*, vol. 230, no. 3, pp. 596–627, 2011.

[81] J. F. Brady and G. Bossis, "Stokesian dynamics," *Annual review of fluid mechanics*, vol. 20, pp. 111–157, 1988.

[82] A. S. Sangani and A. K. Didwania, "Dynamic simulations of flows of bubbly liquids at large reynolds numbers," *Journal of Fluid Mechanics*, vol. 250, pp. 307–337, 1993.

[83] T. E. Tezduyar, J. Liou, and D. K. Ganjoo, "Incompressible flow computations based on the vorticity-stream function and velocity-pressure formulations," *Computers & structures*, vol. 35, no. 4, pp. 445–472, 1990.

[84] T. E. Tezduyar, J. Liou, D. K. Ganjoo, and M. Behr, "Solution techniques for the vorticity-streamfunction formulation of two-dimensional unsteady incompressible flows," *International Journal for Numerical Methods in Fluids*, vol. 11, no. 5, pp. 515–539, 1990.

[85] H. H. Hu, "Direct simulation of flows of solid-liquid mixtures," *International Journal of Multiphase Flow*, vol. 22, no. 2, pp. 335–352, 1996.

[86] H. H. Hu, "Motion of a circular cylinder in a viscous liquid between parallel plates," *Theoretical and Computational Fluid Dynamics*, vol. 7, no. 6, pp. 441–455, 1995.

[87] J. Feng, H. H. Hu, and D. D. Joseph, "Direct simulation of initial value problems for the motion of solid bodies in a newtonian fluid. part 1. sedimentation," *Journal of Fluid Mechanics*, vol. 261, no. 95, p. 134, 1994.

[88] J. Feng, H. H. Hu, and D. D. Joseph, "Direct simulation of initial value problems for the motion of solid bodies in a newtonian fluid. part 2. couette and poiseuille flows," *Journal of Fluid Mechanics*, vol. 277, no. 271, pp. 271–301, 1994.

[89] P. Y. Huang, J. Feng, H. H. Hu, and D. D. Joseph, "Direct simulation of the motion of solid particles in couette and poiseuille flows of viscoelastic fluids," *Journal of Fluid Mechanics*, vol. 343, pp. 73–94, 1997.

[90] P. Y. Huang, H. H. Hu, and D. D. Joseph, "Direct simulation of the sedimentation of elliptic particles in oldroyd-b fluids," *Journal of Fluid Mechanics*, vol. 362, pp. 297–326, 1998.

[91] N. A. Patankar, "Numerical simulation of particulate two-phase flow," 1997.

[92] H. H. Hu, N. A. Patankar, and M. Zhu, "Direct numerical simulations of fluid–solid systems using the arbitrary lagrangian–eulerian technique," *Journal of Computational Physics*, vol. 169, no. 2, pp. 427–462, 2001.

[93] S. Chen and G. D. Doolen, "Lattice boltzmann method for fluid flows," *Annual review of fluid mechanics*, vol. 30, no. 1, pp. 329–364, 1998.

[94] O. Behrend, "Solid-fluid boundaries in particle suspension simulations via the lattice boltzmann method," *Physical Review E*, vol. 52, no. 1, p. 1164, 1995.

[95] D. Qi, "Lattice-boltzmann simulations of particles in non-zero-reynolds-number flows," *Journal of Fluid Mechanics*, vol. 385, pp. 41–62, 1999.

[96] J. Wang, X. Zhang, A. G. Bengough, and J. W. Crawford, "Domain-decomposition method for parallel lattice boltzmann simulation of incompressible flow in porous media," *Physical Review E*, vol. 72, no. 1, p. 016706, 2005.

[97] P. Ahlrichs and B. Dünweg, "Lattice-boltzmann simulation of polymer-solvent systems," *International Journal of Modern Physics C*, vol. 9, no. 08, pp. 1429–1438, 1998.

[98] D. Yu, S. Girimaji, and A. Ladd, "Revised moment propagation method for scalar transport," *Physical Review E*, vol. 78, no. 5, p. 056706, 2008.

[99] M. A. Hyman, "Non-iterative numerical solution of boundary-value problems," *Applied Scientific Research, Section B*, vol. 2, no. 1, pp. 325–351, 1952.

[100] R. Glowinski, T.-W. Pan, T. I. Hesla, and D. D. Joseph, "A distributed lagrange multiplier/fictitious domain method for particulate flows," *International Journal of Multiphase Flow*, vol. 25, no. 5, pp. 755–794, 1999.

[101] P. Singh, D. D. Joseph, T. I. Hesla, R. Glowinski, and T.-W. Pan, "A distributed lagrange multiplier/fictitious domain method for viscoelastic particulate flows," *Journal of Non-Newtonian Fluid Mechanics*, vol. 91, no. 2, pp. 165–188, 2000.

[102] C. S. Peskin, "Numerical analysis of blood flow in the heart," *Journal of computational physics*, vol. 25, no. 3, pp. 220–252, 1977.

[103] J. H. Ferziger and M. Perićn, *Computational methods for fluid dynamics*, vol. 3. Springer Berlin, 2002.

[104] T. E. Tezduyar, "Finite element methods for flow problems with moving boundaries and interfaces," *Archives of Computational Methods in Engineering*, vol. 8, no. 2, pp. 83–130, 2001.

[105] B. F. Smith, "Domain decomposition methods for partial differential equations," in *Parallel Numerical Algorithms*, pp. 225–243, Springer, 1997.

[106] C. S. Peskin, "Flow patterns around heart valves: a numerical method," *Journal of computational physics*, vol. 10, no. 2, pp. 252–271, 1972.

[107] J. Mohd-Yusof, "Combined immersed-boundary/b-spline methods for simulations of ow in complex geometries," *Annual Research Briefs. NASA Ames Research Center= Stanford University Center of Turbulence Research: Stanford*, pp. 317–327, 1997.

[108] L. Lee and R. J. LeVeque, "An immersed interface method for incompressible navier-stokes equations," *SIAM Journal on Scientific Computing*, vol. 25, no. 3, pp. 832–856, 2003.

[109] R. Glowinski, T.-W. Pan, and J. Periaux, "Distributed lagrange multiplier methods for incompressible viscous flow around moving rigid bodies," *Computer methods in applied mechanics and engineering*, vol. 151, no. 1, pp. 181–194, 1998.

[110] R. Mittal and G. Iaccarino, "Immersed boundary methods," *Annu. Rev. Fluid Mech.*, vol. 37, pp. 239–261, 2005.

[111] D. F. Martin and P. Colella, "A cell-centered adaptive projection method for the incompressible euler equations," *Journal of computational Physics*, vol. 163, no. 2, pp. 271–312, 2000.

[112] L. H. Howell and J. B. Bell, "An adaptive mesh projection method for viscous incompressible flow," *SIAM Journal on Scientific Computing*, vol. 18, no. 4, pp. 996–1013, 1997.

[113] D. DeZeeuw and K. G. Powell, "An adaptively refined cartesian mesh solver for the euler equations," *Journal of Computational Physics*, vol. 104, no. 1, pp. 56–68, 1993.

[114] H. S. Udaykumar, W. Shyy, and M. M. Rao, "Elafint: a mixed eulerian–lagrangian method for fluid flows with complex and moving boundaries," *International journal for numerical methods in fluids*, vol. 22, no. 8, pp. 691–712, 1996.

[115] D. M. Ingram, D. M. Causon, and C. G. Mingham, "Developments in cartesian cut cell methods," *Mathematics and Computers in Simulation*, vol. 61, no. 3, pp. 561–572, 2003.

[116] H. Samet, "Applications of spatial data structures," 1990.

[117] A. M. Khokhlov, "Fully threaded tree algorithms for adaptive refinement fluid dynamics simulations," *Journal of Computational Physics*, vol. 143, no. 2, pp. 519–543, 1998.

[118] D. Fuster, G. Agbaglah, C. Josserand, S. Popinet, and S. Zaleski, "Numerical simulation of droplets, bubbles and waves: state of the art," *Fluid dynamics research*, vol. 41, no. 6, p. 065001, 2009.

[119] D. Fuster, J.-P. Matas, S. Marty, S. Popinet, J. Hoepffner, A. Cartellier, and S. Zaleski, "Instability regimes in the primary breakup region of planar coflowing sheets," *Journal of Fluid Mechanics*, vol. 736, pp. 150–176, 2013.

[120] G. Tomar, D. Fuster, S. Zaleski, and S. Popinet, "Multiscale simulations of primary atomization," *Computers & Fluids*, vol. 39, no. 10, pp. 1864–1874, 2010.

[121] R. B. Bird, W. E. Stewart, and E. N. Lightfoot, *Transport phenomena*. John Wiley & Sons, 2007.

[122] H. Johansen and P. Colella, "A cartesian grid embedded boundary method for poisson's equation on irregular domains," *Journal of Computational Physics*, vol. 147, no. 1, pp. 60–85, 1998.

[123] J. Bladel, "On helmholtz's theorem in finite regions," *Antennas and Propagation, IRE Transactions on*, vol. 7, pp. 119–119, December 1959.

[124] W. J. Coirier, *An adaptively-refined, Cartesian, cell-based scheme for the Euler and Navier-Stokes equations*. PhD thesis, Citeseer, 1994.

[125] R. C. Gonzalez and R. E. Woods, "Digital image processing," 2002.

[126] M. J. Aftosmis, M. J. Berger, and J. E. Melton, "Robust and efficient cartesian mesh generation for component-based geometry," *AIAA journal*, vol. 36, no. 6, pp. 952–960, 1998.

[127] M. J. Berger and P. Colella, "Local adaptive mesh refinement for shock hydrodynamics," *Journal of computational Physics*, vol. 82, no. 1, pp. 64–84, 1989.

[128] J. B. Bell, P. Colella, and H. M. Glaz, "A second-order projection method for the incompressible navier-stokes equations," *Journal of Computational Physics*, vol. 85, no. 2, pp. 257–283, 1989.

[129] R. Smith *et al.*, "Open dynamics engine," 2005.

[130] J. B. Kuipers, *Quaternions and rotation sequences*, vol. 66. Princeton university press Princeton, 1999.

[131] R. Clift, J. R. Grace, and M. E. Weber, *Bubbles, drops, and particles*. Courier Dover Publications, 2005.

[132] H. Sakamoto and H. Haniu, "A study on vortex shedding from spheres in a uniform flow," *Journal of Fluids Engineering*, vol. 112, no. 4, pp. 386–392, 1990.

[133] H. Ramkissoon and S. Majumdar, "Drag on an axially symmetric body in the stokes flow of micropolar fluid," *Physics of Fluids (1958-1988)*, vol. 19, no. 1, pp. 16–21, 1976.

[134] X. Xinsheng and W. Minzhong, "General complete solutions of the equations of spatial and axisymmetric stokes flow," *The Quarterly Journal of Mechanics and Applied Mathematics*, vol. 44, no. 4, pp. 537–548, 1991.

[135] H. J. Keh and C. H. Huang, "Slow motion of axisymmetric slip particles along their axes of revolution," *International journal of engineering science*, vol. 42, no. 15, pp. 1621–1644, 2004.

[136] B. Ho and L. Leal, "Inertial migration of rigid spheres in two-dimensional unidirectional flows," *Journal of fluid mechanics*, vol. 65, no. 02, pp. 365–400, 1974.

[137] P. Cherukat and J. B. McLaughlin, "The inertial lift on a rigid sphere in a linear shear flow field near a flat wall," *Journal of Fluid Mechanics*, vol. 263, pp. 1–18, 1994.

[138] D. Leighton and A. Acrivos, "The lift on a small sphere touching a plane in the presence of a simple shear flow," *Zeitschrift für angewandte Mathematik und Physik ZAMP*, vol. 36, no. 1, pp. 174–178, 1985.

[139] Z. Yu, N. Phan-Thien, and R. I. Tanner, "Dynamic simulation of sphere motion in a vertical tube," *Journal of Fluid Mechanics*, vol. 518, pp. 61–93, 2004.

[140] J. D. Anderson Jr, "Ludwig prandtls boundary layer," *Physics Today*, vol. 58, no. 12, pp. 42–48, 2005.

[141] L. Arnold and V. Wihstutz, *Lyapunov exponents: a survey*. Springer, 1986.

[142] A. Wolf, J. B. Swift, H. L. Swinney, and J. A. Vastano, "Determining lyapunov exponents from a time series," *Physica D: Nonlinear Phenomena*, vol. 16, no. 3, pp. 285–317, 1985.

[143] M. T. Rosenstein, J. J. Collins, and C. J. De Luca, "A practical method for calculating largest lyapunov exponents from small data sets," *Physica D: Nonlinear Phenomena*, vol. 65, no. 1, pp. 117–134, 1993.

[144] E. N. Lorenz, "Deterministic nonperiodic flow," *Journal of the atmospheric sciences*, vol. 20, no. 2, pp. 130–141, 1963.

[145] O. E. Rössler, "An equation for continuous chaos," *Physics Letters A*, vol. 57, no. 5, pp. 397–398, 1976.

[146] E. Gavze, M. Pinsky, and A. Khain, “The orientations of prolate ellipsoids in linear shear flows,” *Journal of Fluid Mechanics*, vol. 690, pp. 51–93, 2012.